SANDIA REPORT
SAND2011-6845
Unlimited Release
Printed December 2011

Modeling Ramp Compression Experiments using Large-Scale Molecular Dynamics Simulation

Aidan P. Thompson, J. Matthew D. Lane, Jonathan Zimmerman, Michael P. Desjarlais, Gary S. Grest, Reese E. Jones, Thomas R. Mattsson, Jeremy A. Templeton

Prepared by
Sandia National Laboratories
Albuquerque, New Mexico 87185 and Livermore, California 94550

Sandia National Laboratories is a multi-program laboratory managed and operated by Sandia Corporation, a wholly owned subsidiary of Lockheed Martin Corporation, for the U.S. Department of Energy's National Nuclear Security Administration under contract DE-AC04-94AL85000.

Approved for public release; further dissemination unlimited.

Sandia National Laboratories

Issued by Sandia National Laboratories, operated for the United States Department of Energy by Sandia Corporation.

NOTICE: This report was prepared as an account of work sponsored by an agency of the United States Government. Neither the United States Government, nor any agency thereof, nor any of their employees, nor any of their contractors, subcontractors, or their employees, make any warranty, express or implied, or assume any legal liability or responsibility for the accuracy, completeness, or usefulness of any information, apparatus, product, or process disclosed, or represent that its use would not infringe privately owned rights. Reference herein to any specific commercial product, process, or service by trade name, trademark, manufacturer, or otherwise, does not necessarily constitute or imply its endorsement, recommendation, or favoring by the United States Government, any agency thereof, or any of their contractors or subcontractors. The views and opinions expressed herein do not necessarily state or reflect those of the United States Government, any agency thereof, or any of their contractors.

Printed in the United States of America. This report has been reproduced directly from the best available copy.

Available to DOE and DOE contractors from
U.S. Department of Energy
Office of Scientific and Technical Information
P.O. Box 62
Oak Ridge, TN 37831

Telephone: (865) 576-8401
Facsimile: (865) 576-5728
E-Mail: reports@adonis.osti.gov
Online ordering: http://www.osti.gov/bridge

Available to the public from
U.S. Department of Commerce
National Technical Information Service
5285 Port Royal Rd.
Springfield, VA 22161

Telephone: (800) 553-6847
Facsimile: (703) 605-6900
E-Mail: orders@ntis.fedworld.gov
Online order: http://www.ntis.gov/help/ordermethods.asp?loc=7-4-0#online

SAND2011–6845
Unlimited Release
Printed December 2011

Modeling Ramp Compression Experiments using Large-Scale Molecular Dynamics Simulation

Aidan P. Thompson, J. Matthew D. Lane, Jonathan Zimmerman,
Michael P. Desjarlais, Gary S. Grest, Reese E. Jones, Thomas R. Mattsson, Jeremy A. Templeton

Sandia National Laboratories
P.O. Box 5800
Albuquerque, NM 87185-1322
athomps@sandia.gov

Todd Ditmire, Hernan Quevedo

Center for High Energy Density Science The University of Texas at Austin

Michael I. Baskes

University of California, San Diego

Yogendra M. Gupta, J. Michael Winey

Institute for Shock Physics Washington State University

Abstract

Molecular dynamics simulation (MD) is an invaluable tool for studying problems sensitive to atom-scale physics such as structural transitions, discontinuous interfaces, non-equilibrium dynamics, and elastic-plastic deformation. In order to apply this method to modeling of ramp-compression experiments, several challenges must be overcome: accuracy of interatomic potentials, length- and time-scales, and extraction of continuum quantities. We have completed a 3 year LDRD project with the goal of developing molecular dynamics simulation capabilities for modeling the response of materials to ramp compression. The techniques we have developed fall in to three categories (i) molecular dynamics methods (ii) interatomic potentials (iii) calculation of continuum variables. Highlights include the development of an accurate interatomic potential describing shock-melting of Beryllium, a scaling technique for modeling slow ramp compression experiments using fast ramp MD simulations, and a technique for extracting plastic strain from MD simulations. All of these methods have been implemented in Sandia's LAMMPS MD code, ensuring their widespread availability to dynamic materials research at Sandia and elsewhere.

Contents

I Shock Compression **7**

1 Dynamic compression of polymers **8**

1.1 Introduction . . . 8

1.2 Methodology . . . 10

Density Functional Theory with AM05 . . . 10

Classical reactive interaction potentials . . . 11

Classical non-reactive interaction potentials . . . 11

Construction of the simulation cells . . . 13

1.3 Modeling shock response . . . 15

1.4 Results in dense polymer . . . 16

Shock Hugoniot . . . 16

Chemical structure/dissociation . . . 20

1.5 Results in polymer foam . . . 23

Shock Hugoniot . . . 24

Shock temperature and void collapse . . . 25

1.6 Conclusions . . . 26

2 Dynamic compression of silicon and germanium **28**

2.1 Introduction and methods . . . 28

2.2 Results and discussion . . . 30

2.3 Conclusion . . . 33

3 Laser-driven dynamic melting of silicon **34**

3.1 Introduction . . . 34

3.2 Experimental setup . . . 35

3.3 Results . . . 38

3.4 Conclusions . . . 43

3.5 Appendix . . . 44

4 Dynamic compression of aluminum **47**

4.1 Introduction . . . 47

4.2 Computational Methods . . . 48

MD Simulations . . . 48

Continuum Variables from MD Simulations . . . 48

Nonlinear Elastic Continuum Calculations . . . 49

4.3 Results . . . 51

Elastic shock wave profiles . . . 51
[100] Compression . . . 53
[111] Compression . . . 63
[110] Compression . . . 68
Temperature Calculations . . . 72
4.4 Discussion . . . 72
4.5 Concluding Remarks . . . 75

II Ramp Compression **76**

5 Dynamic Compression of Beryllium **77**
5.1 Introduction . . . 77
5.2 Physical Properties . . . 77
5.3 Phase Diagram . . . 79
5.4 Dynamic Compression . . . 80

6 Time-Position Scaling relation in ramp-loading **88**
6.1 Introduction . . . 88
6.2 Method of characteristics . . . 88
6.3 Method of scaling . . . 96
Kinematic and dynamic similarity . . . 97
Invariance in the wave equation . . . 98
Ramp scaling in the nonlinear elastic response regime . . . 100
Ramp scaling in the plastic response regime . . . 100

III Methods **106**

7 Continuum Properties **107**
7.1 Eulerian Atomistic-Continuum Formulation by Hardy . . . 107
Balance Laws . . . 108
Densities and Localization . . . 108
Energy and Force Assumptions . . . 109
Continuum Expressions . . . 110
7.2 Lagrangian Atomistic-Continuum Formulation . . . 111
Balance Laws . . . 111
Densities and Localization . . . 111
Energy and Force Assumptions . . . 112
Continuum Expressions . . . 112

7.3 Evaluation and Comparison of Spatial and Material Frame Expressions . . . 113
Stress for a constrained finite temperature system . . . 113
Finite temperature deformation . . . 115
Tensile stretching of a center-cracked body . . . 116
7.4 Cauchy-Born Stress and Free Energy Calculation . . . 122
Quasi-harmonic Cauchy-Born model . . . 122
Quasi-harmonic model for pairwise potentials . . . 125
Quasi-harmonic model for EAM potentials . . . 125
Examples of free energy and Cauchy-Born stress calculation . . . 127
7.5 Plastic Deformation Gradients . . . 132
Incremental Approach . . . 132
Total Strain Approach . . . 133
Example calculation: uniaxial stretching . . . 134
Appendix: Thermodynamic integration . . . 137

8 New Methods in LAMMPS 139
8.1 The LAMMPS SHOCK Package . . . 139
Hugoniostat (`fix nphug`) . . . 139
Multiscale Simulation Technique (`fix msst`) . . . 142
Direct Ramp-loading (`fix wall/piston`) . . . 145
Material addition and removal (`fix append_atoms`) . . . 146
8.2 Extensions to ATC package . . . 147

9 Communications 154
9.1 Publications . . . 154
9.2 Presentations . . . 154

10 Acknowledgements 156

Part I
Shock Compression

1 Dynamic compression of polymers

Principal Authors: Thomas R. Mattsson and J. Matthew D. Lane

This section contains a paper entitled "First-Principles and Classical Molecular Dynamics Simulation of Shock Polymers " that was published in *Phys. Rev. B* in 2010. It was authored by Thomas R. Mattsson, J. Matthew D. Lane, Kyle. R. Cochrane, Michael P. Desjarlais, Aidan P. Thompson, Flint Pierce, and Gary S. Grest. [SAND 2009-3918 J]

Abstract

Organic polymers and nanocomposites are increasingly being subjected to extreme environments. Molecular-scale modeling of these materials offers insight into failure mechanisms and response. Density functional theory (DFT) molecular dynamics (MD) and classical MD simulations of the principal shock Hugoniot are presented for two hydrocarbon polymers, polyethylene (PE) and poly(4-methyl-1-pentene) (PMP). DFT results are in excellent agreement with experiment data, which is currently available up to 80 GPa. Further, we predict the PE and PMP Hugoniots up to 350 GPa and 200 GPa, respectively. For comparison, we studied two reactive and two non-reactive interaction potentials. For the latter, the exp-6 interaction of Borodin *et al.* showed much better agreement with experiment than OPLS. For the reactive force fields, ReaxFF displayed decidedly better agreement than AIREBO. For shocks above 50 GPa, only the DFT results are of high fidelity, establishing DFT as a reliable method for shocked macromolecular systems. We extend these results to include low-density polymer foams using NEMD techniques. We find good quantitative agreement with both experiment and hydrocode simulations. Further, we have measured local temperatures to investigate the formation of hot spots and polymer dissociation near foam voids.

1.1 Introduction

Over the last few years, first-principles simulations in combination with increasingly accurate shock experiments at multi-Mbar pressure have yielded important insights into how matter behaves under extreme conditions. While comprehensive advances have been made for many light elements, for example deuterium [2, 3] and carbon [4], progress has been slower for equally important, albeit more challenging, materials like molecular crystals and polymers [5].

Modeling a macro-molecular material requires trade-offs in system size and fidelity of the atomic interaction. It is not clear *a priori* how to best strike the balance between the competing requirements, since the critical variable determining system response may in some cases be the size-specific structure/geometry, or in other cases the bond reactivity and interaction fidelity. In order to resolve this important question, we have simulated shock compression of two different polymers using first-principles Density Functional Theory [6] (DFT) and classical molecular dynamics (MD) simulations using four different interaction potentials: ReaxFF [7], AIREBO [8], OPLS [9], and Borodin *et al.*'s exp-6 potentials [10].

Polymer foam is a crucial part of the dynamic hohlraum platform used to generate intense x-ray radiation at Sandia's Z-machine [11–13] and designs for Inertial Confined Fusion (ICF) often involve foams. As experimental designs are being refined – primarily as a result of an interplay between radiation-hydrodynamics

modeling, improved diagnostics, and improved drivers – the importance of having accurate material models based on a fundamental understanding of the material's behavior is becoming increasingly clear. Modeling both the qualitative and quantitative aspects of shock propagation in polymers and polymer foams is therefore of significant importance.

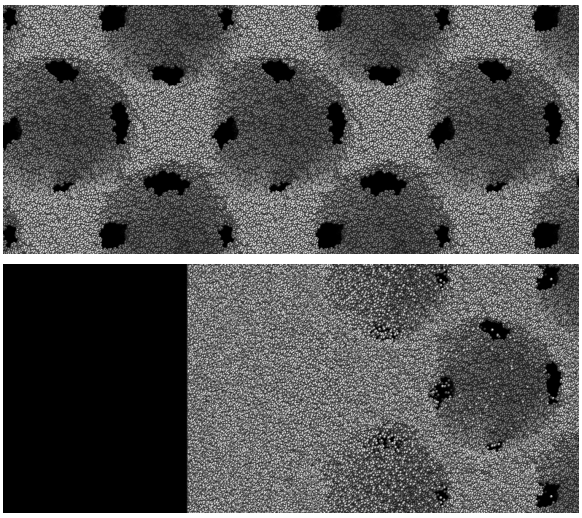

Figure 1: Simulation snapshots of the initial foam structure (top) and of the propagating shock front (bottom). The shock shown is strong enough to dissociate the atoms of the polymer, which can be seen vaporized within the void space ahead of the front. The snapshots are shaded to indicate depth. Black spaces are areas in which void mergers allow unobstructed views through the entire sample.

For generality, we chose to study two polymers, polyethylene (PE) and poly(4-methyl-1-pentene) (PMP or TPX). PE is an extensively used general-purpose plastic with the simplest possible linear alkane structure. Atactic PMP is commonly used in shock studies as a low-density polymer foam and has specialized applications in target materials for inertially confined fusion (ICF) studies. PMP is a branched alkane with a bulky side chain. The two polymers were selected to be representative of two different classes of polymers, as PMP is amorphous at room temperature, while PE is semi-crystalline. We believe the results are likely to be widely applicable to other macromolecular materials. Several experimental studies of shocked PE have been reported [14–17] in addition to the quantitative data for both PE and PMP from the LASL shock handbook [18].

In expanding our work to foams, we note the inherent difficulty presented by the multiple length scales responsible for the shock response in foams. In addition to the atomic length scale response which we have shown DFT and MD can capture well, foams introduce the larger scale of the void structure, wall thickness, and even longer range density inhomogeneity within samples. The likely need to model these larger scales drove us to shift our modeling from DFT/MD to MD/Mesoscale. Thus, although DFT was notably successful in modeling dense polymers, we did not apply these techniques to foam systems. On the mesoscale we report briefly on continuum hydrocode results for comparison with MD. Complete continuum analysis [19] and experimental results [20] will be reported elsewhere.

1.2 Methodology

While DFT is a computationally costly method in which it is necessary to reduce the number of simulation atoms to several hundred at most, it allows for a high-fidelity description of chemical bonds and inter-atomic

repulsion. Reactive force-fields like ReaxFF [7] and AIREBO [8], which have been applied to study shocks in hydrocarbons [21–23], cannot accurately capture the range of responses compared to DFT, however they allow for chemical reactions and significantly larger system sizes. Non-reactive force-fields, like the OPLS potential of Jorgensen *et al.* [9] and the exp-6 potential of Borodin *et al.* [10], are computationally much more efficient and allow for even larger system sizes, but do not allow covalent bonds to break or form, which can become important for strong shocks. The relative speed of the different methods is naturally of interest, OPLS and exp-6 are the fastest potentials, AIREBO is approximately twice as slow while ReaxFF is 30 times slower than OPLS and exp-6. All classical MD simulations were run in LAMMPS [1, 24] while the DFT-MD simulations were performed with VASP 5.1.40 [25, 26].

1.2.1 Density Functional Theory with AM05

DFT is a formally exact representation of the Schrödinger equation. However, in practice, the choice of exchange-correlation functional determines the accuracy. We employed the recently developed multi-purpose Armiento-Mattsson (AM05) functional [27], it is a functional with no empirically determined parameters. It improves upon the local density approximation (LDA) by reproducing two model systems with known solutions: the uniform electron gas and the surface jellium [27, 28]. AM05 has demonstrated high fidelity for many solids [28, 29]; in reference [28], the performance of seven functionals was compared for twenty representative semiconductors, simple metals, transition metals, alkali-halides, and oxides. For AM05, the prediction bias (mean average error) in lattice constant is small while LDA and PBE both exhibit significant bias. On average, AM05 is better than choosing between LDA and PBE for each solid separately (Table I of reference [28]) and does as well as the decidedly more computationally demanding hybrid functionals studied in Refs. [30] and [31]. Furthermore, AM05 also works well for hydrogen bonding in the water dimer [32] and for chemical reaction energies for a large number of molecular reactions [33].

Both polyethylene and poly(4-methyl-1-pentene) are materials where van der Waals forces are important. Although previous work using DFT by Byrd and Rice demonstrated a difficulty in modeling energetic molecular solids at low pressure, they found an increasing accuracy as the external pressure increases [34], and the behavior under strong shocks is dominated by the high pressure response. Furthermore, the lack of van der Waals attraction in AM05 [29] makes it decidedly different from most other exchange-correlation functionals. Since the functional displays a monotonic behavior upon expansion and compression [29], it is arguably suitable for studying compression in van der Waals systems. The applicability of AM05 to shocked energetic materials will be the subject of future work [35].

Finally, AM05 was recently the best suited functional to model quartz [36] up to 1 TPa in the development of a high-pressure shock impedance standard. Taken together, there are ample reasons not only to employ AM05, but to expect high-fidelity results for shock compression.

The DFT-MD simulations were performed with VASP 5.1.40 [25, 26] using stringent convergence settings [3, 37, 38]. The plane wave cutoff was above 800 eV in order to converge the stress-tensor [3, 39]. Pulay errors are minimal due to the high cutoff and the appreciable changes in volume for the different calculations along the Hugoniot [40]. The ionic timestep is between 0.1 and 0.5 fs depending on temperature. Steady-state simulations in the NVT ensemble used a Nosé-Hoover thermostat with a time-constant of 80 timesteps. Velocities were scaled to control temperature in the ramped-temperature simulations. Partition of kinetic energy between hydrogen and carbon was verified by monitoring the temperature for each element separately [41]. Complex k-point sampling with mean-value point $(\frac{1}{4},\frac{1}{4},\frac{1}{4})$ was used due to its high accuracy for disordered structures at high temperature. Electronic states were occupied according to Mermin's

finite-temperature formulation of DFT [42], a factor that is particularly important in the warm-dense matter regime where electrons thermal excitations are significant.

1.2.2 Classical reactive interaction potentials

ReaxFF and AIREBO are reactive potentials which allow the possibility of dynamic bond formation and breaking. ReaxFF uses bond-order and charge equilibration to model local chemical changes. It has been used to simulate a wide variety of materials and processes, including molecular solids under shock and detonation [23, 43, 44]. AIREBO is based on Brenner's REBO potential augmented with explicit 6-12 dispersion terms and has previously been used to model shock propagation in short chain hydrocarbons [22, 45].

Both the AIREBO and ReaxFF calculations were performed using the standard LAMMPS parallel implementations [1], which have been validated against the original serial codes. For AIREBO, a 10.2 Å cutoff was used. For ReaxFF, a 10 Å cutoff was used and the charge equilibration convergence tolerance was set to 10^{-6}. The specific form of the ReaxFF potential in LAMMPS is described in Chenoweth et al. [7]. The ReaxFF parameter values are the same as those used by Strachan et al. [43].

1.2.3 Classical non-reactive interaction potentials

The OPLS and exp-6 potentials have pre-assigned non-breakable bonds. In these potentials, interactions within and between molecules are described by a set of atomic potentials which include van der Waals, electrostatic, molecular bond, angle, and torsion interaction terms.

$$U_{tot} = U_{\text{nonbond}} + U_{\text{bond}} + U_{\text{ang}} + U_{\text{tor}} \tag{1}$$

where U_{nonbond} is the sum of the van der Waals and Coulomb potentials. The bond potential and angle potential are harmonic. The dihedral potentials for the OPLS and exp-6 force fields differ only slightly in form.

An important difference between these potentials is in the form of the nonbonded interactions. The OPLS nonbonded potential is composed of standard 12-6 Lennard-Jones (LJ) and Coulomb potentials [9,46], while the exp-6 force field of Borodin *et al.* [47, 48] utilizes a Buckingham exponential-6 form for the nonbonded pair potential. Nonbonded interactions are calculated between all atom pairs within different molecules and between distant atoms within the same molecule. The respective functional forms are

$$U_{\text{nonbond}}^{\text{OPLS}} = 4\epsilon_{ij}\left[\left(\frac{\sigma_{ij}}{r_{ij}}\right)^{12} - \left(\frac{\sigma_{ij}}{r_{ij}}\right)^{6}\right] + k_{\text{coul}}\frac{q_i q_j}{r_{ij}} \tag{2}$$

and

$$U_{\text{nonbond}}^{\text{exp-6}} = A_{ij}\exp(-B_{ij}r_{ij}) - \frac{C_{ij}}{r_{ij}^6} \tag{3}$$

where ϵ_{ij} sets the energy scale, σ_{ij} sets the separation scale for the ij pair, q is partial charge. A_{ij} is the strength of the potential's repulsive component, B_{ij}^{-1} is the characteristic decay length, and C_{ij} indicates the strength and range of the attractive component. The atoms in the exp-6 potential are uncharged. Both potentials were cut off at 12 Å for the large simulation cells. An 8 Å cutoff was used to equilibrate the

smallest PMP system before running in DFT. The different behavior under compression is shown in Fig 2 and is a most likely reason for the stark differences in shock pressure between the two.

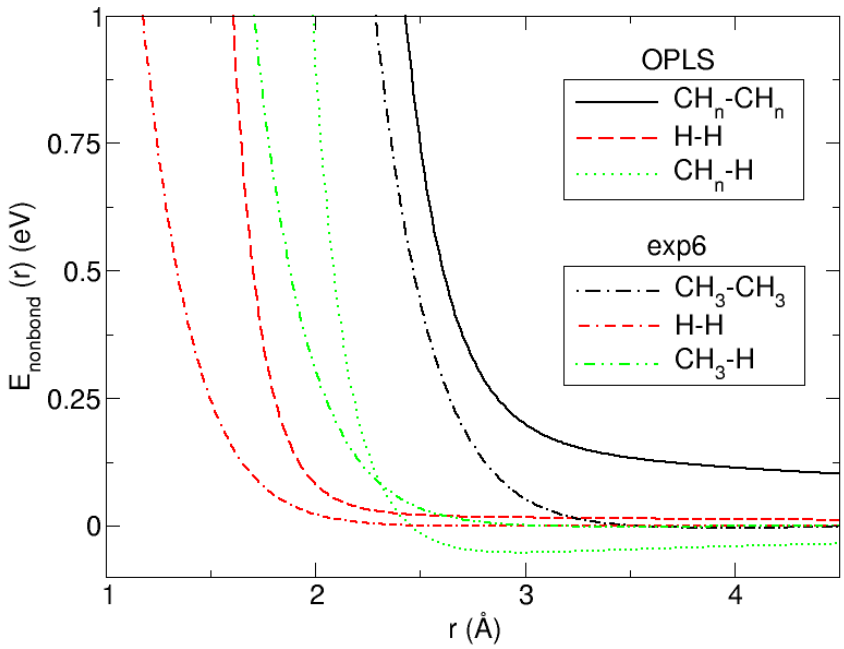

Figure 2: Nonbonded contributions to the OPLS and exp-6 potential for C-C, C-H, and H-H. For C-H and H-H pairs, the OPLS repulsive component is significantly larger than for exp-6 potential, with the largest difference being in H-H.

Long-range Coulomb corrections were included using the Particle-Particle-Particle-Mesh (PPPM) method [49]. A complete set of OPLS and exp-6 force-field paramaters used in this study can be found in reference [50].

1.2.4 Construction of the simulation cells

Polyethylene (PE)

Two periodic crystalline PE samples of different sizes were constructed. The larger sample was built using Accelrys Materials Studio [51] with the polymer builder module and converted to a LAMMPS data structure. It consisted of 168 chains of $C_{44}H_{88}$ in a triangular lattice. This larger system, with 22,176 atoms, was used for all four classical potentials. For each potential, the sample was re-equilibrated at 300 K and constant pressure to produce an initial state for the shock runs. The initial densities for the shock-ready PE samples were $\rho_{0,\mathrm{OPLS}} = 0.986\,\mathrm{g/cm^3}$, $\rho_{0,\mathrm{exp-6}} = 0.962\,\mathrm{g/cm^3}$, $\rho_{0,\mathrm{ReaxFF}} = 0.930\,\mathrm{g/cm^3}$, and $\rho_{0,\mathrm{AIREBO}} = 0.915\,\mathrm{g/cm^3}$.

The smaller crystalline PE sample used in the DFT simulations was built entirely within VASP. It consisted of 4 chains of hexadecane, $C_{16}H_{34}$ with 200 total atoms in a tetragonal unit cell. To produce the reference state the unit cell lattice c/a ratio was adjusted in steps until the stress was minimized while maintaining volume at a density of $\rho_{0,\mathrm{DFT}} = 0.955\,\mathrm{g/cm^3}$. Reference energy and pressure were obtained by equilibration for 11 ps.

Poly(4-methyl-1-pentene) (PMP)

Two periodic amorphous PMP samples of different sizes were constructed. Both samples were built using Accelrys Materials Studio with the polymer and amorphous cell builder modules and converted either to a LAMMPS or VASP data structure. The larger sample consisted of 50 atactic chains of 50 repeat units for a total of 45,100 atoms. Equilibrated samples at pressure of 1 bar and $T = 300K$ were produced for each classical potential. The OPLS sample was obtained by equilibrating at 600 K for 5 ns and cooling to 300 K over 15 ns at a constant pressure of 1 bar. The exp-6 shock-ready state was reequilibrated for 3 ns from the OPLS state. Similarly, the AIREBO and ReaxFF systems were obtained from the equilibrated exp-6 system. The initial densities for the shock-ready PMP samples were $\rho_{0,\mathrm{OPLS}} = 0.822\,\mathrm{g/cm^3}$, $\rho_{0,\mathrm{exp-6}} = 0.829\,\mathrm{g/cm^3}$, $\rho_{0,\mathrm{ReaxFF}} = 0.801\,\mathrm{g/cm^3}$, and $\rho_{0,\mathrm{AIREBO}} = 0.756\,\mathrm{g/cm^3}$. This underestimation of $\rho_{0,\mathrm{AIREBO}}$ for AIREBO is consistent with previous results that found that this potential overestimated the pressure at ambient density for a number of short linear and branched alkanes [8,52]. A generalization [52] of AIREBO which allows the LJ σ and ϵ parameters to each depend on local hybridization has been shown to predict more accurately the pressure at ambient density. However since it still employs the LJ 12-6 form for the interaction, it is not likely to do significantly better at high density than the original version.

The smaller sample consisted of 440 atoms in 4 atactic chains of 6 repeat units in a cubic cell. This sample was equilibrated at 600 K, then cooled to 300 K over 1-2 ns with the exp-6 potential. Two geometries each served as input to the DFT simulations. One was re-thermalized in VASP at 500 K then cooled to 300 K, the second was continued directly. The energy shift from this initial exp-6 equilibrated state to the DFT equilibrated state was less than 10 meV/atom (from -5.6799 to -5.6808 eV/atom). Thus near ambient conditions ($\rho_{0,\mathrm{DFT}} = 0.83\,\mathrm{g/cm^3}$), the DFT methods and non-reactive classical potentials produce nearly identical reference configurations.

Foam PMP systems

PMP foam samples of several densities were created by introducing appropriately sized voids into a dense polymer sample. Our construction methods for the dense polymer have been previously reported [53]. Voids were introduced by growing spherical inclusions at a temperature of 400 K. The system was run at constant pressure in an NPT ensemble. This allowed the overall dimensions of the simulation cell to expand as the inclusions grew. The samples used in this work contained 400 chains of 50 repeat runs or 360,800 atoms. The voids were formed in a regular face center cubic lattice. When the void expansion was completed, the samples were cooled to 300 K over 1 ns, the inclusions were removed and the systems were allowed to equilibrate. The final densities of foam used in this study were 0.245 g/cc and 0.300 g/cc, compared to a bulk polymer density of 0.801 g/cc [53]. The final size of the foam sample was approximately $20 \times 20 \times 20$ nm. Larger samples, of 1.44 million atoms, suitable for shock propagation were produced by replicating these cubical foams to produce elongated samples with dimensions of approximately $20 \times 20 \times 80$ nm. A sample system is shown at the top of Figure 1.

The 0.300 g/cc foam, on which we will concentrate, had voids of radius of 8 nm. During equilibration, these voids shrunk slightly, and opened into each other, so that both the void and the polymer were contiguously connected across the samples.

1.3 Modeling shock response

A shock changes the thermodynamic state of a material; the density ρ, pressure P, internal energy U, and temperature T all jump to new values behind the shock front. Although the detailed time-resolved behavior of a shock wave is complex, the Hugoniot state itself is a state in thermodynamic equilibrium with well-

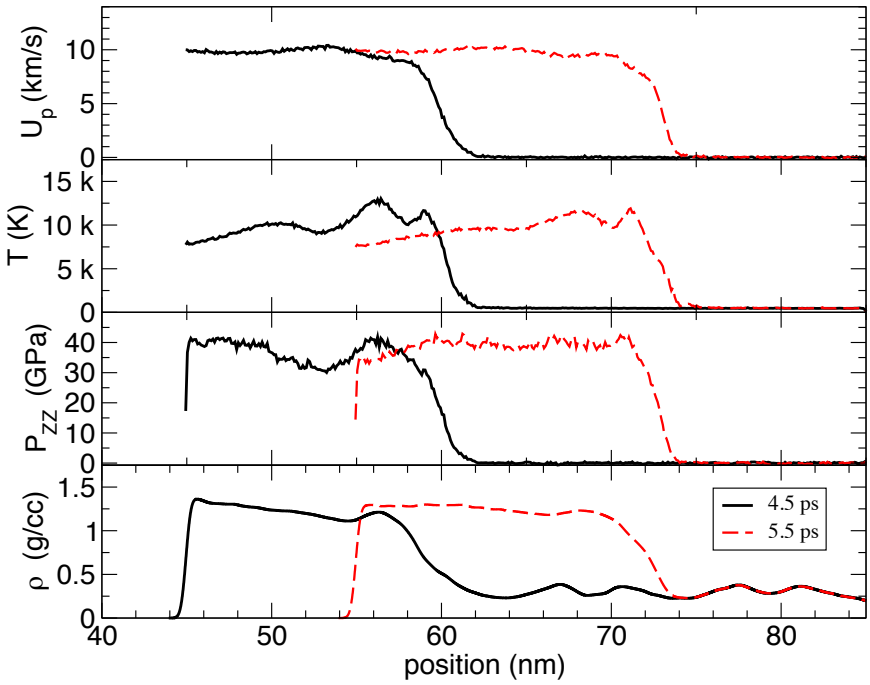

Figure 3: One-dimensional spatial profiles of the propagating shock, with piston velocity of 10 km/s, in 0.3 g/cc PMP foam after 4.5 ps (solid) and 5.5 ps (dashed).

defined thermodynamic properties. We have used two methods to determine the shocked state.

In all DFT simulations, the principal Hugoniot curve is mapped by applying the hydrostatic Rankine-Hugoniot equation

$$(U - U_0) = \frac{1}{2}(P + P_0)(V_0 - V), \tag{4}$$

which is valid for a solid when the applied stress greatly exceeds the yield stress [54]. It relates the final thermodynamic state variables far behind a planar shock wave for a given set of initial thermodynamic state variables. These thermodynamic variables are the initial and final internal energies U_0 and U, respectively; the pressures P_0 and P; and, the volumes V_0 and V.

The DFT Hugoniot points were found using an iterative compression procedure beginning from an equilibrated initial reference state. To determine each Hugoniot state point, the system was instantaneously compressed isotropically and allowed to equilibrate. The ionic- and electronic temperatures are then ramped at a rate of between 0.3-1.0 K/fs, depending on the temperature range, until the *sampled* thermodynamic variables satisfied Eq. 4. To verify these ramped-temperature Hugoniot points, several densities were simulated for long times (tens of ps) in the NVT ensemble, at temperatures just above and below the Hugoniot temperature allowing the Hugoniot pressure to be interpolated.

Classical MD Hugoniot points were produced using a modification of the constant stress uniaxial Hugoniostat (NP$_{zz}$Hug) method of Ravelo *et al.* [55], replacing their integral feedback (Nose-Hoover dynamics) with linear feedback (Berendsen dynamics), in order to avoid oscillatary transients. The relaxation time constants were set to 200 ps for the non-reactive potentials and 20 ps for the reactive potentials. Simulation durations varied depending on the potentials (ranging from 200 ps to 2 ns), and were selected to guarantee that steady final strains and internal energies had reached the values predicted by Eq. 4.

For the foam systems shock waves were driven by moving a warm momentum mirror into the sample,

using nonequilibrium molecular dynamics (NEMD). The sample was initially thermalized at 300 K and had periodic boundary conditions in the directions transverse to the shock propagation. The free surface opposite the piston was frozen to prevent surface relaxation. The simulation duration depended on the speed of shock propagation, but was typically on the order of tens of picoseconds. Simulations were run on 800 processors of Sandia's Red Sky supercomputer for four days per Hugoniot point. The shock strength was controlled by setting the piston velocity, which was held constant throughout the simulations. Piston velocities ranged from 10 km/s to 30 km/s. These velocities produced pressures ranging from tens to hundreds of GPa. All observables were calculated by averaging per-atom quantities over 1 Å wide bands perpendicular to the propagation direction.

Since the modeling methods required slightly different procedures for MD versus DFT calculations, we verified that the results were not overly sensitive to these differences. For example, for the exp-6 potential at target pressures of 40 GPa for PMP, we found that using the DFT procedure (i.e. a single compression stage followed by a temperature ramp) applied to the MD system gave Hugoniot pressures within 1.5% of the result of the Hugoniostat procedure.

All MD simulations were run with the LAMMPS parallel molecular dynamics code [1,24]. The numerical integration was performed using the velocity Verlet algorithm with a time step of 0.025 fs. Even at the highest temperatures, our 0.025 fs was sufficiently small. Select simulations, which were rerun with a 5 times smaller timestep, showed identical results.

1.4 Results in dense polymer

In traditional flyer plate impact experiments, the pressure and density can be straightforwardly deduced from measurements of shock transit times and/or direct shock speeds in combination with shock impedance matching using a known standard [36]. Measuring the temperature, on the other hand, remains a sizeable experimental challenge. In simulations, thermodynamic variables like temperature, internal energy, pressure, and specific heat are readily accessible. While the calculated pressure/density relationship of the principal Hugoniot can be directly compared to experiments, the resulting calculated shock temperatures are used to better understand the final state as well as develop equation of state models. The chemical composition of the material is also accessible from simulations, providing additional information about phase transitions and chemical changes taking place under shock conditions.

1.4.1 Shock Hugoniot

The main focus of this work is a detailed comparison of calculated shock pressure with existing experimental data and predictions for multi Mbar shocks. As stated in the introduction, DFT has demonstrated high fidelity for shock compression of many elements and compounds, for example deuterium [3], carbon [4], quartz [36], water [56], and liquid xenon [57]. However, it was not clear, *a priori* whether one could expect similar agreement between simulation and experiment for polymer systems. Complications might have arisen from long relaxation times, or from polymers systems' significant van der Waals force contributions which often dominate over covalent bond forces.

Polyethylene (PE)

The experimental data presented for shocked polyethylene (PE) in Fig. 4 is taken from the LASL shock handbook [18]. The data is for samples with an initial average density of 0.916 g/cm^3. The later high-

pressure experiments [14] were performed on samples with a higher initial average density (0.952 g/cm^3). Although a small difference, we adjusted for it in Fig. 4 by scaling the shock handbook data to the nominal density of semi-crystalline PE (0.955 g/cm^3) as follows: $\rho' = \rho_0 u_s/(u_s - u_p)$ and $P = \rho_0 u_s u_p$, where ρ_0 is the new reference density and u_s (shock velocity) and u_p(particle velocity) are the experimental data in reference [18]. Likewise, the theoretical results of reference [5] are scaled to the nominal density of semi-crystalline PE.

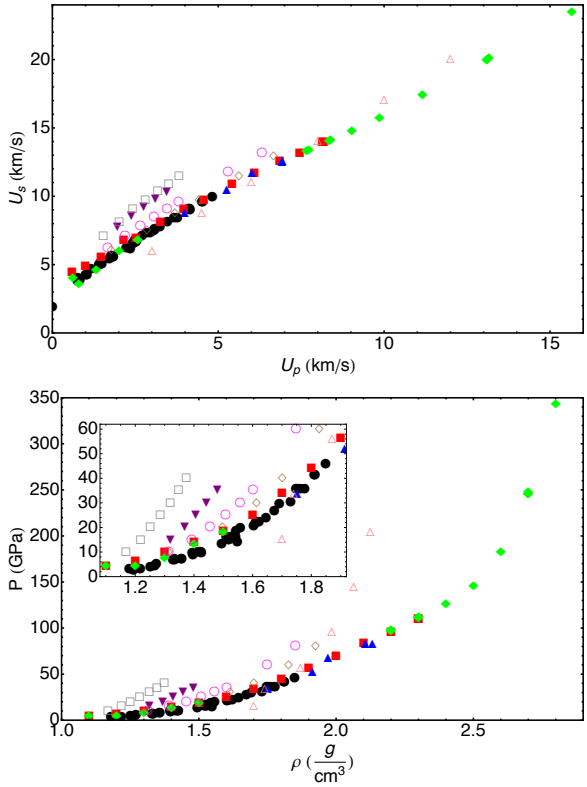

Figure 4: Hugoniot for polyethylene in U_S-U_P (top) and P-ρ (bottom). Experiments: shock handbook [18] scaled to 0.955 g/cm^3 (black filled circles) and Nellis et.al. [14] (blue filled triangle up). Simulations: AIREBO (gray square), OPLS (purple filled triangle down), exp-6 (magenta circle), ReaxFF (brown diamond), tight-binding [5] (pink triangles), DFT-AM05 temperature-ramp (red filled square), and DFT-AM05 steady-state (green filled diamond).

Our PE Hugoniot results, (see Fig. 4) demonstrate that for shocks above 50 GPa, which leads to a final state density of $\sim$1.9 g/cm^3, only DFT predicts mechanical response in close agreement with experimental data. In this regime, both the ramped and steady-state techniques discussed earlier show good agreement, while at lower pressures, the steady-state DFT method is in better agreement with experiment. As a general rule, the classical potentials provide too stiff of a response at high pressures. At lower pressures, closer to ambient conditions where they are parametrized, the model potentials become more quantitatively accurate. Below 30 GPa, a density of 1.7 g/cm^3, ReaxFF deviates from DFT and experiment by less than 10%. Below 15 GPa, a density of 1.3 g/cm^3, the exp-6 potential gives reasonably good agreement. The OPLS and AIREBO potentials are decidedly too stiff, they do not offer accurate predictions for the mechanical loading at pressures significantly above a few GPa. Results from tight-binding calculations [5] are also shown in Fig. 4, demonstrating the long-standing challenge to predict properties for matter under shock compression.

Poly(4-methyl-1-pentene) (PMP)

Our PMP Hugoniot results (see Fig. 5) demonstrate that the DFT simulations are in excellent agreement with experimental data, effectively capturing even the subtle curvature in U_S-U_P. As before, the ReaxFF potential is the most accurate classical potential, followed by the exp-6 potential. These are quantitatively accurate to within 10% at experimental pressures of 30 GPa and 15 GPa, respectively. The OPLS and AIREBO potentials have too stiff of a response in both hydrocarbon polymers even for very weak shocks. Since the OPLS potential does very well in describing normal and branched alkanes at ambient pressures [58], this result suggest that the LJ 12-6 is in general too stiff [59] to model shocks; softer potentials such as the exp-6 appear to be more appropriate.

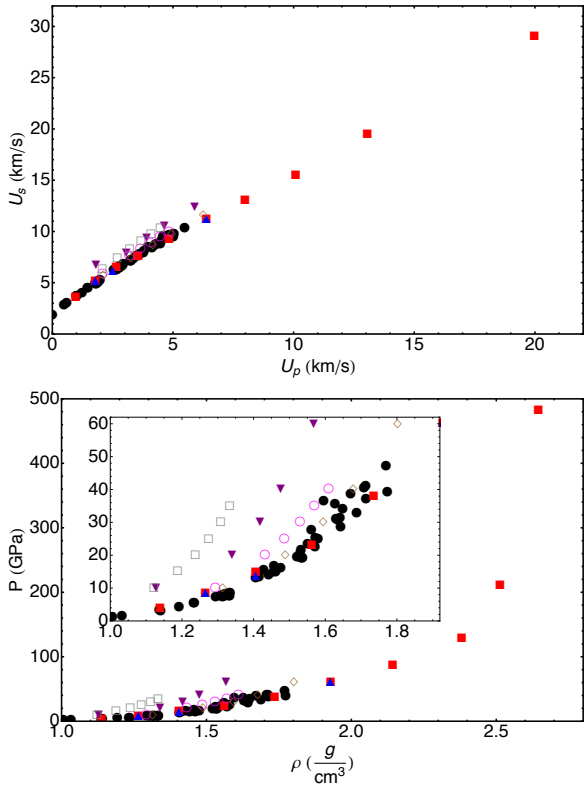

Figure 5: Hugoniot for poly(4-methyl-1-pentene) in U_S-U_P (top) and P-ρ (bottom). Experiment: shock handbook [18] (black filled circle). Simulations: AIREBO (gray square), OPLS (purple filled triangle down), exp-6 (magenta circle), ReaxFF (brown diamond), DFT-AM05 geometry 1 (red filled square), and DFT-AM05 geometry 2 (blue filled triangle up).

The temperature of the shocked state is important in determining the phase, rates of chemical reactions in the shock front, final equilibrium chemical composition, and transport properties like thermal- and electrical conductivity; it is therefore important to model and analyze also the shock temperature. The Hugoniot state can be viewed in the pressure-temperature plane, shown in Fig. 6. Although the stiffness of the Hugoniot in the pressure-density plane (Fig. 4) is also manifest in temperature-density (Fig. 7), the P-T plot reveals that pressure and temperature, with minor exceptions, follow each other closely.

A shock to a certain compression/density reaches a higher temperature and pressure when modeled in AIREBO or ReaxFF than it does in DFT. A shock to a certain pressure, on the other hand, will display

similar temperature in DFT and the model potentials, but for strong shocks result in different compressions of the final state.

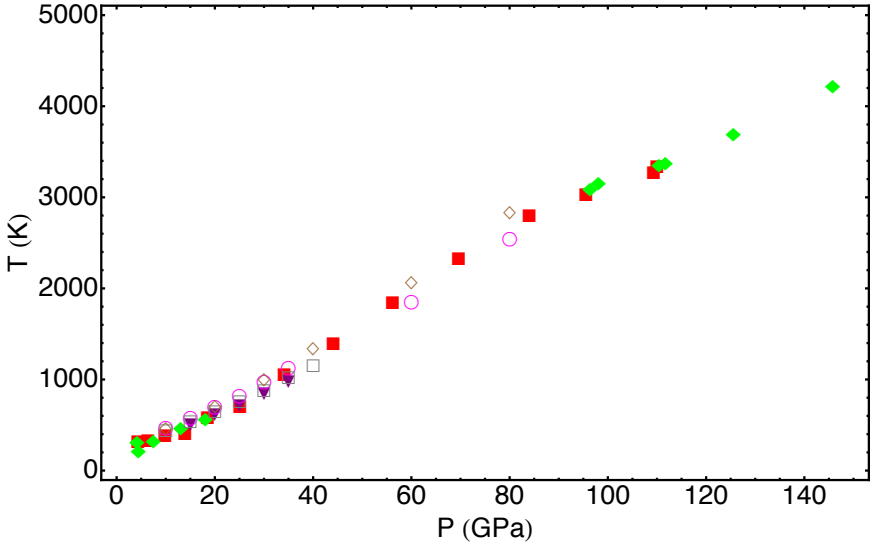

Figure 6: Calculated temperatures as a function of pressure along the polyethylene principal Hugoniot. AIREBO (gray square), OPLS (purple filled triangle down), exp-6 (magenta circle), ReaxFF (brown diamond), DFT-AM05 temperature-ramp (red filled square), and DFT-AM05 steady-state (green filled diamond).

In Fig. 7, the calculated temperature along the Hugoniot is shown for polyethylene. The overall behavior of the shock temperature when comparing the different methods is analogous to that of the pressure. A particular shortcoming of classical potentials as well as ground-state/zero-Kelvin type DFT simulations is the lack of treatment of the effect of temperature on the electronic ground state, which results in a too stiff shock Hugoniot [60]. Since the DFT results for pressure are in agreement with experiments, we will in the following discussion compare the temperatures in the model potential simulations to those from DFT.

AIREBO yields too high temperature compared to the DFT results already for weak shocks, and the deviation grows rapidly with shock strength. The large discrepancy in temperature is particularly problematic for AIREBO since chemical reactivity depends sensitively on the temperature. If the DFT simulations of temperature are of high fidelity, it appears difficult to draw conclusions regarding chemical reactivity under shock conditions from simulations employing AIREBO.

ReaxFF, the second reactive potential investigated, instead shows behavior for compressions smaller than 50% (densities below 1.5 g/cm^3) that agree with DFT. For compressions beyond that, also ReaxFF yields a higher shock temperature than DFT does. As discussed in the next section, these differences occur well below the threshold of dissociation, suggesting that ReaxFF could display significant uncertainties in predictions of chemical reactions resulting from stronger shocks.

Of the non-reactive potentials, exp-6 of Borodin *et al.* behaves well for shock compression below 1.5 g/cm^3 while the temperature raises rapidly compared to the DFT result for stronger shocks. The OPLS potential exhibits a rapid increase in shock temperature beginning already at 30% compression.

The DFT results show an interesting behavior at $2\frac{1}{2}$-fold compression (2.4 g/cm^3) where the temperature rise is suppressed. The feature is more pronounced in temperature than it is in pressure and U_S-U_P, although it is visible in the upper panel of Fig. 4 as a change in curvature at U_P = 10 km/s. The reason is the gradual

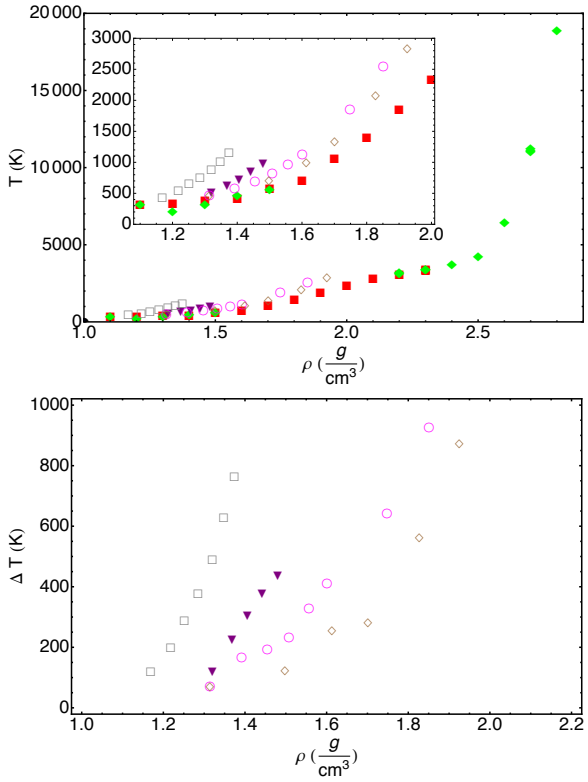

Figure 7: Calculated temperatures as a function of density along the polyethylene principal Hugoniot (top) and relative to the DFT-AM05 temperature (bottom). AIREBO (gray square), OPLS (purple filled triangle down), exp-6 (magenta circle), ReaxFF (brown diamond), DFT-AM05 temperature-ramp (red filled square), and DFT-AM05 steady-state (green filled diamond).

transition into the dissociated/atomic regime; the temperature increases rapidly again after dissociation is complete. The transition occurs at pressures greater than those of existing gas-gun experiments but is within the pressure range of laser- or magnetically launched flyer plate driven experiments. We expect this range of shock compression to be investigated experimentally in the future.

1.4.2 Chemical structure/dissociation

Shock induced dissociation is one of the aspects driving the transition into a dense plasma and is of particular interest due to the many changes associated with it. Although the ambient state of most polymers are electrical insulators, the dense dissociated state is conducting. This leads to substantial changes in thermophysical properties like specific heat and thermal conductivity. From a computational perspective, the onset of dissociation determines the range of applicability for non-reactive potentials like the Borodin exp-6 and OPLS.

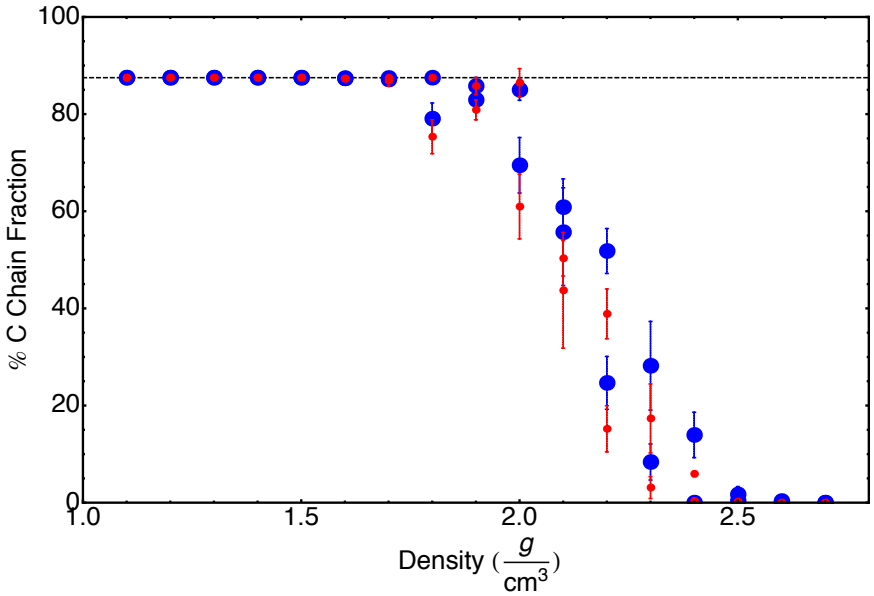

Figure 8: Average fraction of carbon atoms bound in the back-bone in the DFT-AM05 simulations as a function of density along the Hugoniot. When there are two points at the same density, they are for two different temperatures bracketing the Hugoniot state. The error bars are one standard deviation. The cutoff distances used to define bonded atoms were 1.9 Å for C-C, 1.3 Å for C-H, and 0.8 Å for H-H. Results are shown for two cutoff times: 20 fs (large blue circle) and 50 fs (small red circle).

We analyzed the DFT simulations for bond-breaking by recording all neighbors within a cut-off distance of an atom and counting a bond as permanent/steady if it lasted longer than a cutoff time. Although the exact recorded chemical composition depend on the cutoff distances and time [38], the estimation of the density where significant dissociation occurs is not sensitive to the choice of cutoff parameters.

Fig. 8 shows the structural integrity of polyethylene along the Hugoniot as measured by the fraction of carbon atoms in a linear chain. Carbons in the chain will have two C and two H neighbors, except for the end atoms which will have one C and three H neighbors. The initial polyethylene strands are $C_{16}H_{34}$, hence the initial fraction of back-bone carbon atoms is $14/16$ or 87.5 %. The polymer back-bone is no longer intact when the ratio is reduced from that value, so by monitoring how the ratio changes, it is possible to

follow the structural disintegration of the polymer.

In the timescale accessible to the DFT simulations, there is no appreciable dissociation below 1.8 g/cm^3 and no signature of a carbon back-bone remaining above 2.5 g/cm^3. The region of partial dissociation (2.2 - 2.4 g/cm^3) corresponds directly to the plateau in temperature along the pressure Hugoniot shown in Fig. 7 and the inflection in the U_S-U_P relation of Fig. 4.

Under compression, the linear chains break up and structures of carbon atoms with three or more carbon neighbors begin to emerge. An example of that is shown in Fig. 9, where the character of carbon atoms at 2.2 g/cm^3 and 3100 K is plotted as a function of time. At even higher compression, H_2 molecules begin to form and carbon-carbon coordination becomes more pronounced.

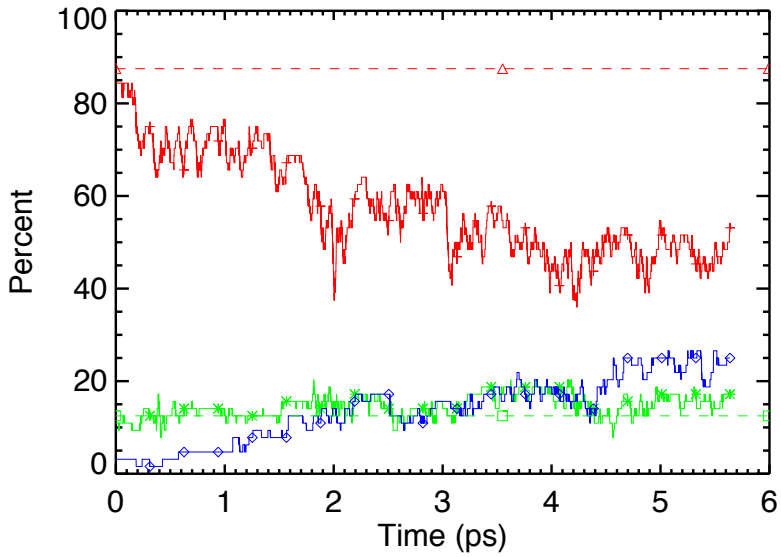

Figure 9: Distribution of carbon as a function of time in the DFT-AM05 simulation at 2.2 g/cm^3 along the Hugoniot at 3100 K presented as sliding averages over 10 fs intervals. Carbon in the back-bone (red line $+$), carbon at the end of a strand (green line $*$), and carbon with three carbon neighbors (blue line $\Diamond$). The dashed lines show the fractions of perfects chains with 87.5 % of carbon atoms in the back bone (red dashed triangle up) and 12.5 % at the end of a strand (green dashed square). The backbone fraction has been reduced to 45% while 24% is bonded to three other carbons; the fraction of carbon atoms at the end of a strand fluctuates above the initial value. The composition changes over the first 3 ps as the system reaches equilibrium. During the last 3 ps, the count of backbone carbon atoms shows no trend, suggesting that the system can reach equilibrium over the timescale accessible in the first-principles simulations.

1.5 Results in polymer foam

Our nonequilibrium molecular dynamics (NEMD) simulations were limited in duration because our samples were relatively small. Thus, total shock propagation times were limited to tens of picoseconds. It is not clear whether the shock profiles have reached true steady state profiles, in the sense required by the Hugoniot-Rankine equations. However, we do observe profiles, such as those presented in Figure 3 which are spatially homogeneous behind the shock front. This allows us to compute average values for the thermodynamic

variables, such as uniaxial pressure, density, temperature, etc.

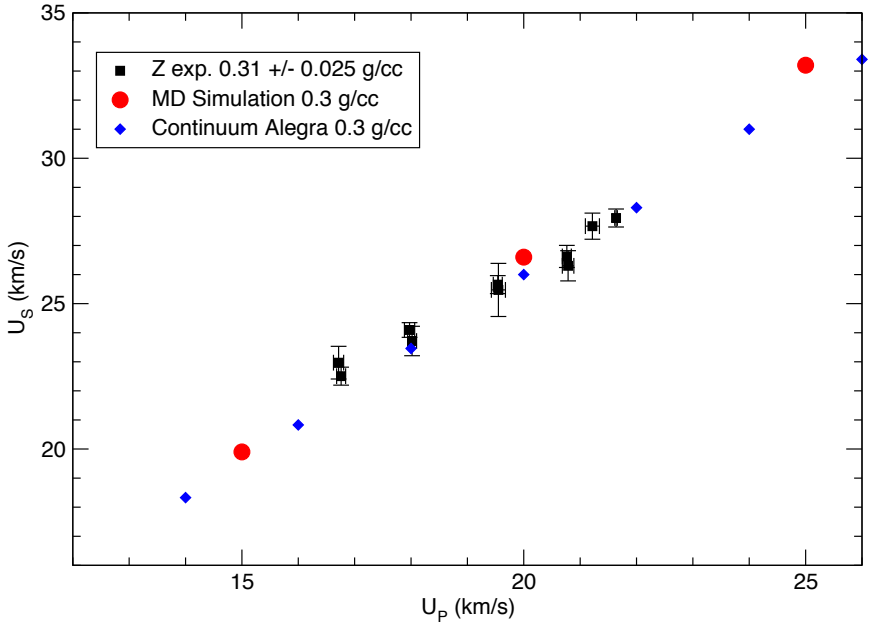

Figure 10: Hugoniot response of PMP foam, showing shock velocity, U_S, vs particle velocity, U_P. Results of experiment, continuum and MD simulation are plotted together.

1.5.1 Shock Hugoniot

Figure 10 shows the Hugoniot response in shock velocity, U_S, versus particle velocity, U_P, space. For comparison, we include both experimental and hydrocode simulation results which will be thoroughly reported elsewhere [19, 20]. As seen in Figure 10 we find good quantitative agreement with both experiment and the hydrocode results in the range of piston velocities explored.

Figure 11 shows the Hugoniot response in uniaxial pressure, P_{ZZ}, versus density, ρ, space. MD results are plotted along with both experimental and hydrocode simulation results. Here we find good agreement with the hydrocode simulations, but the experimental results demonstrate significantly more spread in the final shock density of the foam. This is almost certainly due to significant variation in the initial foam ambient densities both between samples, and even within individual samples. The foam's final shocked density and pressure are both affected by this variation in initial density. In contrast the foams produced for simulation are uniform on the nanometer scale, and densities are precisely known. The MD results run through the center of the spread in experimental values.

1.5.2 Shock temperature and void collapse

Showing good agreement with experimentally observable quantities gives us confidence in using MD to explore quantities which are not easily measured experimentally. Primary among these, is the local temperature of the samples. In Figure 3 we show a profile of the temperature at two simulation times. In Figure 12 we show the average final shock temperature behind the shock front for several shock pressures and for two different initial foam densities. Temperatures are much higher than for comparable shock pressures in dense

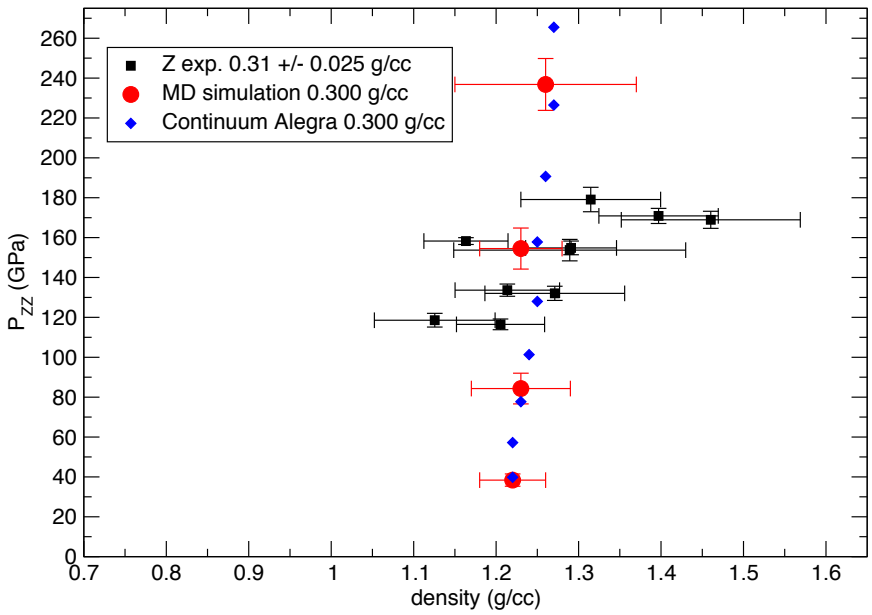

Figure 11: Hugoniot response of PMP foam, showing uniaxial pressure, P_{zz}, vs density, ρ. Results of experiment, continuum and MD simulation are plotted together.

polymer. In fact, the introduction of voids causes an order-of-magnitude increase in shock temperatures.

Our measured temperatures are high enough that one should begin to question whether molecular dynamics can properly model the physics – which is likely to increasingly depend on the electronic degrees of freedom. At 100,000 K, for instance, one would expect that nearly every atom would be ionized to form a plasma. At that temperature, clearly MD would not capture the important physics. It is reasonable to assume that MD results much above 50,000 K would be suspect.

Unlike in the dense polymer case, we see significant dissociation of the PMP polymer in shocked foams. The lower image in Figure 1 shows the vaporized atoms which are blown out as ejecta as the shock propagates through each void. These ejecta can travel faster than the shock speed, and therefore can blur the front for cases where the void spaces are contiguous. In the dense polymer we observed dissociation only above 180 GPA, but in foams, it is observed at our lowest pressures, approximately 50 GPa. This dissociation produced by local heating and hot spot formation is an area that we plan to pursue further.

1.6 Conclusions

We have simulated the behavior under shock compression for two polymers using DFT based molecular dynamics with the AM05 density functional and four different classical force-fields. We conclude that the response to weak shocks in both PE and PMP are well described by the exp-6 of Borodin *et al.* and ReaxFF force-fields, with the latter being valid over a larger range in density and pressure. OPLS and AIREBO both yield significantly too high pressure along the Hugoniot already for weak shocks. For strong shocks, only the DFT based simulations are of high fidelity when compared to existing experimental data up to 80 GPa. Based on the first-principles simulations, we predict a feature in the polyethylene Hugoniot at U_P = 10 km/s due to gradual dissociation between 2.2 and 2.5 g/cm^3.

It is notable that all of the classical model potentials tested begin deviating from the DFT simulations at significantly lower densities, pressures, and temperatures than those required for bonds to break. This

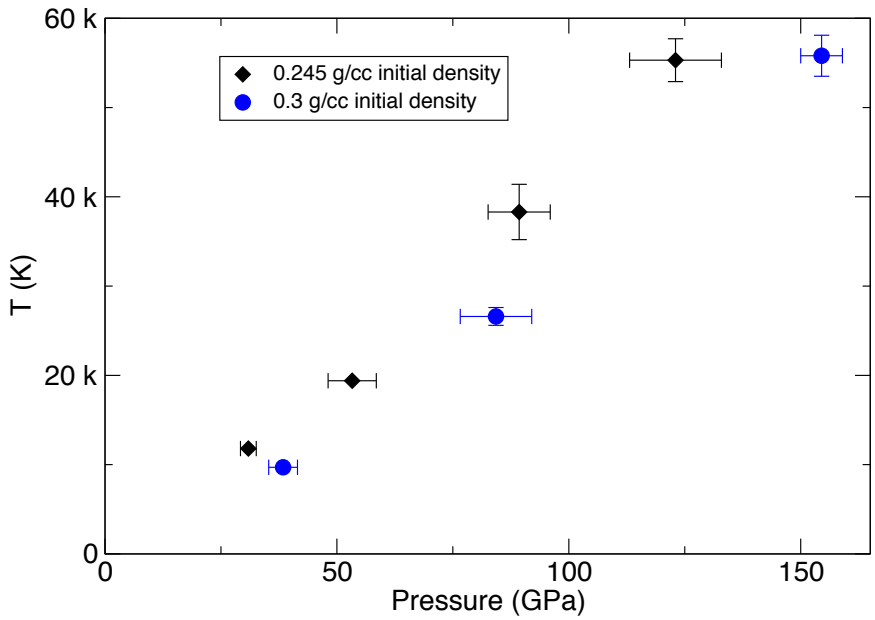

Figure 12: Plot of average temperature vs average uniaxial pressure, P_{zz}, of states behind the shock for two PMP foam densities.

finding carries implications for future development of force-fields, both reactive and non-reactive. Non-reactive force fields for hydrocarbons have a potential maximum range of validity in shock applications of 1.8 g/cm^3, but an improved fidelity for high density will require changes in the non-bonded interaction parameterization. The behavior of AIREBO is incorrect when compared to experimental data for pressure at 20% compression, 1.2 g/cm^3, a region where no dissociation occurs in the DFT simulations, implying that significant revisions are necessary for the potential to be useful for shock problems. ReaxFF has a longer range of validity when compared to experimental pressure data for both PE and PMP, but the temperature difference to DFT above 1.9 g/cm^3 is a point of concern for shock applications.

Further, we have used NEMD to study the shock propagation and material response of polymer foams. Building on the findings of previously published work in dense polymers, we have shown that molecular dynamics, using the ReaxFF interaction, can quantitatively capture the Hugoniot response in hydrocarbon foam. Moreover, MD allows us to explore aspects which are elusive in experimental studies, such as the measurement of local temperatures and the formation of hot spots around voids. We see qualitatively different response in foams, most notably in the pressures at which polymers dissociate.

We expect that the results outlined throughout this paper will provide guidance when it comes to selecting interaction potentials for work employing classical molecular dynamics simulations to study shocks in organic materials in general and hydrocarbon polymers in particular.

2 Dynamic compression of silicon and germanium

Principal Authors: J. Matthew D. Lane and Aidan P. Thompson

This section contains a paper that appeared in the Proceedings of the Conference of the American Physical Society Group on Shock Compression of Condensed Matter, held in Nashville, Tennessee June 28-July 3, 2009. It was authored by J. Matthew D. Lane and Aidan P. Thompson and published in AIP Conference Proceedings 1195, p. 1157 (2009). [SAND 2009-5082 C]

Abstract

Results from shock-wave loading of Germanium are presented. Germanium is known to transition from ambient cubic diamond (cd) phase to the high-pressure body-centered tetragonal (bct) or β-tin phase at pressures between 10 and 12 GPa. Large-scale molecular dynamics (MD) simulations were used to study the phase transition in single-crystal Germanium under uniaxial compression along the $\langle 001 \rangle$ and $\langle 111 \rangle$ orientations. We observed that the transition from the cd phase to the bct phase nucleates through shear banding and advances to relieve uniaxial strain. The macroscopic properties are compared with experimental results for both the Modified Embedded Atom Method (MEAM) and Tersoff potentials.

2.1 Introduction and methods

Germanium is an elemental semiconductor which shares many properties with silicon. Both elements form a cubic diamond (cd) phase at low pressures and temperatures. At higher pressures, both elements transition to a body-centered tetragonal structure (bct). Below 20 GPa, both cd and bct transition to liquid at higher temperatures [61]. This phase similarity makes germanium a good surrogate for studying the properties of the much more technologically significant silicon. Since germanium exhibits each transition at lower pressure and temperature than silicon, its transitions to be studied experimentally with less intense shock pressures. For laser ablation studies this means high-quality 1D studies of the transitions can be accomplished without significant pre-heating or petawatt laser intensities.

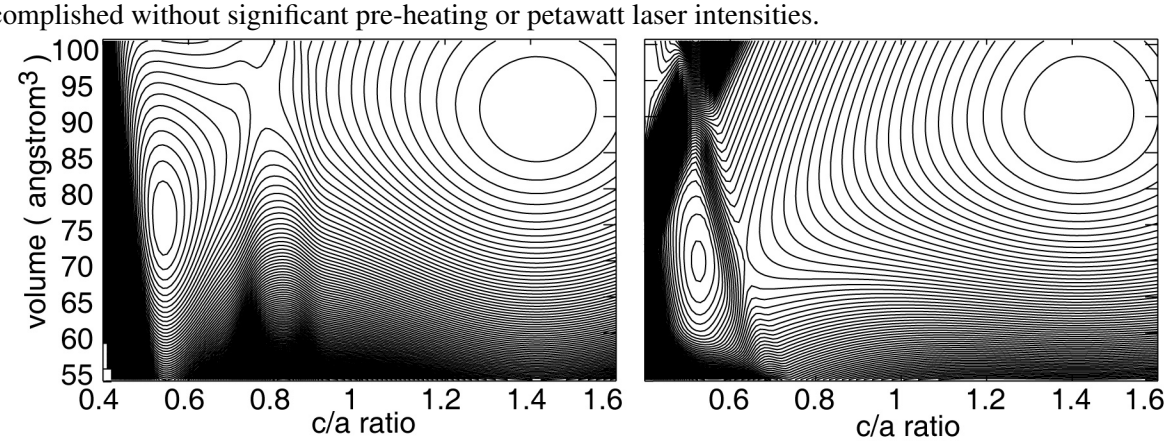

Figure 13: The energy profiles for MEAM (left) and Tersoff (right) potentials plotted as a function of the lattice ratio c/a and the unit-cell volume V. The two local minima in each plot are the low-density cd phase and the high-density bct phase.

Classical MD simulations were run in the publicly-available LAMMPS [24] code. Two potentials, Tersoff [62] and the Modified Embedded Atom Method [63] (MEAM), were used independently to model the

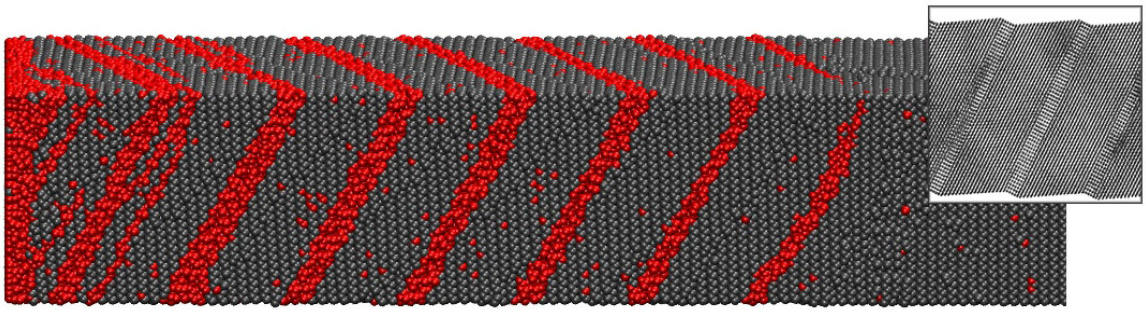

Figure 14: Image of the partial transition of Tersoff germanium. Atoms are colored by coordination number such that the cd phase (coord # ≤ 6) are gray and the bct phase (coord # > 6) are red. Transverse dimensions were 10 nm. Inset shows rotated detail of lattice planes of transformed bct phase.

germanium interactions. The Tersoff potential uses a two-body term and explicit three-body angle terms to model covalent bonding. MEAM is a more general potential which has been parameterized for many elements and alloys. MEAM uses a two-body term as well as an environment dependent term constructed from the effective electron densities of local atoms. The Tersoff potential is less computationally expensive, however, it was initially unclear whether it would be capable of capturing the high-density phase transition. The parameters and cutoffs for both potentials were taken from work cited.

In Figure 13 we plot the energy contour profile for germanium as a function of the ratio of the tetragonal crystal dimensions c/a and the volume V of the the unit cell. As discussed in Ref. [64], the cd structure is a high-symmetry special case of the tetragonal structure making it is possible to move continuously in these variables from the cd to the bct structure. For cd the c/a ratio is $\sqrt{2}$. Figure 13 shows the contours for both the MEAM and Tersoff potentials. Both potentials exhibit the ambient low-density (cd) and high-density (bct) states as local minima, with good agreement near ambient. For high-density (bct) state, the two potentials predict slightly different c/a ratios and have differing energy contours.

The pressure-induced transition was explored by measuring the cd and bct enthalpies as a function of pressure for each potential during isothermal (NPT ensemble) compression from 0 to 20 GPa. Both potentials demonstrated a crossing of the cd and bct enthalpies very near 12 GPa, in good agreement with experiment [61]. The enthalpy crossing determination of the transition pressure does not require an actual structural transition between the states. Therefore, the transition was further confirmed by demonstrating the transition by uniaxial compression along the c axis for both potentials.

The coordination number with cutoff 3.55 Å was used to clearly distinguish between the phases. The cd phase has 4 neighbors within this cutoff, while bct has 10. This criterion was demonstrated to be robust even at high temperature and pressure.

Shock waves were produced by striking single crystal germanium with a warm piston along either the $\langle 001 \rangle$ and $\langle 111 \rangle$ directions. Orientation did not alter the qualitative response, so we report results only for the $\langle 001 \rangle$ direction. The sample was initially thermalized at 300 K and had periodic boundary conditions in the directions transverse to the shock propagation. The ambient density was 5.3 g/cc and the ambient unit cell had dimensions $0.4 \times 0.4 \times 0.27$ nm^3. The transverse dimensions were either 10 nm, 20 nm or 40 nm square. The system was approximately 200 nm long in the propagation direction initially, but grew as large as 0.8 μm as the simulation continued. In order to allow for this system growth, the free surface opposite the piston was frozen to prevent surface relaxation. Whenever the shock front came within 25 nm of this surface a 1 nm slab of lattice-matched material was added so that the shock front could continue to run. A

20 nm region of pristine material ahead of the shock front was kept at 300 K with a Langevin thermostat. This method was described in principle in prior work. [65]

2.2 Results and discussion

We explored shock strengths just above onset of the solid-solid phase transition in germanium. Piston velocities ranged from 0.9 to 1.0 km/s. Figure 14 shows the typical qualitative response of the system. The piston drives an initial elastic shock into the cd crystal which is compressed uniaxially. As the elastic front propagates, stacking faults nucleate in the elastically compressed material. In the image above, these planar faults begin at the piston face and nucleate a shear induced phase transition which runs forward at an angle – advancing through the system as a shear wave. Competition between several planes results in a single propagating plane which wraps around the periodic boundary conditions of the simulation cell. The image shows the planar phase transitioned bct crystal in red, interspersed with compressed cd crystal in gray. The bct region does not grow with time after the shear wave passes. The transformed material is a single crystal bct structure through the sample rotated by 30 degrees from the propagation direction, with compressed and rotated cd phase in between (see Figure 14 inset). This qualitative shear band response is unlike the familiar planar transitions seen in previous literature. [66]

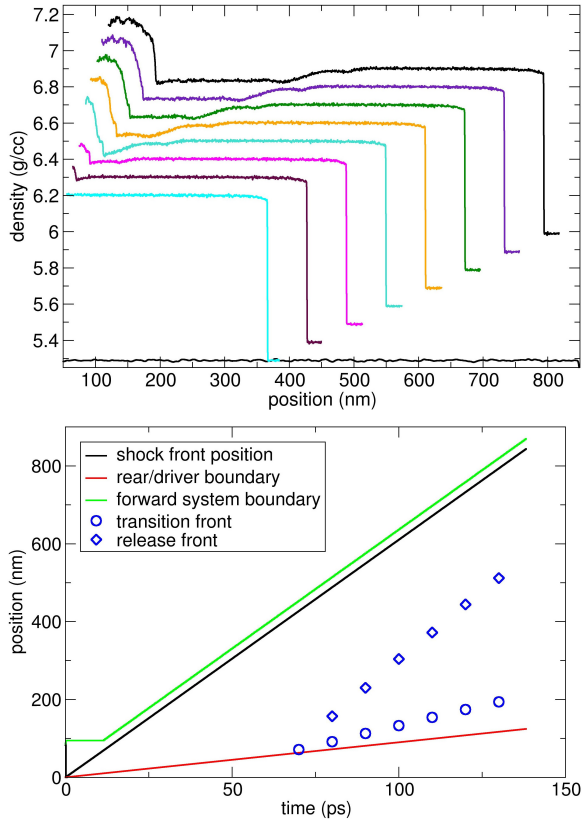

Figure 15: (Top) The shock density profiles showing elastic, transition and relaxation fronts all moving to the right. Each profile is 20 ps separated in time and each shifted upward by 0.1 g/cc on the density scale for clarity. (Bottom) The same simulation presented in $x - t$ form showing the fronts and clearly showing the nucleation delay of the transition. Transverse dimensions were 10 nm.

A two wave response can been clearly seen in which an elastic precursor leads a second partial-transition front. Figure 15 (top) shows the density profile as the shock travels through the material. The shear induced cd-bct transition produces further compression and an associated relaxation wave which travels forward toward the elastic front. Figure 15 (bottom) shows the propagation of the elastic wave, the transition wave, and the relaxation wave in an $x - t$ plot. The system boundary is also plotted to demonstrate that the system is growing to accommodate the travelling wave. Note that the wave traverses nearly a micron of material in the simulation. Finally, it should be noted that this system did not reach the steady state necessary to compare quantitatively to experimental Hugoniot pressures. Steady state would be reached once the elastic wave front was overtaken by the relaxation wave.

Figure 16 shows the stress state of the system after the phase transition. The mean pressure, $\bar{P}$ in the elastically compressed state was approximately 25 GPa. $\bar{P}$ was not significantly relaxed by the phase transition (see Fig 16A). The uniaxial pressure, P_{zz}, however, is significantly lower within the bct transformed state. Clearly the transition, while not significantly reducing the overall stress state, distributes the stress and strain to the transverse directions. This is most clearly illustrated in the bottom image of the shear stress in the material, $\tau = P_{zz} - (P_{xx} + P_{yy})/2$. The shear stress in the elastically compressed state was approximately 12 GPa. τ dropped to nearly zero in the bct phase and to approximately 5 GPa in the remaining cd material. It is hypothesized that the shear stress is the driver for the cd to bct transition in the shocked material. Therefore, the near-total shear stress relaxation explains arrest of the transition and the partial transformation to the bct phase.

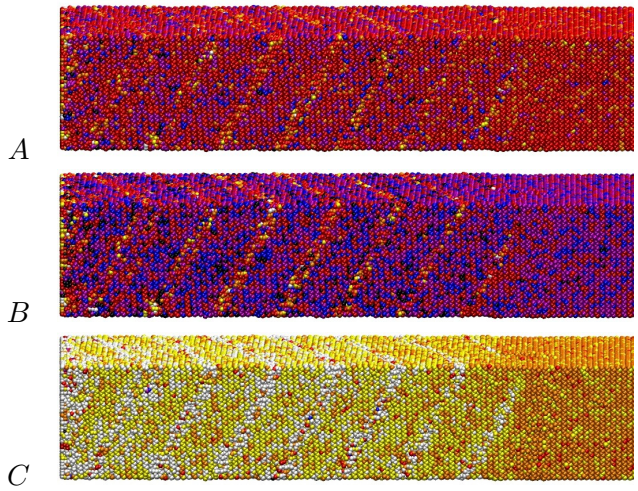

Figure 16: The (A) mean pressure $\bar{P}$, (B) uniaxial pressure P_{zz} and (C) the shear stress $\tau = P_{zz} - (P_{xx} + P_{yy})/2$. Pressure ranges from white, yellow, orange, red, purple, blue to black from 0 GPa to 35 GPa. Transverse dimensions were 10 nm.

System size effects are clearly important to the analysis presented. Because the transition propagates along shear planes which are not oriented along the simulation box, the forward moving transition front wraps around the simulation box and thus a single planar disturbance creates a periodic response. Since general statements about the response must be independent of system size, systems with larger transverse dimensions were studied.

Figure 17 shows the bct phase produced by an identical shock in a system which is twice as large in each of the transverse dimensions. Several important features are immediately apparent. First, that the number of transition nucleation sites grows with the system size, as expected. Second, that the thickness of the bct

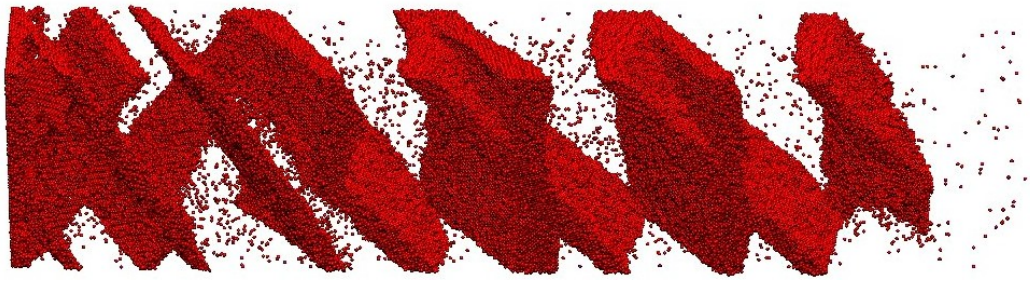

Figure 17: Shock-induced cd-bct transition in Tersoff germanium. Only the bct phase is imaged. Multiple planes of transformed material, emanating from multiple nucleation points interact in larger systems. Transverse dimensions were 20 nm.

phase grows with system size. That is, the systems with twice the transverse dimensions has nearly twice the volume of transformed material per unit propagation. Third, the longitudinal distance separating consecutive sections of a single shear-band increases as the transverse dimension. Finally, multiple transition nucleation points produce multiple planes of bct material which interact as they propagate through the system.

The interaction rules between the several propagating bct transition planes are not completely clear. In some cases, opposing planes compete with one another and one plane arrests. In other cases two planes appear to coexist and move forward entangling. This leads to the conclusion that although each shear-induced transition plane has a characteristic length which is tied to the system-size, there is likely a characteristic lengthscale which is dictated by the nucleation frequency (i.e dislocation density) and the interaction dynamics of the transition planes. So long as the system size is larger than this characteristic length, then the results will be independent of system size. This hypothesis has not yet been tested.

2.3 Conclusion

We observe the solid-solid phase transition in Germanium from cubic diamond to a body-centered tetragonal structure at an appropriate pressure range for both the MEAM and Tersoff potentials. The transition in the $\langle 001 \rangle$ direction is notable as it propagates in shear bands which appear to nucleate from sheared stacking faults. The transition is partial and leaves untransformed cd phase material behind. Large-scale simulations is underway to allow direct comparison with experiment.

3 Laser-driven dynamic melting of silicon

Principal Authors: Todd Ditmire and Hernan Quevedo

This chapter consists of a report documenting experimental work performed in the High Intensity Laser Science Group at the University of Texas at Austin. The work was funded in part by this LDRD project with the goal of developing femtosecond resolution experimental measurements for validating molecular dynamics simulation of shock melting. The report was authored by Todd Ditmire and Hernan Quevedo.

Abstract

The work presented here aims to use circularly polarized third harmonic generation probing to investigate shock-induced phase transitions in silicon and germanium. Results show that the non-linear probing might suggest a phase change while linear reflectivity can present no change or a metallic state response.

3.1 Introduction

Non-linear optical probing has become a very powerful technique for diagnosing the crystalline structure of materials. Initial measurements used second-harmonic generation (SHG) to study semiconductors such as Si and GaAs that are good sources of non-linear light [67,68] These studies lead to time-resolved measurements of laser-induced melting in such materials, with time scales of hundreds of femtoseconds for such events [69]. More recently third-harmonic generation (THG) has been used to study crystalline structure and phase transitions [70]. This is particularly important in centrosymmetric crystals like silicon where SHG in the bulk has a very small contribution. In addition, the use of circular polarized light for THG proved to be very sensitive to laser-induced melting [71] . In this case, the material becomes amorphous and isotropic and THG from the crystal bulk drops becoming negligible since the light angular momentum can no longer be conserved. Experiments conducted in Si and GaAs showed this behavior when melted using intensities $>$300 mJ/cm^2 with 40 fs pulses at 800 nm [72]. The transition to a melted state occurred in a $\sim$350 fs time scale, 20% faster than the increase in linear reflectivity as a result of a transition to a metallic state of the sample when electrons were promoted to the conduction band. These experiments heated and probed the same surface of the sample.

The work presented here aims to use circularly polarized THG probing to investigate shock-induced phase transitions. In particular, we measured the temporal behavior of the crystalline structure of silicon as it was shocked at pressures of 100s of kbars. To perform these time-resolved studies, a pump beam is focused onto an ablator coating on the front surface of the material under study. The coating ablates, expands backwards in the direction of the beam and sends a shock wave through the material. This shock compresses and heats the material to states predicted by the Hugoniot equations. When the shock arrives at the rear surface of the material, a highly synchronized time delayed laser beam probes the crystalline structure. Previous results showed a decrease in the THG before the shock arrival to the rear surface, implying some kind of disordering [73]. However, the pressures used were significantly lower than what was expected to melt the material. Figure 18 shows the P-T phase diagram of silicon and germanium that present similar phases [74, 75]. Shocking from room temperature and atmospheric pressure to above 120 kbar, transitions both materials from the diamond or gray tin phase to the β-tin or white tin phase. To shock melt the materials at pressures achievable by our laser system, $<$300 kbar, some sort of pre heating is required. A higher initial temperature close to the melting point at atmospheric pressure lowers the shock pressure required to melt the material. In this regard, we present in Appendix the development of a resistive

heater to preheat samples close to these conditions. Germanium is preferable to silicon because of its lower melting point however the fabrication of targets is considerably more difficult.

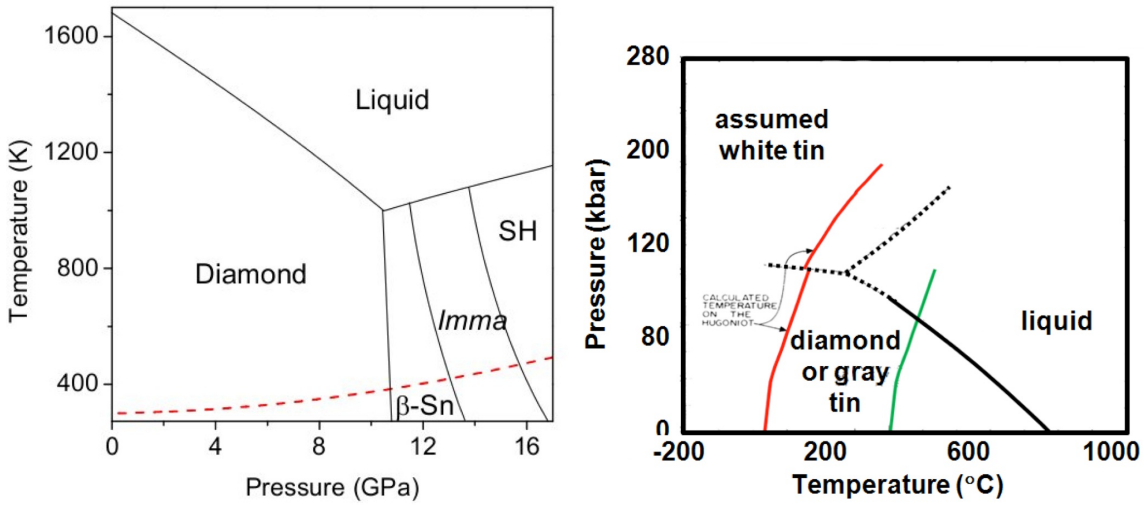

Figure 18: P-T phase diagram of silicon (left) from Tsujino (2008) [75] and germanium (right) modified from McQueen (1964) [74]. The red line indicates the Hugoniot with initial conditions at STP, whereas the green line indicates a potential Hugoniot with an elevated initial temperature.

A shocked material increases its temperature upon compression as shown in Figure 18. This rise in temperature is accompanied by light emission in the form of blackbody radiation. As the temperature increases, the radiation becomes stronger and the peak emission occurs at a frequency given by Wien's Displacement law. When shocking at $\sim$1.5 Mbar, a temperature around $\sim$1 eV can be attained [76] and the radiation is strongest near 250 nm similar to the THG frequency of our experiment. Part of this emission will still be present when we shock at an order of magnitude lower pressure. Since we do not have an apparatus to separate the nanosecond contribution from the blackbody emission and the weak femtosecond THG generation, special care needs to be taken to minimize the blackbody collection and maximize the amount of probe light used.

3.2 Experimental setup

This series of experiments were performed at the University of Texas using the THOR laser. THOR is a 800 nm Ti:sapphire laser that uses chirped pulsed amplification (CPA) technique. The maximum output energy is $\sim$1 J and it can be recompressed to 35 fs with a contrast of $>10^5$. For these time-resolved studies the beam was split in two: the pump and the probe. The pump beam drove the shock in the material using 0.55 J of energy and remained stretched to $\sim$550 ps FWHM pulse duration. The probe beam sampled the shock breakout and used $\sim$2 mJ of energy while compressed to 40 fs. Figure 19 shows the experimental layout after the main beam was split. The pump beam passed through a delay leg to compensate for the travel time of the probe beam inside the compressor. The pump beam was focused down by an f/20 lens to a focal spot of tens of microns at the target to generate laser intensities of $10^{13} - 2 \times 10^{14}$ W/cm^2. The target resided in a vacuum chamber at $\sim$10 mTorr. The probe beam left the compressor through a vacuum window; it was down collimated to $\sim$1 inch diameter and traveled in air to a $\sim$600 mm delay stage. The stage allowed delaying the probe with respect to the pump to sample the history of the shock breakout at the rear side of

the target for ∼4ns.

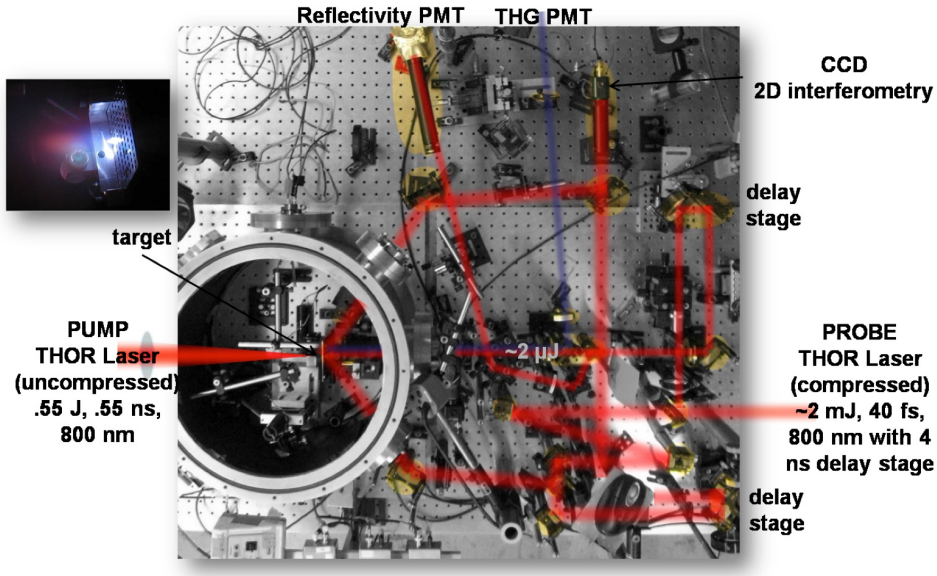

Figure 19: Experimental layout.

The probe beam was split in two after the delay stage, one part formed a 2D Mach-Zehnder interferometer at oblique incidence and the other one was used for reflectivity and THG at normal incidence. The interferometer was used to determine the target particle velocity and shock pressure by taking multiple 2D snapshots of the shock breakout at different temporal delays and calculating the back surface displacement d as given by

$$d = \frac{\lambda \phi(x, y)}{4\pi \cos\theta} \tag{5}$$

where θ is the probe angle of incidence, λ is the laser wavelength and $\phi(x, y)$ is the unwrapped 2D phase shift from the interferograms. The target arm of the interferometer was sent to the rear side of the target at $\theta = 59.5 \pm 0.5$ degrees and contained a telescope to image the small region of the shock breakout onto a regular CCD camera. The reference arm remained in air and contained the same imaging properties. As a result of the long f/# of the collection optic, this diagnostics might not be suitable for reflectivity measurements since light can be reflected out of the optic at breakout. This diagnostics also allowed the positioning of the target with ∼1 μm accuracy as a result of the short pulse coherence distance.

THG and linear reflectivity were used to study the crystalline structure and electronic response of the shocked material respectively. The third harmonic polarization source $\mathbf{P}(\omega)$ for materials like silicon and germanium is given by [68]

$$P_i^{NL}(3\omega) = 3\chi^{(3)}_{xxyy} E_i(\mathbf{E}\cdot\mathbf{E}) + \left(\chi^{(3)}_{xxxx} - 3\chi^{(3)}_{xxyy}\right) E_i^3 \tag{6}$$

where $\mathbf{E}$ is the incident electric field at the fundamental frequency and $\chi^{(3)}$ is the third-order non-linear optical susceptibility. When using circularly polarized light $\mathbf{E} = E_0(\hat{x} \mp i\hat{y})$, as done in our experiment, the first term vanishes ($\mathbf{E}\cdot\mathbf{E} = 0$) and only the anisotropy term remains. For a cubic crystalline structure the two susceptibility terms are different resulting in a non-zero contribution. On the contrary, for an isotropic medium such as amorphous or melted silicon $\chi^{(3)}_{xxxx} = 3\chi^{(3)}_{xxyy}$, and the non-linear contribution for THG vanishes. In the first case one 3ω circularly polarized photon is generated while three 1ω photons of the

opposite polarization are annihilated with a total angular momentum change of $4\hbar$. This angular momentum is taken by the (100) cubic lattice that has a four-fold symmetry and accepts changes in angular momentum in units of $4\hbar$. Amorphous or melted states do not accept the angular momentum change and THG is not allowed. This is a very powerful technique to determine if a material transitions to a melted state or even to a different crystalline structure with the consequent change in $\chi^{(3)}$ and THG response.

Linear reflectivity is measured to study the electronic response of the material and to compare it with THG. Reflectivity depends on the index of refraction of the material and in turn on the dielectric function

$$\epsilon(\omega) = 1 + \chi_{\text{interband}}(\omega) + \chi_{\text{Drude}}(\omega) \tag{7}$$

where the second term represents the contribution from interbank transitions while the last term includes the effect of free carriers using the Drude model for metals

$$\chi_{\text{Drude}}(\omega) = -\frac{\omega_p^2\tau^2}{1+\omega^2\tau^2} + i\frac{\omega_p^2\tau}{\omega(1+\omega^2\tau^2)} \tag{8}$$

with ω_p being the plasma frequency dependent on the number density of carriers and τ the collisional time. When the interband contribution dominates the dielectric function the material is referred to as cold. As the material is heated and melted the Drude contribution dominates and for normal incidence a reflectivity increase of 2.26 is expected compared to cold silicon [73].

The part of the probe beam used for THG and reflectivity was properly delayed to arrive at the target rear surface simultaneously with the interferometer beam. After the delay stage, the beam passed through a half waveplate-polarizer combination to adjust the energy to $\sim$2 μJ. The beam went through a 266-800 nm dichroic mirror that transmitted the 800 nm light that was circularly polarized afterwards using a quarter waveplate. The beam entered the vacuum chamber afterwards and was focused down to a $\sim$5 μm radius spot size where depending on the crystalline structure THG generation occurred. The fluence was set to $\sim$250 mJ/cm^2 to minimize damage of the rear surface while probing. Both THG and linearly reflected 800 nm traveled back to the focusing lens where they were collimated and separated by the dichroic mirror. The 266 nm light was reflected into a photomultiplier tube (PMT) while the 800 nm light was converted back to linear polarization and reflected off the cube polarizer into another PMT. A lens-iris combination before the THG PMT imaged the rear surface of the target acting as a confocal laser scanning microscope to remove as much as possible unwanted light at 266 nm.

We decided to use silicon and germanium as targets because of their crystalline structure and also they are good sources of third harmonic generation (THG), which is the main diagnostic used to identify phase changes from shocks. We have experience manufacturing and working with silicon targets while germanium has the advantage of been already simulated with a molecular dynamics code developed at Sandia National Laboratories. Germanium also presents a lower melting temperature making it easier to pre-heat for shock-induced melting ($\sim$400 °C compared to $\sim$700 °C for silicon). We fabricated single crystal 20 μm thick [100] silicon targets by etching SOI wafers (Figure 20 left). These targets were easily mounted by a $\sim$500 μm thick handle layer (not etched portion of the wafer). The targets were coated with 100 nm aluminum or copper as an ablation layer to absorb the laser energy for driving the shocks. The resulting surface was very smooth as observed under the microscope (Figure 20 left inset). We originally used aluminum to compare with previous experiments. However, it melts at 660 °C which is not suitable for pre-heating samples near similar values. We also used copper as the ablation layer that melts at 1085 °C, much higher than the required pre-heating temperatures. The surface quality was similar to the aluminum coating. The technique used to make silicon targets could not be reproduced in germanium. Instead we purchased a 2 inch diameter

400 μm thick [100] germanium wafer and had it ground down to 20 μm by Valley Design with a mirror finish surface (Figure 20 right). The front surface was coated with copper as the ablator. The problem with the grounding approach is handling a 20 μm thick brittle material without any handle layer. We tested this method first in silicon by etching a full wafer that was cheaper than germanium grounding. The result was a 20 μm layer of silicon that would curl and break in pieces a few cm^2 that were still possible to handle and sandwich in the target holder. Germanium during the removal process did not curl and broke in smaller pieces $\sim$0.5 cm^2 that were impossible to handle for shooting. For these reasons silicon targets were shot in these experiments while a new technique for making germanium targets needs to be developed in the future.

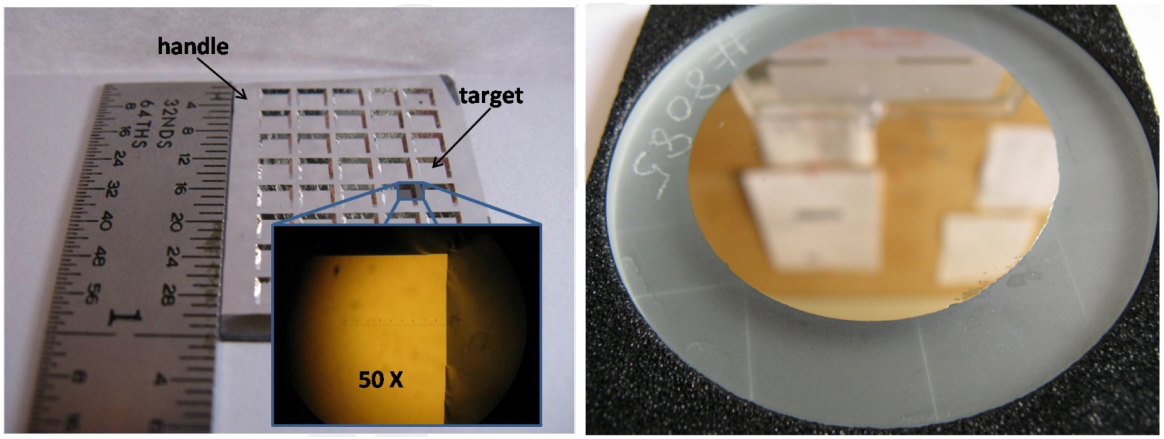

Figure 20: Left: 20 μm thick [100] silicon targets with 100 nm aluminum coating. The inset shows the smooth target surface under a 50$\times$ magnification. Right: 20 μm thick [100] germanium target ground down from 2 inch diameter wafer.

3.3 Results

All three beams (pump, interferometer and TGH/reflectivity) in these experiments were timed up with an accuracy of 20 ps by scattering at the target plane into a 818-BB-21 Newport fast photodiode with <300 ps rise time. Initial shock tests revealed the importance of a good laser pulse contrast in this type of experiments.

Figure 21 left shows the pump beam temporal profile along with the interferometer image captured at $t = 0$ (The probe delay is set to zero when the pump reaches peak intensity at the front surface). The fringes in the interferogram present a significant shift and a dark spot that is a signature of less reflectivity in the material or deflection of the light out of the long f/# collection optics. This amount of displacement is the result of a $\sim 3.5 \times 10^{-2}$ pedestal in the pump beam as shown in the trace before the main pulse. A small misalignment of the seed beam in the regenerative amplifier allowed for extra amplified spontaneous emission in the laser. Better alignment of the seed pulse resulted in no visible pedestal and an oscillation that averaged to zero as Figure 21 right shows. The fringes present a slight shift associated to pre-expansion attributed to the unavoidable pre-pulses and small pedestal or rising edge of the main pulse arrival.

Non-linear diagnostics and THG in particular were used before in laser melting experiments, but here we were probing shocked materials which impose more restrictive conditions. The required shock spot size was small; a few tens of microns, with the current laser system to achieve high pressure states and phase transitions. Accordingly, the probe spot size had to be $\sim$10 microns and well centered with the pump beam. Radiation either from the ablator or the shocked material was emitted at the same wavelength as the THG so there was a minimum probe energy required for a reasonable signal to noise ratio. The THG

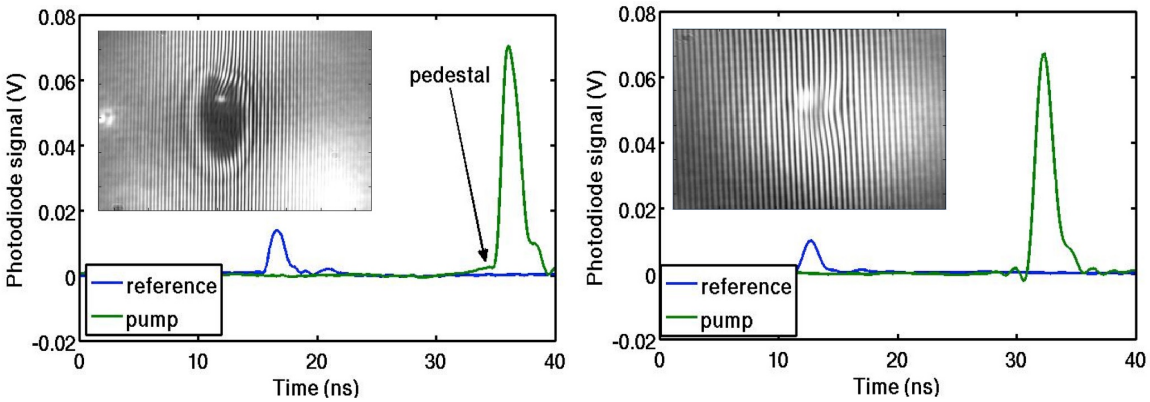

Figure 21: Left: 3.5×10^{-2} pedestal before main pulse. Right: no pedestal observed at this resolution (05/11/2010).

from such a small spot required a probe pulse as short as possible so the probe intensity and THG were maximized. Increasing the probe fluence well beyond the damage threshold of silicon $\sim$130 mJ/cm^2 would create conditions where the probe can modify the material being sampled. It takes $\sim$300 fs to damage the material, time that is much longer than the probe beam; however this time is reduced as the intensity is increased beyond the damage threshold [69].

Since the probe beam compression was optimized in vacuum, going through the different materials in this experiment such as windows, waveplates, filters, and lenses changed the time duration of the pulse. Figure 22 shows a compression scan performed to maximize the intensity of the probe pulse generating the third-harmonic at target. The laser energy was kept constant while the light was measured by the THG PMT and reflectivity PMT. Each position corresponds to 10 probe beam pulses averaged on fresh, not previously probed, silicon for each sample without shocking the material on the front surface. The 1ω signal remains constant as it should since linear reflectivity does not depend on the pulse length. The 3ω signal reaches a peak at around -0.8 mm that corresponds to a minimum pulse width at the target for a maximum intensity and highest THG. As the distance departs from this position, the pulse width increases and the intensity and THG drop.

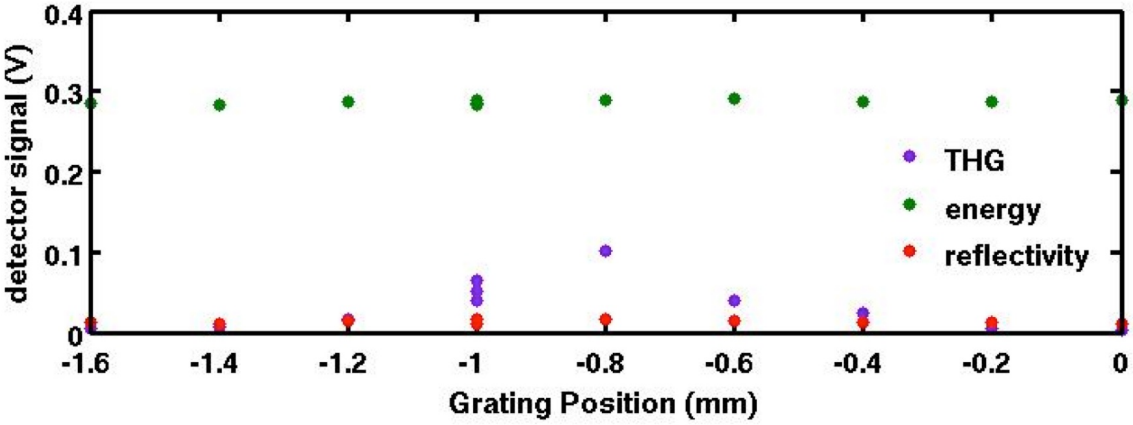

Figure 22: Compression grating scan to maximize THG at target (08/15/2010).

Plasma emission and blackbody radiation limit the minimum amount of probe light that can be used for

THG. The tests were performed shocking the material and reading the 3ω PMT while blocking the probe beam. The chamber walls were covered with black foil and a black mask with a small aperture for probing was used next to the rear side of the target to remove part of the spurious light. Figure 23 left shows one test shot where a reference signal (ref) was recorded with the probe beam unblocked without shocking the material and a shot signal (shot) was taken in the opposite configuration. The amount of spurious light recorded in the shock was about half of the THG in the reference and appeared simultaneously. Increasing the amount of probe light by an order of magnitude would exceed the damage threshold of silicon by the same amount and the probe would most probably affect the measurement. After installing the lens-iris combination similar to a confocal microscope, the spurious light was reduced by about a fourth as shown in Figure 23 left. Even though the result was good we could not exploit the full benefit of this approach because it was difficult to align a tight iris to the image of the probe spot of about $\sim$200 μm diameter. Only a few shots could be taken without repositioning the targets and the THG generation changed non-linearly as a result of pulse duration fluctuations or small changes in spot size. This made scanning the field stop a difficult task. We used an aperture of 1.5 ± 0.5 mm instead of $\sim$200 μm with the reasonable results shown.

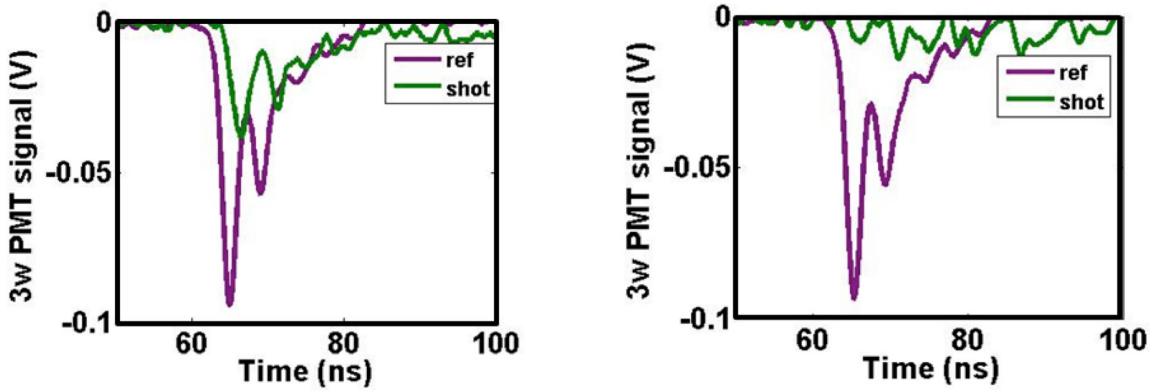

Figure 23: THG (ref) and spurious light (shot) without (left) and with (right) a lens-iris combination (05/14/2010).

We studied the effect of probe energy on silicon without shocking after minimizing the pulse duration and setting a lower THG limit imposed by the spurious 266 nm light. Figure 24 left shows the response of the THG (3ω) and reflectivity (1ω) PMTs when probing the same location of the target consecutively at 0.35 J/cm^2 fluence per shot. The probe beam energy and linear reflectivity remain roughly constant. The THG fluctuates shot to shot but does not seem to damage the material permanently. No light was being scattered into the interferometer camera imaging the rear side of the target. A cumulative effect appears when the probe beam energy is increased as shown in Figure 24 right. The THG and the reflectivity drop after shot #2 and after shot #8 the interferometer camera showed scattered light from the normal incident probe beam and with a clear damaged spot. The fluence is high enough to permanently damage the material. In these experiments, we lowered the probe energy as much as possible to avoid damaging the material while keeping it $\sim 5\times$ stronger than the spurious 266 nm light that could occur.

The THG intensity ($I_{3\omega}$) at normal incidence using circularly polarized light should follow the cubic relationship $I_{3\omega} \propto E_{3\omega}^2 \propto (E_{1\omega}^3)^2 \propto I_{1\omega}^3$. We tested this correlation by probing the sample without shocking and varying the incident light while measuring the linear reflectivity and THG. The target was repositioned at each sample test to probe fresh material. Varying the angle of the waveplate in the probe line allowed a continuous change of the incident light. Figure 25 left shows the reflectivity as a function of waveplate angle where $89 \pm 1^\circ$ corresponds to no light being transmitted. The relationship follows Malus'

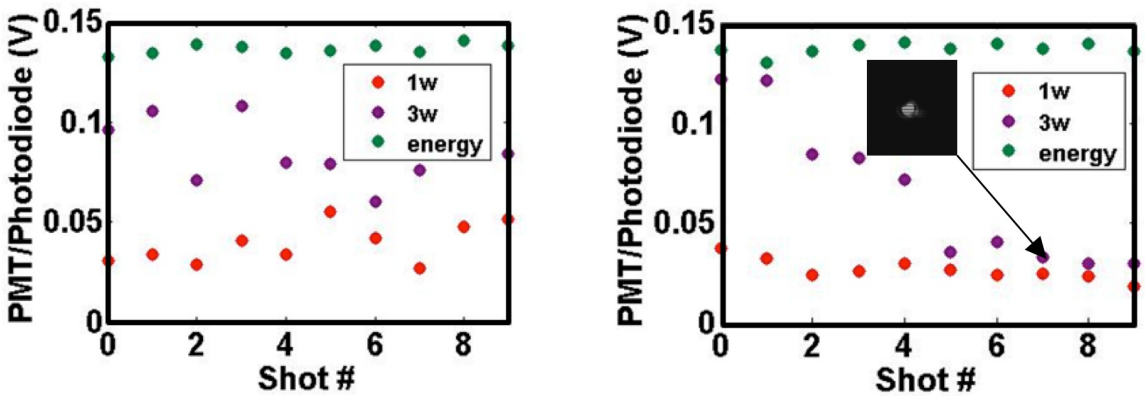

Figure 24: THG (3ω) and reflectivity (1ω) for 0.35 J/cm^2 per pulse (left) and 3.5 J/cm^2 per pulse (right).

law $I = I_0 \cos^2(\theta - \theta_0)$ so the linear reflectivity is proportional to the incoming probe intensity. The THG signal follows and exponential relationship with the incident intensity however the exponent is 1.53 instead of 3. This behavior has not been explained yet.

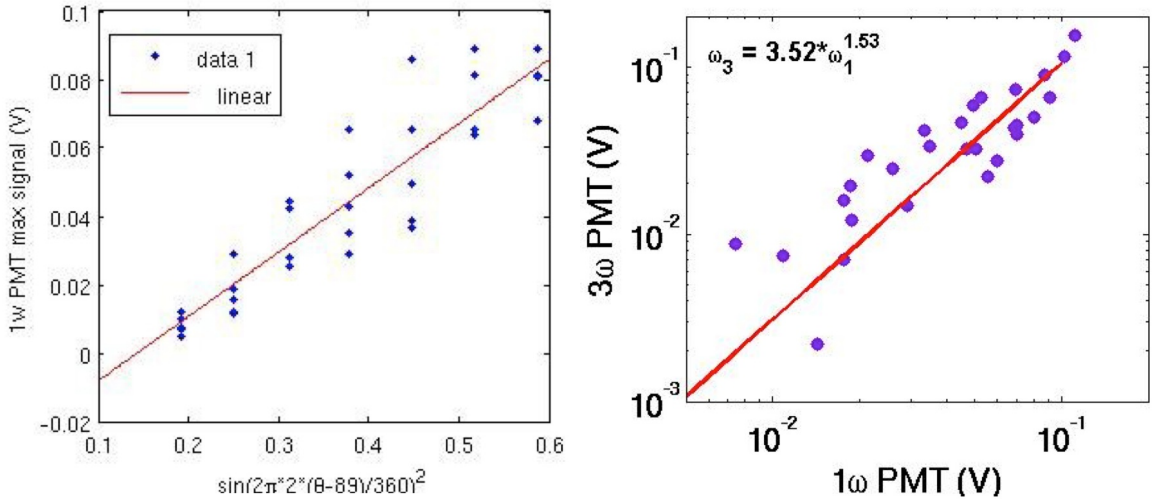

Figure 25: THG (3ω) and reflectivity (1ω) as a function of incident energy (06/23/2010).

The response of shocked silicon at an intensity of $\sim 1.4 \times 10^{13}$ W/cm^2 is shown in Figure 26. The probe delay is set to zero when the pump intensity reaches the peak at the front surface. The shocked data is normalized to non-shocked (cold) silicon values. The normalized linear reflectivity remains about unity for t $<$1 ns while a small pre-expansion occurs as a result of a precursor created possibly by the leading edge of the laser. At t $\sim$1 ns the shock arrives at the rear surface and the reflectivity drops to $<$0.1 in 0.25 ns. The normalized THG is ~ 1 up to t $\sim$0 ns after which it drops to a value of $<$0.25 at t $\sim$0.3 ns and then remains constant during the pre-expansion phase while dropping a little more after shock arrival. This information suggests that during pre-expansion when the linear reflectivity does not change, the material dielectric function does not change either leaving the linear and non-linear Fresnel factors unchanged. This implies that any change in the THG is related solely to a change in $\chi^{(3)}$ and in the lattice structure. The drop in THG indicates that some type of change in the crystalline structure (phase change) might be occurring during this period. After shock arrival both signals drop to ~ 0.1. This could be the result of scattering from surface fragmentation when releasing into vacuum or loss of light in the collection optics as a result of

rear surface expansion. The collection of the normal incidence light by the interferometer camera (oblique angle) for some of these images suggests fragmentation.

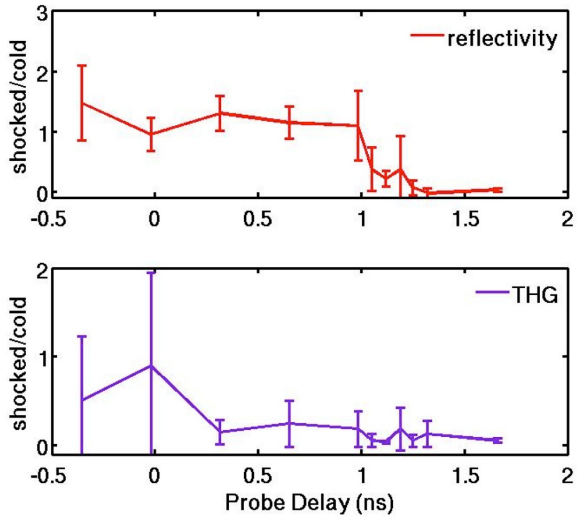

Figure 26: Shocked silicon at $\sim 1.4 \times 10^{13}$ W/cm^2.

Figure 27 shows shocked silicon at an intensity of $\sim 1.4 \times 10^{14}$ W/cm^2. The plots show two different data runs. The data in Figure 27(a) were taken in the same run as the data in Figure 26 while data in Figure 27(b) corresponds to a previous data run. Both data runs show a similar trend for the reflectivity and THG signals with quantitative differences. The plot on the left shows the normalized linear reflectivity increasing by $1.6\times$ during pre-expansion, $t < \sim 0.65$ ns. At t ~ 0.65 ns the shock arrives at the rear surface and the reflectivity drops to <0.3 in about 0.6 ns. The normalized THG remains ~ 1 up to t ~ -0.35 ns after which it drops for about 0.65 ns to a value of <0.15 and then remains constant during the rest of pre-expansion phase. At shock arrival and afterwards, the THG drops to <0.1 similarly to the linear reflectivity. Shocking at an order of magnitude higher intensity makes the shock arrive ~ 0.35 ns earlier than at the lower intensities shown in Figure 26. The increase in reflectivity in the pre-expansion phase suggests a transition to a metallic state of the material as the Drude model predicts (2.2 increase at normal incidence). The difference between the measured 1.6 increase and the 2.2 predicted could be the result of fewer electrons promoted to the conduction band as compared to previously measured values [77]. This metallization as a result of the change in the dielectric constant might be the reason why THG, which also depends on the dielectric constant through the non-linear Fresnel factors, drops. This conjecture requires further analysis. After shock arrival, the reflectivity drops similarly to the low intensity case probably as a result of fragmentation. THG that is already low also drops. The plots in Figure 27(b) are qualitatively similar to the ones in Figure 27(a), but they present a few differences. The linear reflectivity increases to about 3.5 in the pre-expansion phase and the shock arrival occurs ~ 0.3 ns earlier. This might be result of the 10% higher intensities used which probably made the pre-expansion wave travel faster while promoting more electrons into the conduction band setting the material into a more metallic state.

3.4 Conclusions

We found that the third-harmonic generation response is quite different compared to linear reflectivity when probing shocked materials. At laser intensities $\sim 10^{13}$ W/cm^2 and during the pre-expansion phase of the

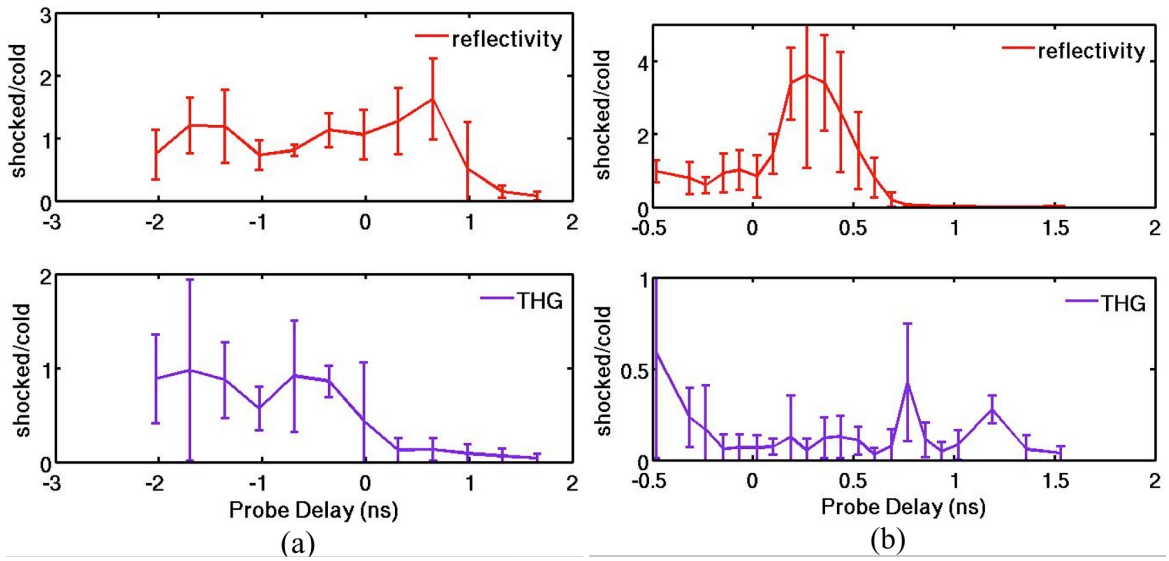

Figure 27: Shocked silicon at $\sim 1.4 \times 10^{14}$ W/cm^2.

material (before shock arrival), no transition to a metallic state was seen as reflectivity remained similar to cold silicon values; however THG presented a substantial drop. Since reflectivity did not change during this phase we could assume that the dielectric function did not change leaving the linear and non-linear Fresnel factors unchanged. This conjecture implies that any change in the THG is related solely to a change in χ^3 and so to a change in the lattice structure. Then, this data suggests that THG can be used to detect changes in the crystalline structure materials. At laser intensities $\sim 10^{14}$ W/cm^2 an increase in reflectivity was observed during the pre-expansion phase suggesting a transition to a metallic state that did not seem to affect the crystalline structure of the material since THG remained roughly constant during that period. After shock arrival the reflectivity dropped close to zero as the result of possible scattering from surface fragmentation when releasing into vacuum. THG at low intensities also dropped for the same reason as the reflectivity but it remained constant and very low at high intensities which has not been explained yet.

If fragmentation occurs at shock arrival, the current setup needs to be modified to study shock-induced phase transitions. Adding a backing window to match the impedance of silicon could forbid fragmentation and allow probing the material structure and not its surface. Also, pre-heating of the samples close to their melting point would allow shock-melt experiments at pressures $\ll 120$ kbar available with our laser system that might not fragment the material upon release.

Upcoming experiments should be aimed to lower the error bars and detect the amount of spurious light collected, for example by using a photomultiplier tube to collect light at a wavelength close to the THG. Shocking with a more energetic beam would allow larger shock breakouts to reduce the pointing error with the probe beam; the probe spot size could also be increased for a better averaging.

3.5 Appendix

Pre-heating of silicon and germanium targets reduces the pressure needed to shock-induce melting to $<$120 kbar (Figure 18) that can be achieved with the THOR laser. Uniformity in the target heating is desirable to provide similar initial conditions for shocks probed at different time delays. At low target temperatures, the dominant heat loss mechanism in vacuum is by conduction with the mount. As the target temperature

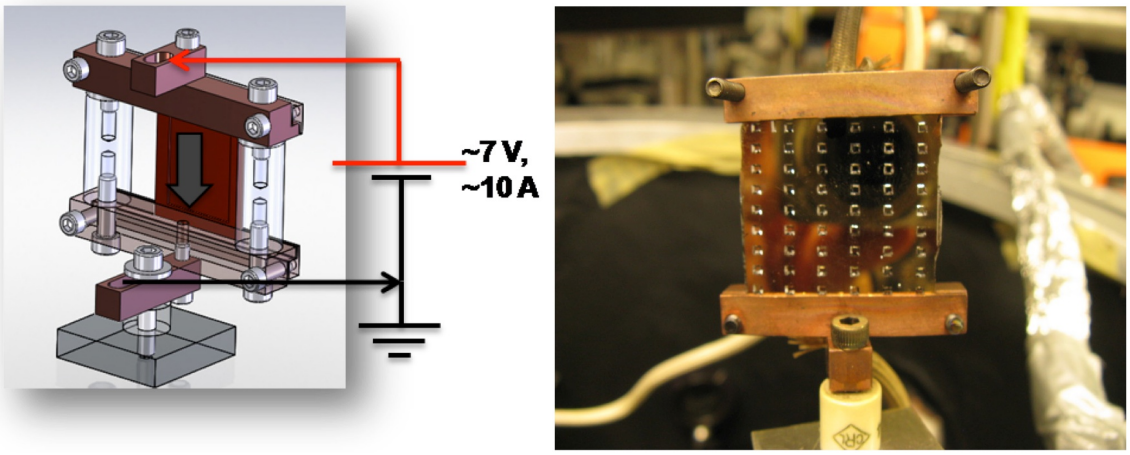

Figure 28: Modified mount used as electrodes to provide current to the ablation layer for ohmic heating.

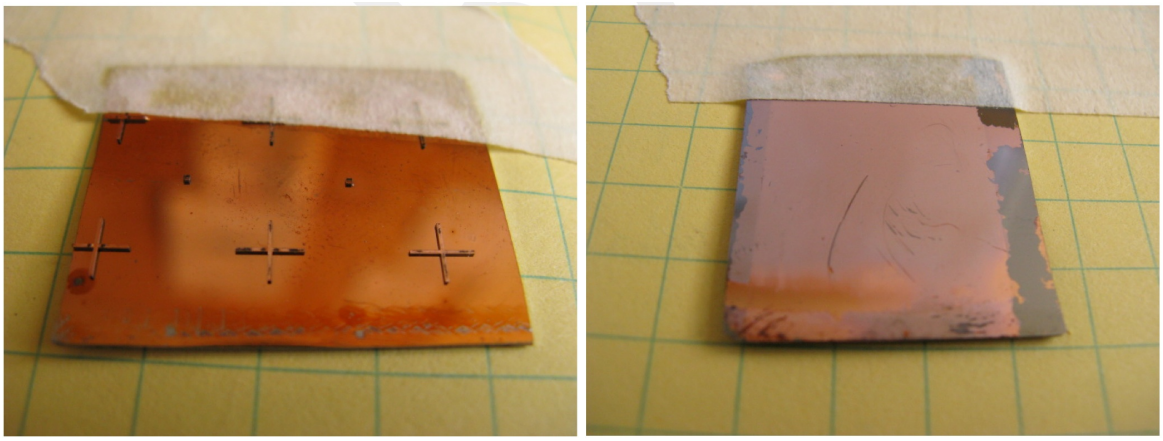

Figure 29: Dummy target that reached 400 °C (left) compared to a one that reached 600 °C (right).

rises, radiation from the target surface area (A) becomes a dominant loss, and the radiated power (P) at a temperature (T) is given by:

$$P \sim A\epsilon\sigma T^4 \tag{9}$$

where ϵ is the emissivity of the surface and σ the Stefan-Boltzmann constant. For a 1 inch square sample and assuming perfect emissivity (blackbody) at $\sim$700 °C the dissipated power is $\sim$30 W. The heating element has to be able to deliver this power to the sample. We decided to use Ohmic heating of the targets (Figure 28) that produced favorable results. We used the ablation coating of the samples as the heat conducting surface. The advantage of this approach is homogenous heating however it requires the ablator be a good conducting surface. The resistivity of copper at room temperature is $\sim$17 nΩm and about 4 times higher at $\sim$700 °C. A square sample connected to the electrodes that serve as the holder presents a total electrical resistance (R):

$$R = \eta/t \tag{10}$$

where η is the electrical resistivity and t the thickness of the conductor. A 100 nm thick ablation layer results in a total resistance of $\sim$0.7 Ω at $\sim$700 °C. We used a power supply that delivered 10 A and 7 V across the electrodes with a total power of $\sim$70 W. This technique proved to be successful in heating up the targets, reaching temperatures of 600 °C as measured on the rear side of the targets with a thermocouple. The coating appears degraded at these high temperatures and after venting the chamber compared to samples that only reached 400 °C (Figure 29). The effect of the coating degradation in laser absorption is unknown. The damage might be the result of copper oxidation even under mTorr vacuum (effect that was seen when testing in air). The temperature of the front surface could also be higher than the probed rear side making the copper closer to its melting point. However this might be unlikely, the temperature gradient should be only a few degrees with the thermal conductivity of silicon $\sim$35 Wm^{-1} K^{-1} at 600 °C.

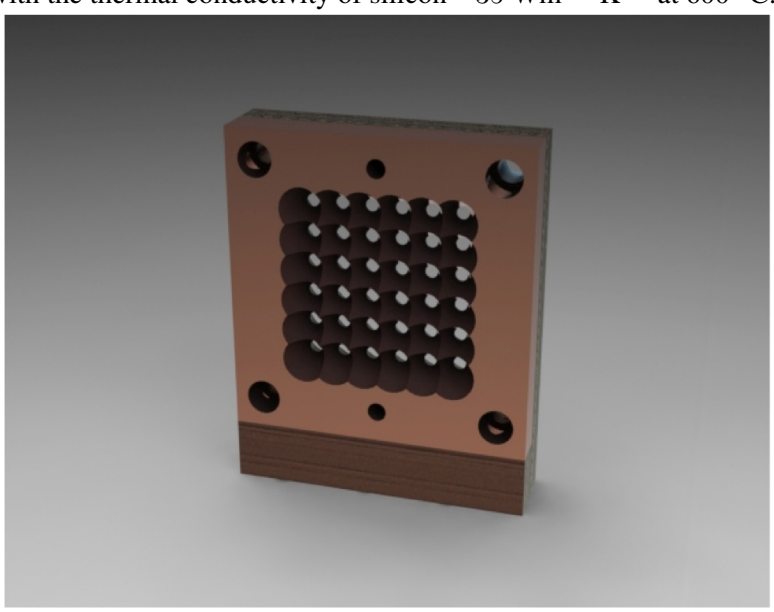

Figure 30: Ohmic heating holder design for non conduction ablators.

Another option to heat up the targets is to sandwich them in a heated holder (Figure 30). An ohmic heater (not present in the figure) is attached to the holder that would conduct the heat to the sample by physical contact. This approach could create thermal gradients in the sample depending on how good the contact is, however it does not require the ablation coating to be a conductor.

4 Dynamic compression of aluminum

Principal Authors: Jonathan A. Zimmerman, J. Michael Winey, Yogendra M. Gupta

This section contains a paper entitled "Elastic anisotropy of shocked aluminum single crystals: use of molecular dynamics simulations" that was published in *Phys. Rev. B* in 2011. It was authored by Jonathan A. Zimmerman, J. Michael Winey and Yogendra M. Gupta. [SAND 2011-0728 J]

In this section, molecular dynamics (MD) calculations are used to examine shock wave propagation along [100], [111], and [110] directions in aluminum single crystals. Four different embedded-atom method (EAM) potentials were used to obtain wave profiles in ideal (defect-free) crystals shocked to peak longitudinal stresses approaching 13 GPa. Time-averaged and spatially-averaged continuum variables were determined from the MD simulations to compare results from different potentials and to provide a direct comparison with results from nonlinear elastic continuum calculations that incorporated elastic constants up to fourth order. These comparisons provide a basis for selecting the optimal potential from among the four potentials examined. MD results for shocks along the [100] direction show significant differences for stresses and densities determined from simulations using different EAM potentials. In contrast, the continuum variables for shocks along the [111] and [110] directions show smaller differences for three of the four potentials examined. Comparisons with the continuum calculations show that the potential developed recently by Winey, Kubota and Gupta [78, 79] provides the best overall agreement between the MD simulations and the continuum calculations.

4.1 Introduction

In recent years, classical molecular dynamics (MD) simulations have been used increasingly to examine the shock compression response of crystalline solids. [80–82] Such simulations can provide important insight into the microscopic mechanisms governing material phenomena such as inelastic deformation and structural phase transformations. Despite the potential usefulness of classical MD simulations for understanding the dynamic response of solids, it is difficult to evaluate the validity of the calculated results since direct comparisons with experiments pose a challenge: the length and time scales of the simulations and experiments differ by orders of magnitude. Also, not all material details (e.g. defects, heterogeneities) can be incorporated realistically into the MD simulations.

Although the above indicated differences are well recognized and they constitute an important impetus for advances in computational capabilities, [83] there is also a fundamental scientific issue that needs attention. Because results from MD simulations depend on the choice of the inter-atomic potentials, establishing the applicability of the potentials for the loading conditions of interest constitutes an important need. Here, we address this need by focusing on the following two key questions: how to ascertain the applicability of a potential for simulations involving shock wave compression, and how to choose the optimal potential when several choices are available.

Our approach to address these questions consists of using MD simulations to examine and analyze shock wave propagation along different crystal orientations in idealized (or defect-free) crystals. The lack of defects in the simulated crystals results in purely elastic deformation for shock loading to peak stresses that would otherwise result in yielding and inelastic deformation in crystals having defects. Therefore, our approach enables a direct comparison between the thermo-mechanical variables determined from MD simulations of shock wave compression and the thermo-mechanical variables from nonlinear elastic continuum

calculations that utilize known second-, third-, and fourth-order elastic constants. By making such comparisons for each of the different inter-atomic potentials, we have a basis for selecting between different potentials. To the best of our knowledge, this approach to selecting an optimal potential has not been carried out previously for MD simulations of shock compression of crystals.

In the present work, we examine the anisotropic response of shocked aluminum single crystals. Aluminum was selected for this study because it is representative of face-centered cubic (FCC) metals having high stacking fault energies and because several embedded-atom method (EAM) potentials for Al are available. [78, 79, 84–87] To address the scientific questions indicated above, we have focused on elastic shock wave propagation along [100], [110], and [111] orientations in Al single crystals. Continuum averages from MD simulations, carried out using four different EAM potentials, are compared with each other and with nonlinear elastic continuum calculations that utilize elastic constants up to fourth order.

4.2 Computational Methods

4.2.1 MD Simulations

MD simulations of defect-free Al single crystals shocked along the [100], [111], and [110] directions were performed using four different EAM potentials: Voter and Chen (VC); [84, 85] Ercolessi and Adams (EA); [86] Mishin, Farkas, Mehl and Papaconstantopoulos (MFMP); [87] and Winey, Kubota and Gupta (WKG). [78, 79] All of our MD simulations were performed using the LAMMPS code. [1] To simulate shock wave propagation in aluminum single crystals, atomic systems containing $\sim$1 million atoms were constructed having approximate dimensions 640 Å (x_1) by 160 Å (x_2) by 160 Å (x_3), where x_i refer to a coordinate system in which the shock wave propagates along the x_1 direction. Free surface boundary conditions were used in the longitudinal (x_1) direction, whereas periodic boundary conditions were applied in the transverse ($x_2 and x_3$) directions. Shock wave propagation was examined along the [100] direction (x_1 - [100], x_2 - [010], x_3 - [001]), the [111] direction (x_1 - [111], x_2 - [$\bar{1}$10], x_3 - [$\bar{1}\bar{1}$2]), and the [110] direction (x_1 - [110], x_2 - [$\bar{1}$10], x_3 - [001]) . The systems were equilibrated for 10 ns (10^7 timesteps of 1 fs each) to bring them to zero stress and 300 K temperature. To produce planar shocks in the equilibrated systems, four atomic layers at one end of the crystal were assigned a fixed velocity for the duration of the simulation, resulting in the propagation of supported shock waves having prescribed particle velocities. Previous work has shown that shock wave propagation in MD simulations is insensitive to the method by which the shocks are produced. [80] The simulations presented here utilized a small timestep (0.01 fs) to adequately capture the dynamics associated with the propagating shock wave.

4.2.2 Continuum Variables from MD Simulations

To calculate mass density, Cauchy stress and temperature from our MD results, we used the method introduced by Hardy, [88] in which two descriptions of a material system are considered. One description constitutes the continuum viewpoint, where the variables are point-wise functions of fixed spatial positions and time. The other description is that the system consists of atoms, each of which has an associated mass, momentum, potential energy and kinetic energy. The two descriptions are connected using a prescribed localization function ψ, which enables the properties of the atoms to be averaged over a localized region surrounding the spatial point and allows the atoms to contribute to continuum properties at that point. For

example, mass density at fixed spatial position x_i is given by

$$\rho\left(x_i,t\right)=\sum_{\alpha=1}^{N}m^{\alpha}\psi\left(x_i^{\alpha}-x_i\right), \tag{11}$$

where N is the number of atoms in the system, m^{α} is the mass of atom α, and x_i^{α} is the spatial position of atom α. By using expressions similar to Eq. (11) for mass, momentum and energy densities in the balance laws of continuum mechanics, Hardy was able to derive an expression for Cauchy stress (assumed positive in compression here), [88]

$$P_{jk}\left(x_i,t\right)=\frac{1}{2}\sum_{\alpha=1}^{N}\sum_{\beta=1,\beta\neq\alpha}^{N}x_j^{\alpha\beta}f_k^{\alpha\beta}B^{\alpha\beta}\left(x_i\right)+\sum_{\alpha=1}^{N}m^{\alpha}\hat{v}_j^{\alpha}\hat{v}_k^{\alpha}\psi\left(x_i^{\alpha}-x_i\right), \tag{12}$$

where$x_j^{\alpha\beta}\equiv x_j^{\alpha}-x_j^{\beta}$, $f_k^{\alpha\beta}$ is the inter-atomic force between atoms α and β, $B^{\alpha\beta}$ is a bond function determined by integrating ψ, and $\hat{v}_j^{\alpha}\left(x_i,t\right)\equiv v_j^{\alpha}-v_j\left(x_i,t\right)$, where v_j^{α} is the velocity of atom α and $v_j\left(x_i,t\right)$ is the continuum velocity field calculated by dividing momentum density by mass density. Within this report, we use the shorthand P_x to refer to P_{11}, P_y to refer to P_{22} and P_z to refer to P_{33}. Although not derivable from the continuum balance laws, Hardy also defined an expression for localized temperature,

$$T\left(x_i,t\right)=\sum_{\alpha=1}^{N}m^{\alpha}\hat{v}_j^{\alpha}\hat{v}_j^{\alpha}\psi\left(x_i^{\alpha}-x_i\right)\Bigg/\left(3k_B\sum_{\alpha=1}^{N}\psi\left(x_i^{\alpha}-x_i\right)\right), \tag{13}$$

where k_B is Boltzmanns constant. Further details about Hardy's method and its use in thermo-mechanical problems can be found in references [89] and [90], as well as elsewhere within this report.

We defined spatial points as the vertices (nodes) on a rectangular grid. For our simulations, this grid consisted of 4,672 elements, each having approximate dimensions: 10 Å by 20 Å by 20 Å. To allow for translation of the atomic system, the grid extended a length of 730 Åin the longitudinal direction to encompass the atomic system plus some free space. Linear interpolation functions between nodes were used to create a tent-shape localization function in three dimensions. Continuum variables were calculated at the spatial points every 0.01 ps (1000 timesteps).

To reduce the statistical uncertainties in the continuum variables, averaging methods were used. First, the 64 nodes located at the same longitudinal position were averaged to create a single value for each continuum variable. Next, to arrive at steady-state estimates of continuum properties behind the shock front, the continuum variables were averaged spatially over a domain of 200 Å and temporally over a domain of 3 ps.

4.2.3 Nonlinear Elastic Continuum Calculations

For comparison with the MD results, continuum variables for shocked Al single crystals were calculated using nonlinear elasticity theory. [91–93] It is convenient to express the differential changes in stress and temperature in terms of the elastic strain increments and entropy change: [91, 92]

$$dt_{ij}=C_{ijkl}d\eta_{kl}-\rho_0\Gamma_{ij}TdS \tag{14}$$

$$dT=-T\Gamma_{ij}d\eta_{ij}+TdSc_{\eta} \tag{15}$$

where C_{ijkl} are the isentropic elastic coefficients and both the thermodynamic (2nd Piola-Kirchhoff) stresses t_{ij} and the Lagrangian strains η_{ij} are referred to the initial configuration. In our calculations, both the Grüneisen tensor Γ_{ij} [91] and the specific heat at constant strain c_η were held constant.

The isentropic elastic coefficients C_{ijkl} are defined as the second derivatives of the internal energy with respect to strain at constant entropy. [92, 93] Therefore, from a truncated expansion of internal energy in powers of elastic strain, the elastic coefficients are given by [93]

$$C_{ijkl}\left(S,\boldsymbol{\eta}\right) = \bar{C}_{ijkl} + \bar{C}_{ijklmn}\eta_{mn} + \frac{1}{2}\bar{C}_{ijklmnpq}\eta_{mn}\eta_{pq}, \tag{16}$$

where $\bar{C}_{ijkl}$, $\bar{C}_{ijklmn}$, and $\bar{C}_{ijklmnpq}$ are the second-, third-, and fourth-order elastic constants, respectively, and the overbar indicates evaluation at the initial configuration. Measured values for the second- and third-order constants for aluminum were taken from Refs. [94] and [95], respectively. For the elastic loading calculations considered here, the entropy dependence of the elastic coefficients can be neglected. For elastic shock waves propagating along [100], [110], or [111] directions in a cubic crystal, the Lagrangian strains are uniaxial and can be written as

$$\eta_{11} = -e + \frac{1}{2}e^2, \tag{17}$$

where $e = 1 - \rho_0/\rho$ is the engineering strain and x_1 is along the wave propagation direction. For uniaxial strain, the Cauchy stresses (positive in compression) are related to the thermodynamic stresses by

$$P_x = -\left(1-e\right)t_{11} \tag{18}$$

$$P_y = -\frac{t_{22}}{(1-e)} \tag{19}$$

$$P_z = -\frac{t_{33}}{(1-e)}. \tag{20}$$

In terms of the Cauchy stresses and engineering strain, the entropy change encountered in shock wave loading is [96]

$$2\rho_0 T dS = e dP_x - P_x de. \tag{21}$$

To determine Cauchy stresses and temperature for shocked Al single crystals, numerical methods were used to obtain a simultaneous solution for Eqs. (14)-(21). The stresses and temperatures determined from the continuum calculations were then compared with analogous quantities from the MD simulations.

The fourth-order elastic constants used in the nonlinear elastic continuum calculations were determined by fitting to available wave propagation data [97] for shock loading and unloading along the [100], [110], and [111] directions in Al single crystals. Because of the limited data available, the Cauchy relations [98] were invoked to reduce the number of independent fourth-order elastic constants from 11 to four. The fitting was performed using a previously developed anisotropic approach for wave propagation simulations in single crystals, [99] along with the known second-order [94] and third-order [95] elastic constants. The resulting fourth-order elastic constants are: C_{1111} = 25000 GPa, C_{1112} = 3000 GPa, C_{1122} = 3000 GPa and C_{1123} = 500 GPa.

4.3 Results

4.3.1 Elastic shock wave profiles

We first wish to quantify the range of piston speeds (u_p) for which only elastic shock wave propagation will occur. The longitudinal stress corresponding to maximum of this range is commonly known as the Hugoniot Elastic Limit (HEL). Figure 31 shows shock wave propagation in the [100] direction at two distinct times (1.5 and 3.0 ps) within a small (128,000 atom) system modeled with the WKG potential. Three piston speeds were examined: 300 m/s, 600 m/s and 1200 m/s. Figure 31 clearly shows that no defects are generated for the two smaller piston speeds, but stacking faults are generated at the largest speed.

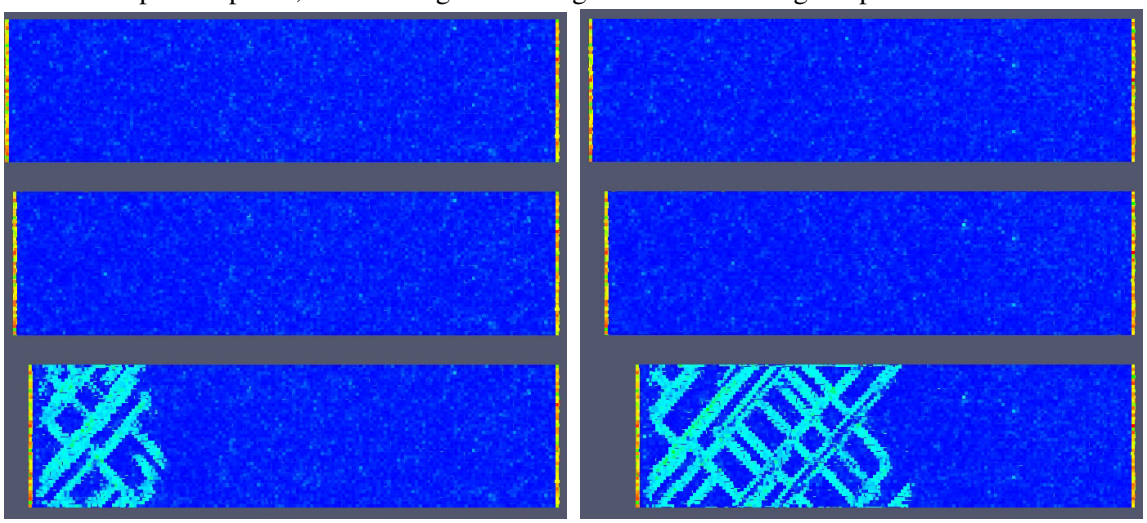

(a) (b)

Figure 31: Aluminum atomic system (modeled using the WKG interatomic potential) during shock wave propagation at (a) 1.5 ps and (b) 3.0 ps after initial motion of the left-hand piston. Three systems are shown in each sub-figure for the piston speeds of 300 m/s (top), 600 m/s (middle), and 1200 m/s (bottom). Atoms filtered and colored by centrosymmetry parameter.

Using this result, simulations were also performed for the other potentials and crystal orientations of interest. These simulations, snapshots from which are shown in Figure 32 for u_p = 600 m/s, confirm that shock waves are elastic in character for $u_p \leq$ 600 m/s in all cases. It is interesting to note that while no discernible crystal defects indicative of plasticity (e.g. stacking faults, dislocation lines) are present in Figure 32, filtering via the centrosymmetry parameter reveals many more isolated atoms for the EA and (even more-so for) the VC potentials than for the WKG and MFMP potentials. Such behavior usually corresponds with atoms displaying variable thermal motion, indicating that temperature rises behind the shock fronts may be higher for the EA and VC potentials (a hypothesis that will be confirmed as will be shown).

4.3.2 [100] Compression

Instantaneous profiles of shock wave propagation

Before comparing space- and time-averaged variables with continuum calculations, we first examine

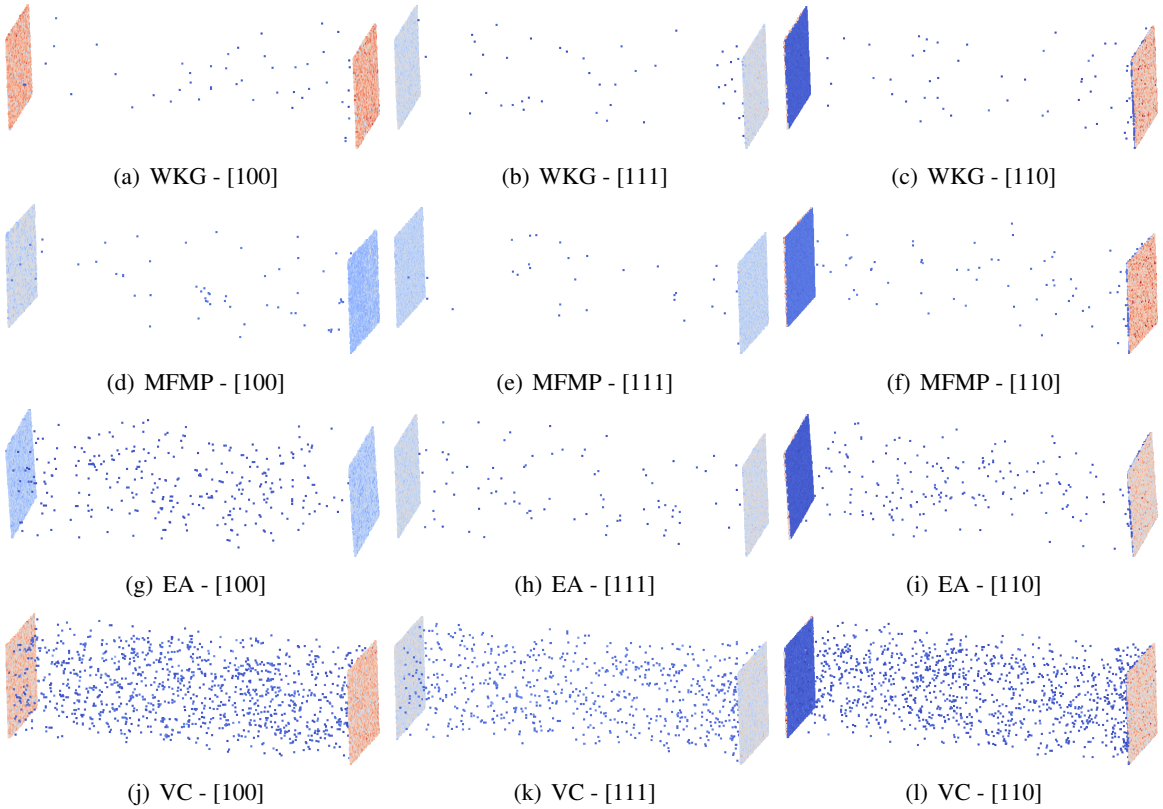

(a) WKG - [100] (b) WKG - [111] (c) WKG - [110]

(d) MFMP - [100] (e) MFMP - [111] (f) MFMP - [110]

(g) EA - [100] (h) EA - [111] (i) EA - [110]

(j) VC - [100] (k) VC - [111] (l) VC - [110]

Figure 32: Aluminum atomic systems during shock wave propagation with u_p = 600 m/s. Atoms filtered and colored by centrosymmetry parameter. Subfigures are labeled with the interatomic potential used, and crystal direction along which planar shock waves are traveling.

some features of the continuum fields and their fluctuations. Figure 33 shows the longitudinal stress field ($\sigma_x = -P_x$) for elastic shock wave propagation ($u_p = 300$ m/s) at a time of 3.0 ps after the piston has initiated motion. We note a few interesting features from this figure: first, spatial fluctuations of σ_x are present in the material both before and after the shock wave has passed. Second, we observe higher magnitudes of compressive stress for the WKG potential, with increasingly lower magnitudes in the MFMP, EA and VC potentials, respectively. Third, we observe that the shock wave travels significantly faster in the WKG material, somewhat faster in MFMP, and slower in the EA and VC materials.

Although this section focuses on compression along the [100] crystal direction, we take this opportunity to compare this spatially-varying field with fields created for compression along [111] and [110] for the WKG potential. These fields are shown in Figure 34. As before, this figure shows spatial fluctuations for all three orientations. We also note that the shock propagates at comparable speeds in all three cases (with the [111] orientation somewhat slower than [100] or [110]), and that non-planar features are present for compression in the [110] direction. This latter observation is no doubt due to the crystal asymmetry that exists as compared with the [100] system.

As noted earlier, our analysis of these continuum fields first involves taking a spatial average among 64 nodes located along the same longitudinal (x_1) position to create a single value to represent the cross-sectional rectangular slab centered on that position. This process is used to generate field profiles along the longitudinal direction at any specified instant of time. As such fields still displayed some aberrant characteristics associated with the discreteness of the atomic lattice, it was decided to combine the values from each slab with its adjacent neighbors (three slabs in all) and recompute average field values at those longitudinal positions. The resulting profiles for longitudinal velocity (v_x, hypothetically equal to u_p), mass density (ρ), and temperature (T) are shown in Figure 35 for both $u_p = 300$ m/s and $u_p = 600$ m/s, and the profiles for normal stress components (σ_x, σ_y and σ_z) are shown in Figure 36.

A few notable features are present in these figures. First, we observe very little deviation in the longitudinal velocity far behind the shock front from the prescribed piston speed. Second, although the points making up these profiles represent spatial averages over thousands of atoms, it still appears that some discreteness of lattice affects the resulting mass density profiles. Third, we note that unlike the EA and VC potentials the WKG potential (and to a lesser degree, the MFMP potential) displays a prominent peak at the shock front for the continuum fields of longitudinal velocity, mass density and stress (all components) at the higher piston speed of 600 m/s. This peak is absent at the lower piston speed of 300 m/s. Finally, we also notice that a shock front peak in temperature field is characteristic of all the potentials examined, although not as prominent in the EA potential as the other three.

An efficient way to combine the information from these time-instantaneous profiles is to view so-called "$x - t$" plots. These plots combine profiles over a range of times using color contours to express field magnitude. Use of $x - t$ plots to examine shock deformation was done extensively by Kubota et al. [100], as we use it similarly here. Figure 37 shows $x - t$ plots for continuum fields in smaller-sized (128,000 atom) VC and WKG systems under [100] compression for a piston speed of 300 m/s. Figure 38 shows similar plots for a piston speed of 600 m/s, and Figure 39 for a piston speed of 1200 m/s.

Many of the features noticed earlier, such as the temperature peaks observed for all potentials and the density and stress peaks for the WKG potential, are found in these $x - t$ plots. In addition, dual elastic and plastic shock wave fronts are visible in the $x - t$ plots for the 1200 m/s piston speed case, along

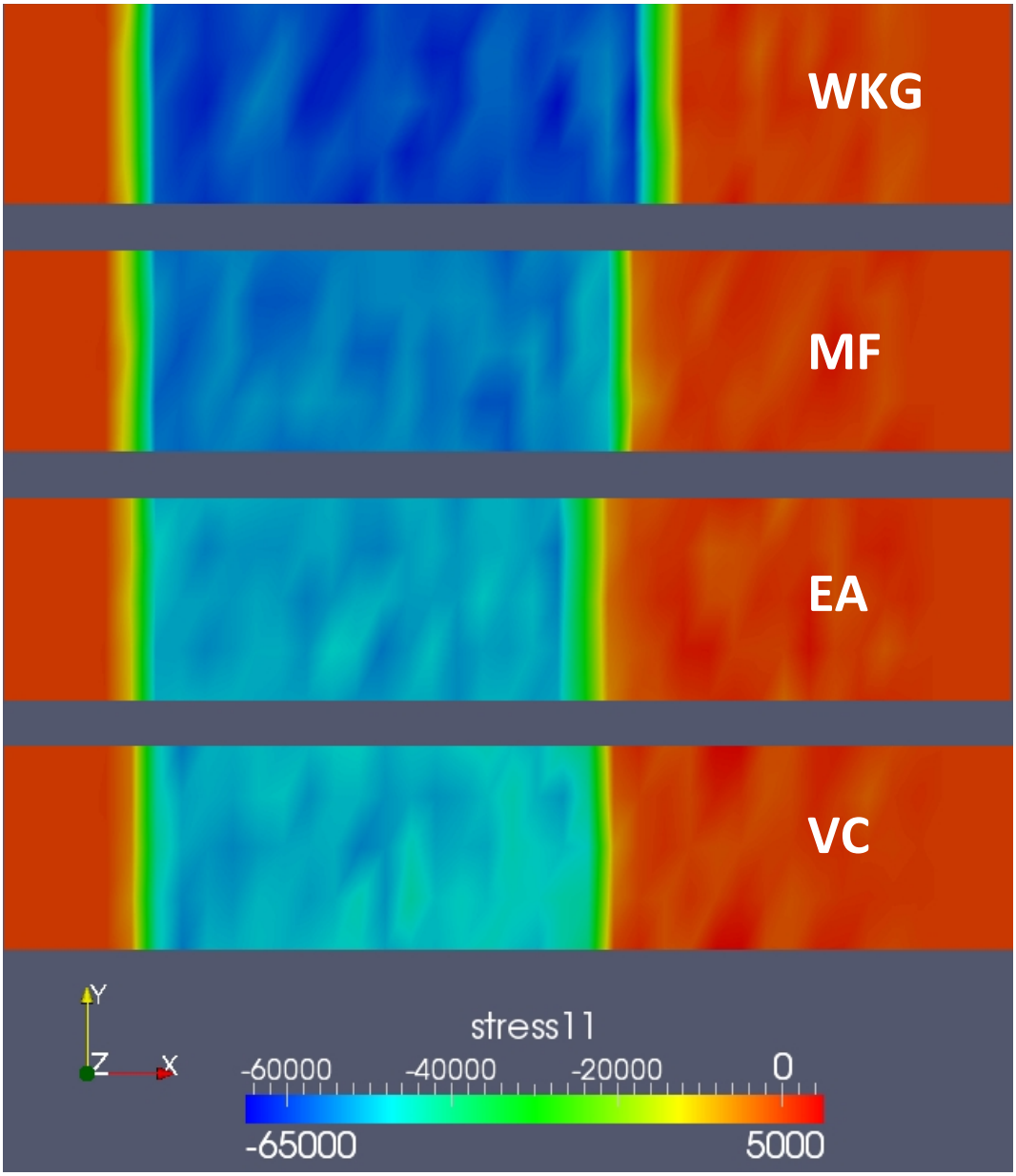

Figure 33: Side view of longitudinal stress field ($\sigma_x = -P_x$) for $u_p = 300$ m/s at time = 3.0 ps. Stress is in units of bars, where 10^4 bars = 1 GPa. Each system is labeled with the potential used.

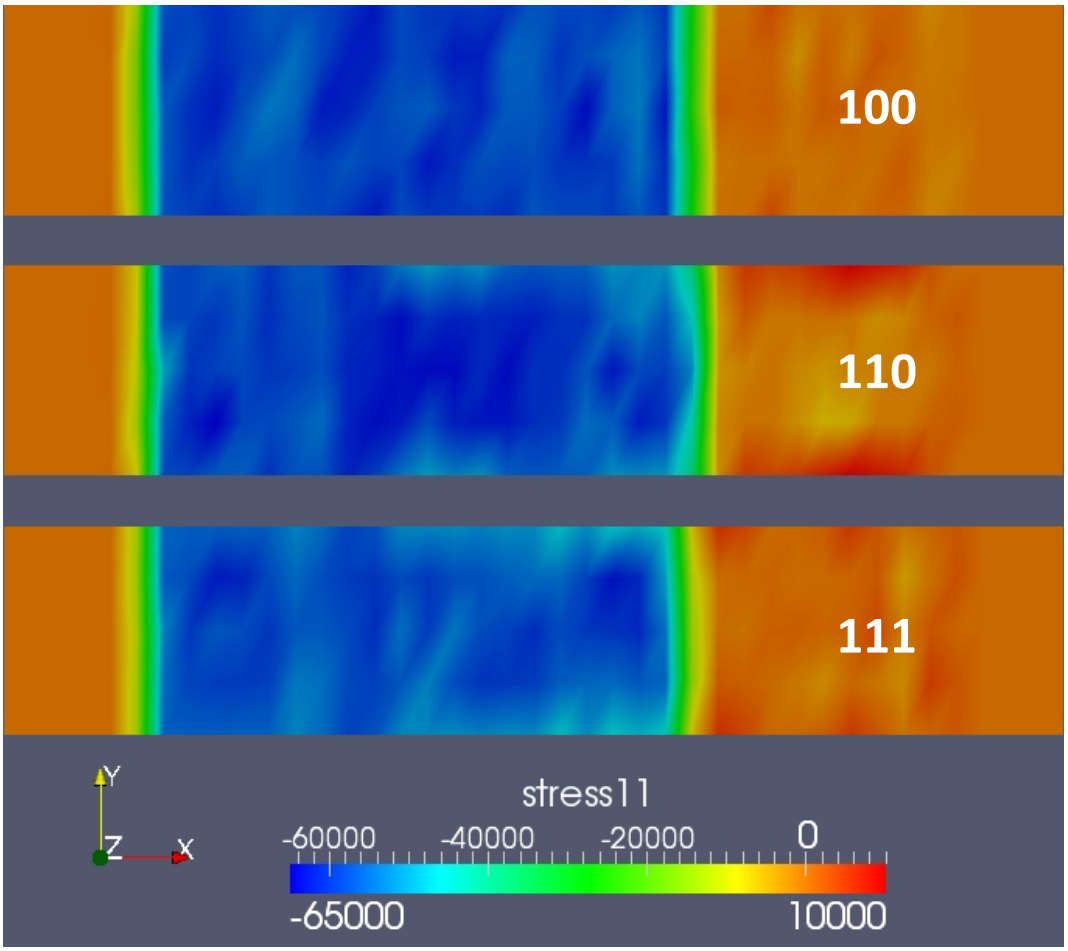

Figure 34: Side view of longitudinal stress field ($\sigma_x = -P_x$) for $u_p = 300$ m/s at time = 3.0 ps for the WKG potential. Stress is in units of bars, where 10^4 bars = 1 GPa. Each system is labeled with the crystal direction along which compression occurs.

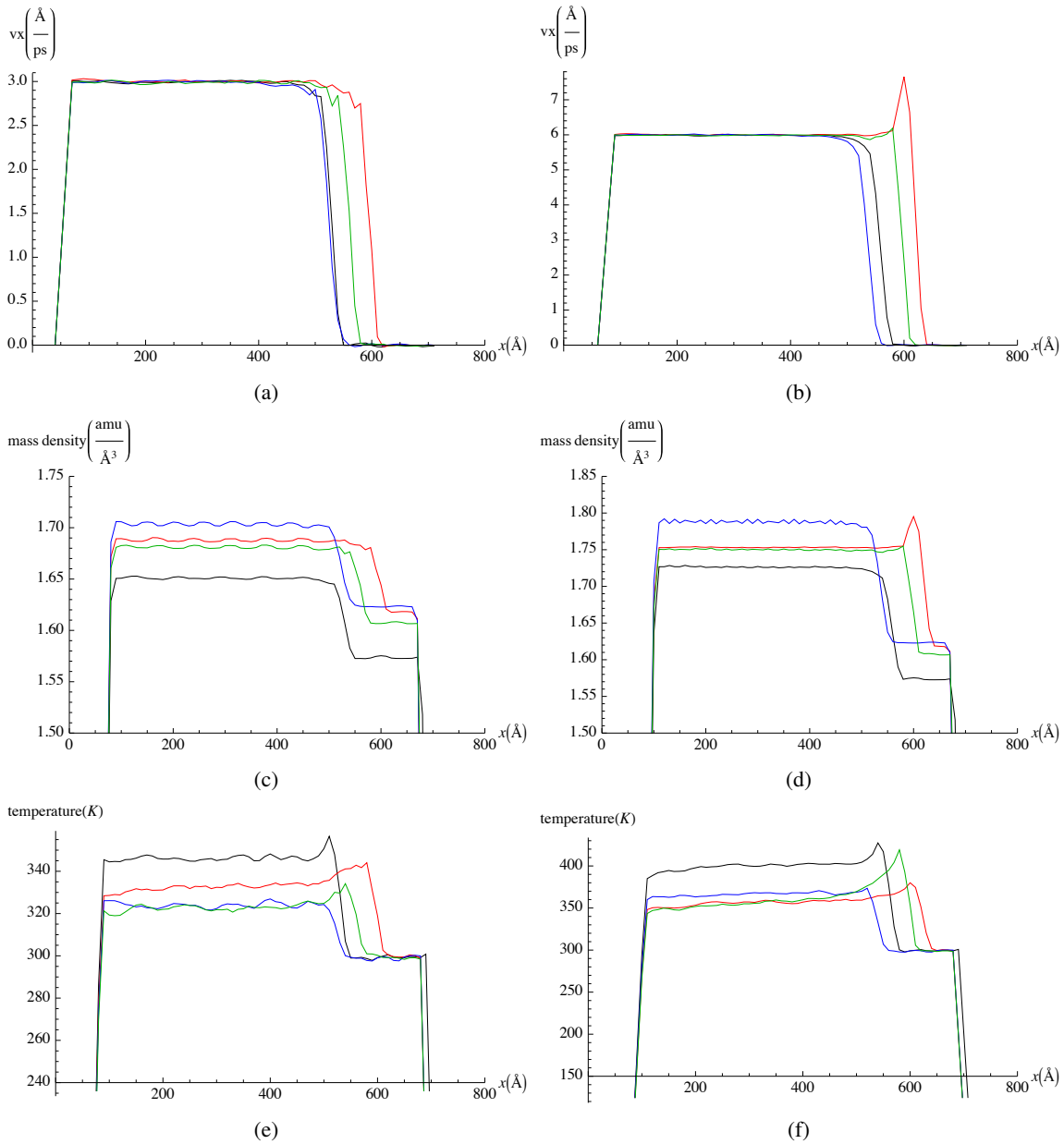

Figure 35: Longitudinal velocity, mass density and temperature profiles during elastic shock wave propagation at (a),(c),(e) u_p = 300 m/s and (b),(d),(f) u_p = 600 m/s along with [100] crystal direction. Color key: WKG, MFMP, EA, VC.

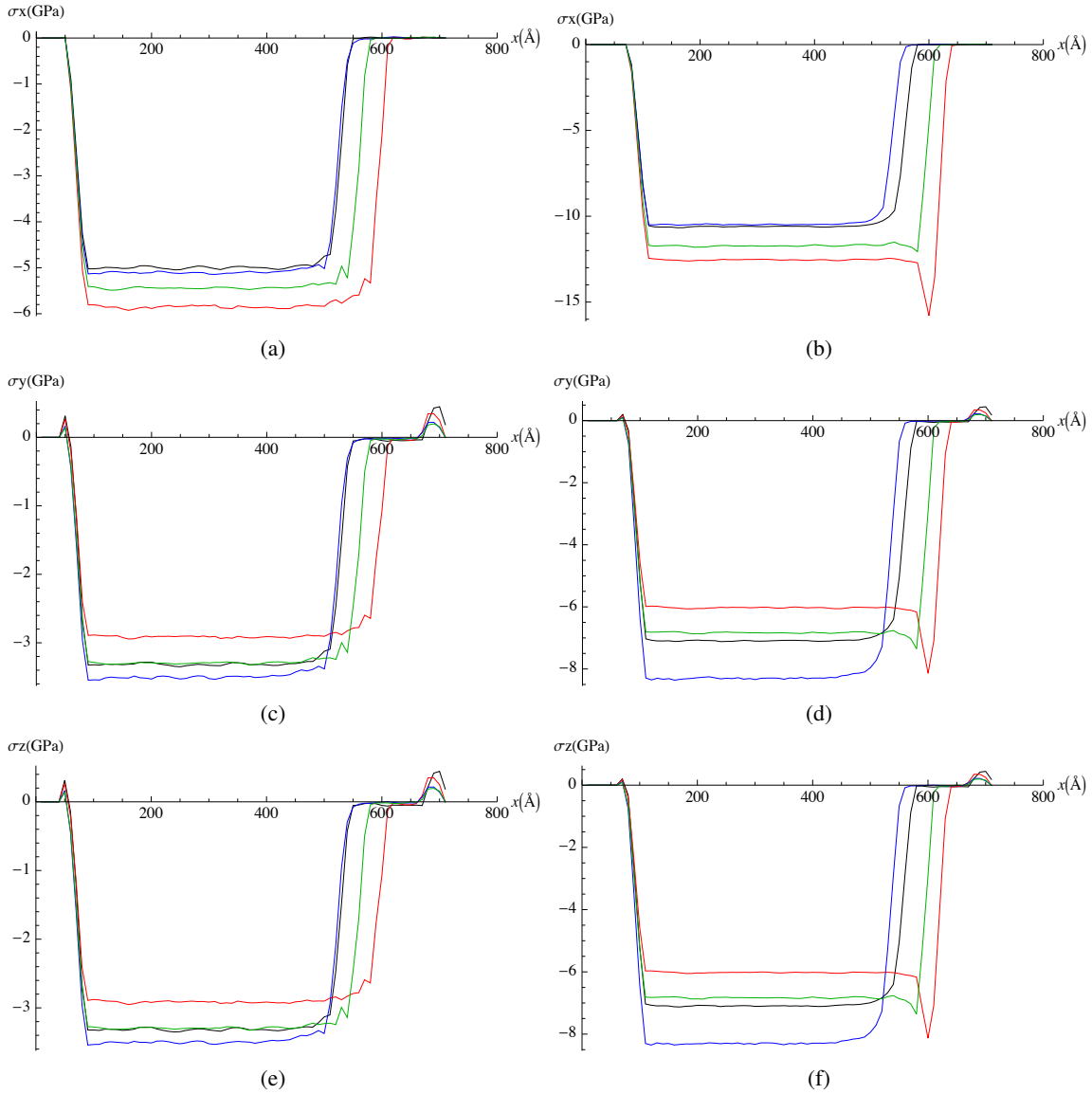

Figure 36: Stress profiles during elastic shock wave propagation at (a),(c),(e) u_p = 300 m/s and (b),(d),(f) u_p = 600 m/s along with [100] crystal direction. Color key: WKG, MFMP, EA, VC.

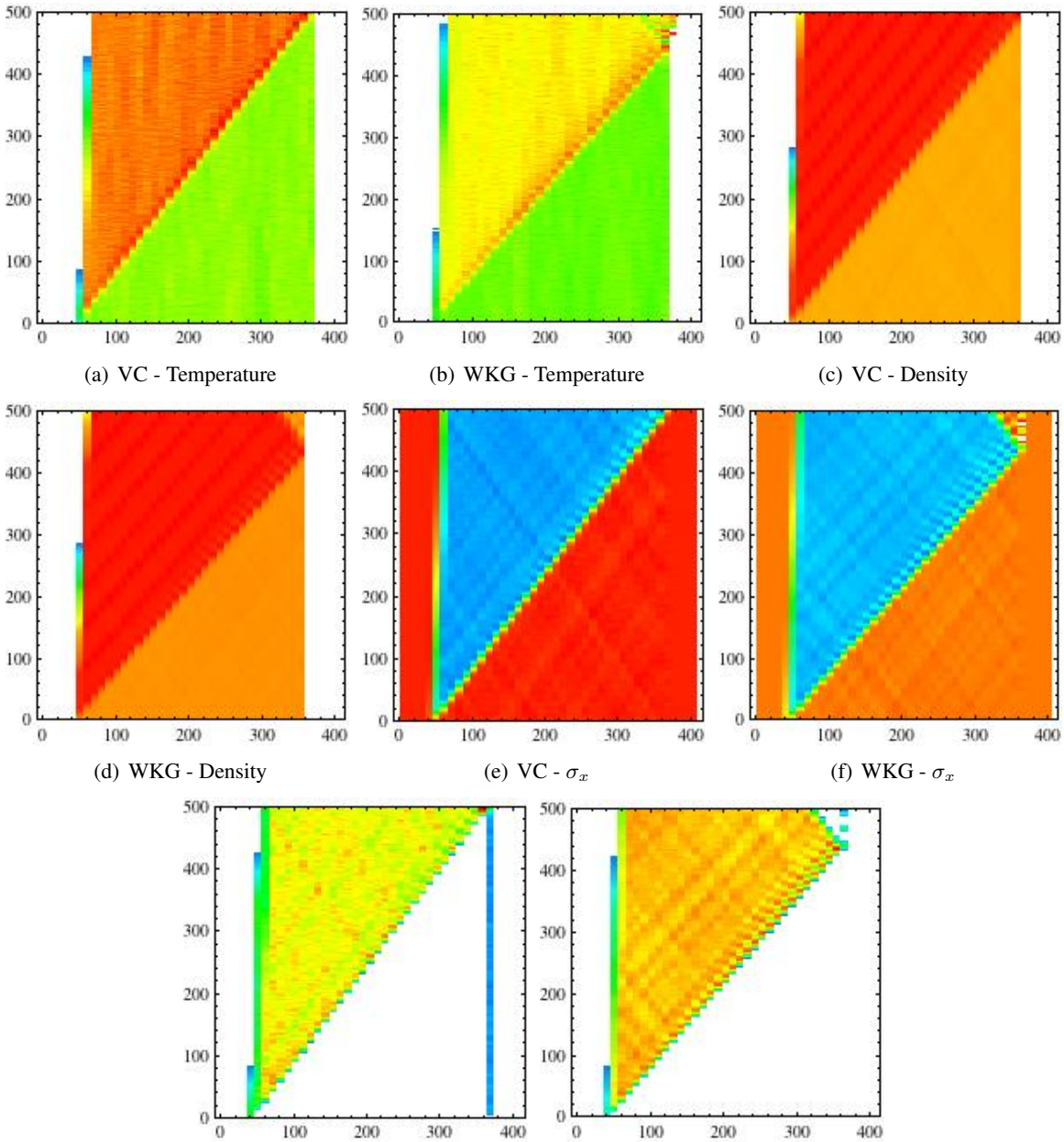

(a) VC - Temperature (b) WKG - Temperature (c) VC - Density

(d) WKG - Density (e) VC - σ_x (f) WKG - σ_x

(g) VC - $|\sigma_x - \sigma_y|$ (h) WKG - $|\sigma_x - \sigma_y|$

Figure 37: $x - t$ plots of the spatial and temporal distributions of continuum fields for the VC and WKG potentials for [100] compression with $u_p = 300$ m/s. Horizontal axis is in units of Å and vertical axis is in units of 0.01 ps.

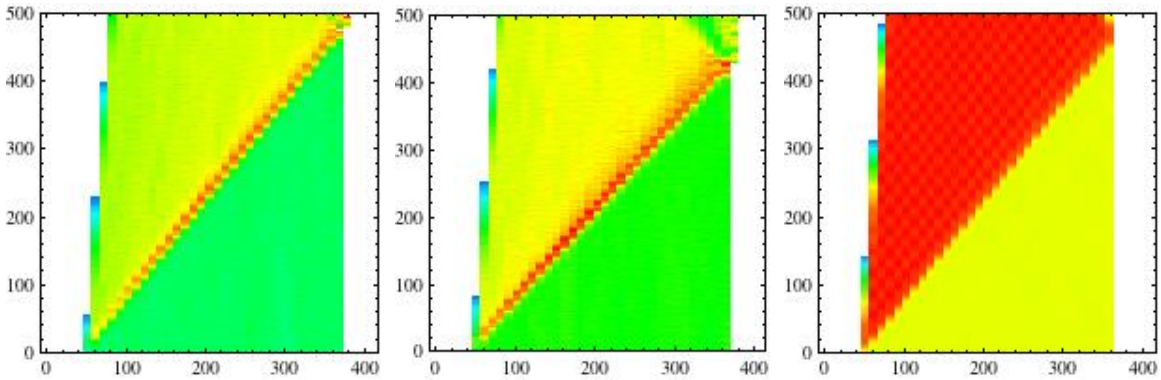

(a) VC - Temperature

(b) WKG - Temperature

(c) VC - Density

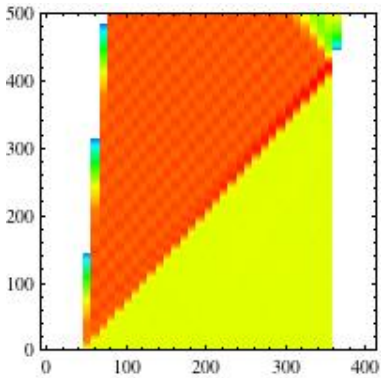

(d) WKG - Density

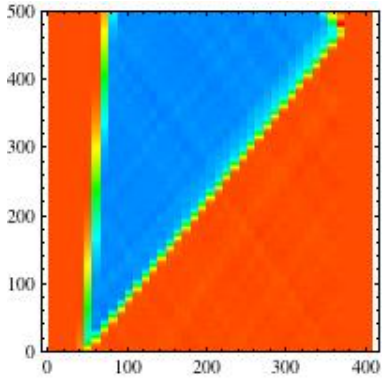

(e) VC - σ_x

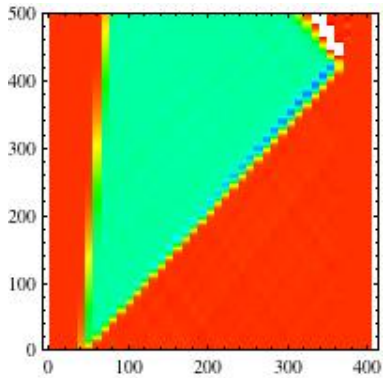

(f) WKG - σ_x

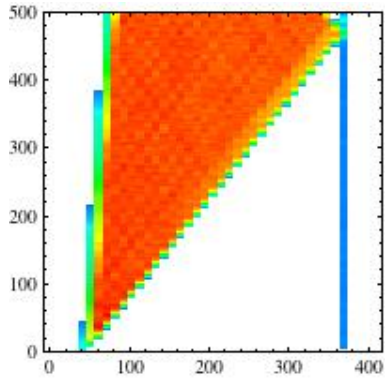

(g) VC - $|\sigma_x - \sigma_y|$

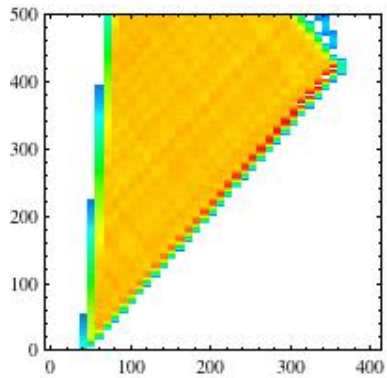

(h) WKG - $|\sigma_x - \sigma_y|$

Figure 38: $x - t$ plots of the spatial and temporal distributions of continuum fields for the VC and WKG potentials for [100] compression with $u_p = 600$ m/s. Horizontal axis is in units of Å and vertical axis is in units of 0.01 ps.

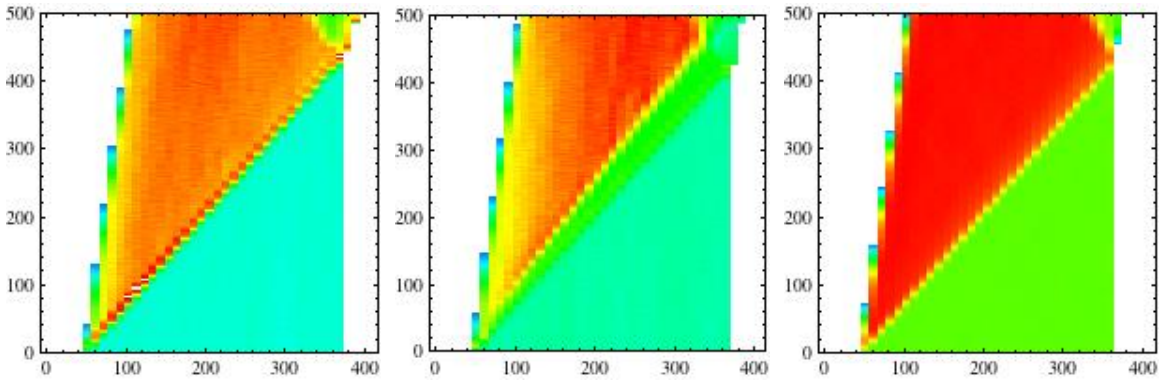

(a) VC - Temperature

(b) WKG - Temperature

(c) VC - Density

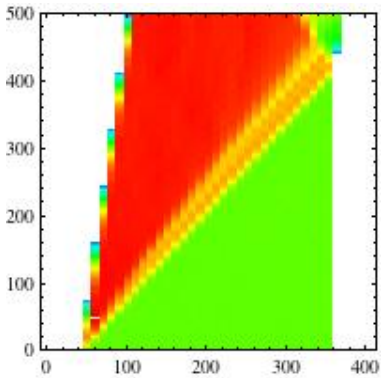

(d) WKG - Density

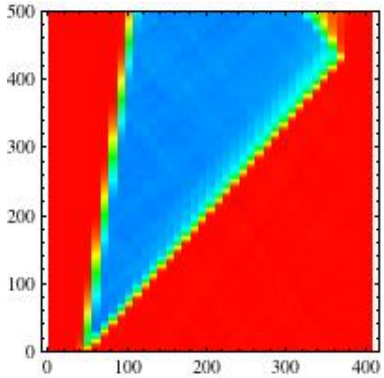

(e) VC - σ_x

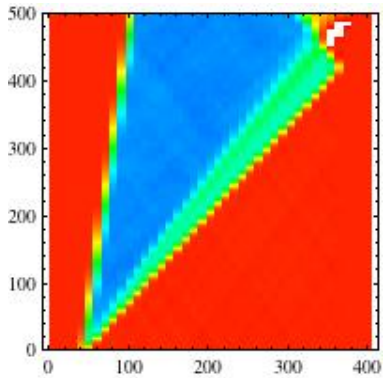

(f) WKG - σ_x

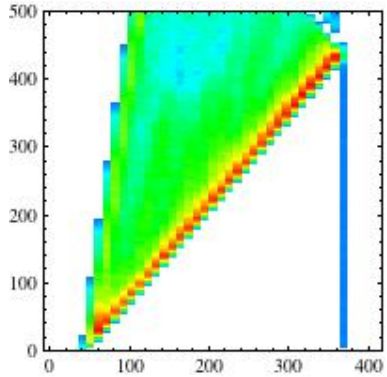

(g) VC - $|\sigma_x - \sigma_y|$

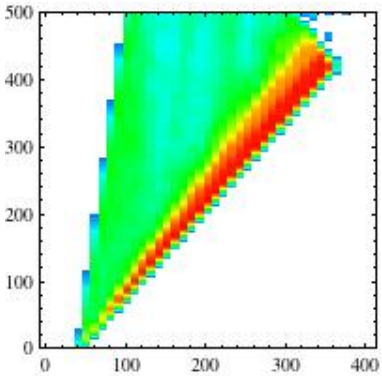

(h) WKG - $|\sigma_x - \sigma_y|$

Figure 39: $x - t$ plots of the spatial and temporal distributions of continuum fields for the VC and WKG potentials for [100] compression with $u_p = 1200$ m/s. Horizontal axis is in units of Å and vertical axis is in units of 0.01 ps.

Table I: Steady-state averaged continuum fields for [100] shock wave propagation. Also shown are the maximum standard deviations for each column's field.

u_p (Å/ps)	potential	ρ/ρ_0	P_x (GPa)	P_y (GPa)	P_z (GPa)	T (K)
±0.013		±0.001	±0.029	±0.024	±0.025	±3.1
3.002	WKG	1.043	5.851	2.917	2.915	331.9
2.989	MFMP	1.046	5.442	3.297	3.298	322.1
3.000	EA	1.050	5.107	3.504	3.504	323.5
2.994	VC	1.049	4.999	3.317	3.316	346.4
6.000	WKG	1.083	12.54	6.028	6.024	355.4
5.988	MFMP	1.089	11.74	6.830	6.829	353.5
6.000	EA	1.102	10.49	8.307	8.310	365.2
5.994	VC	1.097	10.61	7.095	7.093	399.1

with inhomogeneity of the deviatoric stress field ($|\sigma_x - \sigma_y|$) behind the shock front, which indicates plastic defect generation has occurred.

Averaged properties behind the shock front

We now analyze space- and time-averaged subsets of our simulated data to estimate steady-state continuum properties behind the shock front. In Fig. 40, the averaged stresses from the MD simulations, for each of the four potentials, are plotted as a function of density compression for shock wave propagation along the [100] direction. For shocks having a given particle velocity, Fig. 40(a) shows that density compression ρ/ρ_0, longitudinal stress P_x, and lateral stress P_y values determined from the MD simulations are significantly different for the different EAM potentials. Similarly, the stress difference P_x - P_y, shown in Fig. 40(b), differs significantly for different potentials.

Also shown in Fig. 40 are the continuum stress-density curves. Comparisons between the MD results and the continuum curves show that simulations using the WKG potential provide the best agreement with the continuum calculations. Although all the P_y values from the MD simulations are close to the continuum curve in Fig. 40(a), this agreement is somewhat misleading because the density compression values are quite different. Perhaps the most telling results are those shown in Fig. 40(b) for the higher shock amplitude (particle velocity of 600 m/s). The mean stress and the stress difference values are markedly different for the four potentials. The continuum curve provides the basis for selecting between the four potentials. Specific values for the averaged continuum properties for the various interatomic potentials can be found in Table I.

Our method of identifying Hugoniot states using shock wave compression within MD simulations was verified by performing Hugoniotstat simulations for this [100] compression case. The Hugoniotstat algorithm involves inducing a prescribed homogeneous longitudinal pressure to a small system (about 4,000 atoms) and then driving the system to obey the Rankine-Hugoniot relation, $E_0 = E - \frac{1}{2}\left(P_x + P_{x0}\right)\left(V_0 - V\right)$, where quantities with the subscript "0" are those properties in the material prior to the shock wave passing and quantities without this subscript are those properties after the shock wave has passed and a steady-state has been reached. Further details about the Hugoniotstat algorithm can be found elsewhere in this report.

Figure 41 shows the longitudinal and transverse stresses (P_x and P_y, respectively) for the Hugoniot states for [100] compression of the various potentials as determined with the above-described algo-

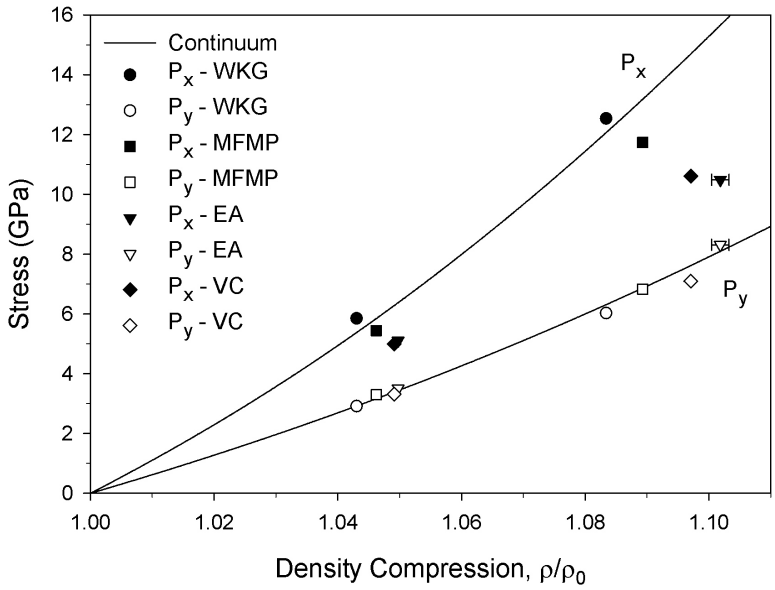

(a)

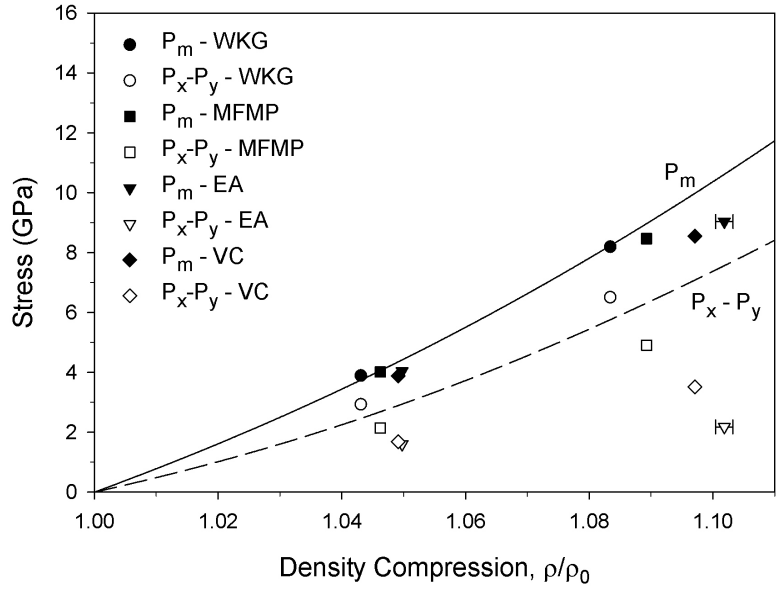

(b)

Figure 40: (a) Longitudinal (P_x) and lateral (P_y) stresses versus density compression and (b) mean stress (P_m) and stress difference (P_x - P_y) versus density compression for Al single crystals shocked along the [100] direction. The lines are continuum stress-density curves calculated using nonlinear elasticity. The symbols denote averaged stresses determined from MD simulations of elastic shock compression. Error bars are shown for simulation results where the statistical uncertainties are larger than the size of the symbols.

rithm. Superimposed are the states quantified using shock compression simulations. We observe that for each potential, the values from the shock compression simulations lie directly on the curve that traces out all Hugioniot states. This confirms that the shock compression simulations are producing Hugoniot states even though they're not constrained to do so. This analysis also shows that the Hugoniot curves for the WKG and MFMP potentials exhibit concave downward behavior past a certain value of density compression (approximately 1.1 for WKG and 1.3 for MFMP), behavior inconsistent with curves measured experimentally for Al. This behavior is most likely an artifact of using a small and highly-constrained atomic system in a compressive regime usually corresponding with plastic behavior. It is not clear that use of the Hugoniostat algorithm will produce meaningful, size-independent results in regimes where generation of crystalline defects is expected. More work in refining this simulation method is warranted.

4.3.3 [111] Compression

Instantaneous profiles of shock wave propagation

As was done for [100] compression, we construct instantaneous-in-time profiles of continuum fields v_x, ρ, T, σ_x, σ_y and σ_z for piston speeds of 300 m/s and 600 m/s as functions of longitudinal positions. These profiles can be seen in Figures 42 and 43. As in the [100] compression case, we observe very little deviation in the longitudinal velocity far behind the shock front from the prescribed piston speed as well as oscillations in the mass density profiles showing interference between the discreteness of the atomic system and the continuum grid. We also notice that while the temperature field still shows a characteristic peak at the shock front for all potentials, the WKG and MFMP no longer display leading peaks in the other continuum fields.

Averaged properties behind the shock front

In Fig. 44, averaged stresses from the MD simulations are plotted as a function of density compression for shock wave propagation along the [111] direction. Compared to the [100] results shown in Fig. 40(a), the MD simulation results in Fig. 44(a) show that differences for the stresses and density compression values, corresponding to the four potentials, are less pronounced. Although the results from the WKG potential again provide the best overall agreement with the continuum curves, the other three potentials show reasonable agreement with the continuum curves. Similar to Fig. 40(b), the stress difference results in Fig. 44(b) are helpful in discriminating between the different potentials. Specific values for the averaged continuum properties for the various interatomic potentials can be found in Table II.

4.3.4 [110] Compression

Instantaneous profiles of shock wave propagation

We again construct instantaneous-in-time profiles of continuum fields v_x, ρ, T, σ_x, σ_y and σ_z for piston speeds of 300 m/s and 600 m/s as functions of longitudinal positions. These profiles can be seen in Figures 45 and 46. These profiles are very similar to the profiles shown for [111] compression regarding the attributes discussed earlier. Once noticeable difference is how the steady-state values of the two transverse stresses (σ_y and σ_z) differ from one another. Not only are the values themselves different, but the ordering between potentials has changed. The ordering of σ_y shows that the WKG

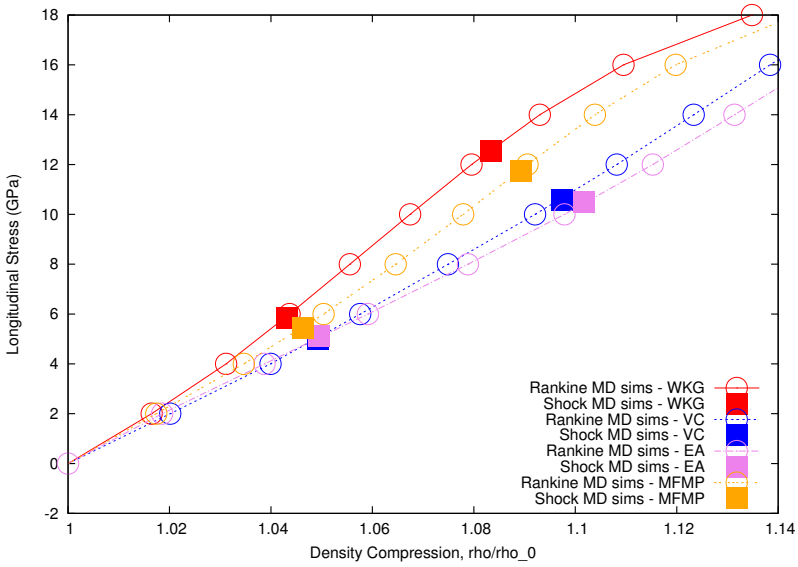

(a)

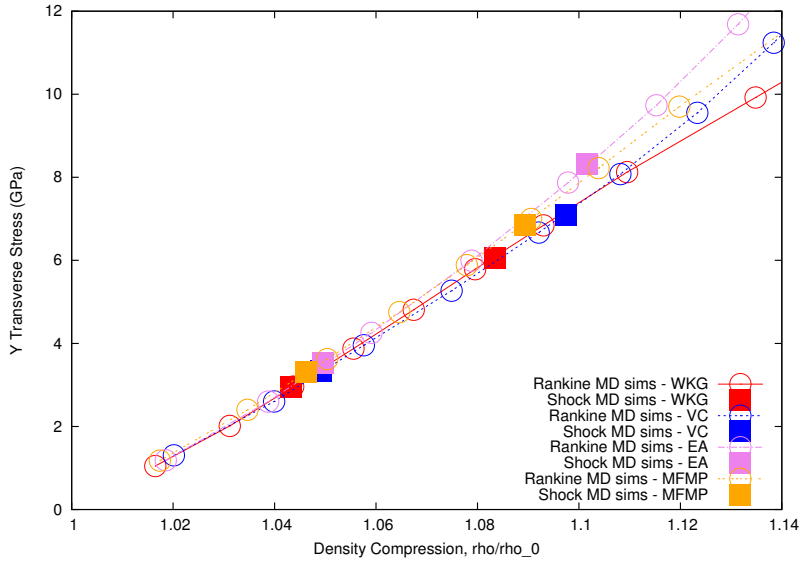

(b)

Figure 41: (a) Longitudinal (P_x) and (b) lateral (P_y) stresses versus density compression or Al single crystals shocked along the [100] direction, as calculated using a Hugioniostat algorithm.

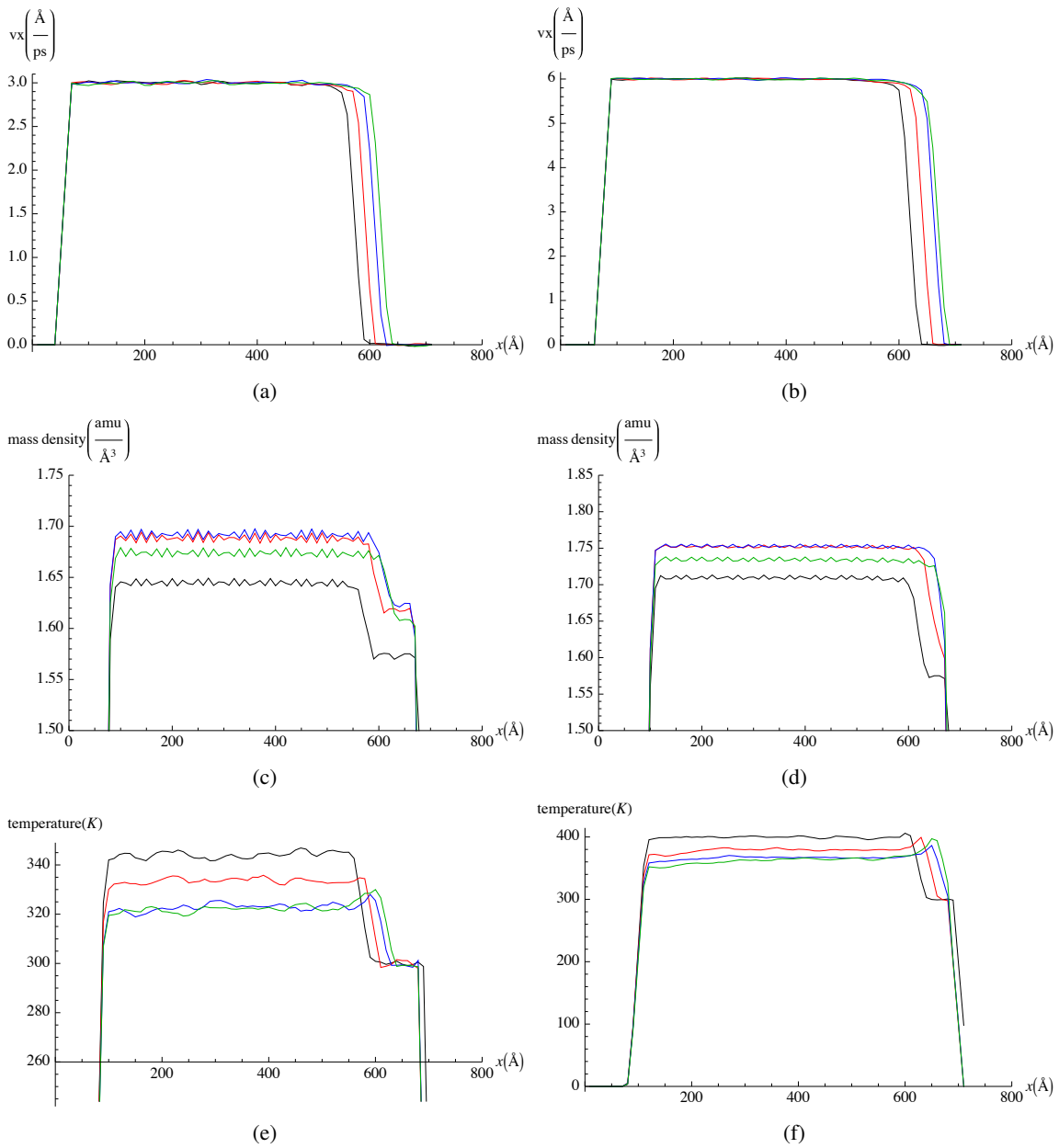

Figure 42: Longitudinal velocity, mass density and temperature profiles during elastic shock wave propagation at (a),(c),(e) u_p = 300 m/s and (b),(d),(f) u_p = 600 m/s along with [111] crystal direction. Color key: WKG, MFMP, EA, VC.

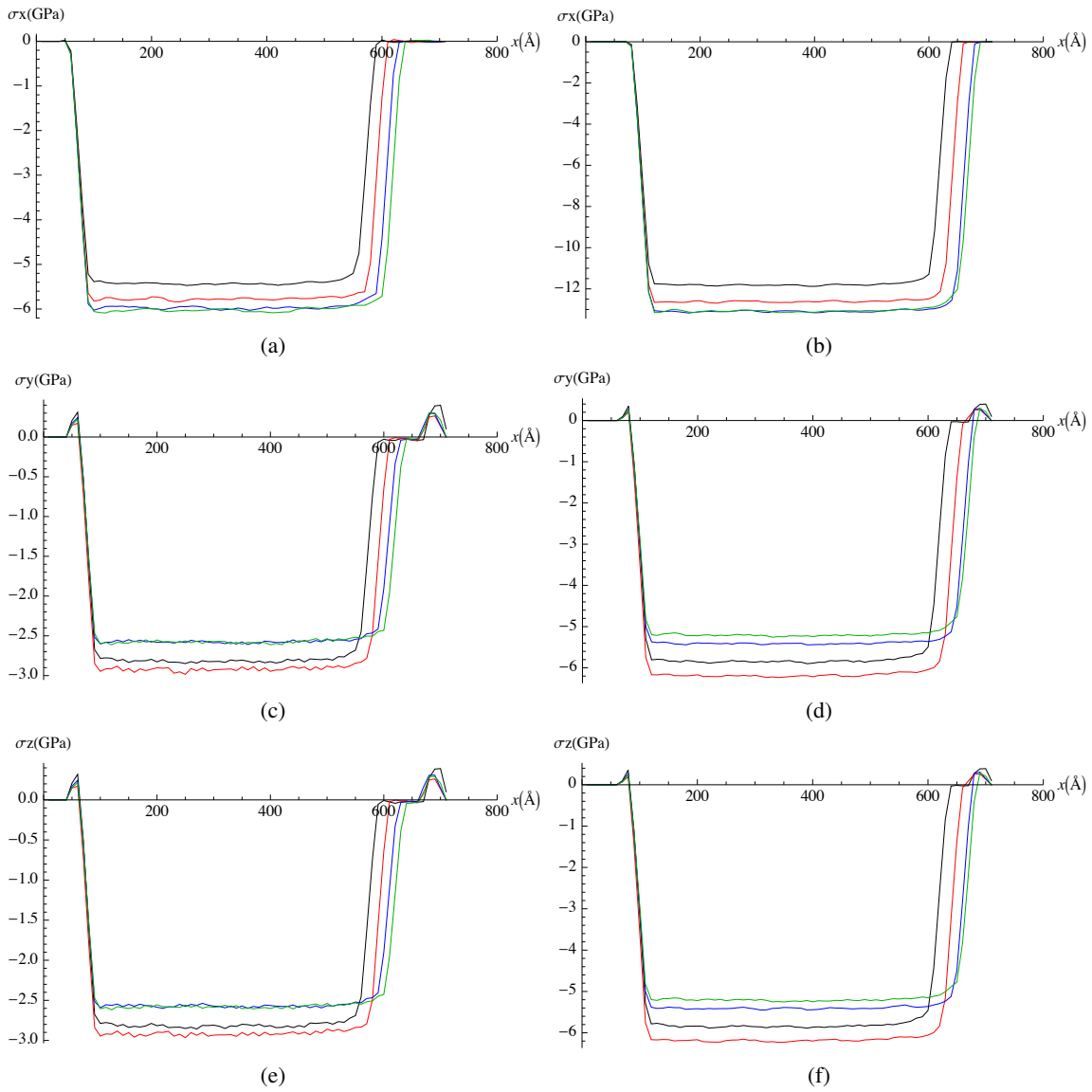

Figure 43: Stress profiles during elastic shock wave propagation at (a),(c),(e) u_p = 300 m/s and (b),(d),(f) u_p = 600 m/s along with [111] crystal direction. Color key: WKG, MFMP, EA, VC.

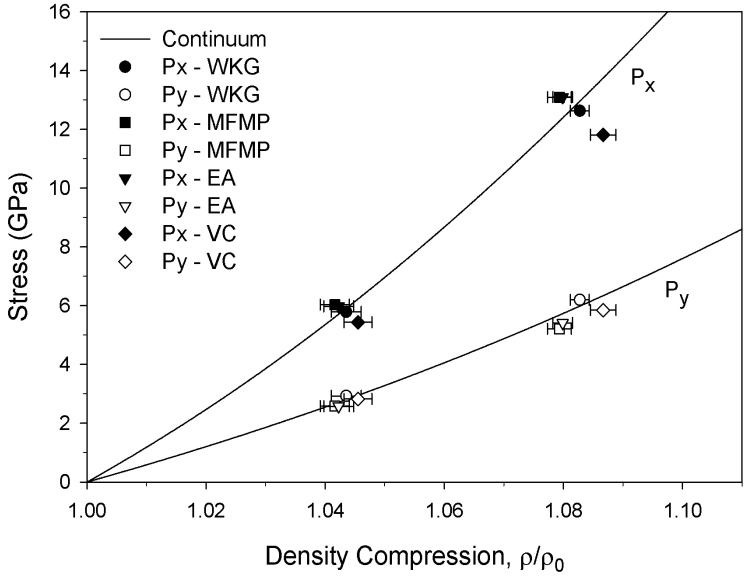

(a)

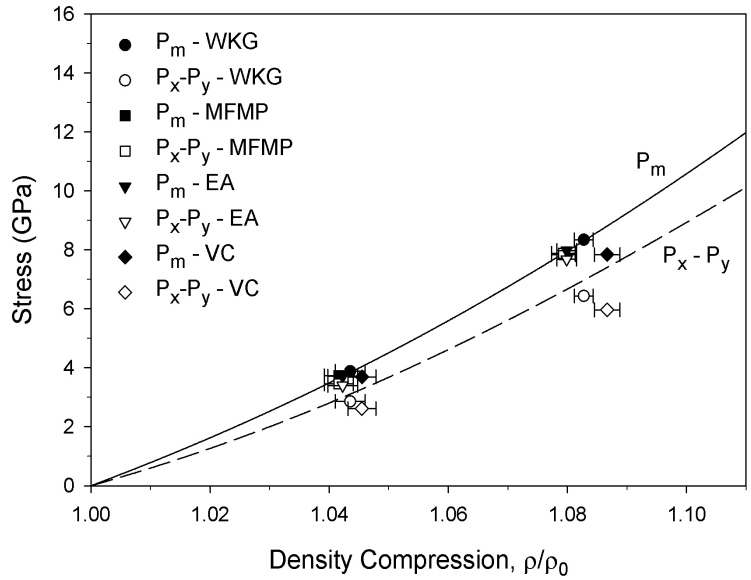

(b)

Figure 44: (a) Longitudinal (P_x) and lateral (P_y) stresses versus density compression and (b) mean stress (P_m) and stress difference (P_x - P_y) versus density compression for Al single crystals shocked along the [111] direction. The meanings of lines, symbols and error bars is the same as stated in the caption for Fig. 40.

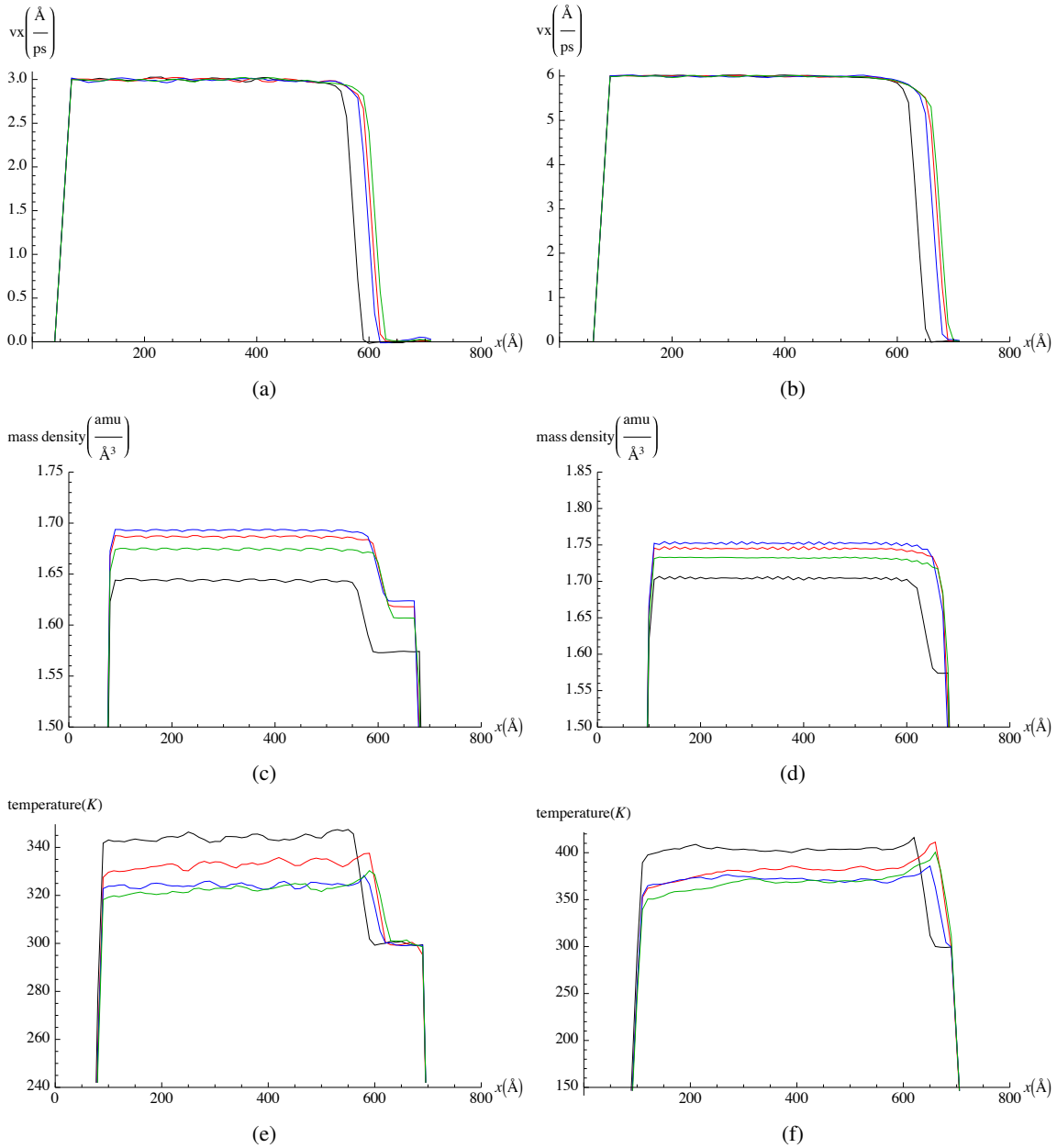

Figure 45: Longitudinal velocity, mass density and temperature profiles during elastic shock wave propagation at (a),(c),(e) u_p = 300 m/s and (b),(d),(f) u_p = 600 m/s along with [110] crystal direction. Color key: WKG, MFMP, EA, VC.

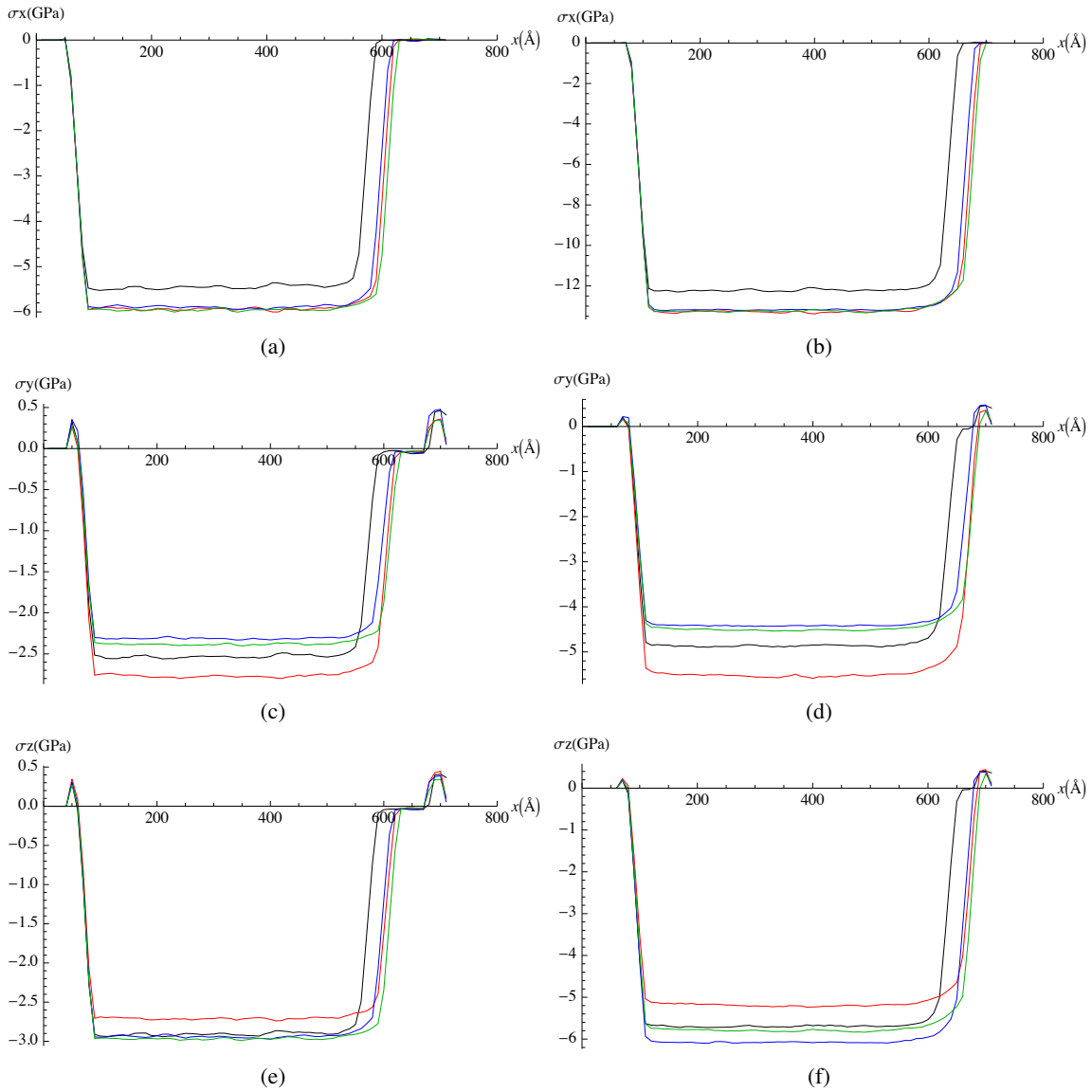

Figure 46: Stress profiles during elastic shock wave propagation at (a),(c),(e) u_p = 300 m/s and (b),(d),(f) u_p = 600 m/s along with [111] crystal direction. Color key: WKG, MFMP, EA, VC.

Table II: Steady-state averaged continuum fields for [111] shock wave propagation. Also shown are the maximum standard deviations for each column's field.

u_p (Å/ps)	potential	ρ/ρ_0	P_x (GPa)	P_y (GPa)	P_z (GPa)	T (K)
±0.015		±0.003	±0.035	±0.021	±0.021	±4.2
3.001	WKG	1.044	5.783	2.928	2.925	333.5
2.999	MFMP	1.042	6.030	2.579	2.580	321.7
3.004	EA	1.042	5.976	2.576	2.574	322.5
3.006	VC	1.045	5.433	2.822	2.819	343.8
6.000	WKG	1.083	12.63	6.196	6.195	378.4
5.999	MFMP	1.079	13.09	5.209	5.209	359.3
6.003	EA	1.080	13.10	5.412	5.412	366.1
6.003	VC	1.087	11.81	5.850	5.848	399.4

potential has the largest magnitude, with $|\sigma_y|_{\text{WKG}} > |\sigma_y|_{\text{MFMP}} > |\sigma_y|_{\text{VC}} \sim |\sigma_y|_{\text{EA}}$. In comparison, this ordering has changed for σ_z to $|\sigma_z|_{\text{MFMP}} \gtrsim |\sigma_y|_{\text{VC}} > |\sigma_y|_{\text{EA}} \sim |\sigma_y|_{\text{WKG}}$. This clearly shows the strong anisotropic behavior that occurs for shock wave compression along the [110] direction.

Averaged properties behind the shock front

In Fig. 47, averaged stresses from the MD simulations are plotted as a function of density compression for shock wave propagation along the [110] direction. In Fig. 47(a), the two lateral stresses P_y and P_z are plotted separately because they are not equivalent for shocks along [110]. The stresses and density compression obtained for three of the four potentials (WKG, MFMP, and EA potentials) are in good agreement with each other. In contrast, the longitudinal stress P_x, mean stress P_m, and stress difference P_x - P_y resulting from using the VC potential show differences when compared to the other potentials. Results using the WKG, MFMP, and EA potentials agree well with the continuum calculations, whereas the agreement for results using the VC potential is not as good.

Results from both the MD simulations and the calculated continuum curves show that the stress difference P_x - P_y is large for shock propagation along the [110] direction and is comparable to the mean stress P_m. This result is in contrast to the results for shock propagation along the [100] and [111] directions, where P_x - P_y is significantly smaller than P_m. As before, specific values for the averaged continuum properties for the various interatomic potentials can be found in Table III.

4.3.5 Temperature Calculations

As expected, temperature increases achieved in both the MD simulations and the continuum calculations for shock propagation along all three crystal orientations are quite modest for the elastic loading examined here; calculated results in Fig. 48 are shown primarily for completeness. Compared to results for the [111] and [110] orientations, temperature-density values from MD simulations of shock wave propagation along the [100] orientation are significantly different. In addition, differences in the temperature-density values, corresponding to the four different potentials, are significantly larger for the [100] orientation, compared to the other orientations. For all the orientations examined, temperatures obtained from the simulations using the VC potential are higher than those obtained using the other potentials.

In contrast to the MD results, the continuum temperature-density curves for shocked Al show only modest

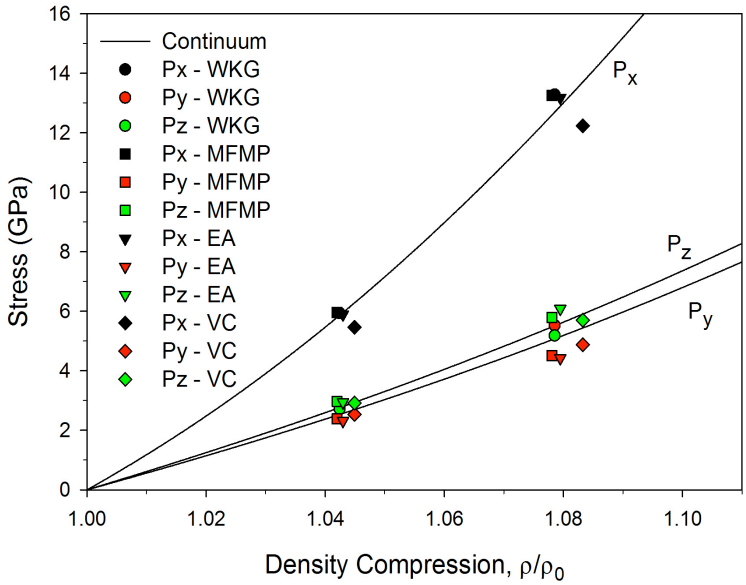

(a)

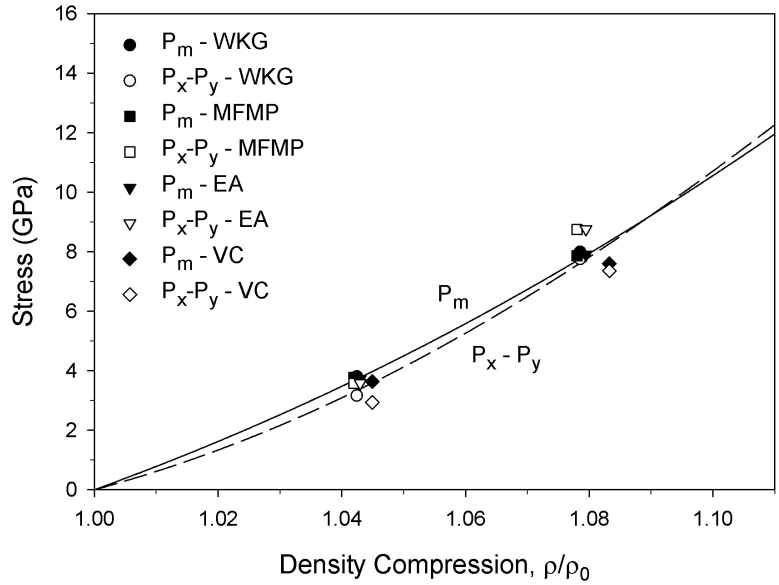

(b)

Figure 47: (a) Longitudinal (P_x) and lateral (P_y) stresses versus density compression and (b) mean stress (P_m) and stress difference (P_x - P_y) versus density compression for Al single crystals shocked along the [110] direction. The meanings of lines, symbols and error bars is the same as stated in the caption for Fig. 40.

Table III: Steady-state averaged continuum fields for [110] shock wave propagation. Also shown are the maximum standard deviations for each column's field.

u_p (Å/ps)	potential	ρ/ρ_0	P_x (GPa)	P_y (GPa)	P_z (GPa)	T (K)
±0.016		±0.001	±0.041	±0.028	±0.030	±5.2
3.002	WKG	1.042	5.938	2.771	2.712	333.1
2.995	MFMP	1.042	5.959	2.385	2.970	322.1
2.994	EA	1.043	5.894	2.315	2.944	323.8
3.001	VC	1.045	5.463	2.535	2.913	344.4
6.002	WKG	1.079	13.28	5.522	5.183	377.3
5.997	MFMP	1.078	13.26	4.513	5.794	363.6
5.992	EA	1.079	13.18	4.423	6.082	372.1
6.006	VC	1.083	12.23	4.870	5.699	404.4

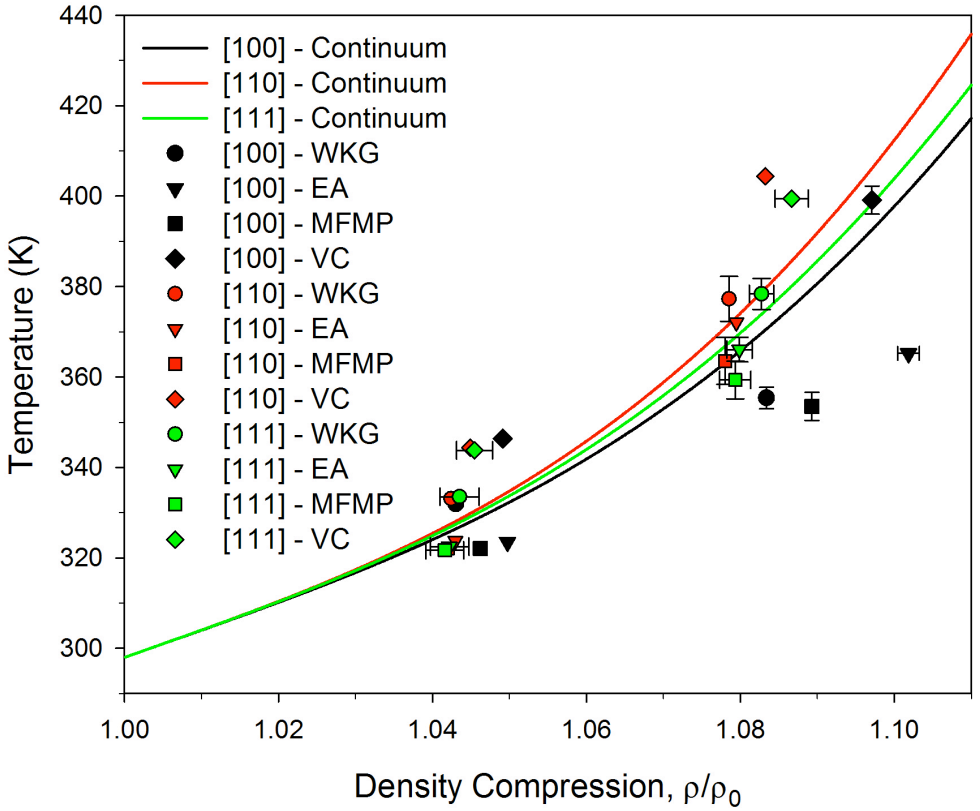

Figure 48: Temperature versus density compression for Al single crystals shocked along the [100], [110], and [111] directions. The meanings of lines, symbols and error bars is the same as stated in the caption for Fig. 40.

differences for shock wave propagation along different crystal orientations. Compared to the other EAM potentials, results obtained using the WKG potential provide somewhat better overall agreement with the continuum curves. Tabulated values of temperature values for the individual potentials can be found in Tables I, II and III.

4.4 Discussion

Our analysis shows important aspects of MD simulations of shock wave compression, and how results from such simulations can be interpreted in a continuum mechanical framework. The results presented specifically in Figs. 40-47 provide a basis for examining the applicability of inter-atomic potentials for use in MD simulations involving shock wave compression. In particular, comparison of results from MD simulations of shock waves in defect-free single crystals with the results from nonlinear elastic continuum calculations enables the optimal potential to be selected from the available choices. Although our method is not the only way that different interatomic potentials can be compared, it provides the only approach currently available for directly comparing results from MD shock wave simulations against a benchmark derived from experimental results.[1]

Examining the stresses plotted in Fig. 40, the significant differences in the results from MD simulations using different EAM potentials clearly demonstrate the importance of comparing inter-atomic potentials to determine their applicability for shock wave compression. Also, differences in the stresses obtained from simulations using different potentials are considerably larger for shock wave propagation along the [100] direction (Fig. 40), in contrast to the [111] and [110] directions (Figs. 44 and 47). This finding demonstrates the need to test inter-atomic potentials by examining shock wave propagation along several orientations, and shows the importance of crystal anisotropy for evaluating different potentials.

For the simulation results shown in Figs. 40-47 the stress difference P_x - P_y exhibits the largest overall variation for MD simulations using different potentials. Therefore, the calculated P_x - P_y values provide the best discriminant for choosing among the potentials examined. In contrast, the differences in the calculated mean stress P_m using different potentials are less pronounced. Hence, examination of P_m alone does not provide a good basis for selecting between available potentials.

For MD simulations of shock wave propagation along the [110] direction (Fig. 47), the stress difference Px - Py and the mean stress P_m are of comparable magnitude, in contrast to results for the [100] and [111] directions, where P_m is significantly larger than P_x - P_y. This feature, resulting from the anisotropic elastic response of Al single crystals, provides an additional constraint for choosing between different potentials.

Because the stress difference P_x - P_y is related to the shear stresses that cause inelastic deformation, the large differences in P_x - P_y for shocks along the [100] direction suggest that MD simulations of the elastic-plastic response in Al single crystals, with defects, will likely be different for different EAM potentials. Thus, our results demonstrate the need to consider the anisotropic elastic response, in addition to properties such as the stacking fault energy, width of extended dislocations, etc., when choosing the optimal potential for simulating shock wave propagation in crystals having defects, where inelastic deformation is anticipated. Whether the differences observed here for elastic compression will also hold for elastic-plastic compression

[1]We note that atomistic simulation codes such as LAMMPS [1] can be used to perform static uniaxial strain compression calculations along different crystal directions. Such calculations, which provide stress-density values along the T = 0K isotherm, require much less effort compared to the shock wave propagation simulations presented here (as pointed out by a reviewer). Because the focus of our work is on establishing the applicability of interatomic potentials for MD simulations of shock wave propagation at room temperature and higher, we did not undertake static, isothermal, uniaxial strain calculations at T = 0K.

is a question that needs to be explored in the future.

Comparing the MD results with the calculated continuum curves in Figs. 40-48 shows that MD simulations using the WKG potential [78, 79] provide better overall agreement with the continuum results, compared to the other potentials. Therefore, the WKG potential is recommended for use in simulations of shock wave propagation in aluminum single crystals. This conclusion represents the end result of our evaluation and demonstrates the efficacy of our approach for selecting an optimal potential for MD simulations involving shock wave compression.

The differences in P_x and P_y for MD results using different potentials, shown in Fig. 40(a), indicate that the elastic coefficients governing shock compression, which depend on second- and higher-order elastic constants (see Eq. (16)), are significantly different for different EAM potentials. In contrast, previous simulations showed that the second-order elastic constants of Al resulting from using different potentials are not much different at ambient pressure and temperatures less than 400 K. [78, 79] Therefore, the differences in stresses and density compression shown in Fig. 40(a) are due to differences in the higher-order elastic constants resulting from using different potentials. These results indicate the importance of using higher-order elastic constants in the development of interatomic potentials, as was done for the WKG potential, [78, 79] because the higher-order constants contain information about anharmonicity and crystal anisotropy under mechanical loading that is not contained in the second-order constants.

4.5 Concluding Remarks

The applicability of available inter-atomic potentials for molecular dynamics (MD) simulations involving shock wave compression was examined by simulating shock wave propagation along [100], [111], and [110] directions in defect-free Al single crystals using four different EAM potentials. MD results for shocks along the [100] direction show significant differences for stresses, density compression, and temperatures determined from simulations using different EAM potentials. In contrast, the continuum variables for shocks along the [111] and [110] directions show smaller differences for three of the four potentials examined. These results demonstrate the need to test potentials using simulations of shock wave compression along more than one crystal orientation and, more generally, indicate the importance of crystal anisotropy in the evaluation of potentials.

Our results also show that the stress difference P_x - P_y provides the best overall discriminant among the different potentials. In addition, the large differences in P_x - P_y for shock wave compression along the [100] direction (Fig. 1b) suggest that the elastic-plastic response resulting from shock wave simulations of Al single crystals using different EAM potentials will likely be different. Therefore, testing the anisotropic elastic response under shock wave compression is an important factor (along with stacking fault energy, width of extended dislocations, etc.) for selecting a potential for use in MD simulations involving shock-induced inelastic deformation. Comparison of the MD results with the nonlinear elastic continuum calculations shows that the potential developed recently by Winey, Kubota and Gupta (WKG) [78, 79] provides better overall agreement among continuum variables, compared to the other three potentials considered here.

In general, the work presented here shows that MD simulations of elastic shock wave propagation in defect-free single crystals, in combination with nonlinear elastic continuum calculations, constitute an important step in establishing the applicability of classical MD potentials for shock wave simulations.

Part II
Ramp Compression

5 Dynamic Compression of Beryllium

Principal Authors: Aidan P. Thompson, J. Matthew D. Lane and M. I. Baskes

5.1 Introduction

Our goal is to develop a potential for beryllium that accurately describes mechanical properties and phase equilibria up to and including melting on the principal Hugoniot curve, corresponding to a pressure of approximately 200 GPa, and a temperature of 5000 K. At ambient conditions, beryllium exhibits a variety of unusual properties, such as very low Poisson ratio and non-ideal hexagonal crystal structure. Many of these anomalies are likely due to the presence of directional bonding not normally found in metals [101,102]. While the effect of directional bonding is less important at elevated temperatures and pressures, we can not ignore this effect in our potential, for the following reason. The vast majority of experimental measurements on beryllium are performed at ambient conditions. Attempting to fit this data using a model that is missing important effects may produce a potential that does not extrapolate well. For this reason, we decided not to attempt fitting to spherically-symmetric potentials such as EAM or its close relative Sutton-Chen [103]. Instead we focused on the MEAM potential, which explicitly includes directional-dependent contributions.

For pure elements, MEAM has about ten freely-adjustable parameters. We refer to a set of specific values for these parameters as a parameterization. Two previous MEAM parameterizations for beryllium have been published [104,105]. Initial testing indicated that while these potentials very accurately represented the properties of beryllium in its ground state hexagonal close-packed crystal structure (HCP), they exhibited unphysically low melting points (< 100 K). We have developed a new parameterization, which we refer to as Ba09i. Independently, Dremov *et al.* have recently produced an improvement on their original parameterization, which we refer to here as Dr09 [106]. Both of these parameterizations are listed in Table IV. For a complete description of how these parameters define the MEAM potential, see Ref. [107].

Ba09i was arrived at by an iterative process of trial-and-error, via the unpublished parameterizations Ba09a through Ba09h. At each iteration, the parameters were first adjusted to reproduce zero-temperature properties such as the lattice and elastic constants, unrelaxed vacancy energies, stacking fault energies and relative stabilities of different crystal structures. The parameterization was then used to calculate the static compression curve up to 200 GPa and the melting temperature at zero pressure. The equilibrium melting curve and Hugoniot calculations were not used as part of the iterative parameterization process, and so can be regarded as predictions.

5.2 Physical Properties

In Table V the experimentally-determined physical properties of beryllium are compared with calculated values using Dr09 and Ba09i. All calculations were performed using the MEAM potential implemented in the LAMMPS molecular dynamics (MD) package [1, 24]. HCP lattice constants a and c were determined by energy minimization w.r.t. periodic cell dimensions. Elastic constants were determined by applying small strains in appropriate directions, followed by energy minimization w.r.t. atom positions. The elastic

Parameters	Dr09	Ba09i
reference	hcp	fcc
$G(\Gamma)$	$\exp(\Gamma/2)$	$\exp(\Gamma/2)$
α	3.8501	3.9
$\beta^{(0)}$	0.24826	2.0
$\beta^{(1)}$	0.0041610	5.0
$\beta^{(2)}$	0.33524	6.0
$\beta^{(3)}$	3.8426 $\times 10^{-7}$	2.0
r_e	2.2433361	3.19
E_c	3.43	3.43
A	1.1801	0.93
$\tau^{(0)}$	1.0	1.0
$\tau^{(1)}$	4.5561	10.0
$\tau^{(2)}$	21.956	8.0
$\tau^{(3)}$	-10.234	-5.0
δ	0.01	0.02
C_{min}	1.1	0.6
C_{max}	1.5	2.8
r_{cut}	3.5	4.2

Table IV: MEAM potential parameterizations for Beryllium: Dremov *et al.* (Dr09) [106] and this work (Ba09i).

constants were then computed as the change in the appropriate component of the stress tensor divided by the strain. By converging the minimization to high accuracy ($||F|| < 10^{-10}$), we were able obtain results that were very insensitive to strain magnitudes in the range $10^{-4} - 10^{-8}$.

Both Dr09 and Ba09i underpredict the atomic volume v and the predicted c/a ratios are closer to the ideal HCP value of $\sqrt{8/3}$ than is observed in nature. The elastic constants agree reasonably well with experiment [108], with the most significant errors arising in C_{12} and C_{44}.

The static compression curves were generated by first equilibrating a $5 \times 5 \times 5$ HCP crystal at 300 K and zero pressure. The applied pressure was then ramped from 0 to 200 GPa over the course of a 10 ps MD simulation using NPT dynamics [109]. The instantaneous pressure and volume were averaged over 1 ps intervals. In Fig. 49, we compare the results from Dr09 and Ba09i with the diamond anvil cell measurements of Evans *et al.* [110]. In both cases the agreement with experiment is excellent. In particular, there is no evidence of plastic deformation or phase change.

5.3 Phase Diagram

The melting point for Ba09i at low pressure was determined using the two-phase method. First, a $32 \times 4 \times 4$ HCP crystal was equilibrated at an estimated melting point T_0 and an average stress tensor equal to zero. Then, with the cross-section fixed, but constant stress still enforced in the x direction, half of the crystal was melted at a high temperature, followed by re-equilibration at T_0, followed by further relaxation without a thermostat, corresponding to the $NP_{xx}A_{yz}H$ ensemble. Finally, 2.5 ns of NVE dynamics was run, using a timestep of 0.25 fs. As can be seen from Fig. 50 this resulted in the establishment of a stable solid-liquid interface at zero average stress. From the average temperature, we estimate $T_m = 1390\ K$, somewhat lower

Quantity	Units	Expt.	Dr09	Ba09i
B	[GPa]	117	113	115
C_{11}	[GPa]	294	331	259
C_{33}	[GPa]	357	309	329
C_{12}	[GPa]	27	-11	77
C_{13}	[GPa]	14	18	9
C_{44}	[GPa]	162	19	65
C_{66}	[GPa]	133	171	91
v	[Å^3]	16.2	16.0	16.1
c/a	[–]	1.57	1.60	1.62
M.P.	[K]	1550	—	1390

Table V: Comparison of experimental and calculated properties using the MEAM interatomic potential for beryllium: Dremov *et al.* (Dr09) [106] and this work (Ba09i).

than the experimental value of 1550 K. We attempted to apply the same methodology to the Dr09 potential. However, we were unable to produce a stable HCP/liquid interface with this potential, because the HCP crystal became unstable at about 600 K, transforming to another crystal phase.

Starting with the low-pressure result for Ba09i, we extended the low-pressure melting point calculation to the entire melting curve up to a pressure of 300 GPa and a temperature of 5450 K. The intersection of the principal Hugoniot with this melting curve provides an estimate of where shock-melting is expected to occur. We started with a two-phase configuration of 2,048 atoms containing a slab of HCP crystal sandwiched between layers of liquid. A Langevin thermostat was used to maintain an average temperature of 1390 K, the previously established ambient melting point. The three periodic cell dimensions were coupled to independent Berendsen barostats, so as to maintain zero average stress in the three principal directions. Starting from this equilibrated state, we ran a short (2.5 ps) MD simulation during which the barostat set pressure was ramped from zero to 10 GPa and the thermostat set temperature was ramped from 1350 K to 1700 K. The latter value was found by trial and error to prevent either rapid freezing or melting of the sample. This was followed by a longer (25 ps) MD simulation at the final set points of the thermostat and barostat. Starting from this equilibrated state, several 25 ps MD simulations were performed at slightly higher and lower temperatures. The growth of the solid or liquid phase was observed by monitoring the average potential energy per atom as a function of time. In this way, a robust estimate of the equilibrium melting temperature could be obtained. The procedure was repeated for pressures of 20, 40, 70, 100, 150, 200, 250, and 300 GPa. In each case, the starting point was an equilibrated state at the previous pressure. The MD timestep was 0.125 fs, the thermostat relaxation time was 100 fs, and the barostat relaxation rate was $0.01\ \mathrm{fs}^{-1}\mathrm{GPa}^{-1}$.

Fig. 51 (top) shows the potential energy trajectories used to estimate the melting point at 150 GPa. At 4100 K, all of the liquid layer freezes in about 10 ps. Conversely, at 4400 K, all of the solid melts in about the same time. These results provide reliable upper and lower bounds on the melting point. In the simulation at 4200 K, the solid slab appears to be slowly melting. Linear regression of melting/freezing rate versus temperature predicted zero melting rate at a temperature of 4170 K. The simulation at this temperature verified that the net melting is indistinguishable from zero after 25 ps. Fig. 51(bottom) shows a snapshot taken from the final trajectory at 300 GPa, confirming that the two-phase structure (HCP and liquid) was preserved throughout the entire set of simulations. The full set of estimated melting points are plotted in Fig. 52. The agreement with the previous estimates using DFT [111] and a recently published equation of state [101] is surprisingly good. We conclude that the Ba09i MEAM potential provides a good description

of the important regions of the potential energy surface for the HCP and liquid phases up to pressures and temperatures relevant for dynamic melting.

5.4 Dynamic Compression

In order to efficiently survey the dynamic response of beryllium as represented by Dr09 and our Ba09i potential, we have used uniaxial Hugoniostat MD simulations. The method is that of Selezenev *et al.* [114], and is similar to the NP_{zz}Hug method developed by Ravelo *et al.* [115]. The primary difference is that instead of controlling temperature and pressure using integral feedback with damping (akin to the Nose-Hoover thermostat), we use linear feedback (akin to the Berendsen thermostat). Beginning with an equilibrated HCP crystal, $10 \times 10 \times 10$ 4-atom units cells, the system was uniaxially compressed to a specified axial stress while scaling the atom velocities to meet the Rankine-Hugoniot jump conditions. The compression rise time was 10 ps, while the total duration of each simulation was 50 ps. The average final volume, temperature and stress tensor were obtained from the final 5 ps of the simulation. An MD timestep of 0.5 fs was used. Except for the case of elastic-plastic shockwaves occuring at intermediate shock strengths, the final states from these Hugoniostat simulations can be expected to closely match those obtained from direct NEMD simulation of a shockwave travelling through a long sample.

In Fig. 53 we show axial stress for different degrees of compression oriented along the a-axis (top) and c-axis (bottom). For both orientations and both potentials, we see qualitatively similar results. A smoothly increasing initial elastic response at low shock strength is followed by a rather jumpy plastic response at higher shock strengths, and finally a smoothly increasing response at the highest shock strengths corresponding to molten beryllium. The elastic-plastic transition, or Hugoniot elastic limit (HEL), occurs at much higher shock strengths than is observed in experiments on polycrystalline beryllium [113], where the HEL is less than 1 GPa. This is to be expected, since the usual mechanisms for initiating plasticity, pre-existing defects and grain boundaries, are absent from the simulations. Above the HEL, both potentials exhibit a plastic reponse that agrees quite well with the experiments, although our Ba09i potential exhibits quite large jumps in compression. We expect that for larger system sizes, these jumps will tend to smooth out. The location of the melting transitions for both potentials are indicated by the solid (Dr09) and dashed (Ba09i) horizontal lines.

The melting transitions are more apparent in Fig. 54, where we have plotted axial stress versus temperature. For both orientations and both potentials, we observe a drop in temperature at the melting point (indicated by the solid (Dr09) and dashed (Ba09i) vertical lines), corresponding to a jump from the solid Hugoniot to a point on the liquid Hugoniot. For Dr09, this transition occurs around 180 GPa and 2500 K for both orientations, which is substantially below that predicted by previous DFT calculations [111]. For our Ba09i potential, the transition occurs around (4500-5500 K, 225-230 GPa). The solid Hugoniot extends to somewhat above the equilibrium melting curve, which is consistent with a small amount of superheating. The liquid Hugoniot begins below the equilibrium melting curve, indicating that the liquid is slightly supercooled. For both orientations, the Ba09i solid and liquid Hugoniot points near the melting transition fall quite close to previous DFT calculations [111]. This indicates that the Ba09i potential quite accurately captures the potential energy surface of HCP and liquid beryllium over the entire range of pressures from 0 to 300 GPa.

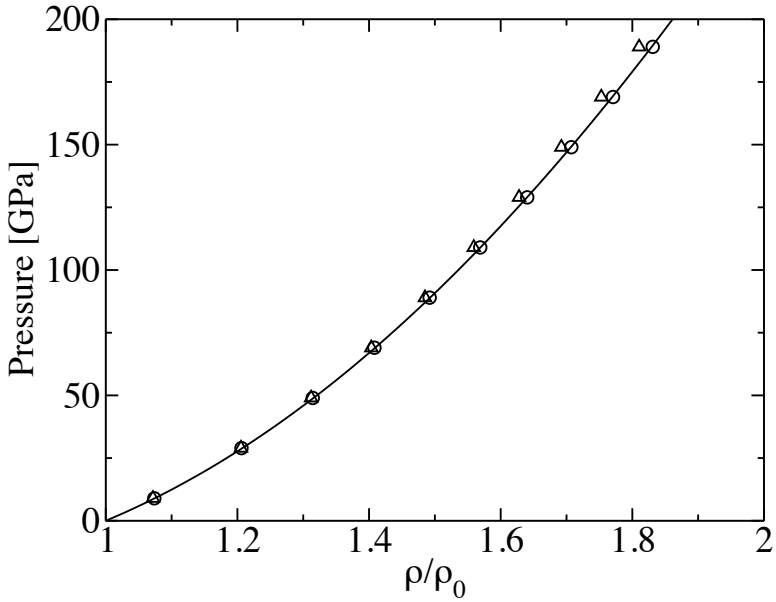

Figure 49: Pressure versus degree of compression for static compression of beryllium. MD simulations of single crystal using the Dr09 (circles) and our Ba09i (triangles) parameterizations; quasihydrostatic measurements on polycrystalline beryllium (line) [110].

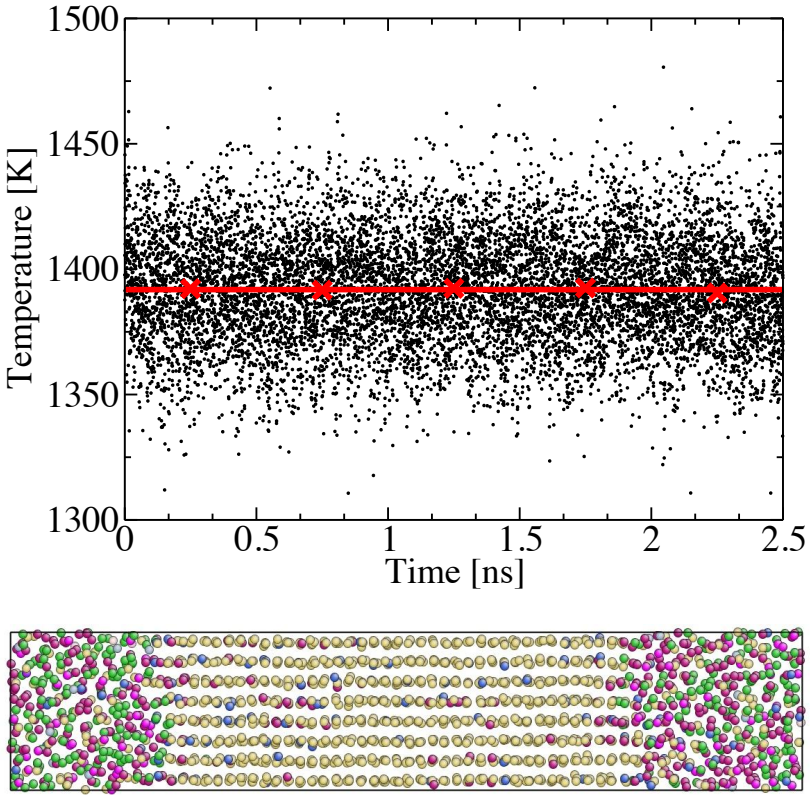

Figure 50: a) Temperature from NVE MD simulation of equilibrated solid-liquid interface using Ba09i: instantaneous temperature (black dots), temperature averaged over 0.5 ns blocks (red crosses), and overall average temperature (red line); b) Visualization of final state from NVE MD simulation. Atoms are shaded by coordination number.

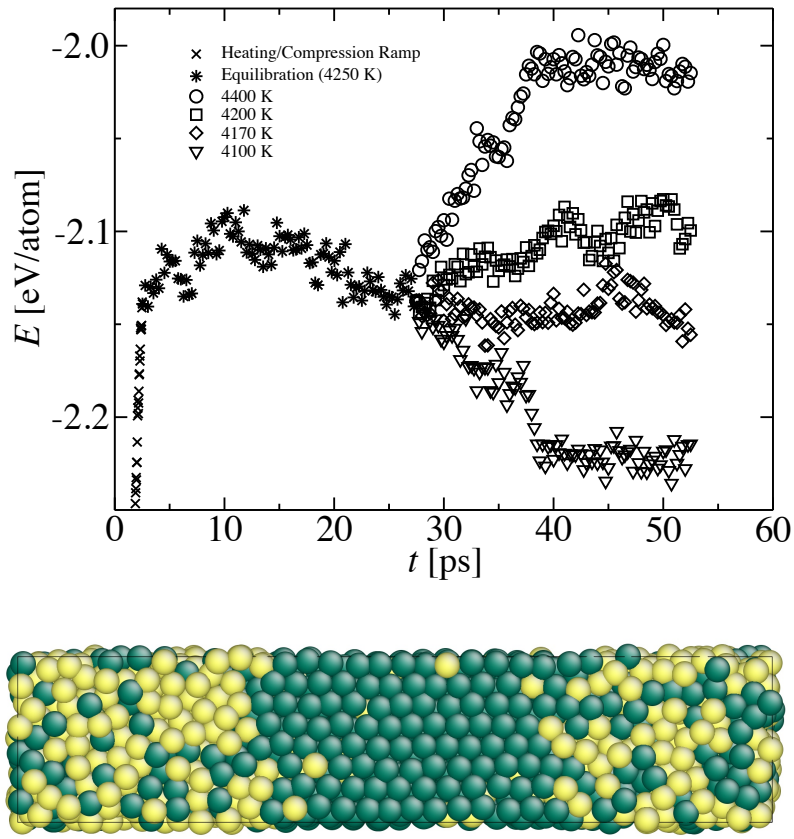

Figure 51: Top: Variation of potential energy during two-phase calculations at 150 GPa; Bottom: Visualization of configuration from two-phase simulation at 300 GPa and 5450 K. Atoms are colored by the value of their centrosymmetry parameter ϕ [112], green/dark indicating $\phi < 3.8$, yellow/light indicating $\phi > 3.8$.

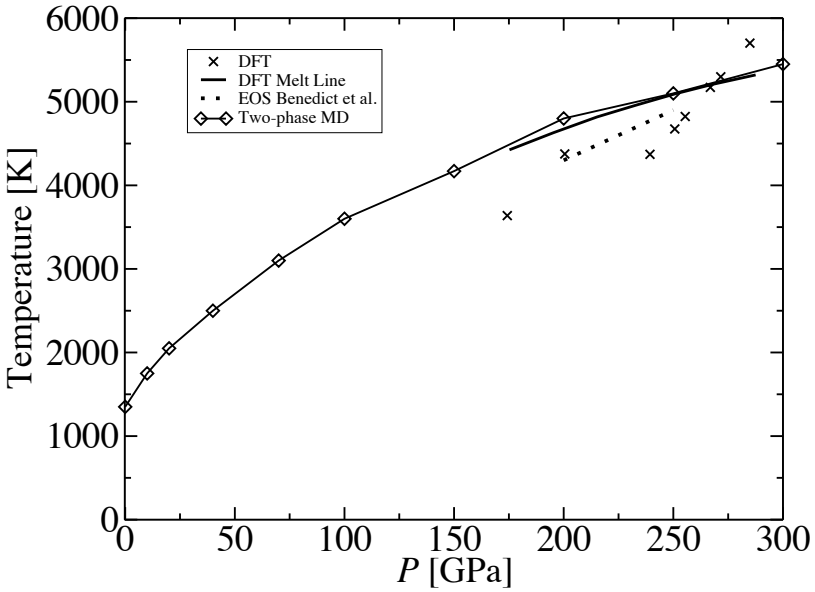

Figure 52: Equilibrium melting line (temperature versus pressure) for the Ba09i potential (diamonds). Also shown are estimates from DFT calculations of HCP and liquid Hugoniot states (crosses) [111], the melting line estimated from these calculations (solid line), and the melting line from the equation of state of Benedict *et al.* (dotted line) [101]

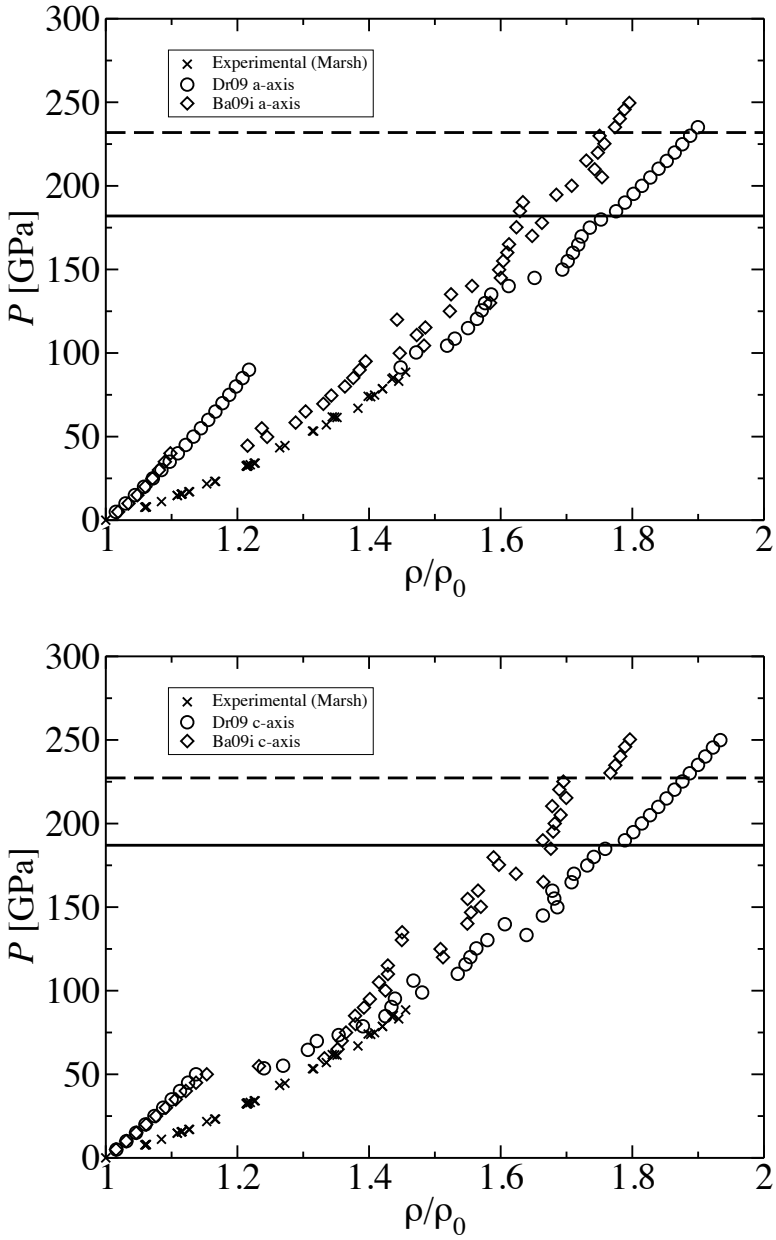

Figure 53: Plot of axial stress versus compression ratio from Hugoniostat MD simulations using the Dr09 (circles) and our Ba09i (diamonds) potentials. Results for compression along the a-axis (top) and c-axis (bottom) crystal orientations are compared to experimental data for polycrystalline beryllium (crosses) [113]. The horizontal lines indicate the location of the shock melt pressure for Dr09 (solid) and our Ba09i (dashed) potentials.

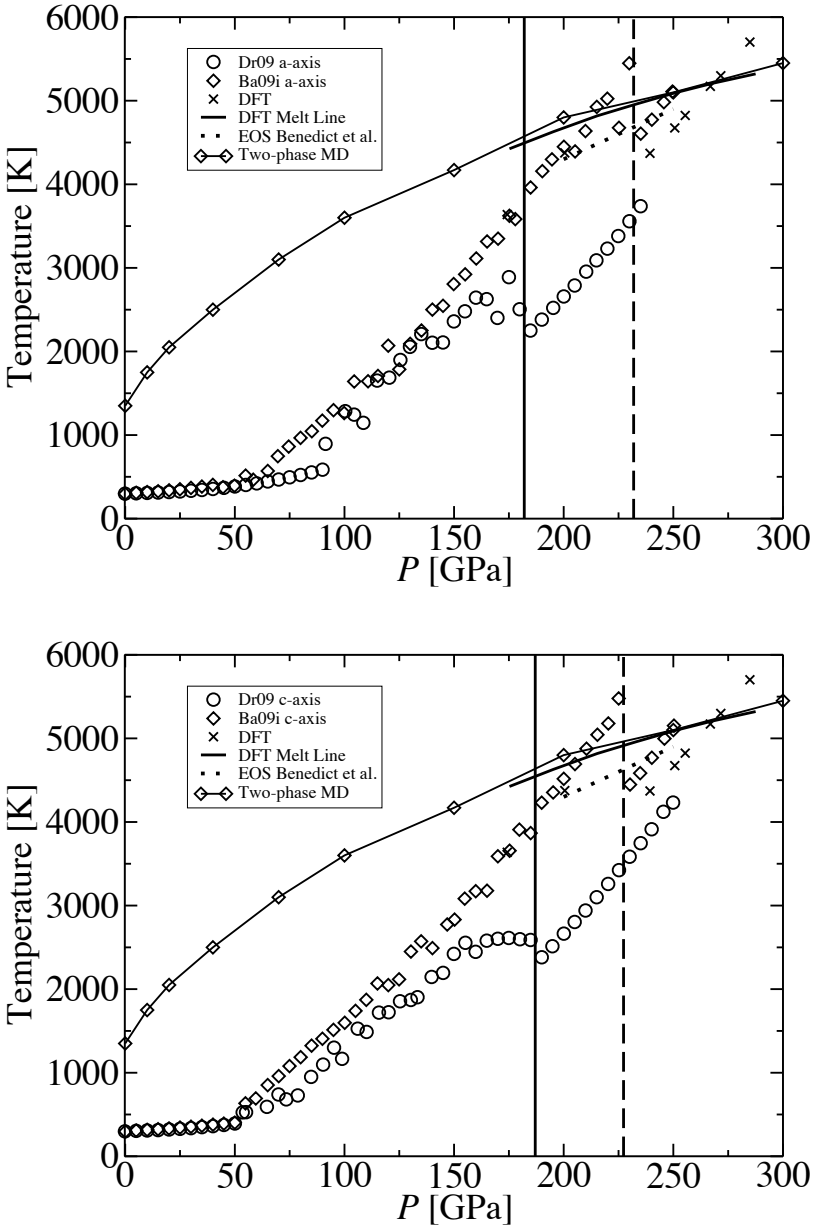

Figure 54: Plot of temperature versus axial stress from Hugoniostat MD simulations using the Dr09 (circles) and our Ba09i (diamonds) potentials. Results for compression along the a-axis (top) and c-axis (bottom) crystal orientations are shown. The vertical dashed lines indicate the location of the melt pressure for Dr09 (solid) and our Ba09i (dashed) potentials. Also shown is the equilibrium melting curve for the Ba09i potential (solid line with diamonds), DFT calculations of HCP and liquid Hugoniot states (crosses) [111], the melting line estimated from these calculations (solid line), and the melting line from the equation of state of Benedict (dotted line) *et al.* [101]

6 Time-Position Scaling relation in ramp-loading

6.1 Introduction

Sandia leads the world in characterizing materials in off-Hugoniot regions of phase space using experimental ramp wave loading. However, leadership in dynamic material response also requires state-of-the-art theory and modeling. Molecular dynamics simulation (MD) is an invaluable tool for studying problems sensitive to atom-scale physics such as structural transitions, non-equilibrium dynamics, and elastic-plastic deformation. There are, however, significant difficulties in utilizing MD for extreme environments. First, as has already been discussed, current atomic potentials are based on ambient material properties and are inadequate for multi-megabar and high-temperature regimes. Second, ramp loading on Z, shock-induced transitions, and melting occur over time scales too long to be simulated with today's MD methods. By generalizing recent innovative methods developed for shock loading, we have extended MD timescales by orders of magnitude, enabling us to model ramp compression and other longer timescale phenomena. The techniques we have developed will allow us to contribute significantly to the understanding of shock and quasi-isentropic physics, as well as to substantially expand understanding of several current critical areas of material behavior.

Previous work by Lane [65] had shown that ramp loading could be applied to reduced systems to model the shock conditions near the shock front. In that work, it was shown that velocity ramp rate, $\dot{v}_p$, system size L and the ambient wave speed C_o are related by a non-dimensional ramp-rate $\tilde{\dot{v}}_p = \dot{v}_p L/C_o^2$. We describe, here, a similar method which we have proposed and tested that scales time and position while holding the piston velocity loading path constant.

6.2 Method of characteristics

The method of characteristics has long been used to analyze and visualize complex solutions to the wave equations. Characteristics, or characteristic curves, are a visual representation of a wave's evolution through time and space. For a one dimensional wave a characteristic can depict concisely the entire spatio-temporal history of a propagating wave in a 2D x-t plot. The ability to extract characteristic curve representations from a molecular dynamics simulation means that we can represent the history of a ramp wave as it propagates and steepens into a shock wave. Further, we can compare two such wave evolutions. In the next section we will offer a scaling argument which we argue allows us to equivalently model a ramp experiment with a much smaller system. Characteristic curve analysis gives us a mechanism to validate this assertion.

For a forward-propagating simple wave in a linear elastic material characteristic curves have a particularly clear meaning. Figure 55 represents how curves can be extracted from a time series of wave profiles. In this simple case, three spatial profiles of material velocity from t_0 to t_2 show the steepening of a wave pulse. For this class of wave one can simply extract the (x, t) points for given values of material velocity, u. Take, for example, the maximum value, u_2. The location of this maximum as a function of time defines a characteristic curve for this wave evolution. The bottom plot in Fig. 55 shows three such curves extracted from the profiles shown. Steepening of the front of the pulse is represented by a convergence of the characteristic curves. The back of the pulse is spreading, which is represented in the divergence of the characteristic curves. Notice that for an unchanging wave profile, the characteristic curves would be parallel. It should be stressed that extraction of characteristics is significantly simplified in this special case of a forward-propagating simple wave. A more general definition is necessary.

For a full mathematical description of characteristics, see the text by Courant and Friedrichs [116]. For a wonderful conceptual description in the context of both linear and nonlinear elastic response, see Drumheller

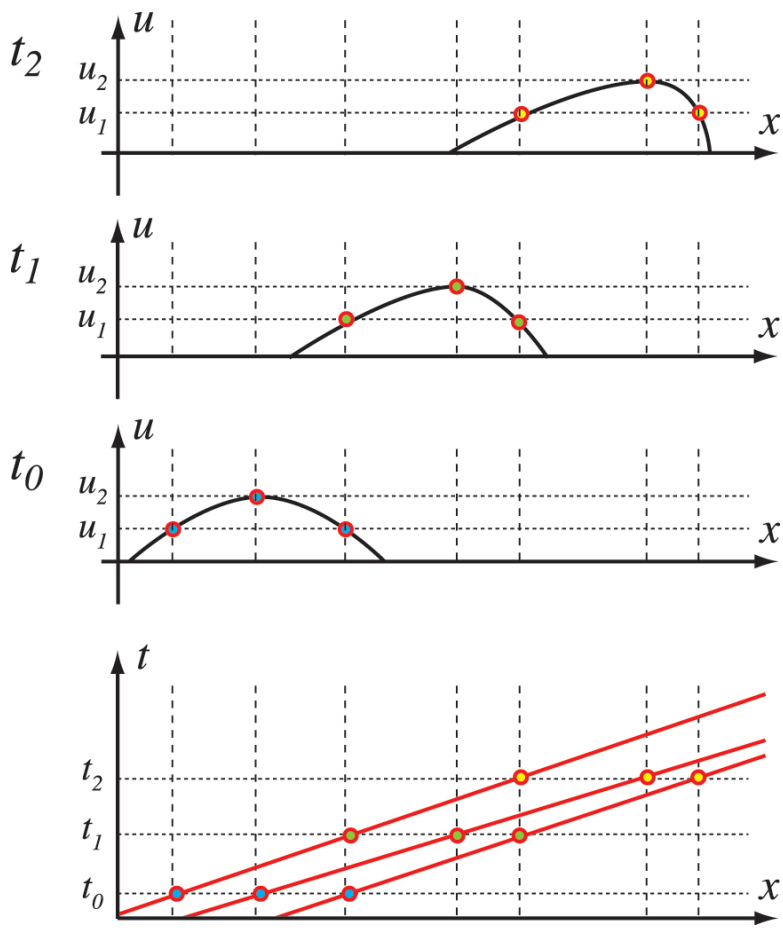

Figure 55: Wave profiles of velocity, u, vs position, x, for three times t_0, t_1 and t_2 (top three images). Characteristic curves for this simple case are plotted in $x - t$ space for the wave evolution depicted in the wave profiles (bottom).

[117]. We briefly summarize, here, points necessary to motivate our method for extracting characteristic curves from molecular dynamics simulations.

It can be shown that characteristic curves are determined by the simple relation,

$$\frac{dx}{dt} = v + c \,, \tag{22}$$

for a nonlinear elastic wave in a spatial frame, where v is the local material velocity and c is the local wave speed. dx/dt is the inverse slope of the characteristic in $x - t$ space. In cases where both the velocity and the wavespeed are explicit functions of time and position, this ordinary differential equation can be analytically intractible. However, numerical integration can always be used to produce characteristic curves from simulation.

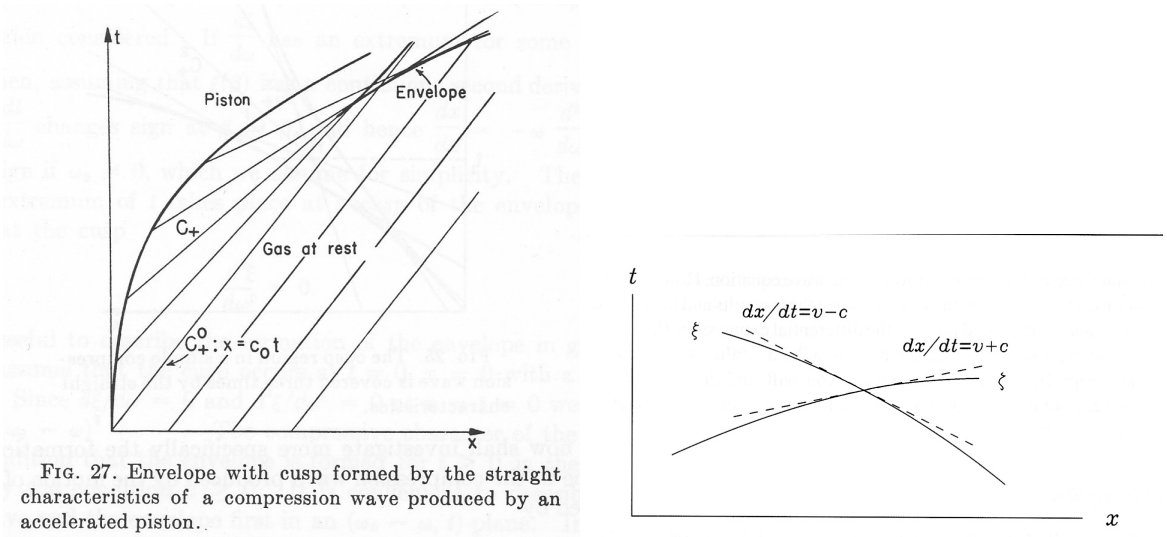

Figure 56: Two figures from the text by Courant and Friedrichs [116] showing depictions of characteristic curves. Characteristic curves are often approximately straight lines, but curve when nonlinear response is significant. Characteristics can never cross, as schematically shown in the left image.

In the context of shock and ramp loading, two misrepresentations of characteristic curves are common. First, characteristics are often represented as straight line curves, and second these straight lines are often depicted as crossing in $x - t$ space. These crossing points are, of course, impossible since the slope of a characteristic is single valued for a given position and time. These two misrepresentations are related and arise from the simplifying assumption that the wave speed in a material is constant. This is, of course, a good assumption for small amplitude wave motion, but fails when amplitudes are large, as is always the case in ramp and shock loading. Figure 56 shows two $x - t$ plots from Courant and Friedrichs which illustrate important features of characteristic curves. On the left, an overly simplified characteristics plot for an accelerating piston illustrates the crossing straight-line characteristics. On the right in the same figure is a more accurate depiction of the curving characteristics which are possible in nonlinear elastic theory. Later in this section, we will extract characteristic curves for an MD simulation of a ramp-shock transition where the curvature of characteristics was directly observed.

Figure 57 depicts the methodology employed to extract characteristic curves from a time series of molecular dynamics simulation states. The figure depicts a number of system snapshops, stacked vertically, taken from a dynamic trajectory. Each snapshot is discretized spatially into bins over which state variables, such as

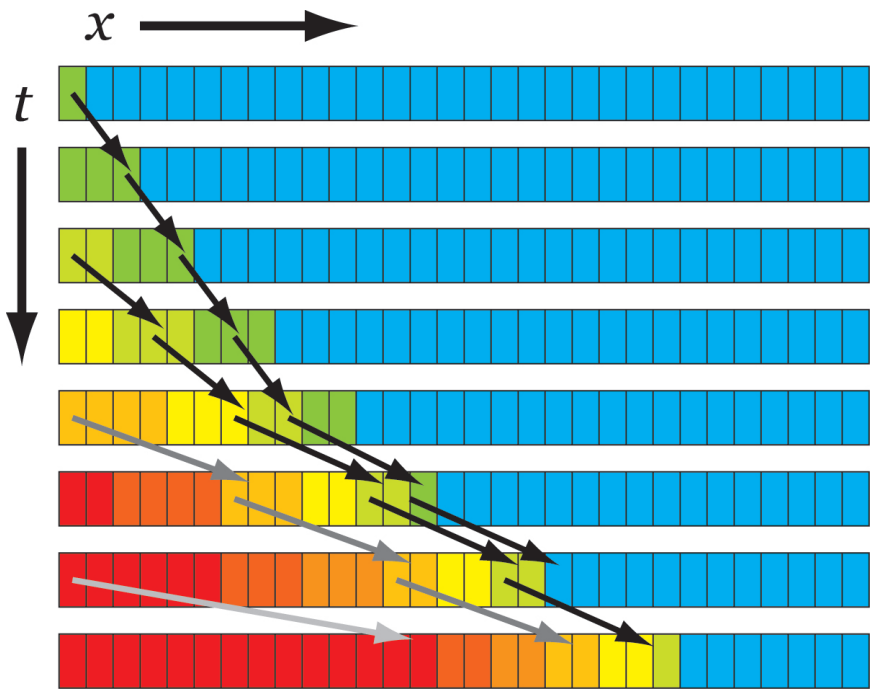

Figure 57: A diagram describing the methodology for integrating up the characteristic curve points in $x - t$ space. Each point (x_{n+1}, t_{n+1}) can be calculated from the current point and the slope, which is uniquely determined by the state variables at the current point.

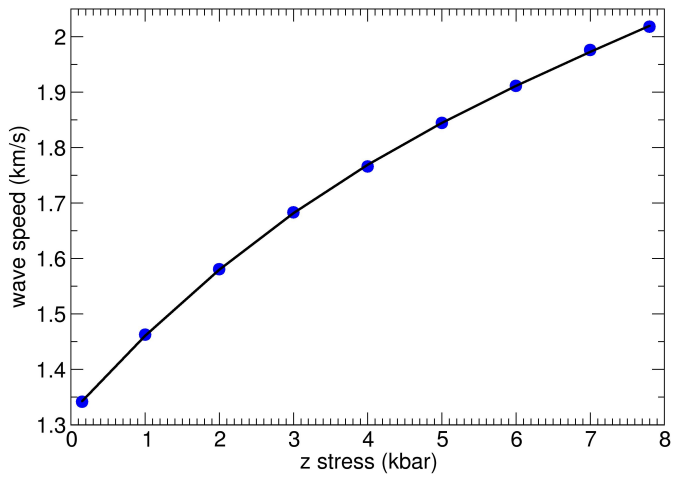

Figure 58: A plot of the wave speed within an Lennard-Jones system as a function of the pressure. This data was measured using a series of independent time-of-flight measurements for small amplitude pulses. The points are measured and then a smooth analytic fit was applied for the characteristic analysis.

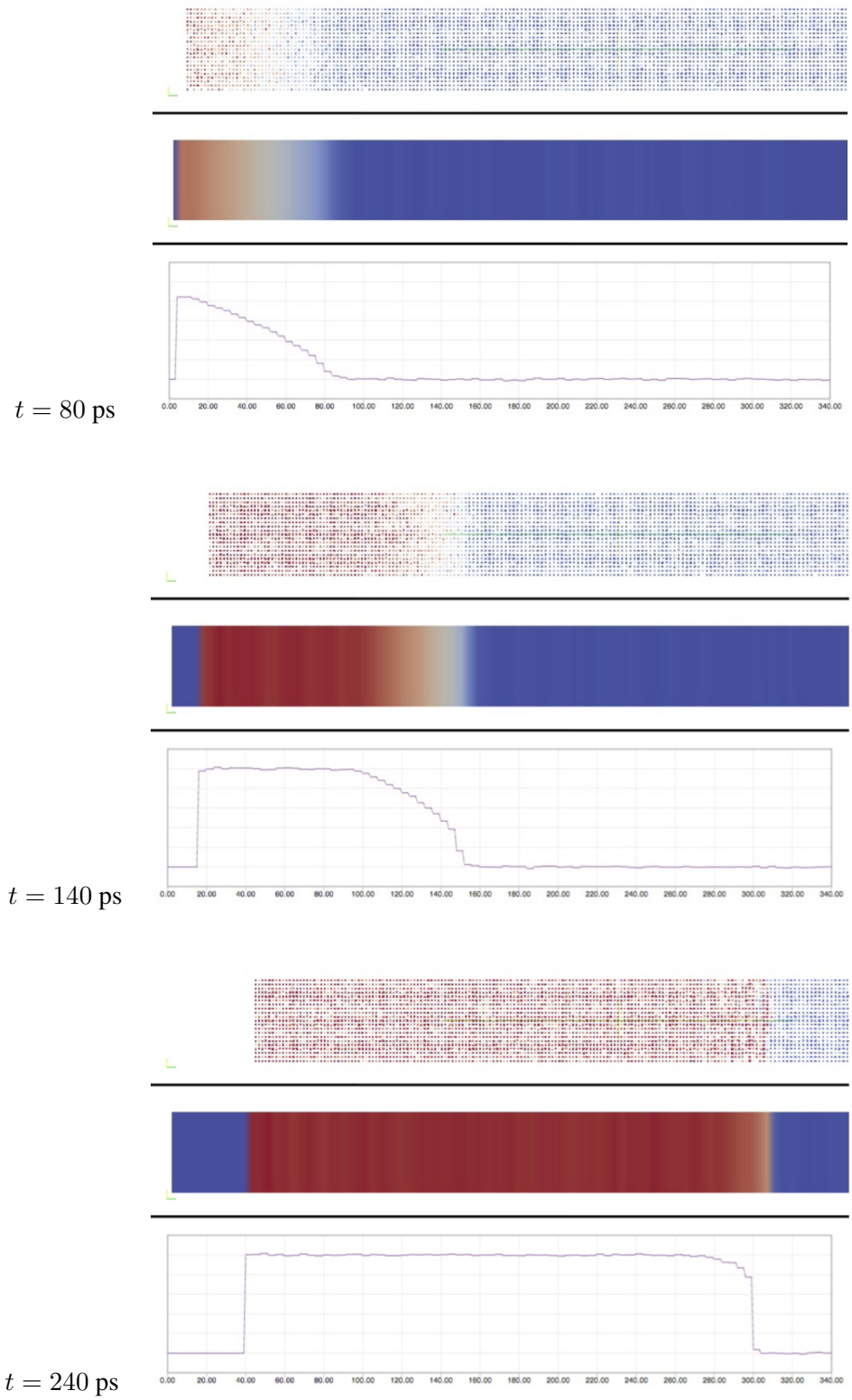

Figure 59: Three snapshots from an MD simulation of a ramp wave in Lennard-Jonesium. For each snapshot an atomistic view, discretized view and wave profile view. Color represents the local material velocity, where red is high velocity and blue is low velocity.

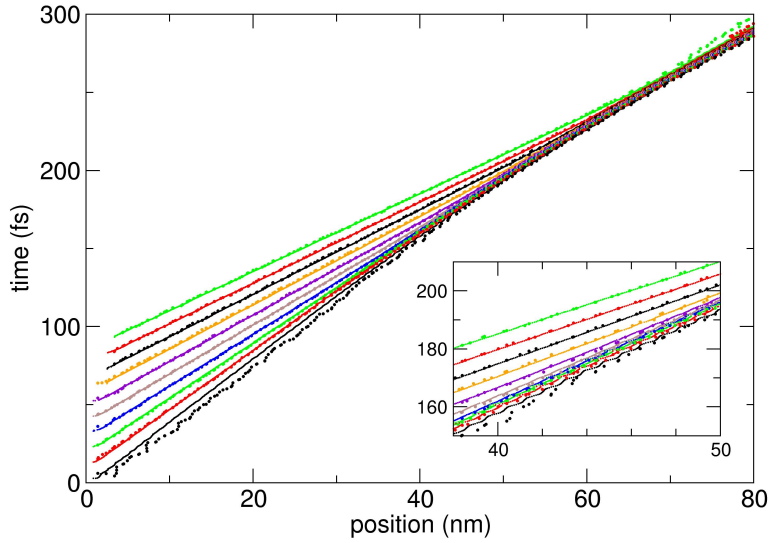

Figure 60: $x - t$ plot showing characteristic curves extracted from a molecular dynamics simulation of Lennard-Jonesium. Characteristic curves can be seen bending, rather than crossing, as the ramp wave becomes a shock wave. Inset shows detail in the merging characteristics.

density, pressure, temperature and material velocity, can be averaged. Beginning at a given x_o, t_o trajectory point, one can determine the slope of the characteristic through that point from Equation 22. This requires only that the local material velocity, v and the local wave speed, c, be known. The local material velocity is easily measured from MD. The wavespeed is not easily calculated on the fly. Instead, a separate set of time-of-flight calculations were made for a range of material state variables. The wave speed was then tabulated as a function of P, T, and ρ. For elastic shock waves, we found that we could parameterize the wave speed, c, as a function of P alone, as seen in Figure 58 for a solid argon system. Once the characteristic slope was determined, the next (x_{n+1}, t_{n+1}) trajectory point can be mapped recursively by numerical integration.

$$t_{n+1} = t_n + \Delta t \tag{23}$$

$$x_{n+1} = x_n + \left.\frac{dx}{dt}\right|_n \Delta t \,, \tag{24}$$

where Δt is the gap between system snapshots. This entire process is then repeated for the initial condition of each characteristic.

Ramp compression simulations were conducted in a solid argon model system using the Lennard-Jones potential. A linear velocity ramp was imposed to a warm momentum mirror piston. A one-dimensional wave was produced in a system of 344,000 atoms with overall dimensions 5.38 nm $\times$ 5.38 nm $\times$ 462.7 nm. Periodic boundary conditions were implemented in the directions transverse to the wave propagation. In Figure 59, we see various representations of a 250 m/s ramp wave accelerated from rest over 100 ps. These snapshots were taken after 80 ps (top), 140 ps (middle) and 240 ps (bottom). We see in the profiles that the linear ramp quickly steepens into a shock wave.

For the characteristic analysis of this trajectory, the system was spatially discretized with bins of size 4.6

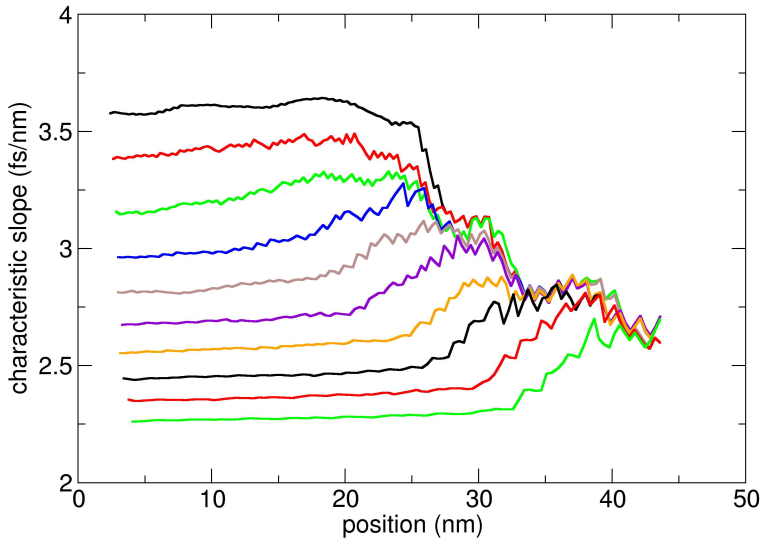

Figure 61: Plot showing the slope of characteristic curves as a function of position from a molecular dynamics simulation of Lennard-Jonesium. Colors correspond to the colored characteristics in Fig. 60

nm and temporally discretized into snapshots separated by $\Delta t = 10$ ps. Figure 60 shows the characteristics we extracted. We see clearly the converging characteristic curves which are indicative of a steepening front. The characteristics are, in fact, straight lines for the majority of the simulation trajectory. However, in the vicinity of the shock front, where the wave speed is rapidly changing due to gradients in the pressure state, we see that the lines bend, or curve and turn parallel, rather than cross.

Figure 61 shows the slope of the characteristics from Fig. 60 plotted as a function of position. Again, each characteristic has a constant slope, different for each, because each emanates from an accelerating piston at a different time. We see that for early times, as the first characteristics converge, i.e. as the ramp first begins to "shock up," the characteristics curve slopes drop. At later times, however, after the shock is well formed, converging characteristics bend the other way, with slopes increasing. The ability to study such wave properties is particularly interesting in investigations of the transition from quasi-isentropic processes to the entropy-producing shock state.

A similar analysis was conducted for aluminum, using the Voter-Chen parameterization of the EAM potential. Figure 62 show the corresponding plot of sound speed as a function of stress state and a plot of characteristic curves extracted for a system 4.09 nm $\times$ 4.09 nm $\times$ 655.0 nm, which was driven by a piston linearly ramped from rest to $v = 750$ m/s over 24 ps, then held for 72 ps. Interestingly, one can identify a small shock steepening well before a true shock forms, which is due to the kink seen in the wave speed plot. The aluminum work was conducted as a demonstration that the techniques are applicable to more complex materials than solid fcc argon.

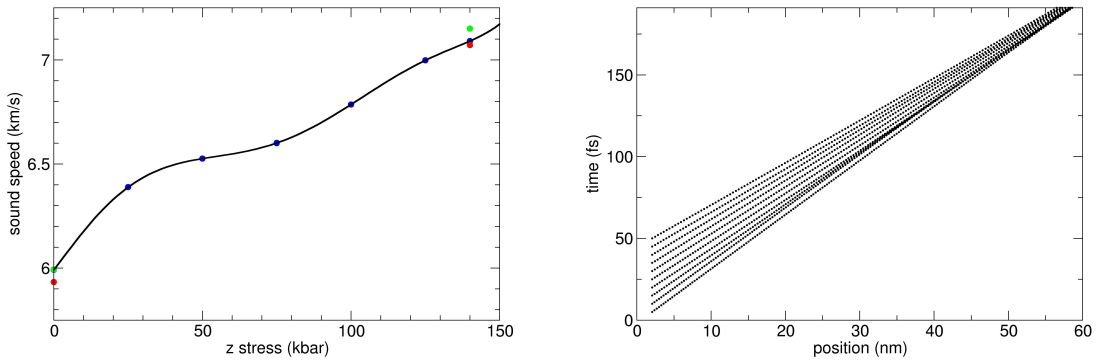

Figure 62: (left) A plot of the wave speed within a Voter-Chen aluminum system as a function of the pressure. (right) $x - t$ plot showing characteristic curves extracted from a molecular dynamics simulation of Voter-Chen alumninum.

6.3 Method of scaling

As has been described, the simulation of ramp waves becomes extremely costly as the ramp rates get slower, because longer simulation durations are required, which in turn require correspondingly larger systems through which to propagate. There is, therefore, significant motivation to devise a method which can capture the material response without such computational expense. To do this we will turn to scaling arguments which allow us to model full-scale experiments with much smaller systems and shorter times.

Just as properly scaled-down mockups of airplanes can tell us how their larger cousins will behave, we propose to model experimental-scale ramp waves with smaller MD simulations. To do this we alter the ramp piston loading length and time scales, but do not alter the physical properties of the material. The interatomic potential, lattice dimensions, and initial temperature, for instance, are unchanged.

The one-dimensional piston trajectory is scaled by a symmetric scaling of both position and time, which together keeps the velocity in the scaled coordinates unchanged. The scaling is given by,

$$\begin{aligned} t' &= \frac{1}{M} t \\ x'(t') &= \frac{1}{M} x(t) \\ v'(t') &= v(t) \end{aligned} \tag{25}$$

where the primed variables are the scaled values and M is the scaling factor.

This transformation reduces the system volume by a factor of $1/M$, since only lengths in the propagation direction are scaled and not the transverse directions. A quasi-one-dimensional wave is assumed. Further, the duration of the simulation is reduced by a factor of $1/M$. Thus one can readily see that this approach reduces the total computational effort by $1/M^2$.

6.3.1 Kinematic and dynamic similarity

Dynamic scaling is a technique frequently used in fluid mechanics and nonlinear dynamics. It is closely related to the approaches of dimensional analysis and nondimensionality, but is most identifiable as the approach which allows engineers to build less costly scale models of large systems for tabletop studies to validate designs. Here, we propose to make use of these methods to transform experimental scales down to those that can be modeled with molecular dynamics. In this work, we test our approach by using the technique to transform between two MD simulations: one M^2 more costly than the other, where M is the scale factor in Equations 25.

We imagine a true system and model system of a one-dimensional ramp wave on which we can test that our proposed scaling satisfies the conditions of kinematic similarity and dynamic similarity. Kinematic simularity is simply the condition that $v(t) = v'(t')$, which is one of our scaling assumptions and thus is satisfied intrinsicly. The more stringent test would be dynamic similarity which demands that all forces are proportionally scaled. We further demand that the forces are unchanged, which allows us to leave the interatomic potential unscaled and thereby the material unchanged. We look at the ratio of forces $F_{\text{model}}/F_{\text{true}}$ and study how each dimension scales.

$$\begin{aligned}
\frac{F_{\text{model}}}{F_{\text{true}}} &= \frac{M_{\text{m}}\frac{L_{\text{m}}}{T_{\text{m}}^2}}{M_{\text{t}}\frac{L_{\text{t}}}{T_{\text{t}}^2}} = \frac{\rho_{\text{m}} A \frac{L_{\text{m}}^2}{T_{\text{m}}^2}}{\rho_{\text{t}} A \frac{L_{\text{t}}^2}{T_{\text{t}}^2}} \\
&= \left(\frac{\rho_m}{\rho_t}\right)\left(\frac{L_m}{L_t}\right)^2\left(\frac{T_t}{T_m}\right)^2 \\
&= \lambda_\rho \left(\frac{\lambda_L}{\lambda_T}\right)^2 \qquad (26)
\end{aligned}$$

where M, L, and T represent dimensions of mass, length and time, respectively. Note that in expanding the mass units we use density $\times$ volume. Assuming one-dimensional flow, we have taken $M = \rho A L$, where A is the unscaled cross-sectional area. In the final step of Equation 26, λ is the ratio between model and true systems for a given dimensional unit, e.g. $\lambda_M = M_m/M_t$. Our scaling proposal from Equation 25 equates to,

$$\lambda_L = \lambda_T = \frac{1}{M} \qquad (27)$$

$$\lambda_\rho = 1 \qquad (28)$$

plugging into Equation 26 gives

$$\lambda_F = \frac{F_{\text{model}}}{F_{\text{true}}} = 1 \qquad (29)$$

which shows that the forces are invariant to the proposed scaling. A similar analysis can be used to show that velocity, strain, stress, temperature and density are invariant to the transformation. Not all observables, however, are invariant. Acceleration, strain rate, viscosity, time, distance and any extensive variable are not invariant. Specifically,

$$\lambda_{\text{acceleration}} = \lambda_{\text{strain rate}} = M$$

$$\lambda_T = \lambda_L \quad = \quad \frac{1}{M} \tag{30}$$

.

We would expect, given our assumptions, that this proposed scaling would break down in several circumstances. First, clearly, when the dynamics are significantly three dimensional, rather than quasi 1D. Our analysis assumes that the volume scales like $1/M$, not $1/M^3$ as it would if the dynamics were 3D. Such a change in the volume scaling would destroy the invariance of the force and thus destroy the dynamic similarity. In 3D, dynamic similarity might be recovered by scaling the interatomic potential or the material density, but this has not been investigated. Further, it should be noted that we would expect this scaling to breakdown in cases where the dynamics and/or forces are strongly dependent on the strain rate, however we have not seen direct evidence of this in our test systems.

6.3.2 Invariance in the wave equation

An alternate viewpoint from which to evaluate the proposed scaling is to look to the wave equation. For the nonlinear elastic wave equation we have,

$$\frac{\partial v}{\partial t} + C\frac{\partial v}{\partial x} = \frac{1}{\rho_o C}\left(\frac{\partial T}{\partial t} + C\frac{\partial T}{\partial x}\right) \tag{31}$$

where C is the material wave speed and T is the stress. If we execute the scaling transformation by applying the chain rule,

$$\frac{\partial}{\partial t} = \frac{dt'}{dt}\frac{\partial}{\partial t'} = \frac{1}{M}\frac{\partial}{\partial t'} \tag{32}$$

$$\frac{\partial}{\partial x} = \frac{dx'}{dx}\frac{\partial}{\partial x'} = \frac{1}{M}\frac{\partial}{\partial x'} \tag{33}$$

then we see that the transformation simply adds the same scale factor to each term. Multiplying through by M returns the wave equation unchanged in the new coordinates.

As before, this analysis depends on our assumption of one-dimensional dynamics. We have also assumed here that the stress and wave speed depend only implicitly on x and t.

Figure 63 illustrates examples of the relationships between scaled and unscaled variables through plots of velocity and position versus time. The left plots show two loading paths, linear (top) and stairstepped (bottom). The plots clearly show that the velocity history is the same for v and v' in each plot. v' is simply compressed in time. The right plots show the corresponding displacement of the piston for each velocity profile. Note that unlike the velocity, where $v'\left(\frac{1}{M}t_f\right) = v(t_f)$, here, $x'\left(\frac{1}{M}t_f\right) = x'(t'_f) = \frac{1}{M}x(t_f)$. These two loading pathways are exactly those which we will use as examples in the two test cases which follow in the next two subsections. The validity of our scaling argument will be tested in the nonlinear-elastic case and the plastic case.

6.3.3 Ramp scaling in the nonlinear elastic response regime

We chose a solid argon model system, modeled with the highly-efficient Lennard-Jones potential, on which to examine the validity of our scaling proposition. We constructed two systems, one $10\times$ larger than the other. The larger system consisted of 800,000 atoms in an fcc lattice, 53.8 nm $\times$ 53.8 nm $\times$ 1077.3 nm. The

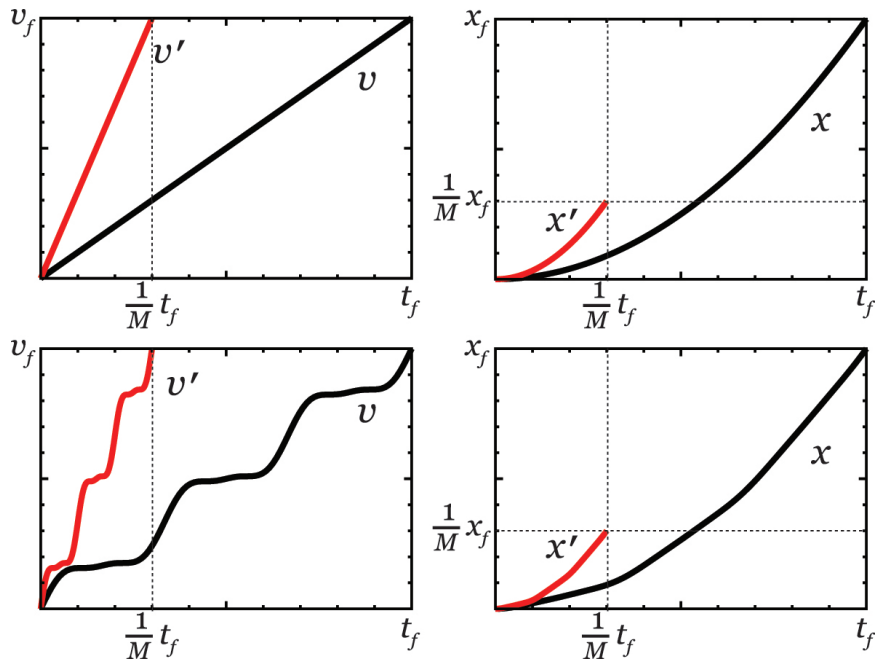

Figure 63: Plots of piston loading paths for original (black) and scaled (red) variables. The top two images are the velocity (left) and position (right) for a linear ramp. The bottom two images are the same plots for a stairstep ramp.

smaller system consisted of 80,000 atoms in the same fcc lattice, 53.8 nm $\times$ 53.8 nm $\times$ 107.7 nm. Both were equilibrated at 6 K. An LJ cubic spline potential was used with cutoff of just under 6 Å . The material properties of both systems were identical, only the size of the systems differed.

We drove these two systems with accelerating warm pistons moving into the samples. The velocity and position of the piston has an analytic form,

$$v = a_z \left[\frac{t}{M} + \frac{4}{3\omega} \sin\left(\omega \frac{t}{M}\right) + \frac{1}{3\omega} \sin\left(2\omega \frac{t}{M}\right) \right] \tag{34}$$

$$z = z_o + a_z \left[\frac{t^2}{2M} + \frac{4M}{3\omega^2} \left(1 - \cos\omega \frac{t}{M}\right) + \frac{M}{6\omega^2} \left(1 - \cos 2\omega \frac{t}{M}\right) \right] \tag{35}$$

where $\omega = 6\pi/t_f$, and for the large system M was 1 and for the small system M was 10. The final ramp piston velocity was 250 m/s in both systems, which is low enough that the shock response was entirely in the elastic shock regime.

Figure 64 shows the velocity profiles at three times for the ramp wave response within the larger system. We see that the ramp wave steepens into four small shocks and these shocks ultimately merge into a single shock front.

Figure 65 shows the system response of the two systems in characteristic curves. We can see the characteristic lines converge and merge into four shocks which eventually merge into a single shock at late time. For the large system this process occurs over $\sim$ 300 nm and $\sim$ 225 ps. In the small system the shock up occured over $\sim$ 30 nm and $\sim$ 22.5 ps.

Figure 66 shows the same two systems where the lengths and times have been multiplied by the scale factor $M = 10$. We see excellent agreement between the two sets of characteristics. Because characteristics

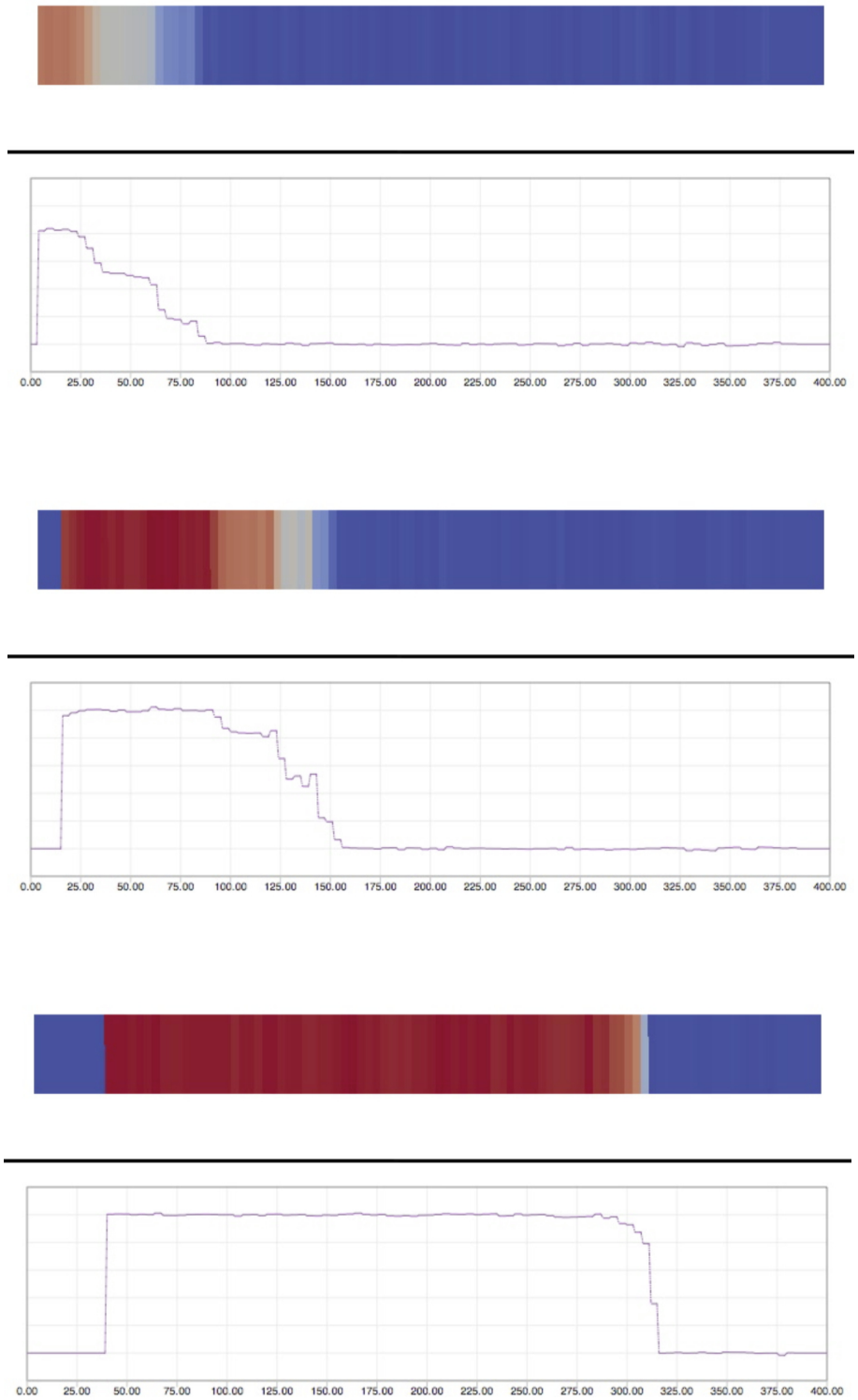

Figure 64: Particle velocity profiles showing the propagation of a ramp wave as it steepens into a shocks which ultimately merge into a single shock front. The initial pulse was a smooth stair step function.

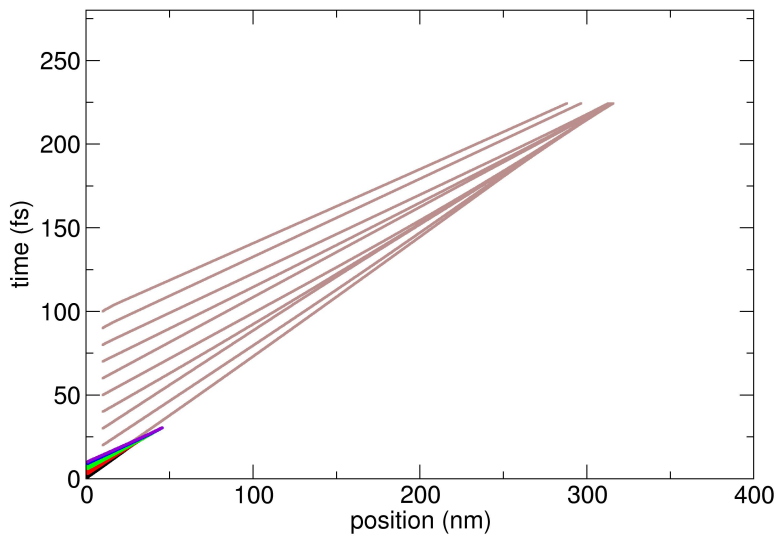

Figure 65: The characteristic curves extracted from ramp wave simulations. These two sets of curves for a large original system and a scaled smaller system are plotted together. All values are as measured from the two simulations.

capture the entire spatio-temporal evolution of the ramp wave, the overlap of characteristic curves means that the systems have evolved in exactly the same manner and shocked up in identical trajectories, except that the scaled system did so over 1/10th the time and in 1/10th the space. Thus, the scaled simulation captured exactly the same physics with 1/100th the computational effort.

6.3.4 Ramp scaling in the plastic response regime

Our second validation makes use of the same two argon systems, but with ramp waves driven with a superlinear piston ramp to velocities well into the plastic response regime for our model material. The higher order in t suppresses shock formation. The piston motion was given by

$$v = a_z \frac{t^2}{M t_f} \tag{36}$$

$$x = z_o + \frac{1}{3} a_z \frac{t^3}{M t_f} \tag{37}$$

where again M is 1 for the larger system and 10 for the small system. The final velocity was 1500 m/s for both cases.

Figure 67 shows spatial profiles for the wave propagation at timesteps separated by 100 ps for the large system and 10 ps for the small system. Plots show the stress (top), velocity (middle) and temperature (bottom), with real coordinates on the left and nondimensional positions on the right.

Our characteristic methods allow us to compare two waves over all spatio-temporal points in its evolution. However, our characteristic methods have not been generalized to plastic waves. The issue is determining

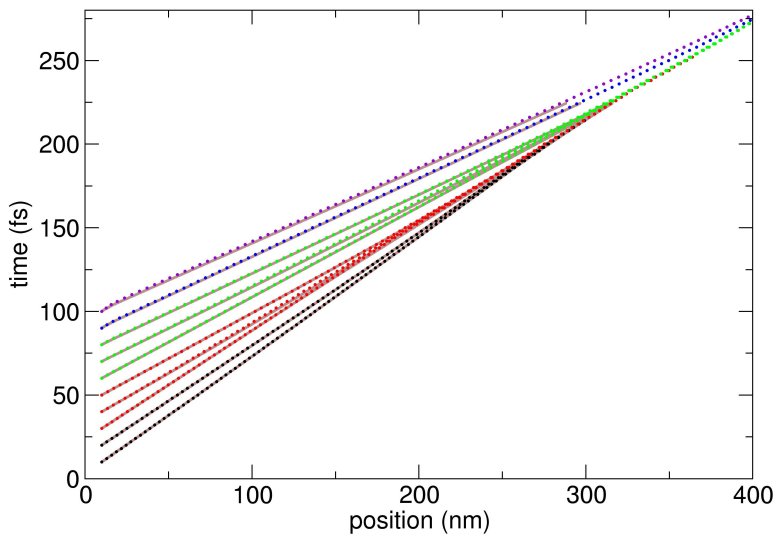

Figure 66: The characteristic curves from Fig. 65 are replotted. Here, the times and positions of the smaller scaled system are multiplied by the scale factor. We see excellent agreement with the original system which required 100× more computation.

the local wave speed. In the case of plastic waves, the wave speed is not single valued for a given pressure, but depends on temperature and density as well. A reliable method for extracting instantaneous wave speed from simulation is not currently available, so our scaling comparisons must depend solely on snapshot profiles.

In both the stress and velocity profiles, we see extremely good agreement between the original and scaled systems in the plots to the right. The agreement is near perfect until the onset of plasticity and then afterward agrees within the local fluctuations in the system. It is likely that the agreement would be better if better statistics were available, as would be the case with larger systems.

The only significant deviation from the predicted scaling evident in the profiles of Figure 67 is in the temperature profiles. Unlike the stress and local velocity, temperature can be strongly affected by poor statistics. We, therefore, believe that the somewhat weaker agreement may be due to poor statistics in the smaller systems. However these finite system size effects in the plastically deformed systems complicate, but do not destroy the scaling. We predict that making the smaller systems larger would mitigate this issue.

Finally, it should be noted that systems exhibiting plasticity violate several of the assumptions which were made in motivating this scaling method. Plasticity couples the 1D propagation with the transverse dimensions which are not explicitly handled within our scaling. This plasticity, being dependent on noninvariant quantities such as shear stresses, strength and viscosity, do not rigorously obey our scaling conditions. However, with this caveat, we see very good scaling regardless. This perhaps indicates that the plasticity events, such as stacking fault generation and local melting only weakly perturb the quasi-1D wave and that these processes appear to be local, and somewhat independent of scale. This is an exciting result, which indicates that this scaling may be applicable outside the nonlinear-elastic regime in which it is proposed. However, the response may depend strongly on the particular material properties of a system and the processes associated

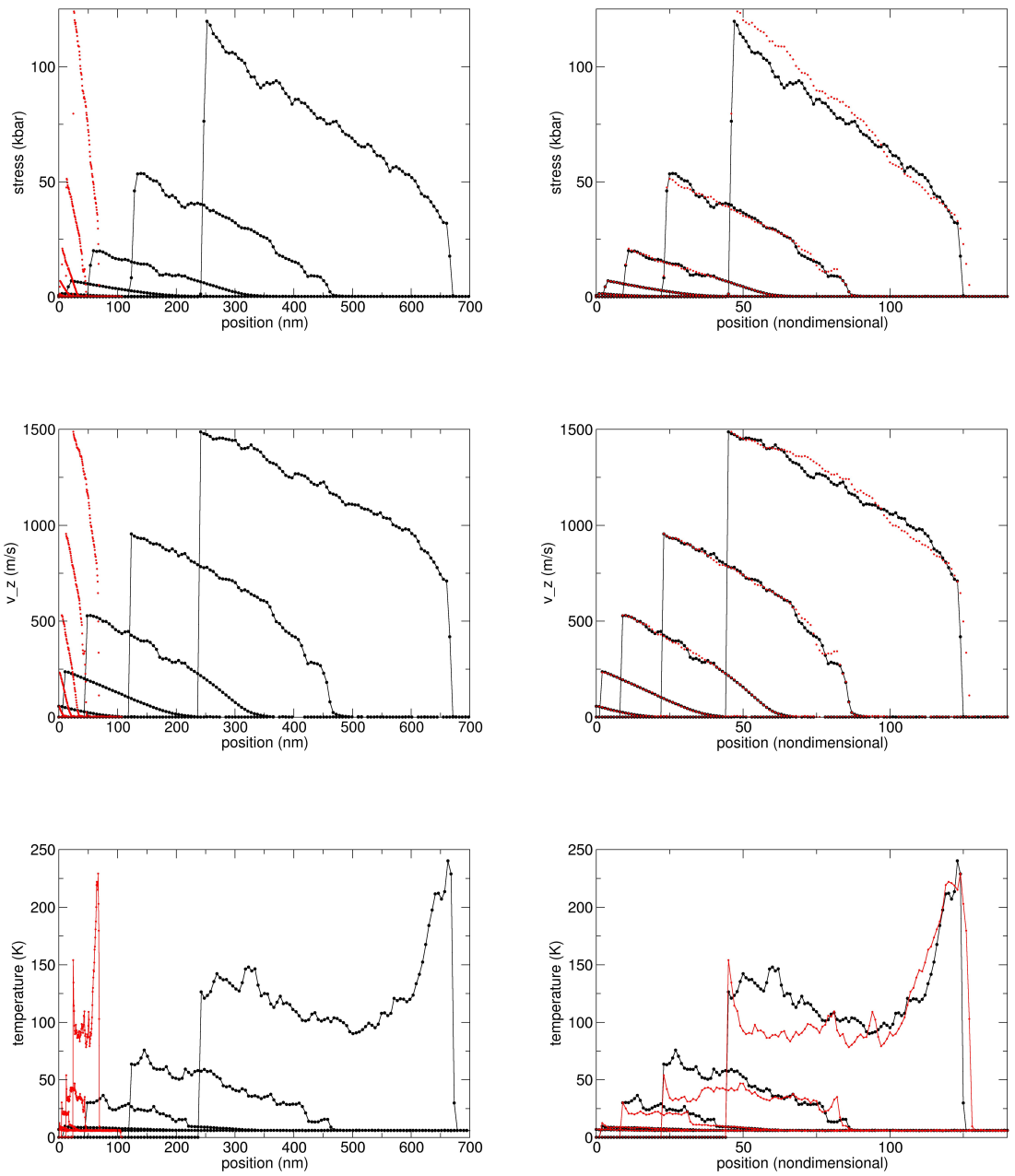

Figure 67: Profiles of ramp wave propagation through solid argon in original and scaled systems. The plots on the left show the true coordinates of the simulations. The plots to the right multiply the position by the scale factor to compare results in original and scaled systems. Very good agreement is seen between original (black) and scaled down (red) systems in all of the profiles, stress (top), velocity (middle) and good agreement is seem in temperature profiles (bottom).

with the plastic response.

Part III
Methods

7 Continuum Properties

Principal Authors: Jonathan A. Zimmerman, Reese E. Jones, Jeremy A. Templeton

This section contains a paper entitled "A Material Frame Approach for Evaluating Continuum Variables in Atomistic Simulations" that was published in *Journal of Computational Physics* in 2010. It was authored by Jonathan A. Zimmerman, Reese E. Jones, Jeremy A. Templeton. [SAND 2008-5503 J]

Earlier in this report, we presented several examples where molecular simulations are used to illuminate the behavior of materials experiencing shock and ramp compression. Two pertinent questions to ask when performing such simulations are: How does one have confidence that such simulations are emulating real material behavior?, and How can these simulations help to improve the material response models used at macroscopic scales?

A reasonable answer to the first question is by comparing molecular simulation results with information obtained from experimental studies of high rate deformation. However, this information is usually in the form of continuum properties such as temperature and pressure locally measured as a function of time with respect to the propagation of the shock or ramp wave. These properties are not intrinsic to molecular simulation; thus, metrics are needed that translate the characteristic information of atomistics (*e.g.* atomic velocities, interatomic forces) to continuum variables. This section will review several such formalisms that contain these metrics.

The estimation of spatially and temporally varying continuum fields also provides a partial answer to the second question posed. However, in continuum mechanics it is common to separate the elastic and inelastic response of material deformation, construct coupled equations that govern the evolution of these separate deformation metrics, and then recombine them to predict the full material behavior. A simple example of this is modeling metals that exhibit strain hardening; the material has an initial (often assumed linear) elastic behavior until it reaches a critical stress and strain (the yield point) at which the material hardens, *i.e.* the material deforms inelastically or plastically such that the yield stress increases with increasing strain. Constitutive models are constructed to describe both the elastic (*i.e.* elastic constants) and hardening (*i.e.* flow rule) responses. The ability for molecular simulation to impact the functional forms and parameters of these models relies on the ability to separate our atom-to-continuum deformation expressions into elastic and inelastic portions, a non-trivial requirement. In this section, we report on efforts made to perform this separation and estimate plastic strain and dissipative work.

7.1 Eulerian Atomistic-Continuum Formulation by Hardy

In this section, we briefly describe the Eulerian (spatial) frame formulation developed by R. J. Hardy [88] whereby expressions for continuum mechanical variables such as stress and heat flux are derived from atomic scale quantities intrinsic to molecular simulation. This formulation is ideally suited for developing an atomistic-to-continuum correspondence for fluid mechanics problems, as well as solid mechanics problems undergoing high rates of deformation. Hardy's method uses a finite-valued and finite-ranged localization function to average atomic properties in the vicinity of a fixed spatial point, resulting in expressions for field variables that satisfy the continuum balance laws. While the range and characteristic size of this function

can be chosen arbitrarily, the resulting expression for stress contains terms that, theoretically, should remain constant for different size volumes.

7.1.1 Balance Laws

In the Eulerian or spatial frame, the the balance equations for mass, linear momentum and energy are as follows:

$$\frac{\partial \rho}{\partial t} + \nabla_{\mathbf{x}} \cdot (\rho \mathbf{v}) = 0 \tag{38}$$

$$\frac{\partial (\rho \mathbf{v})}{\partial t} = \nabla_{\mathbf{x}} \cdot (\boldsymbol{\sigma} - \rho \mathbf{v} \otimes \mathbf{v}) + \rho \mathbf{b} \tag{39}$$

$$\frac{\partial (\rho e)}{\partial t} = \nabla_{\mathbf{x}} \cdot (\boldsymbol{\sigma} \cdot \mathbf{v} - \rho e \mathbf{v} - \mathbf{q}) + \rho \mathbf{b} \cdot \mathbf{v} + \rho h \tag{40}$$

In equations (38) through (40) ρ is mass density, $\mathbf{v}$ is velocity, $\boldsymbol{\sigma}$ is Cauchy stress, $\mathbf{b}$ is body force per unit mass, e is total energy per unit mass, ϵ is internal energy per unit mass (total energy contains contributions from both internal energy and continuum kinetic energy: $e = \epsilon + \frac{1}{2}v^2$), $\mathbf{q}$ is heat flux and h is energy generation per unit mass.

7.1.2 Densities and Localization

We consider a body to be a system of N atoms, where each atom α is characterized by its mass m^α, its position in the reference configuration $\mathbf{X}^\alpha$, its position in the current configuration $\mathbf{x}^\alpha(t)$, its velocity $\mathbf{v}^\alpha(t) = \frac{d\mathbf{x}^\alpha}{dt}$, and a displacement $\mathbf{u}^\alpha(t) \equiv \mathbf{x}^\alpha(t) - \mathbf{X}^\alpha$. Hardy relates these atomic properties to the continuum mass $\rho(\mathbf{x}, t)$, momentum $\mathbf{p}(\mathbf{x}, t)$, and energy density $\rho e(\mathbf{x}, t)$ fields through use of a localization function ψ which spatially averages the properties of the atoms, and allows many atoms to contribute to a continuum property at a specific position and time. In his original formulation, Hardy expressed ψ as a function of current position. The continuum densities are thus defined as:

$$\rho(\mathbf{x}, t) = \sum_{\alpha=1}^{N} m^\alpha \psi(\mathbf{x}^\alpha - \mathbf{x}) \tag{41}$$

$$\mathbf{p}(\mathbf{x}, t) = \sum_{\alpha=1}^{N} m^\alpha \mathbf{v}^\alpha \psi(\mathbf{x}^\alpha - \mathbf{x}) \tag{42}$$

$$\rho(\mathbf{x}, t) e(\mathbf{x}, t) = \sum_{\alpha=1}^{N} \left\{ \frac{1}{2} m^\alpha \left(v^\alpha\right)^2 + \phi^\alpha \right\} \psi(\mathbf{x}^\alpha - \mathbf{x}). \tag{43}$$

A few important things to note:

- The localization function $\psi(\mathbf{r})$ is non-negative,[2] *i.e.* $\psi(\mathbf{r}) \geq 0$.
- $\psi(\mathbf{r})$ has dimensions of inverse volume.

[2] While it is possible to choose localization functions that are not non-negative (as discussed on p. 77 of [118]), in practice this is rarely done as it contains the potential to admit unbounded values for the extremum. In such instances, additional regularity requirements are needed.

- $\psi(\mathbf{r})$ is a normalized function, thus

$$\int_{\Omega} \psi(\mathbf{r}) d^3 r = 1, \tag{44}$$

where $\Omega \subset R^3$ is the domain of interest containing the collection of atoms.

- In equation (43), the total potential energy density of the system is expressed as the summation of individual atomic potential energies, ϕ_α.

- The velocity field $\mathbf{v}$ is defined by the expression

$$\mathbf{v}(\mathbf{x}, t) \equiv \frac{\mathbf{p}(\mathbf{x}, t)}{\rho(\mathbf{x})} = \frac{\sum_{\alpha=1}^{N} m^\alpha \mathbf{v}^\alpha \psi(\mathbf{x}^\alpha - \mathbf{x})}{\sum_{\alpha=1}^{N} m^\alpha \psi(\mathbf{x}^\alpha - \mathbf{x})}. \tag{45}$$

which is effectively a mass weighted average. With velocity defined in this manner, a definition for the displacement field $\mathbf{u}$ is not straight-forward as multiple time-dependent terms within equation (45) prevent easy integration to obtain such a field.

We note that in his earlier works [88, 119], Hardy established an important property of the localization function ψ. Given regularity of ψ, a bond function $B^{\alpha\beta}(\mathbf{x})$ between atoms α and β can be defined by the expression

$$B^{\alpha\beta}(\mathbf{x}) \equiv \int_0^1 \psi(\lambda \mathbf{x}^{\alpha\beta} + \mathbf{x}^\beta - \mathbf{x}) d\lambda, \tag{46}$$

where $\mathbf{x}^{\alpha\beta} = \mathbf{x}^\alpha - \mathbf{x}^\beta$.

7.1.3 Energy and Force Assumptions

Hardy makes four key assumptions about the forms of the energies of, and forces on, the atoms in the system:

1. The total potential energy of the system, Φ, can be considered to be the summation of individual potential energies of each atom within the system,

$$\Phi = \sum_{\alpha=1}^{N} \phi^\alpha. \tag{47}$$

2. The force on any atom can be expressed by the summation

$$\mathbf{f}^\alpha \equiv -\frac{\partial \Phi}{\partial \mathbf{x}^\alpha} = \sum_{\beta \neq \alpha}^{N} \mathbf{f}^{\alpha\beta}. \tag{48}$$

While it is not always clear what the physical meaning of $\mathbf{f}^{\alpha\beta}$ is, this partition can always be made.

3. The atomic potential energies depend only on the relative inter-atomic distances, $\phi^\alpha = \phi^\alpha(x^{\alpha\beta}, x^{\alpha\gamma}, \ldots, x^{\beta\gamma})$, so

$$\mathbf{f}^\alpha = -\sum_{\beta \neq \alpha}^{N} \frac{\partial \Phi}{\partial x^{\alpha\beta}} \frac{\mathbf{x}^{\alpha\beta}}{x^{\alpha\beta}} = -\sum_{\beta \neq \alpha}^{N} \sum_{\gamma=1}^{N} \frac{\partial \phi^\gamma}{\partial x^{\alpha\beta}} \frac{\mathbf{x}^{\alpha\beta}}{x^{\alpha\beta}}. \tag{49}$$

This expression includes the possibility that $\alpha = \gamma$. This assumption can be shown to be true for any potential form.

4. Each atomic potential energy depends only on the distances between the atom under consideration and all other atoms, $\phi^\alpha = \phi^\alpha(x^{\alpha\beta}, x^{\alpha\gamma}, \ldots, x^{\alpha N})$. Thus, the force between atoms α and β can be expressed as

$$\mathbf{f}^{\alpha\beta} = -\left\{ \frac{\partial \phi^\alpha}{\partial x^{\alpha\beta}} + \frac{\partial \phi^\beta}{\partial x^{\alpha\beta}} \right\} \frac{\mathbf{x}^{\alpha\beta}}{x^{\alpha\beta}} = -\mathbf{f}^{\beta\alpha}. \tag{50}$$

While pair potentials and EAM qualify for this assumption, it is not generally true.

7.1.4 Continuum Expressions

Substitution of the expressions for mass, momentum and energy densities into the continuum balance laws enables derivation of expressions for Cauchy stress ($\boldsymbol{\sigma}$) and heat flux vector ($\mathbf{q}$). This was done originally in [88], and rederived and discussed more thoroughly in more recent articles by Zimmerman, Webb and colleagues [89, 90]. Here, we merely present the resulting expressions.

Cauchy Stress

The expression for Cauchy stress at a fixed spatial point is:

$$\boldsymbol{\sigma}(\mathbf{x}, t) = -\frac{1}{2} \sum_{\alpha=1}^{N} \sum_{\beta \neq \alpha}^{N} \mathbf{f}^{\alpha\beta} \otimes \mathbf{x}^{\alpha\beta} B^{\alpha\beta}(\mathbf{x}) - \sum_{\alpha=1}^{N} m^\alpha \hat{\mathbf{v}}^\alpha \otimes \hat{\mathbf{v}}^\alpha \psi(\mathbf{x}^\alpha - \mathbf{x}). \tag{51}$$

In this expression, the relative velocity $\hat{\mathbf{v}}^\alpha$ is defined

$$\hat{\mathbf{v}}^\alpha(\mathbf{x}, t) \equiv \mathbf{v}^\alpha - \mathbf{v}(\mathbf{x}, t)\ . \tag{52}$$

and has the property

$$\sum_{\alpha=1}^{N} m^\alpha \hat{\mathbf{v}}^\alpha \psi(\mathbf{x}^\alpha - \mathbf{x}) = \mathbf{0}. \tag{53}$$

Heat Flux

The expression for heat flux at a fixed spatial point is:

$$\mathbf{q} = -\sum_{\alpha=1}^{N} \left[\sum_{\beta \neq \alpha}^{N} \frac{\partial \phi^\beta}{\partial x^{\alpha\beta}} \frac{\mathbf{x}^{\alpha\beta} \otimes \mathbf{x}^{\alpha\beta}}{x^{\alpha\beta}} B^{\alpha\beta}(\mathbf{x}) \right] \cdot \hat{\mathbf{v}}^\alpha + \sum_{\alpha=1}^{N} \left\{ \frac{1}{2} m^\alpha \left(\hat{v}^\alpha\right)^2 + \phi^\alpha \right\} \hat{\mathbf{v}}^\alpha \psi(\mathbf{x}^\alpha - \mathbf{x}). \tag{54}$$

Temperature

Hardy and colleagues also derived [120] an expression for temperature by considering the equipartition theorem and the kinetic energy associated with atomic velocities relative to the velocity of the continuum at a spatial point,

$$\mathrm{T}(\mathbf{x}, t) = \frac{1}{3k_B} \frac{\sum_{\alpha=1}^{N} m^\alpha \left(w^\alpha\right)^2 \psi(\mathbf{x}^\alpha - \mathbf{x})}{\sum_{\alpha=1}^{N} \psi(\mathbf{x}^\alpha - \mathbf{x})}, \tag{55}$$

which is a simple weighted average as opposed to the volume average in (41) for example. Here, k_B is Boltzman's constant.

7.2 Lagrangian Atomistic-Continuum Formulation

In this section, we present expressions from a material frame formulation analogous to the spatial frame formulation developed by Hardy. Derivation of these expressions was accomplished in [121]. The resulting P-K stress tensor, unlike the Cauchy expression, has no explicit kinetic contribution. The referential heat flux vector likewise lacks the kinetic contribution appearing in its spatial frame counterpart. Using molecular dynamics simulations, we show that our P-K stress expression nonetheless represents a full measure of stress that is consistent with both the system virial and the Cauchy stress expression developed by Hardy.

7.2.1 Balance Laws

In the Lagrangian or material frame, the balance equations for mass, linear momentum and energy are as follows:

$$\frac{d\rho_0}{dt} = 0 \tag{56}$$

$$\rho_0 \frac{d\mathbf{v}}{dt} = \nabla_{\mathbf{X}} \cdot \mathbf{P} + \rho_0 \mathbf{b} \tag{57}$$

$$\rho_0 \frac{d\epsilon}{dt} = \mathbf{P} : \frac{d\mathbf{F}}{dt} - \nabla_{\mathbf{X}} \cdot \mathbf{Q} + \rho_0 h \tag{58}$$

In these equations, ρ_0 is reference mass density (mass per unit reference volume), $\mathbf{P}$ is 1st Piola-Kirchhoff stress (force per unit reference area), $\mathbf{F}$ is the deformation gradient ($\frac{\partial \mathbf{x}}{\partial \mathbf{X}}$), and $\mathbf{Q}$ is the reference heat flux (energy per unit reference area per unit time). These variables in equations (56)-(58) are all functions of the reference coordinate $\mathbf{X}$ and time t, with the material time derivative retaining its earlier definition, $\frac{d\mathbf{g}(\mathbf{X},t)}{dt} = \left.\frac{\partial \mathbf{g}}{\partial t}\right|_{\mathbf{X}}$.

7.2.2 Densities and Localization

For a Lagrangian analysis, we note that both the localization function ψ and bond function B are now considered as functions of material coordinate $\mathbf{X}$ and the reference positions of atoms, e.g. $\mathbf{X}^\alpha$. With this change, all the properties and relationships discussed earlier remain intact.

7.2.3 Energy and Force Assumptions

For a Lagrangian analysis, we note that the same energy and force assumptions made for the spatial frame formulation are used as stated above without change.

7.2.4 Continuum Expressions

Displacement

For a Lagrangian formulation, the velocity field $\mathbf{v}$ is now defined by the expression

$$\mathbf{v}(\mathbf{X}, t) \equiv \frac{\mathbf{p}_0(\mathbf{X}, t)}{\rho_0(\mathbf{X})} = \frac{\sum_{\alpha=1}^{N} m^\alpha \mathbf{v}^\alpha \psi(\mathbf{X}^\alpha - \mathbf{X})}{\sum_{\alpha=1}^{N} m^\alpha \psi(\mathbf{X}^\alpha - \mathbf{X})}. \tag{59}$$

With velocity defined in this manner, the displacement field $\mathbf{u}$ can be properly defined as

$$\mathbf{u}(\mathbf{X},t) = \frac{\sum_{\alpha=1}^{N} m^{\alpha}\mathbf{u}^{\alpha}\psi(\mathbf{X}^{\alpha}-\mathbf{X})}{\sum_{\alpha=1}^{N} m^{\alpha}\psi(\mathbf{X}^{\alpha}-\mathbf{X})}, \tag{60}$$

which is consistent with the velocity field defined as a time derivative of a displacement field, *i.e.* $\mathbf{v} = \frac{d\mathbf{u}}{dt}$. With a displacement field we can construct the motion of material points $\mathbf{X}$ from reference to current configuration as a function of time in the usual way $\mathbf{x}(\mathbf{X},t) = \mathbf{X} + \mathbf{u}(\mathbf{X},t)$.

1st Piola-Kirchhoff Stress

The expression for 1st P-K stress at a material point is:

$$\mathbf{P}(\mathbf{X},t) = -\frac{1}{2}\sum_{\alpha=1}^{N}\sum_{\beta\neq\alpha}^{N} \mathbf{f}^{\alpha\beta}\otimes\mathbf{X}^{\alpha\beta}B^{\alpha\beta}(\mathbf{X}). \tag{61}$$

We note that this expression is connected to the underlying atomic displacements through the inter-atomic forces $\mathbf{f}^{\alpha\beta}$, and it is through this connection that $\mathbf{P}$ is implicitly dependent on thermal motion of the atomic system. Our expression defines stress without the need to necessarily define a deformation gradient field or a hyperelastic stored energy function. Equation (61) contains only force terms on the right-hand side; no explicit dependence on velocity is present, unlike the Cauchy stress expression. Finally, the P-K expression also differs from the Cauchy expression in that it gives a zero value for the somewhat degenerate case of a non-interacting gas regardless of temperature.

Referential Heat Flux

The expression for heat flux at a material point is:

$$\mathbf{Q}(\mathbf{X},t) = -\sum_{\alpha=1}^{N}\sum_{\beta\neq\alpha}^{N}\left(\frac{\partial\phi^{\beta}}{\partial x^{\alpha\beta}}\frac{\mathbf{x}^{\alpha\beta}}{x^{\alpha\beta}}\cdot\hat{\mathbf{v}}^{\alpha}\right)\mathbf{X}^{\alpha\beta}B^{\alpha\beta}(\mathbf{X}). \tag{62}$$

We note that like the expression for stress this expression contains only a potential term and not a kinetic term, unlike the spatial frame heat flux expression. Nevertheless, thermal motion does enter this expression through the derivatives of the potential energy, the inter-atomic positions $\mathbf{x}^{\alpha\beta}$, and the relative velocities $\hat{\mathbf{v}}^{\alpha}$.

Referential Temperature

Similar to what Hardy and colleagues did for their spatial formulation, we define a temperature field using our densities expressed in the reference configuration,

$$\mathrm{T}(\mathbf{X},t) = \frac{1}{3k_B}\frac{\sum_{\alpha=1}^{N} m^{\alpha}\left(\hat{v}^{\alpha}\right)^2\psi(\mathbf{X}^{\alpha}-\mathbf{X})}{\sum_{\alpha=1}^{N}\psi(\mathbf{X}^{\alpha}-\mathbf{X})}. \tag{63}$$

This definition is consistent with the allocation of $\frac{1}{2}k_BT$ of kinetic energy per degree of freedom for an atomic system. For solids, this allocation is somewhat inexact due to constraints, e.g. periodic boundary conditions, that may be acting on the system, but this difference is minimal for systems where the number of atoms is much larger than the number of constraints.

7.3 Evaluation and Comparison of Spatial and Material Frame Expressions

In this section, we examine the behavior of our P-K stress expression for several molecular dynamics simulations. These simulations will confirm that our expression for P-K stress is consistent with both the virial stress and the Cauchy stress expression defined by Hardy.[3] All of our simulations involve system of copper modeled using the EAM potential by Foiles *et al.* [122]. This potential creates an equilibrium, face-centered-cubic crystal of Cu of lattice parameter equal to 3.615 Å at zero temperature. For molecular dynamics simulations, a timestep of 0.001 ps is used. Calculations are done using specialized routines written for ParaDyn [123] and the Large-scale Atomic/Molecular Massively Parallel Simulator (LAMMPS) [1], molecular simulation codes developed at Sandia National Laboratories. For the analyses presented in this section, the choice of the zero temperature, undeformed system is used as our material configuration.

7.3.1 Stress for a constrained finite temperature system

In this and the following example, we present simulations of a system containing 4,000 atoms, where periodic boundary conditions are enforced on all sides of the simulation box. Two sets of calculations are performed: one using a single point in the center of system with a spherical localization volume of radius 15 Å and a quartic polynomial localization function, and another using a step function where both ψ and $B^{\alpha\beta}$ equal the quantity V_0^{-1} (where V_0 is the system size at zero temperature and deformation).

We first examine the situation where our system is constrained to remain at the reference volume, but heated to a finite, non-zero temperature. In this instance $\mathbf{F} = \mathbf{1}$ and $J = 1$; hence, the values of 1st P-K and Cauchy stress should coincide. Figure 68 shows the variation of instantaneous pressure with time for a system that is heated to 100 K. 'Pressure' in this case refers to the negative of the hydrostatic stress for each stress measure, *i.e.* the P-K pressure equals $-\frac{1}{3}\text{Trace}(\mathbf{P}) = -\frac{1}{3}P_{kk}$, the Cauchy pressure equals $-\frac{1}{3}\text{Trace}(\boldsymbol{\sigma})$ and the same relation is used for the system virial. The distributions of P-K and Cauchy nearly perfectly overlap with one another, and both distributions are centered around the virial distribution. Also, since the volume of material used for evaluation is a subset of the whole system, the variations from the mean value are larger in magnitude for both P-K and Cauchy pressures as compared with the variation observed in the virial.

The agreement between our stress measures and the virial is easier to see by using the data in Figure 68 to calculate cumulative time averaged pressures. Figure 69 shows the variation of these time averaged pressures with time for the same duration, 10^6 timesteps. This figure shows that the time averaged pressures essentially converge within 500,000 timesteps (0.5 ns), and that the converged values of P-K, Cauchy and virial pressures are very close to one another. This agreement is more clearly shown in Table VI, which compares the converged values of P-K pressure (after 10^6 timesteps) with the virial pressure for both the point-based analysis shown in Figure 69 and the step-based analysis. We note in Table VI that the percent difference between P-K and virial pressures is much less than 1%, and that this difference is smaller for the step-based analysis (which uses all atoms in the system) than for the point-based analysis.

Table VI also shows the converged time averaged pressures for systems heated to 300 K and 675 K, values approximately 22% and 50%, respectively, of the melting temperature of copper. It can be seen that the agreement between P-K pressure and the virial remains excellent even at these high temperatures and stress levels. This close agreement is emphasized in Figure 70, which graphically shows the variation of

[3] In this section, all calculations of Cauchy stress ($\boldsymbol{\sigma}$) are determined using equation (51), where the fixed spatial point $\mathbf{x}$ coincides with the material point $\mathbf{X}$ used to calculate $\mathbf{P}$ via equation (61).

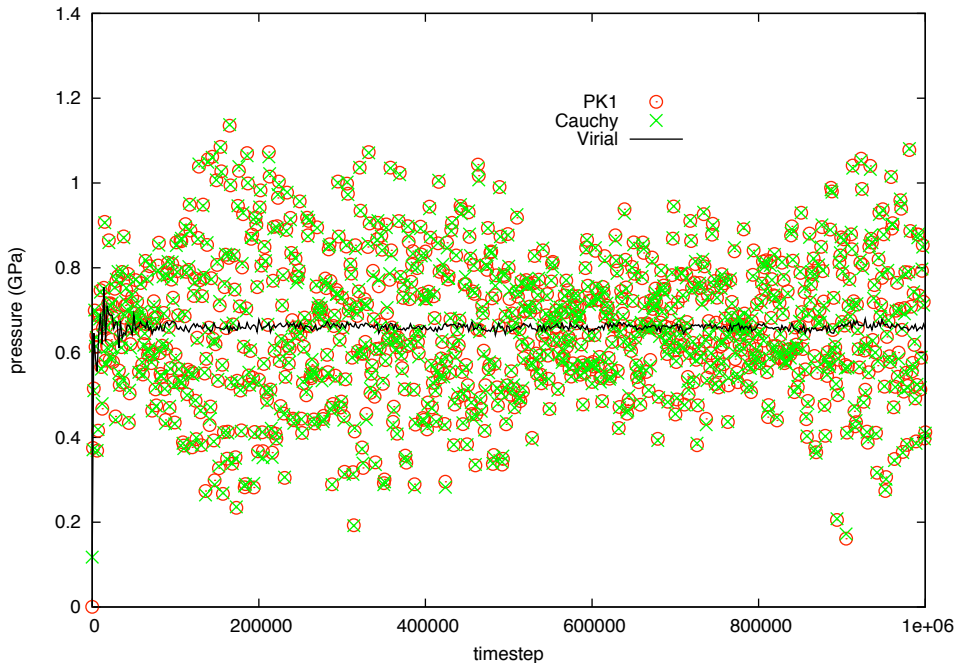

Figure 68: Variation of instantaneous pressure with time for a constrained system at 100 K.

Table VI: Time averaged pressures after 10^6 timesteps for constrained volume simulations.

Temperature (K)	Point / Step	virial pressure (GPa)	P-K pressure (GPa)	% difference
100	Point	0.6613775	0.6618136	0.06653
100	Step	0.6614168	0.6613937	-0.00350
300	Point	1.944335	1.944422	0.00448
300	Step	1.944465	1.944413	-0.00264
675	Point	4.335872	4.334868	-0.02316
675	Step	4.335840	4.336577	0.01699

pressure with increasing temperature for this constrained system. It was also observed that, at the highest temperature simulated of 675 K, agreement between the P-K pressure and the virial improved if a longer time average is taken.

7.3.2 Finite temperature deformation

For the situation of a constrained volume, the values of P-K and Cauchy stress were not anticipated to differ by any significant amount. However, we have yet to consider a case for which deformation occurs and the two values should be related by the Piola transform $\boldsymbol{\sigma} = \frac{1}{J}\mathbf{P} \cdot \mathbf{F}^T$. We now examine the scenario where our system starts out at zero temperature, is heated over the course of 10^6 timesteps (1 ns) to a finite temperature but allowed to expand in order to maintain a condition of zero pressure, is equilibrated for an additional 10^6 timesteps at that non-zero temperature and zero pressure, and is then triaxially stretched an additional 1% or 5% from this expanded state.

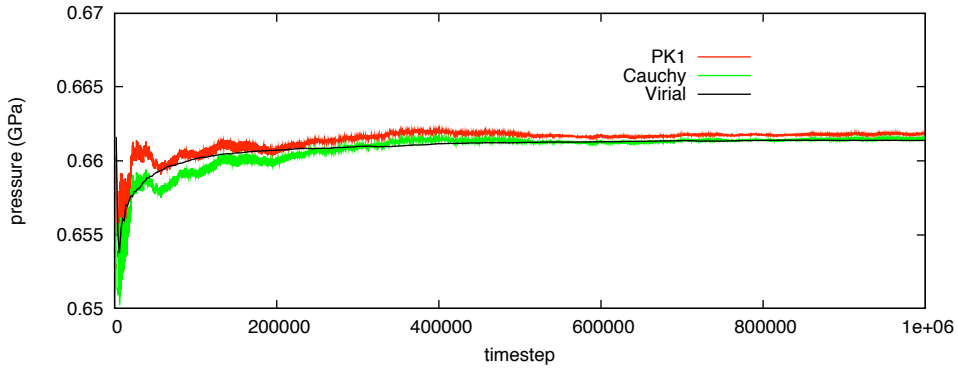

Figure 69: Variation of time averaged pressure with time for a constrained system at 100 K.

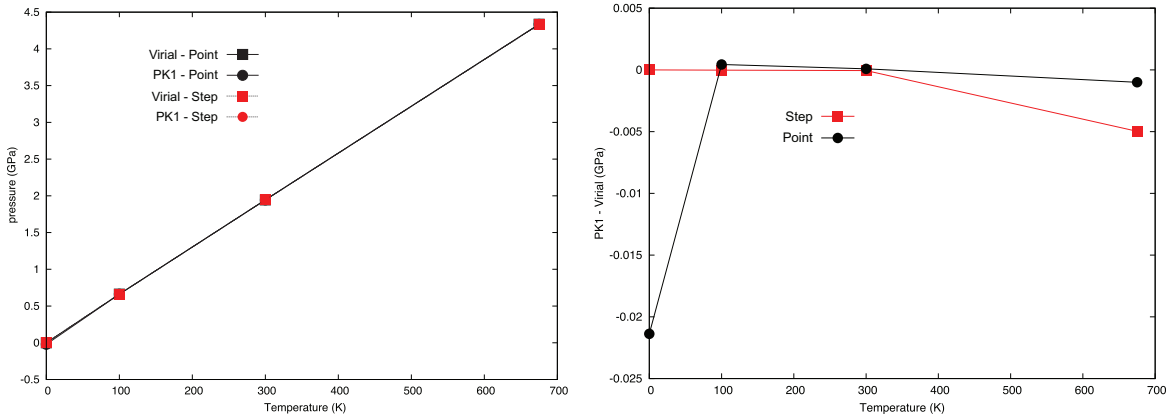

(a) (b)

Figure 70: (a) Time averaged pressures after 10^6 timesteps for constrained volume simulations performed at various temperatures. (b) Differences between P-K and virial measures of pressure at various temperatures.

Figure 71 compares the transformed stress $\frac{1}{J}\mathbf{P} \cdot \mathbf{F}^T$ to the Cauchy stress and virial for a stretch of 1% after equilibration at 100 K, and demonstrates that the transformed P-K stress is in close correspondence with the Cauchy measure. In this figure, we see that the distributions of transformed Piola-Kirchhoff stress and Cauchy stress nearly perfectly overlap with one another, and both distributions are centered around the virial distribution. We note that close agreement also exists for stress evaluations at specific instants in time, as shown in Figure 71.

Figure 72 shows the cumulative time averages of the four stress values ($\mathbf{P}$, σ, virial and transformed $\mathbf{P}$). It is observed that the system virial approaches its long time average in a short amount of time, $\sim$ 20,000 timesteps (0.02 ns), and that both the Cauchy stress and transformed P-K stress approach this same value within approximately 200,000 timesteps (0.2 ns). The P-K stress also approaches its own long time average within this same amount of time, and the value is appropriately higher. Values of these long time averages are listed in Table VII. These results clearly show a negligible difference between the transformed P-K stress value and the virial of the system. Thus, we again conclude that our derived expression is consistent with the continuum relation between Cauchy and P-K stress despite the absence of a kinetic term.

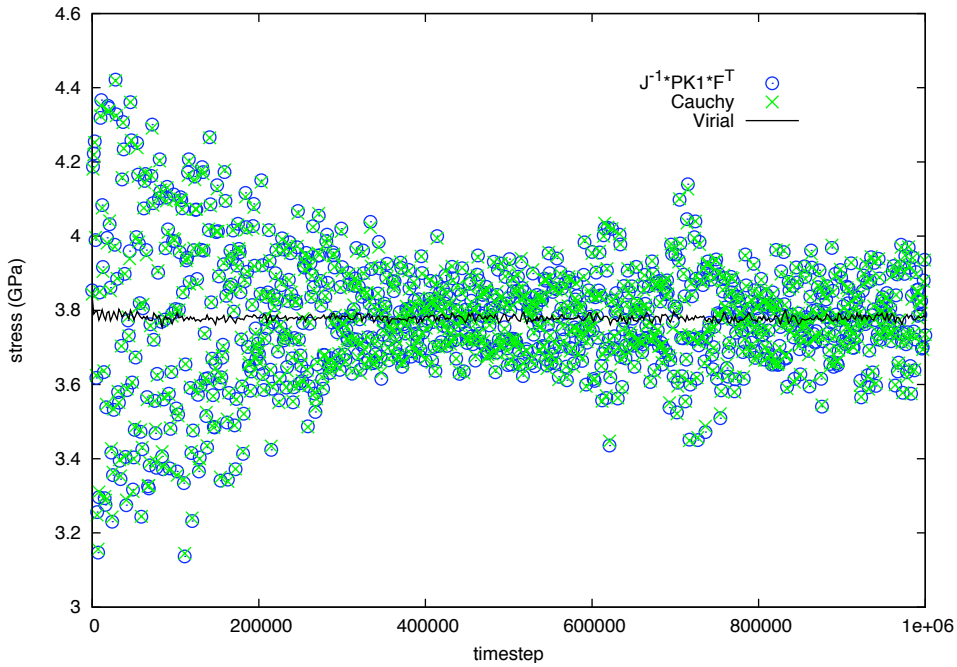

Figure 71: Variation of the instantaneous hydrostatic stresses for $\frac{1}{J}\mathbf{P}\cdot\mathbf{F}^T$, $\boldsymbol{\sigma}$ and the system virial for a stretch of 1% after equilibration at 100 K and zero pressure.

Table VII: Time averaged stresses after 10^6 timesteps for simulations of a heated and triaxially strained system. Here,'% difference' refers to the difference between transformed P-K stress (the 6th column) and the virial.

T (K)	Point / Step	total strain	virial (GPa)	P-K (GPa)	$\frac{1}{J}$(P-K)$\mathbf{F}^T$	% difference
0	Point	0.01	3.876275	3.954033	3.876123	-0.00394
0	Step	0.01	3.876273	3.954190	3.876277	-0.00009
0	Point	0.05	14.70036	16.20713	14.70035	-0.00009
0	Step	0.05	14.70036	16.20710	14.70032	-0.00026
100	Point	0.01168	3.779846	3.868452	3.779658	-0.00499
100	Step	0.01163	3.782552	3.871040	3.782538	-0.00038
100	Point	0.05169	14.26000	15.77334	14.26085	0.00597
300	Point	0.01495	3.581698	3.690054	3.582124	0.01190
300	Step	0.01495	3.579387	3.687273	3.579472	0.002386
300	Point	0.05515	13.30167	14.80901	13.30142	-0.00186
675	Point	0.02174	3.194773	3.334715	3.194304	-0.01469
675	Step	0.02174	3.194821	3.303813	3.164701	-0.94278
675	Point	0.06221	11.33258	12.78735	11.33345	0.00768

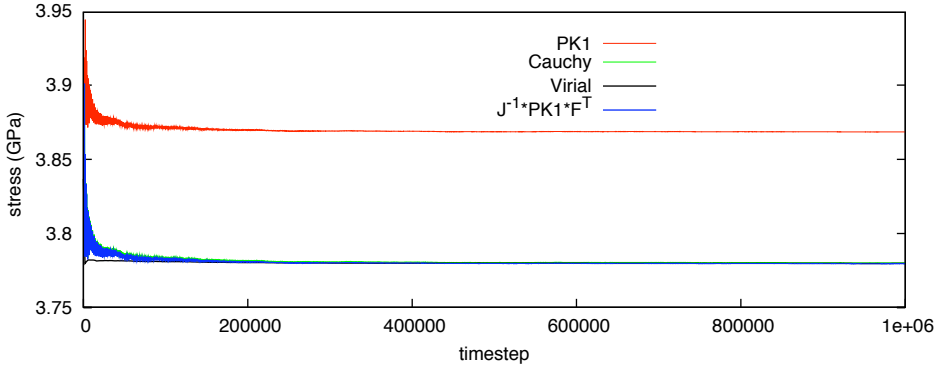

(a)

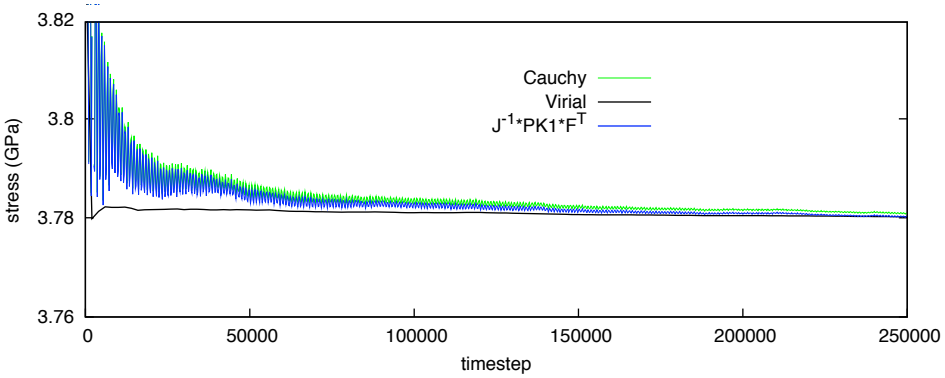

(b)

Figure 72: (a) Variation of time averaged hydrostatic stress measures with time for a stretch of 1% after equilibration at 100 K and zero pressure. (b) Close-up of (a) for the first 250,000 timesteps.

In addition to our simulation results for the case of 1% stretch at 100 K, Table VII also shows results for systems heated to 300 K and 675 K for stretches of both 1% and 5% following thermal equilibration at zero pressure. We observe that in all cases, the difference between the hydrostatic virial stress and the hydrostatic transformed P-K stress is very small with a difference of, at most, 1%. The results in Figures 73(a) and (b) show near perfect agreement of the virial and the transformed P-K stress across a range of temperatures.[4]

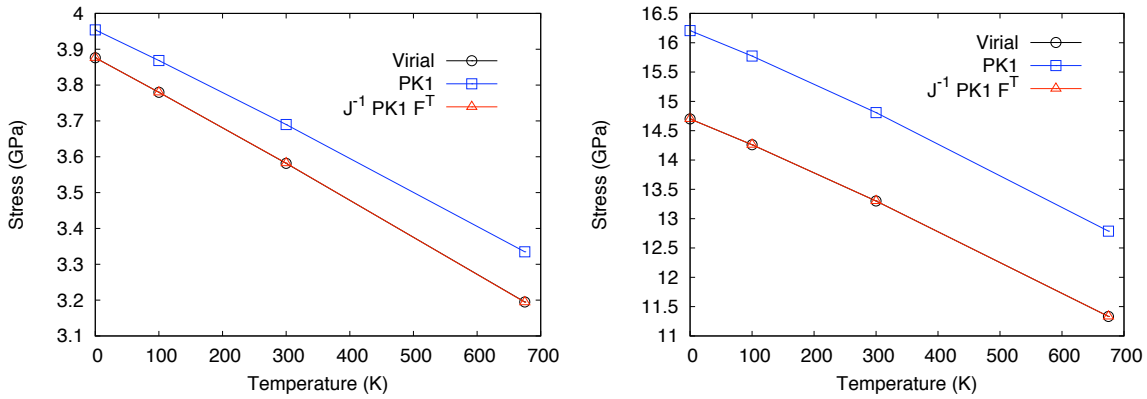

Figure 73: Variation of time-averaged hydrostatic stress measures after 10^6 timesteps with temperature for a stretch of (a) 1%, and (b) 5 % after equilibration at that temperature.

7.3.3 Tensile stretching of a center-cracked body

The previous two examples show that our formulation enables the calculation of 1st Piola-Kirchhoff stress that is consistent with estimates of the Cauchy stress, either using the system virial or the original Hardy formulation. However, these examples only produce a single value of stress representative of the entire system, *i.e.* systems subjected to a homogeneous deformation state. The strength of our formulation lies in its ability to produce a field of spatially varying values of stress for cases where an inhomogeneous deformation is produced.

In this example, we examine a system containing a center crack and compare the inhomogeneous stress fields that arise due to tensile stretching. Our system consists 9,840 atoms, approximately 20 x 20 x 6 unit cells, that contains a center crack 4 unit cells wide in the center. We acknowledge that this is a small and highly constrained system, and use it only as a means to show our ability to estimate spatially varying stress fields. The crack is created by excluding interactions between atoms above the center-plane of the system (and within the 4 unit cell width) and atoms below the center-plane. Periodic boundary conditions are used in the horizontal and thickness directions, while atoms within 2 unit cells of the system's upper and lower boundaries are controlled by prescribing a fixed velocity of ± 0.1 Å/ps, respectively. Given the dimensions of our system, this produces an approximate strain rate of initial value 3.46 x 10^{-3} ps^{-1} = 3.46 x 10^9 sec^{-1}. Before inducing the stretching, our system is relaxed using a conjugate gradient minimization algorithm in order to relax the upper, lower and crack boundaries and set the reference configuration.

To calculate stress at material points, we use localization volumes consisting of rectangular parallelepipeds,

[4]These figures reveal that at higher temperatures a lower amount of stress is produced within the system. This result can be attributed to the temperature dependence of the elastic constants that softens (decreases) their value with increasing temperature.

and localization functions that are multiples of three linear shape functions, one for each orthogonal direction, as in the finite element method. For this system, our mesh consists of 10 x 15 x 1 = 150 elements where our mesh extends beyond the atomic system in the vertical direction by 2.5 unit cells at both the upper and lower boundaries.

Figure 74 shows the displaced atoms, colored by the values of the component u_y of their displacement vector, as well as u_y displacement field evaluated at nodes and interpolated through elements, for the center-cracked body vertically stretched by approximately 6.9%. The left portion of Figure 74 clearly shows that

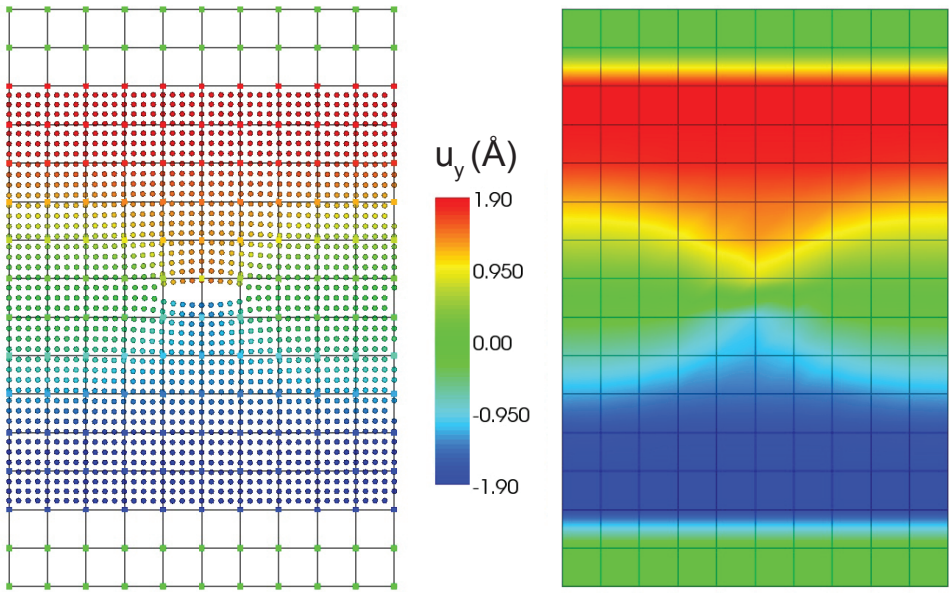

Figure 74: Displacement field u_y for a center-cracked body vertically stretched 6.9%. Left: Atoms pictured with overlaying mesh and nodes. Right: Mesh elements showing contours of continuum displacement field; mesh is shown with gray lines to identify elements.

the nodal values of displacement agree with the values of nearby atoms, while the right portion displays a displacement field consistent with expectations from fracture mechanics. It is interesting to note that the normalization present in equation (60) enables approximately correct values of u_y to be calculated at nodes bordering the boundaries of the atomic system, even though 1/2 of each node's localization volume is empty. This is because the normalization produces a displacement value corresponding to the center of mass of the localization volume and assigns that value to the node. And, since each element only contains a small number of atoms, the difference between the nodal position and the center of mass position is relatively small. Obviously, special care should be taken to use small elements near the boundary of an enclosed atomistic system, or near any region for which mass is unevenly distributed within the localization volume in the reference configuration. Nodes with localization volumes that are completely empty of atoms are assigned a zero value.

Figure 75 shows the fields of P_{yy} and σ_{yy} for the same stretch state of 6.9%. These fields are consistent with expectations from fracture mechanics, possessing features such as zero stress in the crack opening region and concentrations of tensile stress near the crack tips. Consistency between our formulation and Hardy's is shown by the qualitative similarity of the fields, with values of σ_{yy} having, in general, a slightly higher magnitude than the corresponding value of P_{yy}. Quantitative consistency can be evaluated by com-

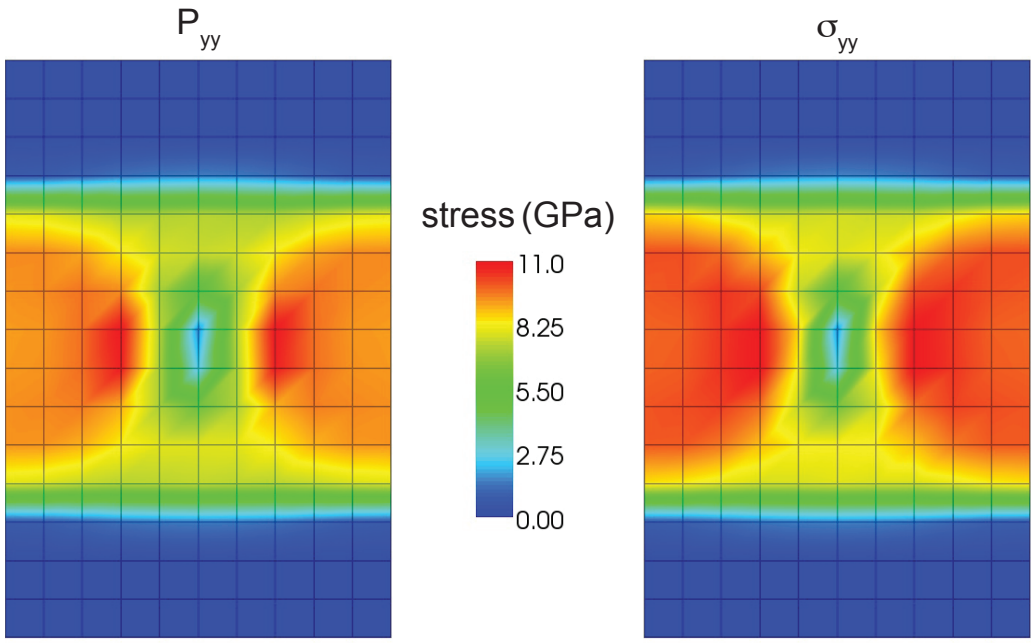

Figure 75: Stress fields for a center-cracked body vertically stretched 6.9%. Left: Mesh elements showing contours of continuum field P_{yy}. Right: Mesh elements showing contours of continuum field σ_{yy} as determined from the original Hardy formulation. In both pictures, the mesh is shown with gray lines to identify elements.

paring the values at a specific material point. We choose a node near the crack tip, at a position of {21.69 Å, 10.845 Å, 10.845 Å} (6 elements down from the top of the system, and 2 elements from the right edge). At this node, the value of P_{yy} equals 9.40327 GPa, and the value of σ_{yy} is 10.0719 GPa. Using our method to estimate displacement gradient $\nabla_{\mathbf{X}}\mathbf{u}$, and by using the relation $\mathbf{F} = \mathbf{1} + \nabla_{\mathbf{X}}\mathbf{u}$, the value of transformed P-K stress is calculated to be 9.48638 GPa. This value is somewhat lower than the expected value from the Hardy expression (a difference of about -5.81%). However, our earlier simulation examples indicate that this agreement may improve if the system is fixed at a given (inhomogeneous) deformation state and stress values are time averaged for periods $\sim$ 1 ns. It may also be the case that displacement gradient values are actually higher in magnitude than estimated here due to the small size of the system and the use of (relatively) large localization volumes near the crack tip, *i.e.* the estimated displacement gradient also has errors associated with it.

The analyses presented above clearly show that our derived expression for P-K stress is a full thermomechanical measure of stress despite the fact that it contains only a potential and not a kinetic term, unlike the Cauchy stress expression derived by Hardy. Our analysis also shows that our expression for $\mathbf{P}$ is consistent with Cauchy stress via the Piola transformation $\boldsymbol{\sigma} = \frac{1}{J}\mathbf{P} \cdot \mathbf{F}^T$.

7.4 Cauchy-Born Stress and Free Energy Calculation

An alternative method for estimating continuum variables such as energy density and stress is by use of the Cauchy-Born rule. Unlike the Hardy formulation, or simpler variants such as use of an atomic-level virial stress [89, 90], this approach involves using local metrics of deformation gradient and temperature with a

virtual atomic crystal at each point of interest and the governing interatomic potentials to define thermodynamic variables. While this method contains an underlying assumption of homogeneous deformation of the virtual crystal, its construction is useful as it provides a means for isolating the elastic portion of the deformation gradient. Here, we use the Cauchy-Born rule with the Quasi-harmonic approximation to define continuum variables for atomic systems at finite temperature governed by either pair or EAM potentials.

7.4.1 Quasi-harmonic Cauchy-Born model

The basic thermodynamic quantities can be related to the partition function Z [124, Chapter 7] of the lattice of atoms comprising the body occupying the region Ω. The free energy density

$$\Psi = U - TS = -\frac{k_B T}{V} \log Z \tag{64}$$

is a Legendre transform of the internal energy density

$$U = -\frac{1}{V}\frac{\partial}{\partial \bar{\beta}} \log Z \tag{65}$$

via the entropy density

$$S = \frac{k_B}{V}\left(\log Z - \bar{\beta}\frac{\partial}{\partial \bar{\beta}} \log Z\right) \tag{66}$$

where $\bar{\beta} = (k_B T)^{-1}$, k_B is Boltzmann's constant and V is a reference volume for the system. Note that we are using densities as opposed to the extensive versions that are more traditional in the literature, see, e.g. [125]. We define a tributary volume for an atom as $V_\alpha = V/N$ where N is the number of atoms in the system volume V.

The classical harmonic partition function [126, Section 4.5] for a quasi-harmonic (QH) system is based on the harmonic approximation of the Hamiltonian H

$$H \approx H_{QH} = \Phi_0(\mathbf{F}) + \frac{1}{2}\sum_{i=1}^{n}\left(\omega_i^2 m_i q_i^2 + \frac{1}{m_i}p_i^2\right) \tag{67}$$

with the atomic positions $\mathbf{x}_\alpha$ in the current configuration following the decomposition $\mathbf{x}_\alpha = \mathbf{F}\mathbf{X}_\alpha + \mathbf{q}_\alpha$, and the momenta $\mathbf{p}_\alpha$ begin given their usual definition. Here, and throughout this section, we will use a Greek subscript to refer to an enumeration of atomic quantities, e.g. $\mathbf{x}_\alpha$, and a Latin one for enumeration based on degrees of freedom, e.q. q_i, where i runs 1 to $n \approx 3N$. The resulting partition function Z is

$$\begin{aligned} Z_{QH} = Z_{QH}(\mathbf{F}, T) &= h^{-n}\int_\Gamma \exp\left(-\bar{\beta}H(\mathbf{q},\mathbf{p};\mathbf{F})\right)\, d\mathbf{q}\, d\mathbf{p} = h^{-n} Z_{\mathbf{q}} Z_{\mathbf{p}} \\ &= \exp(-\bar{\beta}\Phi_0) h^{-n}\prod_{i=1}^{n}\int_{-\infty}^{\infty}\exp\left(-\frac{1}{2}\bar{\beta}\frac{1}{m_i}p_i^2\right)\, dp_i \int_{-\infty}^{\infty}\exp\left(-\frac{1}{2}\omega_i^2\bar{\beta}m_i q_i^2\right)\, dq_i \\ &= \exp(-\bar{\beta}\Phi_0) h^{-n}\prod_{i=1}^{n}\frac{2\pi}{\bar{\beta}\omega_i} = \exp(-\bar{\beta}\Phi_0)\prod_{i=1}^{n}\frac{k_B T}{\hbar\omega_i} \end{aligned} \tag{68}$$

We have non-dimensionalized Z by a factor of Planck's constant h (raised to the power $-n$) to connect with the quantum partition function, see *e.g.* [124, Chapter 7], in the the classical high temperature limit

($\hbar\omega_i \ll k_B T$)[5] . Hence, the Helmholtz free energy density, Ψ, of a crystalline solid is determined from the potential energy density, Φ_0, of the atoms in their average positions $\mathbf{F}\mathbf{X}_\alpha$ and the vibrational spectrum of frequencies, ω_i, [127, Section 16] as

$$\Psi_{QH} = \Phi_0 + \frac{k_B T}{V} \log \prod_{i=1}^{n} \frac{\hbar\omega_i}{k_B T} \tag{69}$$

The term in Eq. (69) depending on the vibrational modes of the lattice can be connected to eigenvalues of the dynamical matrix. The dynamical matrix, $\mathbb{D}_{\alpha\beta} = \mathbb{D}_{\alpha\beta}(\mathbf{F})$, is simply

$$\mathbb{D}_{\alpha\beta} \equiv \frac{V}{\sqrt{m_\alpha m_\beta}} \frac{\partial^2 \Phi}{\partial \mathbf{q}_\alpha \partial \mathbf{q}_\beta}, \tag{70}$$

where $V\Phi$ is the total potential energy of the crystal, and $\mathbf{q}_\alpha = \mathbf{x}_\alpha - \mathbf{F}\mathbf{X}_\alpha$ is the displacement of atom α from the (homogeneously) deformed state $\mathbf{F}\mathbf{X}_\alpha$. It is important to realize that Φ is distinct from Φ_0 as the former represents the true potential energy density while the latter is an approximation based on the assumption of homogeneous deformation.

Clearly, the vibrational frequencies ω_i are the eigenvalues of the dynamical matrix, and their product is related to the determinant of the dynamical matrix by

$$\prod_{i=1}^{n} \omega_i = \sqrt{\det \mathbb{D}} \tag{71}$$

where $\mathbb{D}$ is the system dynamical matrix assembled from the constituent $\mathbb{D}_{\alpha\beta}$ matrices. If the deformation gradient is uniform and the crystal is free of defects, infinite, and composed of a single element (so that $m_\alpha = m$), then each $\mathbb{D}_{\alpha\beta}$ is identical and, by translational invariance, the row of the dynamical matrix associated with any atom is identical (given an appropriate rotation of the indices). In this case, we can restrict our attention to interactions between a representative atom, denoted as $\beta = 0$, and all other atoms in the lattice

$$\mathbb{D}_\alpha \equiv \frac{V}{m} \frac{\partial^2 \Phi}{\partial \mathbf{q}_0 \partial \mathbf{q}_\alpha} \tag{72}$$

The local harmonic (LH) approximation [128] neglects the coupling between interacting atoms. For a homogeneous system, the LH simplification reduces the QH dynamical matrix to a single 3×3 matrix by dropping all the elements of the dynamical matrix except for $\alpha = \beta = 0$.

$$\mathbb{D}_{LH} \equiv \mathbb{D}_0 = m^{-1} \frac{\partial^2 \Phi}{\partial \mathbf{q}_0 \partial \mathbf{q}_0} \tag{73}$$

The free energy density is:

$$\Psi_{LH} = \Phi_0 + \Theta_{LH} \tag{74}$$

where

$$\Theta_{LH} = \frac{k_B T}{V_\alpha} \log \left(\left(\frac{\hbar}{k_B T} \right)^3 \sqrt{\det \mathbb{D}_{LH}} \right) . \tag{75}$$

[5]Note $\int_{-\infty}^{\infty} \exp(-\frac{1}{2}\bar{\beta}x^2)\, dx = \sqrt{\frac{2\pi}{\bar{\beta}}}$. Also, it is necessary for the potential energy $\Phi_0 = \Phi(\mathbf{F})$ to be independent of q_i, and for the system to be in equilibrium $\frac{\partial \Phi}{\partial \mathbf{x}_\alpha} = \mathbf{0}$ to obtain this form.

The internal energy density in this approximation is

$$U = \Phi_0 + \frac{n}{V} k_B T = \Phi_0 + c_v T \tag{76}$$

via (65), where nk_BT is the equilibrium total energy above the ground state $\Phi_0(\mathbf{F})$ and c_v is the heat capacity per volume at constant volume. For a classical system, the law of Dulong and Petit [129, Chapter 21] identifies the heat capacity c_v with

$$c_v = \frac{nk_B}{V} = \frac{3k_B}{V_\alpha} \tag{77}$$

Using the expression for free energy density in equation (74), we can derive the expression for the 1st Piola-Kirchhoff stress,

$$\mathbf{P} = \frac{\partial \Psi_{LH}}{\partial \mathbf{F}} = \frac{\partial \Phi_0}{\partial \mathbf{F}} + \frac{\partial \Theta_{LH}}{\partial \mathbf{F}}. \tag{78}$$

Substitution of equation (75) into this expression yields:

$$\mathbf{P} = \frac{\partial \Phi_0}{\partial \mathbf{F}} + \frac{k_B T}{V_\alpha} \left\{ 3 \log \left(\frac{\hbar}{k_B T} \right) + \frac{1}{2} \left(\det \mathbb{D}_{LH} \right)^{-1} \frac{\partial \det \mathbb{D}_{LH}}{\partial \mathbf{F}} \right\} \tag{79}$$

Kimmer and Jones [130] showed that the term $\frac{\partial \det \mathbb{D}_{LH}}{\partial \mathbf{F}}$ can be expressed in terms of the derivative $\frac{\partial \mathbb{D}_{LH}}{\partial \mathbf{F}}$ and cofactors of the full matrix $\mathbb{D}_{LH}$. Details can be found in [130]. Taking the derivative of this expression with respect to $\mathbf{F}$, these authors were also able to define an expression for the tangent modulus in the material frame, $\mathbb{B} \equiv \frac{\partial \mathbf{P}}{\partial \mathbf{F}}$.

7.4.2 Quasi-harmonic model for pairwise potentials

In the case of pairwise potentials the potential energy density for the system is given by

$$\Phi = \frac{1}{2V} \sum_{\alpha}^{N} \sum_{\beta \neq \alpha}^{N} \phi(r_{\alpha\beta}), \tag{80}$$

where ϕ is the pairwise interaction which depends solely on the distance $r_{\alpha\beta}$ between two atoms and V is the volume of the undeformed crystal. The LH dynamical matrix for a monoatomic lattice is

$$\mathbb{D}_{LH} = \frac{V}{m} \frac{\partial^2 \Phi}{\partial \mathbf{u}_0^2} = \frac{1}{m} \sum_{\beta \neq 0} \left(\phi''(r_{\beta 0}) \frac{\mathbf{r}_{\beta 0}}{r_{\beta 0}} \otimes \frac{\mathbf{r}_{\beta 0}}{r_{\beta 0}} + \phi'(r_{\beta 0}) \frac{1}{r_{\beta 0}} \left[\mathbf{I} - \frac{\mathbf{r}_{\beta 0}}{r_{\beta 0}} \otimes \frac{\mathbf{r}_{\beta 0}}{r_{\beta 0}} \right] \right). \tag{81}$$

7.4.3 Quasi-harmonic model for EAM potentials

For embedded-atom method (EAM) potentials, the potential energy density for the system of a uniform material is given by

$$\Phi = \frac{1}{V} \sum_{\alpha=1}^{N} \left\{ F(\rho_\alpha) + \frac{1}{2} \sum_{\beta=1, \beta \neq \alpha}^{N} \phi(r_{\alpha\beta}) \right\}, \tag{82}$$

where V is the volume of the system, ϕ is the pairwise interaction between atoms of α and β that depends on their separation distance $r_{\alpha\beta}$, F is the embedding that depends on the electron density, ρ_α, at an atom's location that is calculated from a pairwise contribution of atomic charge densities from nearby atomic neighbors, *i.e.*

$$\rho_\alpha = \sum_{\beta=1,\beta\neq\alpha}^{N} f(r_{\alpha\beta}). \tag{83}$$

The expression for the dynamical matrix $\mathbb{D}$ for the local harmonic (LH) approximation of free energy for our atomic system is

$$\begin{aligned}\mathbb{D} = \frac{1}{m}\Bigg[F''(\rho_0)\mathbf{l}_0\otimes\mathbf{l}_0 + \sum_{\beta=1,\beta\neq 0}\Bigg\{\Big[F'(\rho_0)f''(r_{0\beta}) + F''(\rho_\beta)\left(f'(r_{0\beta})\right)^2 \\ +F'(\rho_\beta)f''(r_{0\beta}) + \phi''(r_{0\beta})\Big]\frac{\mathbf{r}_{0\beta}\otimes\mathbf{r}_{0\beta}}{r_{0\beta}^2} \\ + \left[F'(\rho_0)f'(r_{0\beta}) + F'(\rho_\beta)f'(r_{0\beta}) + \phi'(r_{0\beta})\right]\frac{r_{0\beta}^2\mathbf{I} - \mathbf{r}_{0\beta}\otimes\mathbf{r}_{0\beta}}{r_{0\beta}^3}\Bigg\}\Bigg],\end{aligned} \tag{84}$$

where $\mathbf{l}_0 = \sum_{\beta=1,\beta\neq 0} f'(r_{0\beta})\frac{\mathbf{r}_{0\beta}}{r_{0\beta}}$. This can be further simplified by noting that for a homogeneous deformation, $F'(\rho_0) = F'(\rho_\beta) = F_0'$ and $F''(\rho_0) = F''(\rho_\beta) = F_0''$. Hence,

$$\begin{aligned}\mathbb{D} = \frac{1}{m}\Bigg[F_0''\mathbf{l}_0\otimes\mathbf{l}_0 + \sum_{\beta=1,\beta\neq 0}\Bigg\{\frac{1}{r_{0\beta}}\left[2F_0'f'(r_{0\beta}) + \phi'(r_{0\beta})\right]\mathbf{I} \\ + \left[F_0''\left(f'(r_{0\beta})\right)^2 + 2F_0'f''(r_{0\beta}) + \phi''(r_{0\beta}) - \frac{1}{r_{0\beta}}\left(2F_0'f'(r_{0\beta}) + \phi'(r_{0\beta})\right)\right]\frac{\mathbf{r}_{0\beta}\otimes\mathbf{r}_{0\beta}}{r_{0\beta}^2}\Bigg\}\Bigg]\end{aligned} \tag{85}$$

To calculate the temperature-dependent (entropic) terms of the stress tensor, it is necessary to calculate the derivative of the dynamical matrix with respect to the deformation gradient that exists in the neighborhood of atom "0", $\mathbf{F}$. Starting with equation (84), calculating the necessarily derivatives with respect to $\mathbf{F}$, and again simplifying for the case of homogeneous deformation, we obtain:

$$\begin{aligned}\frac{\partial\mathbb{D}}{\partial\mathbf{F}} =& \frac{1}{m}\left[F_0'''\mathbf{l}_0\otimes\mathbf{l}_0\otimes\mathbf{L}_0 + F_0''\left((\mathbf{l}_0\otimes\mathbb{M}_0)^t + \mathbf{l}_0\otimes\mathbb{M}_0\right)\right. \\ &+ \sum_{\beta=1,\beta\neq 0}\Bigg\{a_{0\beta}\left(\mathbf{I}\otimes\mathbf{r}_{0\beta}\otimes\mathbf{R}_{0\beta}\right) + \left(a_{0\beta} + \frac{1}{r_{0\beta}^2}F_0''\left(f'(r_{0\beta})\right)^2\right)\left(\mathbf{I}\odot\mathbf{r}_{0\beta}\otimes\mathbf{R}_{0\beta} + \mathbf{r}_{0\beta}\otimes\mathbf{I}\otimes\mathbf{R}_{0\beta}\right) \\ &\left.+\frac{1}{r_{0\beta}}2F_0''f'(r_{0\beta})\mathbf{I}\otimes\mathbf{L}_0 + b_{0\beta}\left(\mathbf{r}_{0\beta}\otimes\mathbf{r}_{0\beta}\otimes\mathbf{L}_0\right) + c_{0\beta}\left(\mathbf{r}_{0\beta}\otimes\mathbf{r}_{0\beta}\otimes\mathbf{r}_{0\beta}\otimes\mathbf{R}_{0\beta}\right)\Bigg\}\right]\end{aligned} \tag{86}$$

where

$$\mathbb{M}_0 = \frac{\partial\mathbf{l}_0}{\partial\mathbf{F}} = \sum_{\beta=1,\beta\neq 0}\left(\frac{1}{r_{0\beta}}f'(r_{0\beta})\mathbf{I} + \left(f''(r_{0\beta}) - \frac{1}{r_{0\beta}}f'(r_{0\beta})\right)\frac{\mathbf{r}_{0\beta}\otimes\mathbf{r}_{0\beta}}{r_{0\beta}^2}\right)\otimes\mathbf{R}_{0\beta} \tag{87}$$

$$a_{0\beta} \equiv \frac{1}{r_{0\beta}^2}\left(2F_0' s_{0\beta} + t_{0\beta}\right) \quad , \quad b_{0\beta} \equiv \frac{1}{r_{0\beta}^2}\left(F_0'''\left(f'(r_{0\beta})\right)^2 + 2F_0'' s_{0\beta}\right) \tag{88}$$

$$c_{0\beta} \equiv \frac{1}{r_{0\beta}^3}\left(2F_0'' f'(r_{0\beta}) s_{0\beta} + 2F_0' u_{0\beta} + v_{0\beta}\right) \tag{89}$$

$$s_{0\beta} \equiv f''(r_{0\beta}) - \frac{1}{r_{0\beta}} f'(r_{0\beta}) \quad , \quad t_{0\beta} \equiv \phi''(r_{0\beta}) - \frac{1}{r_{0\beta}}\phi'(r_{0\beta}) \tag{90}$$

$$u_{0\beta} \equiv f'''(r_{0\beta}) - \frac{3}{r_{0\beta}} f''(r_{0\beta}) + \frac{3}{r_{0\beta}^2} f'(r_{0\beta}) \quad , \quad v_{0\beta} \equiv \phi'''(r_{0\beta}) - \frac{3}{r_{0\beta}}\phi''(r_{0\beta}) + \frac{3}{r_{0\beta}^2}\phi'(r_{0\beta}). \tag{91}$$

The notation $(\mathbf{l}_0 \otimes \mathbb{M}_0)^t$ denotes a transpose only on the first two (spatial) indices of the fourth-order mixed tensor (*i.e.* if $\mathbb{A} = \mathbf{l}_0 \otimes \mathbb{M}_0$, then in index notation $A_{ijkL} = l_i M_{jkL}$ and $A^t_{ijkL} = A_{jikL} = l_j M_{ikL}$) and the notation $\mathbf{I} \odot \mathbf{r}$ denotes a dyad product between a second order tensor and a vector such that in index notation: $(\mathbf{I} \odot \mathbf{r})_{ijk} = \delta_{ik} r_j$. In index notation,

$$\begin{aligned}\frac{\partial D_{ij}}{\partial F_{kL}} =& \frac{1}{m}\Big[F_0'''\left(l_i l_j L_{kL}\right) + F_0''\left(l_j M_{ikL} + l_i M_{jkL}\right) \\ &+ \sum_{\beta=1,\beta\neq 0}\Bigg\{a_{0\beta}\left(\delta_{ij} r_k R_L\right) + \left(a_{0\beta} + \frac{1}{r^2}F_0''\left(f'(r)\right)^2\right)\left(\delta_{ik} r_j R_L + r_i \delta_{jk} R_L\right) \\ &+ \frac{1}{r} 2F_0'' f'(r)\left(\delta_{ij} L_{kL}\right) + b_{0\beta}\left(r_i r_j L_{kL}\right) + c_{0\beta}\left(r_i r_j r_k R_L\right)\Bigg\}\Big],\end{aligned} \tag{92}$$

where the subscripts "0β" and "0" have been omitted on some terms for clarity.

7.4.4 Examples of free energy and Cauchy-Born stress calculation

- Pair potential system — For this study we use a Lennard-Jones (LJ) model of Au with lattice constant $a = 4.08$ Å and parameter values $\epsilon = 0.72427860$ eV, $\sigma = 2.59814680$ Å, as representative of a well-behaved atomic solid. This inter-atomic potential is truncated at a separation of $r_c = 2.1\sigma = 5.45610827$ Å, and smoothed such that pair energy and forces are zero at this distance, see [131, equation (121)]. This parametrization leads to elastic constants , $C_{11} = 497.478$ GPa, $C_{12} = C_{44} = 281.58$ GPa [6] , and a surface energy of 0.1599 eV/Å^2. For reference, the experimentally measured Debye temperature for Au is $170\,K$ and its melt temperature is $1337\,K$. Since the LJ model over-estimates the elastic constants of Au ($C_{11} = 186$ GPa, $C_{12} = 157$ GPa, $C_{44} = 42$ GPa), the approximate effective Debye and melt temperatures are $280\,K$ and $5200\,K$, respectively [7] .

  To validate the use of a LH model of free energy, we compare Ψ_{LH} to estimates of Ψ from thermodynamic integration (TI – see the Appendix for this section) for four (one-parameter) deformations: (a) uniaxial stretch $\mathbf{F} = \lambda \mathbf{e}_1 \otimes \mathbf{E}_1$, (b) simple shear $\mathbf{F} = \lambda \mathbf{e}_1 \otimes \mathbf{E}_2$, (c) biaxial stretch / pure shear $\mathbf{F} = \lambda \mathbf{e}_1 \otimes \mathbf{E}_1 + 1/\lambda \mathbf{e}_2 \otimes \mathbf{E}_2$, and (d) volumetric dilation $\mathbf{F} = \lambda \mathbf{I}$, through $\{\mathbf{F}, T\}$ space, where $\mathbf{F} = \mathbf{I} + \mathbf{H}$. The Cartesian bases $\mathbf{e}_i$ and $\mathbf{E}_i$, in the current and reference configurations respectively, are aligned with the lattice basis in the reference configuration. To perform TI we fitted the $\mathbf{P}$ vs $\mathbf{F}$ and

[6] These elastic constants were determined analytically and verified empirically.

[7] The Debye temperature T_{Debye} is estimated using the fact that it is proportional to the speed of sound in the material so that $T_{Debye} \sim \sqrt{C_{11}}$. The melt temperature T_{melt} is proportional to the depth of the potential well and can be approximated by $k_B T_{melt} \approx 0.62\epsilon$ where k_B is the Boltzmann constant.

U vs T trends (for small values of λ and T) from NVT MD data using the Nosé-Hoover thermostat (NH) and integrated these fits to obtain Ψ_{TI}. It was also necessary to take a single temperature close to zero where we assumed $\Psi_{TI} \equiv \Psi_{LH}$ for all deformations. The correspondence of Ψ_{LH} and Ψ_{TI} at higher temperatures justifies the somewhat arbitrary choice of 1 K for this reference temperature.

First, we take a temperature excursion from $1K$ to $600K$ for: a uniaxial stretch (a) $F_{11} = 1.015$ and a volumetric dilation (d) $F_{11} = F_{22} = F_{33} = 1.045$. Figure 76 shows the excellent comparison of Ψ_{LH} and Ψ_{TI} for the uniaxial case and, likewise, Figure 77 shows similar results for the volumetric case. Both Figure 76a and Figure 77a exhibit similar slopes, 1.52163×10^{-5} and 1.52176×10^{-5} eV/(K-Å)^3, respectively corresponding to the heat capacity $c_v = 1.52256 \times 10^{-5}$ eV/(K-Å)^3 based on the reference V_α in (77). The intercepts, -0.23112 and -0.22945 eV/Å^3 respectively, depend on deformation as Eq. (76) indicates. The temperatures at which U crosses Ψ and is henceforth strictly greater than Ψ are 12.2 K and 14.1 K respectively as can be seen in the insets of Figures 76(b) and 77(b).

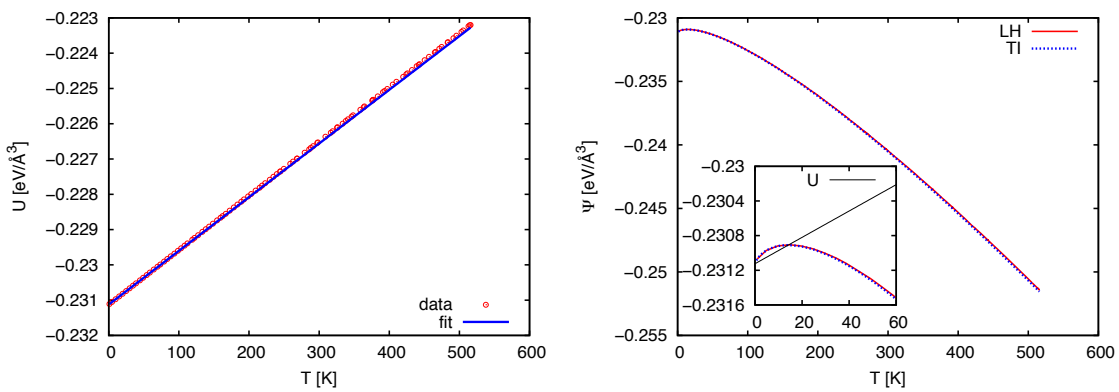

(a) (b)

Figure 76: (a) Internal, and (b) Free energy density variation with temperature for the LJ-gold system at a uniaxial stretch of 1.015 and T_{ref} = 1 K.

Second, we deform for simple shear (b) and biaxial stretch (c) at a sequence of constant temperatures $T = 30, 100, 300$ K. The reader should note that biaxial stretch effects a "pure" shear state with respect to a coordinate system rotated by $\pi/4$ about the $\mathbf{E}_3$ axis and that $F_{12} \equiv H_{12}$. These shear deformation modes are particularly rigorous tests of the LH model. Figure 78 shows reasonable correlation between the LH and TI estimates of free energy for simple shear (b) and Figure 79 shows similar results for biaxial stretch. It is apparent that the behavior of the LH estimate is less noisy for a temperature process than for a deformation process, perhaps due to the differencing of atomic positions required in the Hardy based estimate of $\mathbf{F}$. The discrepancies are clearly temperature dependent and are not noticeable at the lowest temperature. These tests demonstrate that there is thermodynamic consistency between the derivative of the free energy and the stress measure. As expected, the respective moduli are relatively insensitive to temperature. For our material, the modulus for simple shear is C_{12} = 281.58 GPa which is slightly higher than the modulus for pure shear $(C_{11} - C_{12})$ = 215.898 GPa.

The results displayed in this section are typical for temperatures below half melt and strains below

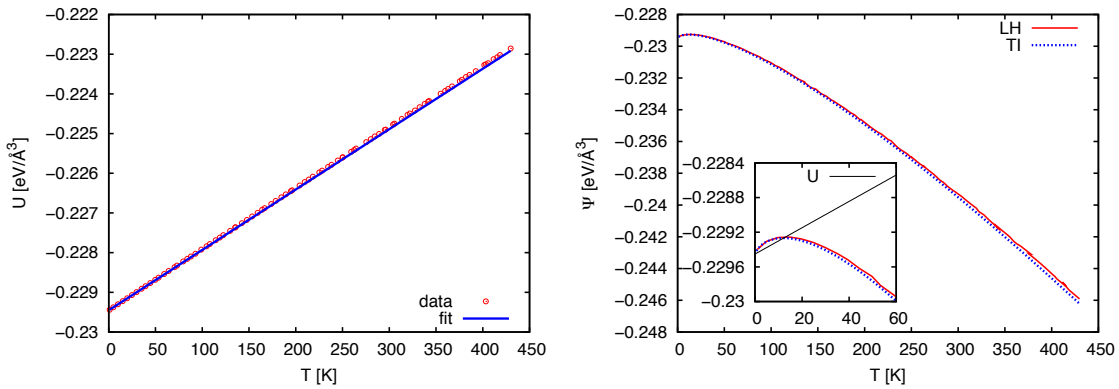

(a) (b)

Figure 77: (a) Internal, and (b) Free energy density variation with temperature for the LJ-gold system at a volumetric stretch of 1.045 and T_{ref} = 1 K.

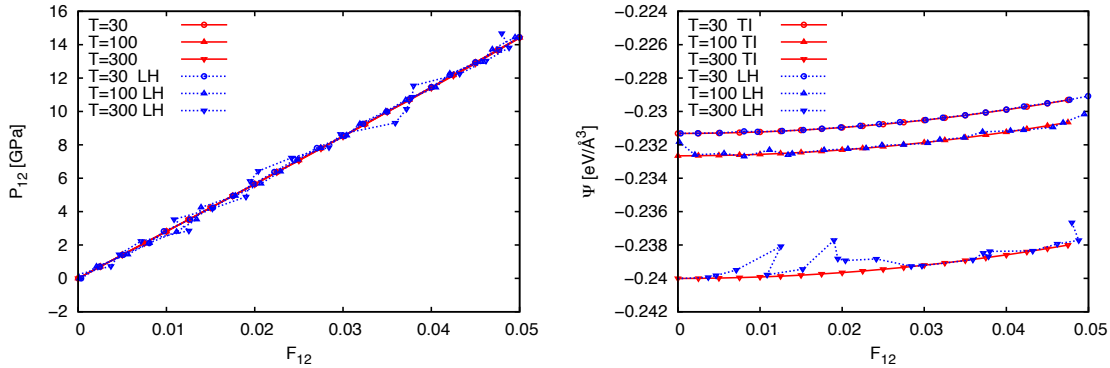

(a) (b)

Figure 78: Simple shear at $T = 30, 100, 300\,K$. (a) P_{12} vs. F_{12} and (b) U, Ψ_{LH} and Ψ_{TI} vs. F_{12}.

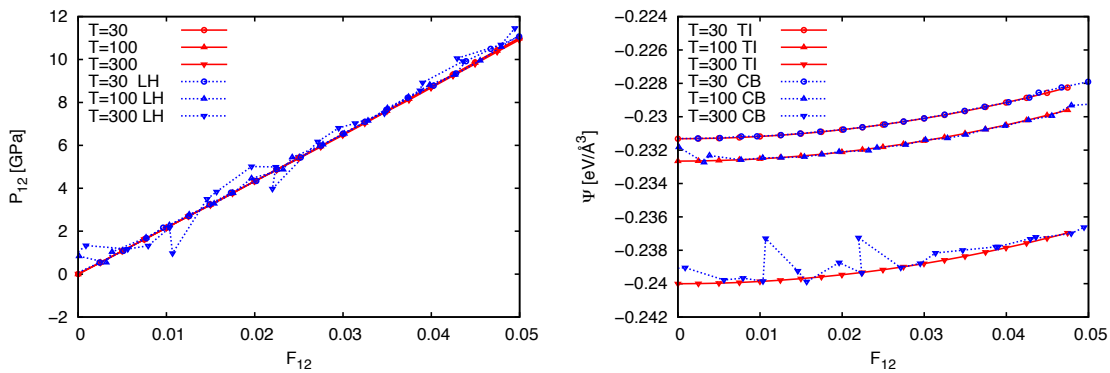

(a) (b)

Figure 79: Biaxial stretch at $T = 30, 100, 300\,K$. (a) P_{12} vs. F_{12} and (b) U, Ψ_{LH} and Ψ_{TI} vs. F_{12}.

10%. Although not completely verified, it appears that our test system is behaving in manner consistent with a linear thermo-elastic material with a free energy of the form [132]:

$$\Psi = \frac{1}{2}\mathbf{H} \cdot \mathbb{C}\mathbf{H} - T\boldsymbol{\alpha} \cdot \mathbf{H} - \frac{1}{2}c_v T^2 \tag{93}$$

where $\mathbb{C} = \frac{\partial^2 \Psi}{\partial \mathbf{H} \partial \mathbf{H}}$ is a (fourth-order) elastic modulus tensor and $\boldsymbol{\alpha} = \frac{\partial^2 \Psi}{\partial \mathbf{H} \partial T}$ is a thermal expansion tensor. It should also be noted that $\boldsymbol{\alpha}$ can be related to a Grüneisen-like tensor $\boldsymbol{\gamma} = -\frac{1}{c_v}\boldsymbol{\alpha}$, which is a well-known measure of the sensitivity of entropy to deformation as well as stress to changes in temperature and therefore related to how the vibrational modes ω_i are affected by these changes.

- EAM system — We performed a similar simulation on a copper system modeled with an EAM potential. The potential used is the one by Foiles et al. [122]. This system is 864 atoms (6 x 6 x 6 unit cells) initially set at the zero temperature lattice constant of 3.615 Å. The system is held at constant volume while being heated up to a temperature of 600 K. Figure 80(a) shows the evolution of internal energy density as measured by the Hardy expression in the Lagrangian frame. As was the case for the pair potential examples, we observe that the variation of internal energy density with temperature is closely approximated by the relation $U = c_v T + U_0$, where c_v is estimated to be 2.1806 x 10^{-5} eV/K (compared with the theoretical value of 2.18892 x 10^{-5} eV/K) and U_0 is estimated to be -0.2997221 eV. Using this approximate relation, we can compare our Cauchy-Born estimate for free energy with one obtained via thermodynamic integration of the internal energy density. This comparison is shown in Figure 80(b). We observe excellent agreement between the two curves shown up to the highest temperature tested of 600 K.

  Finally, we can compare our Cauchy-Born estimate of 1st Piola-Kirchhoff stress with the one obtained via the Hardy formulation. The variation of these estimates with temperature is shown in Figure 81. This figure shows that our three estimates of stress (Hardy's formulation, the Cauchy-Born expression, and the system virial as measured by LAMMPS directly) are in very good agreement, in general. Some discrepancy does occur for temperatures higher than 300 K. This discrepancy is most probably due to approximations used in the Cauchy-Born method, such as use of a local harmonic approximation of the dynamical matrix.

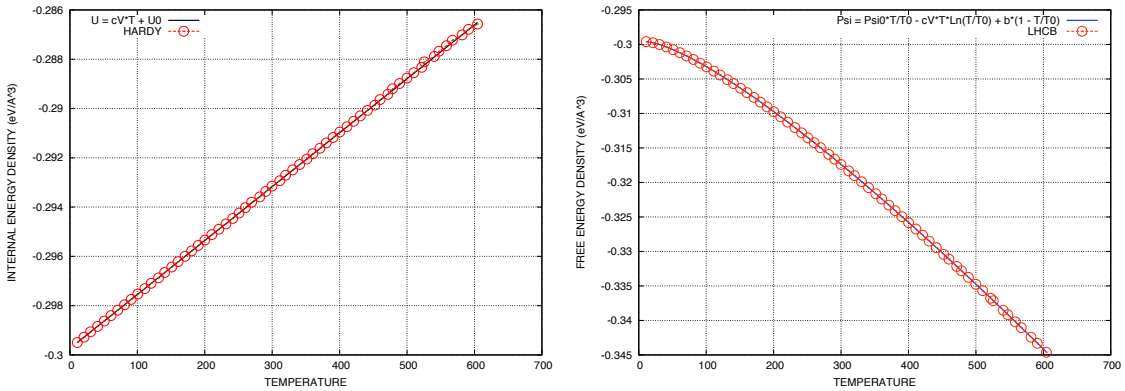

(a) (b)

Figure 80: (a) Internal energy density and (b) free energy density variation with temperature for an EAM-Cu system at constant volume and T_{ref} = 1 K.

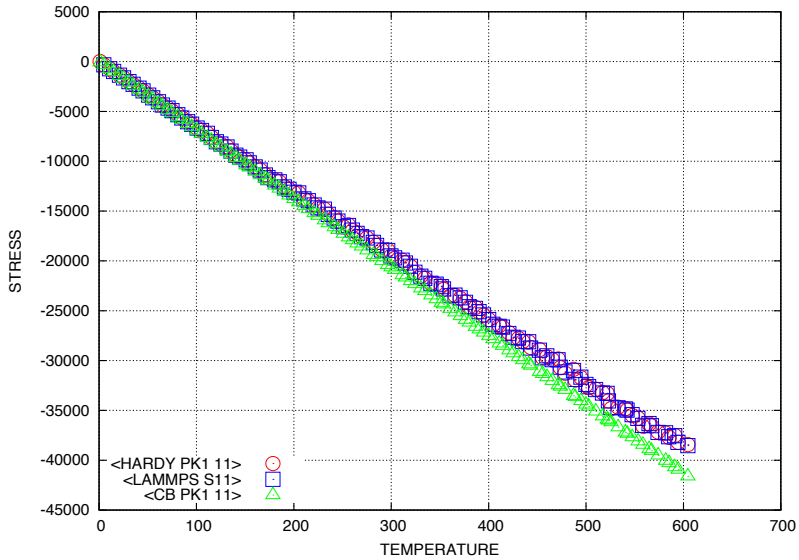

Figure 81: Variation of P_{11} with temperature for an EAM-Cu system at constant volume and T_{ref} = 1 K.

In needs to be emphasized that both MD and QH require high enough temperatures $h\omega \gg k_B T$ for their classical behavior to correspond to real materials, but QH has the additional restriction that the temperature needs to be sufficiently low so that harmonic approximation is still valid. Our results show that that behavior at temperatures at least as high as one-eighth of the effective melt temperature can be simulated sufficiently accurately with LH model. More accurate models like the Modified Local Harmonic (MLH) approximation [130] may extend this result to higher temperatures.

7.5 Plastic Deformation Gradients

Combined use of the Hardy formulation and finite temperature Cauchy-Born method has the potential for separating the elastic and plastic (inelastic) portions of locally-quantified deformation within an atomistic simulation. Performing such a separation enables researchers to use atomistic simulation to gain better insight into the formulation of constitutive models used in continuum mechanical-based finite element analysis. In a continuum framework, the elastic and plastic contributions to strain and deformation gradient is commonly separated in either an additive or multiplicative decomposition. For the incremental case, the full strain increment is taken to be an additive decomposition of elastic and plastic strain, *i.e.*

$$\Delta\boldsymbol{\epsilon} = \Delta\boldsymbol{\epsilon}^e + \Delta\boldsymbol{\epsilon}^p, \tag{94}$$

whereas for the total deformation is a multiplicative decomposition of elastic and plastic deformations, *i.e.*

$$\mathbf{F} = \mathbf{F}^e\mathbf{F}^p, \tag{95}$$

where the side-by-side placement of these two, second-order tensors implies a dot product in the above expression.

Once this separation has been accomplished, it is straightforward to use these individual portions to estimate quantities such as total plastic strain ($\boldsymbol{\epsilon}^p$) and dissipated work due to plastic deformation ($\mathcal{W}^p$). In this section, we propose two such paths for performing this separation, and discuss some of the finer points that need to be considered. Implementation of the formulas defined by these paths is in progress.

7.5.1 Incremental Approach

Here, we consider strain increments between deformation steps. The elastic strain increment is determined using the approximation of linearity in the relationship with stress increment, *i.e.*

$$\Delta\boldsymbol{\epsilon}^e = \mathbb{C}^{-1}(\boldsymbol{\sigma}, T)\Delta\boldsymbol{\sigma}. \tag{96}$$

Here, $\mathbb{C}$ is the 4th order tangent modulus tensor. The plastic strain increment can be calculated by subtracting the elastic strain increment from the total strain increment,

$$\Delta\boldsymbol{\epsilon}^p = \Delta\boldsymbol{\epsilon} - \Delta\boldsymbol{\epsilon}^e, \tag{97}$$

where the total strain increment is estimated by a difference in the symmetric portion of the displacement gradient between loading steps, *i.e.*

$$\Delta\boldsymbol{\epsilon} \approx \left[\frac{1}{2}\left(\frac{\partial\mathbf{u}}{\partial\mathbf{x}} + \left(\frac{\partial\mathbf{u}}{\partial\mathbf{x}}\right)^T\right)\right]_n - \left[\frac{1}{2}\left(\frac{\partial\mathbf{u}}{\partial\mathbf{x}} + \left(\frac{\partial\mathbf{u}}{\partial\mathbf{x}}\right)^T\right)\right]_{n-1}. \tag{98}$$

In this approach, there are several issues that need to be addressed before implementation can occur.

- Issue #1: How should $\mathbb{C}$ be defined? — As we have already learned, the Cauchy-Born rule relates the potential energy of a region of atoms governed by an inter-atomic potential, along with the local temperature, to the free energy density Ψ of a corresponding continuum. The second order derivative of this free energy density with respect to various deformation measures results in different tangent moduli. For example, when Ψ is a function of the Lagrangian strain tensor, $\mathbf{E} = \frac{1}{2}\left(\mathbf{F}^T\mathbf{F} - \mathbf{1}\right)$, the derivative $\mathbb{C} = \frac{\partial^2\Psi}{\partial\mathbf{E}\partial\mathbf{E}}$ is referred to as the material tangent modulus and satisfies the relation

$$\Delta\mathbf{S} = \mathbb{C}\Delta\mathbf{E}, \tag{99}$$

where $\mathbf{S}$ is the 2nd Piola-Kirchoff stress tensor, $\mathbf{S} = \frac{\partial\Psi}{\partial\mathbf{E}}$. Alternatively, when Ψ is a function of $\mathbf{F}$, the derivative $\mathbb{B} = \frac{\partial^2\Psi}{\partial\mathbf{F}\partial\mathbf{F}}$ is referred to as the effective tangent modulus (Gao, *J. Mech. Phys. Solids*, 1996) and satisfies the relation

$$\Delta\mathbf{P} = \mathbb{B}\Delta\mathbf{F}, \tag{100}$$

where $\mathbf{P} = \frac{\partial\Psi}{\partial\mathbf{F}}$. The relation between $\mathbb{B}$ and $\mathbb{C}$ is

$$\mathbb{B} = \mathbf{1}\otimes\mathbf{S} + \mathbf{F}\mathbb{C}\mathbf{F}^T, \tag{101}$$

or, in index notation,

$$B_{iJkL} = \delta_{ik}S_{JL} + F_{iM}C_{MJNL}F_{kN}. \tag{102}$$

Use of the Hardy spatial or material formulations produces the Cauchy stress ($\boldsymbol{\sigma}$) or the 1st P-K stress ($\mathbf{P}$) and both require transformation to arrive at the 2nd P-K stress:

$$\mathbf{S} = \mathbf{F}^{-1}\mathbf{P} = J\mathbf{F}^{-1}\boldsymbol{\sigma}\mathbf{F}^{-T}, \tag{103}$$

where $J = \det(\mathbf{F})$. If $\mathbb{B}$ is known and $\mathbf{S}$ is determined, $\mathbb{C}$ can be found via the relation

$$\mathbb{C} = \mathbf{F}^{-1}\left(\mathbb{B} - \mathbf{1}\otimes\mathbf{S}\right)\mathbf{F}^{-T}. \tag{104}$$

- Issue #2: How do we accumulate plastic strain increments for a total plastic strain? Is knowing the total plastic strain desirable? — It is probable that straight-forward addition of plastic strain increments (in tensor form) is not the correct method to arrive at a total plastic strain for the body. Likewise, addition of elastic strain increments is also incorrect. Many analysts talk in terms of equivalent plastic strain, a scalar summation of the Von Mises equivalent of the strain tensor increments, *i.e.*

$$\epsilon^p = \sum\frac{1}{2}\left(\Delta\boldsymbol{\epsilon}^p : \Delta\boldsymbol{\epsilon}^p - \mathrm{tr}(\Delta\boldsymbol{\epsilon}^p)\right) \tag{105}$$

7.5.2 Total Strain Approach

This approach also uses the Cauchy-Born rule in combination with a thermodynamic relation between stress and strain, this time expression the free energy density as a function of deformation gradient, $\Psi = \Psi(\mathbf{F})$. Hence,

$$\mathbf{P} = \frac{\partial\Psi}{\partial\mathbf{F}} \tag{106}$$

It is assumed in the C-B rule that this deformation is entirely elastic in nature ($\mathbf{F} = \mathbf{F}^e$), and that the hyperelastic function Ψ can be inverted:

$$\mathbf{F}^e = \Psi^{-1}(\mathbf{P}) \tag{107}$$

$\mathbf{P}$ is quantified using the Hardy material frame formulation and fed into the function Ψ^{-1}.

As an analytic form of the free energy density function is not usually known, an alternative methodology is to use an iterative approach with the tangent modulus $\mathbb{B}$. At a given state of deformation, we can estimate $\mathbf{P}$ with both the Hardy expression ($\mathbf{P}_H$) and the Cauchy-Born expression ($\mathbf{P}_{CB}$). For cases of homogeneous deformation (i.e. cases without defect generation), these two estimates will be approximately equal, as we have seen. For cases in which defects are generated and inhomogeneous deformation is induced, they will not be equal as $\mathbf{P}_{CB}$ theoretically depends only on the elastic portion of the deformation gradient, $\mathbf{F}^e$. However, assuming that $\mathbf{F}$ and $\mathbf{F}^e$ are relatively "close" to one another, we can approximate $\mathbf{F}^e$ using the relation

$$\mathbf{P}_H = \mathbf{P}_{CB} + \mathbb{B}\Delta\mathbf{F}, \tag{108}$$

where $\Delta\mathbf{F} = \mathbf{F}^e - \mathbf{F}$. As already mentioned, this process is iterative; starting with a given atomic configuration, we calculate $\mathbf{P}_H$, $\mathbf{F}$, and T using the Lagrangian Hardy formulation. We then use $\mathbf{F}$ and T to compute initial estimates for $\mathbf{P}_{CB}$ and $\mathbb{B}$. Assuming $\mathbb{B}$ is invertible, we then calculate the change $\Delta\mathbf{F}$ needed to satisfy the above equation, i.e. $\Delta\mathbf{F} = \mathbb{B}^{-1}\left(\mathbf{P}_H - \mathbf{P}_{CB}\right)$. This $\Delta\mathbf{F}$ is used to create a new estimate of deformation gradient ($\hat{\mathbf{F}} = \mathbf{F} + \Delta\mathbf{F}$) which is then used for new estimates of the C-B stress and tangent modulus ($\hat{\mathbf{P}}_{CB}$ and $\hat{\mathbb{B}}$, respectively). Upon convergence (i.e. $\hat{\mathbf{P}}_{CB} = \mathbf{P}_H$ to some tolerance), $\hat{\mathbf{F}}$ should equal $\mathbf{F}^e$. From this, plastic deformation can be extracted via a manipulation of the normal multiplicative decomposition,

$$\mathbf{F}^p = \left(\mathbf{F}^e\right)^{-1}\mathbf{F}. \tag{109}$$

As mentioned, implementation of this algorithm is in progress along with testing for simple configurations. Once $\mathbf{F}^p$ is determined, its values between consecutive loading steps should be able to be used to identify a plastic strain increment. Certainly, we can quantify $\Delta\mathbf{F}^p \approx \mathbf{F}^p_n - \mathbf{F}^p_{n-1}$. Alternatively, we can separately define the quantity $\mathbf{E}^p \equiv \frac{1}{2}\left(\left(\mathbf{F}^p\right)^T\mathbf{F}^p - \mathbf{1}\right)$ as a measure of plastic strain relative to some intermediate configuration (*i.e.* neither the reference nor deformed configurations) and then take increments of this quantity, $\Delta\mathbf{E}^p$, between load steps.

Once plastic strain increments are defined in some fashion, we can add them to get an indication of dissipative or plastic work,

$$\mathcal{W}^p \equiv \sum_n \boldsymbol{\sigma}_n : \Delta\boldsymbol{\epsilon}^p, \tag{110}$$

for the incremental approach or,

$$\mathcal{W}^p \equiv \sum_n \mathbf{P}_n : \Delta\mathbf{F}^p \tag{111}$$

for the total strain approach.

7.5.3 Example calculation: uniaxial stretching

We implemented the total strain approach outlined in the last section and used it to examine dislocations and stacking faults created during uniaxial stretching beyond the elastic limit. We simulated an atomic system of gold of dimensions 20 x 20 x 3 unit cells (81.6 Å x 81.6 Å x 12.24 Å) modeled using the EAM potential by Foiles [133]. The system was stretched at increments of 0.5% engineering strain and energy minimization was performed after each increment. Figure 82 shows the system at a total strain of 10.5%, the first point at which inelastic material defects form. This figure, with atoms colored according to their local crystal structure (*i.e.* fcc, hcp, amorphous) shows the formation of partial edge dislocations and stacking faults. It is

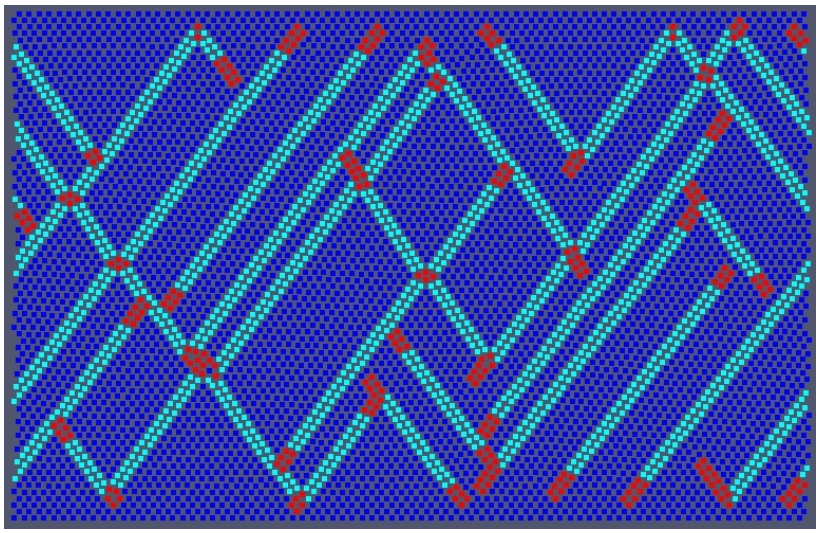

Figure 82: A gold crystal uniaxially stretched to a total engineering strain of 10.5% Atoms are colored according to their local structure (dark blue = fcc, light blue/cyan = hcp, red = no specific structure).

presumed that dislocations form due to local instabilities, then propagate through the crystal leaving stacking faults in their wakes. The dislocations stop propagating when they reach the top or bottom boundary (due to the roller boundary conditions used there), or when they intersect an already-formed stacking fault.

Figure 83(a) shows the same system with atoms colored according to their value of horizontal displacement. We observe a fairly uniform gradient of displacement with minor perturbations due to the created stacking faults and dislocations. This is confirmed in Figure 83(b), which shows the 11-component continuum-estimated displacement gradient field, $\nabla_{\mathbf{X}}\mathbf{u}$. This field is fairly uniform through most of the overlying FE mesh, with some variations.

Figure 84(a) shows the same system with atoms colored according to their value of vertical displacement. We clearly observe strong variations due to the formation of stacking faults. These variations result in non-zero inelastic strains, *i.e.* $\mathbf{F}^p \neq \mathbf{1}$ and $\mathbf{F}^e \neq \mathbf{F}$. Figure 84(b) shows the 11-component elastic deformation gradient field, ($\mathbf{F}^e$). This field shows strong variations that loosely correspond with the faults and dislocations depicted in Figure 82. The field does not show anticipated behavior for $\mathbf{F}^e$ as it does not clearly show the stacking fault line segments present in Figure 82. Further work is in progress to improve our implementation.

7.5.4 Appendix: Thermodynamic integration

To verify our Cauchy-Born based expressions for free energy, we can use direct thermodynamic integration (TI) [134] to calculate the free energy difference between two states connected by a reversible path. TI is based on the differentials of the Helmholtz free energy state function $\Psi(\mathbf{F}, T)$

$$d\Psi = d\Psi(V,T) = d(U - TS) = (TdS - \mathbf{P} \cdot d\mathbf{F}) - TdS - SdT = \mathbf{P} \cdot d\mathbf{F} - SdT \qquad (112)$$

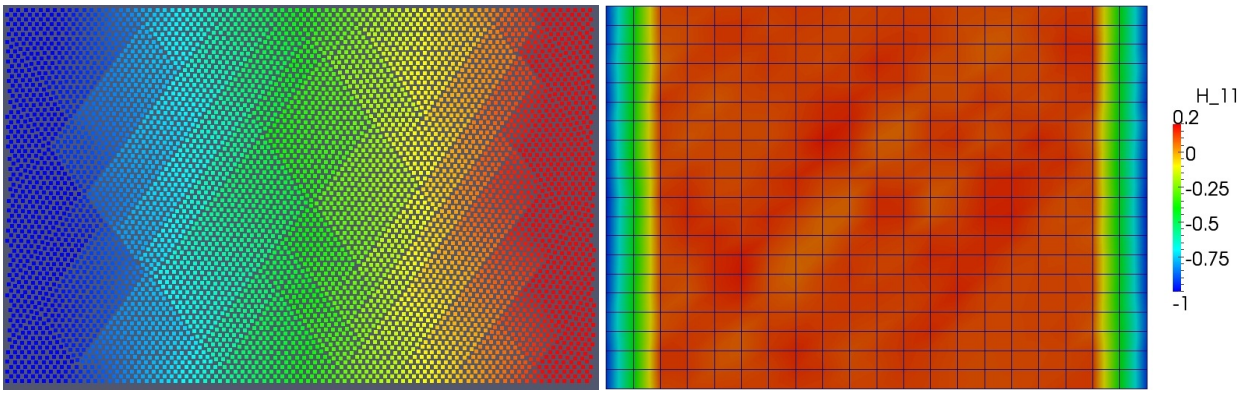

(a) (b)

Figure 83: A gold crystal uniaxially stretched to a total engineering strain of 10.5%: (a) Atomic crystal with atoms colored according to their value of horizontal displacement (range of -10 to 10 Å). (b) Continuum overlay with elements colored according to interpolated nodal values of horizontal displacement gradient.

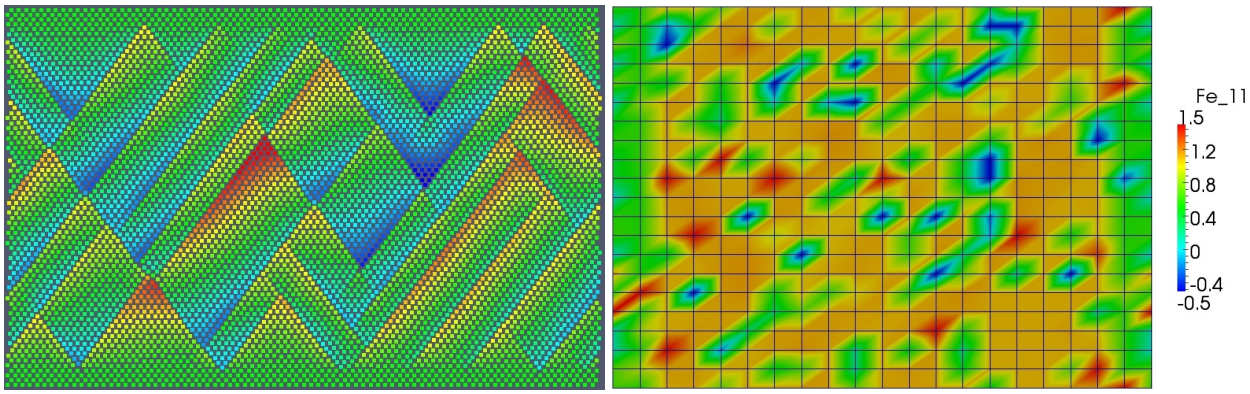

(a) (b)

Figure 84: A gold crystal uniaxially stretched to a total engineering strain of 10.5%: (a) Atomic crystal with atoms colored according to their value of vertical displacement (range of -1.5 to 1.5 Å). (b) Continuum overlay with elements colored according to interpolated nodal values of horizontal elastic deformation gradient.

where $\frac{\partial \Psi}{\partial T}\Big|_{\mathbf{F}} = -S$, $\frac{\partial \Psi}{\partial \mathbf{F}}\Big|_{T} = \mathbf{P}$. Now, a path at constant temperature leads to

$$\Delta\Psi = \int \langle \mathbf{P} \rangle_{NVT} \cdot d\mathbf{F} \quad \rightarrow \quad \Psi_1 = \Psi_0 + \int \langle \mathbf{P} \rangle_{NVT} \cdot d\mathbf{F} \tag{113}$$

and likewise

$$\Delta\left(\frac{\Psi}{T}\right) = \int \langle U \rangle_{NVT}\, dT \quad \rightarrow \quad \Psi_1 = \Psi_0 \frac{T_1}{T_0} + T_1 \int_0^1 \langle U \rangle_{NVT}\, d(1/T) \tag{114}$$

for a path at constant deformation. An example of the first formula for a uniaxial deformation $\mathbf{F} = \lambda \mathbf{e}_1 \otimes \mathbf{E}_1 + \mathbf{e}_2 \otimes \mathbf{E}_2 + \mathbf{e}_3 \otimes \mathbf{E}_3$ is

$$\Psi_1 = \Psi_0 + \int_{\lambda_0}^{\lambda_1} \langle P_{11} \rangle_{NVT}\, d\lambda \tag{115}$$

The second statement (114) is a result of

$$\frac{\Psi}{T} = \frac{U}{T} - S \quad \rightarrow \quad d\left(\frac{\Psi}{T}\right) = U d\left(\frac{1}{T}\right) + \frac{1}{T} dU - dS \quad \rightarrow \quad d\left(\frac{\Psi}{T}\right) = U d\left(\frac{1}{T}\right) \tag{116}$$

which comes from the definition $dS = dS(V,T) = \frac{1}{T} dU$, the assumption that dU is equal to the differential of net heat absorbed, and the differential of the internal energy state function

$$dU = dU(\mathbf{F}, S) = \frac{\partial U}{\partial S}\bigg|_{\mathbf{F}} dS + \frac{\partial U}{\partial \mathbf{F}}\bigg|_{S} d\mathbf{F} = T dS + \mathbf{P} \cdot d\mathbf{F} \tag{117}$$

restricted to constant deformation.

It is well-known that (114) is problematic starting from $T_0 = 0$. Even at small temperatures where the approximation

$$U|_{\mathbf{F}} = aT + b \tag{118}$$

(see Eq. (76)) is valid for a classical system and

$$\tilde{\Psi} = (\Psi_0 - b)\frac{T}{T_0} - aT_0 \frac{T}{T_0} \log\left(\frac{T}{T_0}\right) + b \tag{119}$$

we see that the limit $\lim_{T_0 \to 0} \tilde{\Psi}$ does not exist. Instead we define

$$\Psi_{TI} \approx (\Psi_{\text{ref}} - b)\frac{T}{T_{\text{ref}}} - aT_{\text{ref}} \frac{T}{T_{\text{ref}}} \log\left(\frac{T}{T_{\text{ref}}}\right) + b \tag{120}$$

with $\Psi_{\text{ref}} = \Psi_{LH}(\mathbf{F}, T_{\text{ref}})$ for $T_{\text{ref}} \ll T_{Debye}$. We use this approximation in TI for small temperatures above T_{ref} to avoid the cost of a logarithmic density of quadrature points (i.e. MD samples) needed to accurately evaluate (114) for temperatures near zero.

We observe that $\Psi = U$ at two temperatures. The first point is, of course, at $T = 0$ K. The second point is the the maximum of the $\Psi(T)$ curve at

$$T_{\text{max}} = T_{\text{ref}} \exp\left(\frac{\Psi_{\text{ref}} - b}{aT_{\text{ref}}} - 1\right) \tag{121}$$

which results from solving $\frac{d\Psi}{dT} = 0$. Substituting equation (121) into (120), we verify

$$\begin{aligned}\Psi_{LH}(T_{\text{max}}) &= (\Psi_{\text{ref}} - b)\,\frac{T_{\text{max}}}{T_{\text{ref}}} - aT_{\text{ref}}\frac{T_{\text{max}}}{T_{\text{ref}}}\log\left(\frac{T_{\text{max}}}{T_{\text{ref}}}\right) + b \\ &= aT_{\text{ref}}\exp\left(\frac{\Psi_{\text{ref}} - b}{aT_{\text{ref}}} - 1\right) + b = aT_{\text{max}} + b = U(T_{\text{max}}).\end{aligned} \tag{122}$$

assuming $a = c_v$ and $b = \Phi_0$. This observation provides an independent check on the accuracy of our two methods of estimating the free energy (namely QH and TI).

8 New Methods in LAMMPS

8.1 The LAMMPS SHOCK Package

Principal Authors: J. Matthew D. Lane, Aidan P. Thompson

The LAMMPS SHOCK package supports a set of commands that can be used to perform MD simulations of materials undergoing shock and ramp compression. The list of SHOCK commands are:

```
fix nphug
fix msst
fix wall/piston
fix append_atoms
```

`fix nphug` applies the $NP_{zz}Hug$ Hugoniostat method [115]. `fix msst` applies the Multiscale Shock Technique (MSST) [135]. `fix wall/piston` drives a thermostatted slab of material at a constant or time-dependent velocity, producing a non-equilibrium molecular dynamics simulaiton (NEMD) of shock or ramp compression. `fix append atoms` enables the addition of new material at one end of the sample during an NEMD shock simulation. These commands are described in more detail below.

8.1.1 Hugoniostat (`fix nphug`)

This command is a variant of the Nose-Hoover "fix npt" fix style. It performs time integration of the Hugoniostat equations of motion developed by Ravelo et al. [115]. These equations take a 3D periodic cell and compress it to a state with average axial stress or pressure equal to the specified target value and that satisfies the Rankine-Hugoniot (RH) jump conditions for steady shocks. The syntax for this command is:

fix ID group-ID nphug keyword value ...

where ID, group-ID are documented in fix command. The following keywords may be appended: $temp$, iso, $aniso$, tri, x, y, z, $couple$, $tchain$, $pchain$, mtk, $tloop$, $ploop$, $nreset$, $drag$, $dilate$, $scaleyz$, $scalexz$, $scalexy$. These retain the same meaning as for the "fix npt" command, and are described briefly below:

- $temp$ values = Value1 Value2 Tdamp
  - Value1, Value2 = Nose-Hoover target temperatures, ignored by Hugoniostat
  - Tdamp = temperature damping parameter (time units)
- iso or $aniso$ or tri values = Pstart Pstop Pdamp
  - Pstart,Pstop = scalar external pressures, must be equal (pressure units)
  - Pdamp = pressure damping parameter (time units)
- x or y or z or xy or yz or xz values = Pstart Pstop Pdamp
  - Pstart,Pstop = external stress tensor components, must be equal (pressure units)
  - Pdamp = stress damping parameter (time units)
- $couple$ = none or xyz or xy or yz or xz

- $tchain$ value = length of thermostat chain (1 = single thermostat)
- $pchain$ values = length of thermostat chain on barostat (0 = no thermostat)
- mtk value = yes or no = add in MTK adjustment term or not
- $tloop$ value = number of sub-cycles to perform on thermostat
- $ploop$ value = number of sub-cycles to perform on barostat thermostat
- $nreset$ value = reset reference cell every this many timesteps
- $drag$ value = drag factor added to barostat/thermostat (0.0 = no drag)
- $dilate$ value = all or partial
- $scaleyz$ value = yes or no = scale yz with lz
- $scalexz$ value = yes or no = scale xz with lz
- $scalexy$ value = yes or no = scale xy with ly

Examples:

```
fix myhug all nphug temp 1.0 1.0 10.0 z 40.0 40.0 70.0
fix myhug all nphug temp 1.0 1.0 10.0 iso 40.0 40.0 70.0 &
drag 200.0 tchain 1 pchain 0
```

The compression can be performed either hydrostatically (using keywords iso, $aniso$, or tri) or uniaxially (using keywords x, y, or z). In the hydrostatic case, the cell dimensions change dynamically so that the average axial stress in all three directions converges towards the specified target value. In the uniaxial case, the chosen cell dimension changes dynamically so that the average axial stress in that direction converges towards the target value. The other two cell dimensions are kept fixed (zero lateral strain).

This leads to the following additional restrictions on the keywords:

- One and only one of the following keywords should be used: iso, $aniso$, tri, x, y, z
- The specified initial and final target pressures must be the same.
- The keywords xy, xz, yz may not be used.
- The only admissible value for the couple keyword is xyz, which has the same effect as keyword iso
- The temp keyword must be used to specify the time constant for kinetic energy relaxation, but initial and final target temperature values are ignored.

Essentially, a Hugoniostat simulation is an NPT simulation in which the user-specified target temperature is replaced with a time-dependent target temperature T_t obtained from the following equation:

$$T_t - T = \frac{\left(\frac{1}{2}\left(P + P_0\right)\left(V_0 - V\right) + E_0 - E\right)}{N_{dof} k_B} = \Delta E \tag{123}$$

where T and T_t are the instantaneous and target temperatures, P and P_0 are the instantaneous and reference pressures or axial stresses, depending on whether hydrostatic or uniaxial compression is being performed, V and V_0 are the instantaneous and reference volumes, E and E_0 are the instantaneous and reference internal energy (potential plus kinetic), N_{dof} is the number of degrees of freedom used in the definition of temperature, and k_B is the Boltzmann constant. ΔE is the negative deviation of the instantaneous temperature from the target temperature. When the system reaches a stable equilibrium, the value of ΔE should fluctuate about zero.

The values of E_0, V_0, and P_0 are the instantaneous values at the start of the simulation. These can be overridden using the "fix_modify" keywords $e0$, $v0$, and $p0$ described below.

IMPORTANT NOTE: Unlike the fix temp/berendsen command which performs thermostatting but NO time integration, this fix performs thermostatting/barostatting AND time integration. Thus you should not use any other time integration fix, such as "fix nve" on atoms to which this fix is applied. Likewise, this fix should not be used on atoms that have their temperature controlled by another fix - e.g. by "fix langevin" or "fix temp/rescale" commands.

This fix computes a temperature and pressure at each timestep. To do this, the fix creates its own computes of style "temp" and "pressure", as if one of these two sets of commands had been issued:

```
compute fix-ID_temp group-ID temp
compute fix-ID_press group-ID pressure fix-ID_temp

compute fix-ID_temp all temp
compute fix-ID_press all pressure fix-ID_temp
```

See the "compute temp" and "compute pressure" commands for details. Note that the IDs of the new computes are the "fix-ID + underscore + 'temp'" or "fix–ID + underscore + 'press'". The group for the new computes is "all" since pressure is computed for the entire system. Note that these are NOT the computes used by thermodynamic output (see the "thermo_style" command) with ID = "thermo_temp" and "thermo_press." This means you can change the attributes of this fix's temperature or pressure via the "compute_modify" command or print this temperature or pressure during thermodynamic output via the "thermo_style custom" command using the appropriate compute-ID. It also means that changing attributes of "thermo_temp" or "thermo_press" will have no effect on this fix.

This fix writes the values of E_0, V_0, and P_0, as well as the state of all the thermostat and barostat variables to binary restart files. See the read_restart command for info on how to re-specify a fix in an input script that reads a restart file, so that the operation of the fix continues in an uninterrupted fashion. The fix_modify $e0$, $v0$ and $p0$ keywords can be used to define the values of E_0, V_0, and P_0. Note the the values for $e0$ and $v0$ are extensive, and so must correspond to the total energy and volume of the entire system, not energy and volume per atom. If any of these quantities are not specified, then the instantaneous value in the system at the start of the simulation is used.

The "fix_modify temp" and "fix_modify press" options are supported by these fixes. You can use them to assign a compute you have defined to this fix which will be used in its thermostatting or barostatting procedure, as described above. If you do this, note that the kinetic energy derived from the compute temperature should be consistent with the virial term computed using all atoms for the pressure. LAMMPS will warn you if you choose to compute temperature on a subset of atoms. The fix_modify energy option is supported by these fixes to add the energy change induced by Nose/Hoover thermostatting and barostatting

to the system's potential energy as part of thermodynamic output. Either way, this energy is *not* included in the definition of internal energy E when calculating the value of ΔE in the above equation.

These fixes compute a global scalar and a global vector of quantities, which can be accessed by various output commands. The scalar value calculated by these fixes is "extensive"; the vector values are"intensive". The scalar is the cumulative energy change due to the fix. The vector stores three quantities unique to this fix (ΔE, U_s, and u_p), followed by all the internal Nose/Hoover thermostat and barostat variables defined for "fix_style npt". ΔE is the deviation of the temperature from the target temperature, given by the above equation. U_s and u_p are the shock and particle velocity corresponding to a steady shock calculated from the RH conditions. They have units of distance/time.

The optional keyword defaults are the same as those for "fix npt." $p0$, $v0$, and $e0$ are calculated on the first step.

8.1.2 Multiscale Simulation Technique `(fix msst)`

This command performs the Multi-Scale Shock Technique (MSST) integration to update positions and velocities each timestep to mimic a compressive shock wave passing over the system. See [135] for a detailed description of this method. The MSST varies the cell volume and temperature in such a way as to restrain the system to the shock Hugoniot and the Rayleigh line. These restraints correspond to the macroscopic conservation laws dictated by a shock front. The LAMMPS implementation of this method was created primarily by Evan Reed, now at Standford University, with assistance from Aidan Thompson. The syntax of the command is as follows:

fix ID group-ID msst dir shockvel keyword value ...

- ID, group-ID are documented in fix command
- $msst$ = style name of this fix
- dir = x or y or z
- $shockvel$ = shock velocity (strictly positive, distance/time units)

The following optional keywords may be appended:

- keyword = q or mu or $p0$ or $v0$ or $e0$ or $tscale$
- q value = cell mass-like parameter ($mass^2/distance^4$ units)
- mu value = artificial viscosity ($mass/length/time$ units)
- $p0$ value = initial pressure in the shock equations ($pressure$ units)
- $v0$ value = initial simulation cell volume in the shock equations ($distance^3$ units)
- $e0$ value = initial total energy ($energy$ units)
- $tscale$ value = reduction in initial temperature (unitless fraction between 0.0 and 1.0)

Examples:

```
fix 1 all msst y 100.0 q 1.0e5 mu 1.0e5
fix 2 all msst z 50.0 q 1.0e4 mu 1.0e4  v0 4.3419e+03  &
p0 3.7797e+03 e0 -9.72360e+02 tscale 0.01
```

$shockvel$ determines the steady shock velocity that will be simulated. To perform a simulation, choose a value of q that provides volume compression on the timescale of 100 fs to 1 ps. If the volume is not compressing, either the shock speed is chosen to be below the material sound speed or $p0$ has been chosen inaccurately. Volume compression at the start can be sped up by using a non-zero value of $tscale$. Use the smallest value of $tscale$ that results in compression. Under some special high-symmetry conditions, the pressure (volume) and/or temperature of the system may oscillate for many cycles even with an appropriate choice of mass-like parameter q. Such oscillations have physical significance in some cases. The optional mu keyword adds an artificial viscosity that helps break the system symmetry to equilibrate to the shock Hugoniot and Rayleigh line more rapidly in such cases. $tscale$ is a factor between 0 and 1 that determines what fraction of thermal kinetic energy is converted to compressive strain kinetic energy at the start of the simulation. Setting this parameter to a non-zero value may assist in compression at the start of simulations where it is slow to occur. If keywords $e0$, $p0$,or $v0$ are not supplied, these quantities will be calculated on the first step, after the energy specified by $tscale$ is removed. The value of $e0$ is not used in the dynamical equations, but is used in calculating the deviation from the Hugoniot. Values of $shockvel$ less than a critical value determined by the material response will not have compressive solutions. This will be reflected in lack of significant change of the volume in the MSST. For all pressure styles, the simulation box stays orthogonal in shape. Parrinello-Rahman boundary conditions (tilted box) are supported by LAMMPS, but are not implemented for MSST.

This fix computes a temperature and pressure each timestep. To do this, the fix creates its own computes of style "temp" and "pressure", as if these commands had been issued:

```
compute fix-ID_temp group-ID temp
compute fix-ID_press group-ID pressure fix-ID_temp
```

See the "compute temp" and "compute pressure" commands for details. Note that the IDs of the new computes are the "fix-ID + underscore + 'temp'" or "fix_ID + underscore + 'press'". The group for the new computes is "all". This fix writes the state of all internal variables to binary restart files. See the read_restart command for info on how to re-specify a fix in an input script that reads a restart file, so that the operation of the fix continues in an uninterrupted fashion. The progress of the MSST can be monitored by printing the global scalar and global vector quantities computed by the fix. The scalar is the cumulative energy change due to the fix. This is also the energy added to the potential energy by the fix_modify energy command. With this command, the thermo keyword $etotal$ prints the conserved quantity of the MSST dynamic equations. This can be used to test if the MD timestep is sufficiently small for accurate integration of the dynamic equations. See also thermo_style command. The global vector contains four values in this order:

[$dhugoniot$, $drayleigh$, $lagrangian_speed$, $lagrangian_position$]

- $dhugoniot$ is the departure from the Hugoniot (temperature units).
- $drayleigh$ is the departure from the Rayleigh line (pressure units).
- $lagrangian_speed$ is the laboratory-frame Lagrangian speed (particle velocity) of the computational cell (velocity units).

- $lagrangian_position$ is the computational cell position in the reference frame moving at the shock speed. This is usually a good estimate of distance of the computational cell behind the shock front.

To print these quantities to the log file with descriptive column headers, the following LAMMPS commands are suggested:

```
fix  msst all msst z
fix_modify       msst energy yes
variable dhug    equal f_msst[1]
variable dray    equal f_msst[2]
variable lgr_vel equal f_msst[3]
variable lgr_pos equal f_msst[4]
thermo_style     custom step temp ke pe lz pzz etotal &
v_dhug v_dray v_lgr_vel v_lgr_pos f_msst
```

The optional keyword defaults are q = 10, mu = 0, $tscale$ = 0.01. $p0$, $v0$, and $e0$ are calculated on the first step.

8.1.3 Direct Ramp-loading (`fix wall/piston`)

This command bounds the simulation with a moving wall which reflect particles in the specified group and drives the system with an effective infinite-mass piston capable of driving shock waved. The syntax for this command is as follows:

fix ID group-ID wall/piston face arg ... keyword value ...

- ID, group-ID are documented in fix command
- $wall/piston$ = style name of this fix command
- $face$ = zlo

The following optional keywords may be appended pos, vel, $ramp$, $units$

- pos args = z coordinate at which the piston begins (distance units)
- vel args = vz, final velocity of the piston (velocity units)
- $ramp$ = use a linear velocity ramp from 0 to vz
- $temp$ args = $target\ damp\ seed\ extent$
  - $target$ = target velocity for region immediately ahead of the piston
  - $damp$ = damping paramter (time units)
  - $seed$ = random number seed for langevin kicks
  - $extent$ = distance ahead of the piston within which the thermostat is active (distance units)
- $units$ value = lattice or box

- lattice = the wall position is defined in lattice units
- box = the wall position is defined in simulation box units

Examples:

```
fix xwalls all wall/piston zlo
fix walls all wall/piston zlo pos 1.0 0.0 0.0 vel 0.0 0.0 10.0 units box
fix top all wall/piston zlo vel 0.0 0.0 10.0 ramp
```

A momentum mirror technique is used, which means that if an atom (or the wall) moves such that an atom is outside the wall on a timestep by a distance delta (e.g. due to "fix nve"), then it is put back inside the face by the same delta, and the velocity relative to the moving wall is flipped in z. For instance, a stationary particle hit with a piston wall moving at vz, will end the timestep with a velocity of $2vz$.

Currently only one wall, zlo, may be specified in a single command. This refers to a piston that reflects particles that move to a z coordinate less than the wall position, back in the positive direction. The initial position of each wall can be specified by the pos keyword. The final velocity in z of the wall/piston can be specified by the vel keyword. The $ramp$ keyword will cause the wall/piston to adjust the velocity linearly from zero velocity to vz over the course of the run. If the ramp keyword is omitted then the wall/piston moves at a constant velocity defined by vz.

The $temp$ keyword will cause the region immediately in front of the wall/piston to be thermostated with a Langevin thermostat. This region moves with the piston. The damping and kicking are measured in the reference frame of the piston. So, a temperature of zero would mean all particles were moving at exactly the speed of the wall/piston. The $units$ keyword determines the meaning of the distance units used to define a wall position, but only when a numeric constant is used. The value box selects standard distance units as defined by the units command, e.g. Angstroms for units = real or metal. The value $lattice$ means the distance units are in lattice spacings. The "lattice" command must have been previously used to define the lattice spacings. The zlo boundary must be of type s (shrink-wrapped). The zhi boundary may be any boundary type other than periodic.

The default values for the optional keywords are pos = 0, vel = 0, $units$ = lattice.

8.1.4 Material addition and removal (fix append_atoms)

This fix creates atoms on a lattice, appended on the zhi edge of the system box. This can be useful when a shock or wave is propagating from zlo. This allows the system to grow with time to accommodate an expanding wave. The command syntax is as follows:

fix ID group-ID append_atoms face arg ... keyword value ...

- ID, group-ID are documented in fix command
- $append_atoms$ = style name of this fix command
- $face$ = zhi

The following optional keywords may be appended: $size$, $freq$, $temp$, $random$, $units$.

- $size$ = z coordinate at which the piston begins (distance units)

- $freq$ = the number of timesteps between append events
- $temp$ args = target damp seed extent
  - target = target velocity for region immediately ahead of the piston
  - damp = damping paramter (time units)
  - seed = random number seed for langevin kicks
  - extent = distance from the zhi boundary within which the thermostat is active (distance units)
- $random$ args = xmax ymax zmax seed
  - xmax, ymax, zmax = maximum displacement in particular direction (distance units)
  - seed = random number seed for random displacement
- $units$ value = lattice or box
  - lattice = the wall position is defined in lattice units
  - box = the wall position is defined in simulation box units

Examples:

```
fix 1 all append_atoms zhi size 5.0 freq 295 units lattice
fix 4 all append_atoms zhi size 15.0 freq 5 units box
fix A all append_atoms zhi size 1.0 freq 1000 units lattice
```

Description:

Before using this command, a simulation box must already exist, which is typically created via the "create_box" command. A lattice must also be defined using the "lattice" command. This fix will automatically freeze atoms on the zhi edge of the system, so that overlaps are avoided when new atoms are appended. The $size$ keyword defines the size in z of the chuck of material to be added. The $random$ keyword will give the atoms random displacements around their lattice points to simulate some initial temperature. The $temp$ keyword will cause a region to be thermostated with a Langevin thermostat on the zhi boundary. The size of the region is measured from zhi and is set with the $extent$ argument. The $units$ keyword determines the meaning of the distance units used to define a wall position, but only when a numeric constant is used. The value box selects standard distance units as defined by the units command, e.g. Angstroms for units = real or metal. The value $lattice$ means the distance units are in lattice spacings. The "lattice" command must have been previously used to define the lattice spacings. The zhi boundary on which atoms are added with append_atoms must be of type s (shrink-wrapped). The zlo boundary may be any boundary type other than periodic. The default values for the optional keywords are $size$ = 0.0, $freq$ = 0, and $units$ = lattice.

8.2 Extensions to ATC package

Principal Authors: Jonathan A. Zimmerman, Reese E. Jones, Jeremy A. Templeton

The USER-ATC (Atoms-To-Continuum) package was created to instantiate Eulerian and Lagrangian versions of the Hardy atomistic-continuum formulation discussed earlier in this report. This code operates through a LAMMPS-style fix (atc) that contains routines for constructing a mesh with nodes that act as

fixed spatial or material points, designating the type and characteristics of the localization function used, and calculating the Hardy and Cauchy-Born expressions of various continuum fields, their gradients and time derivatives. Below is a listing of the essential commands used:

fix atc

description: This fix is the beginning to creating an on-the-fly estimation of continuum fields. After instantiating this fix, several other fix_modify commands will be needed to set up the problem, e.g. define the finite element mesh.

syntax: fix [fixID] [group] atc [type] [parameter_file]

- fixID = name of fix
- group = name of group fix is to be applied
- type
  - = hardy : on-the-fly post-processing using kernel localization functions
  - = field : on-the-fly post-processing using mesh-based localization functions
- parameter_file = name of the file with material parameters. For use with estimation of Cauchy-Born fields.

examples

```
fix AtC internal atc hardy
fix AtC internal atc field
fix AtC internal atc Cu_eam.mat
```

---

fix_modify create mesh

description: Creates a uniform mesh in a rectangular region.

syntax: fix_modify [fixID] create mesh [nx] [ny] [nz] [region-id] [f | p] [f | p] [f | p]

- nx ny nz = number of elements in x, y, z
- region-id = id of region that is to be meshed
- f p p = periodicity flags for x, y, z (f = fixed, p = periodic)

examples

```
fix_modify AtC create mesh 10 1  1  feRegion p p p
```

---

fix_modify atom_element_map

description: Sets or changes frame of reference to eulerian or lagrangian and sets the frequency for which the map from atoms to elements is reformed and all the attendant data is recalculated.

syntax: fix_modify [fixID] atom_element_map [eulerian | lagrangian] [frequency]

- frequency (int) : frequency of updating atom-to-continuum maps based on the current configuration - only for eulerian

examples

```
fix_modify atc atom_element_map eulerian 100
```

---

fix_modify kernel

description: Sets type and characteristics of kernel used as localization/averaging function in hardy-based estimation of continuum fields.

syntax: fix_modify [fixID] kernel [type] [parameters]

- type (keyword) = mesh, step, cell, cubic_bar, cubic_cylinder, cubic_sphere, quartic_bar, quartic_cylinder, quartic_sphere
- parameters:

  mesh = none
  step = radius (double)
  cell = hx, hy, hz (double) or h (double)
  cubic_bar = half-width (double)
  cubic_cylinder = radius (double)
  cubic_sphere = radius (double)
  quartic_bar = half-width (double)
  quartic_cylinder = radius (double)
  quartic_sphere = radius (double)

examples

```
fix_modify AtC kernel cell 1.0 1.0 1.0
fix_modify AtC kernel quartic_sphere 10.0
```

---

fix_modify reset_atomic_reference_positions

description: Resets the atomic positions ATC uses to perform point to field operations. In can be used to use perfect lattice sites in ATC but a thermalized or deformed lattice in LAMMPS.

examples

```
fix_modify atc reset_atomic_reference_positions
```

---

fix_modify fields

description: Allows modification of the fields calculated and output by the post-processing transfer class. The commands are cumulative, e.g.

```
fix_modify AtC fields none
```

followed by

```
fix_modify AtC fields add velocity temperature
```

will only output velocity and temperature fields.

syntax:
fix_modify [fixID] fields [all | none]
fix_modify [fixID] fields [add | delete] [list_of_fields]

- all | none (keyword) = output all or no fields
- add | delete (keyword) = add or delete the listed output fields
- fields (keyword) =

  density : mass per unit volume
  displacement : displacement vector
  momentum : momentum per unit volume
  velocity : defined by momentum divided by density
  projected_velocity : simple kernel estimation of atomic velocities
  temperature : temperature derived from the relative atomic kinetic energy (as done by)
  kinetic_temperature : temperature derived from the full kinetic energy
  number_density : simple kernel estimation of number of atoms per unit volume
  stress : Cauchy stress tensor for eulerian analysis (atom_element_map), or 1st Piola-Kirchhoff stress tensor for lagrangian analysis
  transformed_stress : 1st Piola-Kirchhoff stress tensor for eulerian analysis (atom_element_map), or Cauchy stress tensor for lagrangian analysis
  heat_flux : spatial heat flux vector for eulerian, or referential heat flux vector for lagrangian
  energy : total energy (potential + kinetic) per unit volume
  potential_energy : potential energy per unit volume
  number_density : number of atoms per unit volume
  eshelby_stress: configurational stress (energy-momentum) tensor defined by Eshelby
  vacancy_concentration: volume fraction of vacancy content
  type_concentration: volume fraction of a specific atom type
  cauchy_born_energy: free energy per unit volume calculated via the finite temperature Cauchy-Born method
  cauchy_born_stress: Cauchy stress tensor for eulerian analysis (atom_element_map), or 1st Piola-Kirchhoff stress tensor for lagrangian analysis calculated via the finite temperature Cauchy-Born method

examples

```
fix_modify AtC fields add velocity temperature
```

---

fix_modify gradients

description: Requests calculation and ouput of gradients of the fields from the post-processing transfer class. These gradients will be with regard to spatial or material coordinates for eulerian or lagrangian analysis, respectively, as specified by atom_element_map.

syntax: fix_modify [fixID] gradients [add | delete] [list_of_fields]

- add | delete (keyword) = add or delete the calculation of gradients for the listed output fields
- fields (keyword) = gradients can be calculated for all fields listed in 'fix_modify fields'

examples

```
fix_modify AtC gradients add temperature velocity stress
fix_modify AtC gradients delete velocity
```

---

fix_modify rates

description: Requests calculation and ouput of rates (time derivatives) of the fields from the post-processing transfer class. For eulerian analysis, these rates are the partial time derivatives of the nodal fields, not the full (material) time derivatives.

syntax: fix_modify [fixID] rates [add | delete] [list_of_fields]

- add | delete (keyword) = add or delete the calculation of rates for the listed output fields
- fields (keyword) = rates can be calculated for all fields listed in 'fix_modify fields'

examples

```
fix_modify AtC rates add temperature velocity stress
fix_modify AtC rates delete velocity
```

---

fix_modify computes

description: Calculates continuum fields corresponding to specified per-atom computes created by LAMMPS.

syntax: fix_modify [fixID] computes [add | delete] [per-atom compute id] [volume | number]

- add | delete (keyword) = add or delete the calculation of an equivalent continuum field for the specified per-atom compute as volume or number density quantity

- per-atom compute id = name/id for per-atom compute, fields can be calculated for all per-atom computes available from LAMMPS
- volume — number (keyword) = field created is a per-unit-volume quantity or a per-atom quantity as weighted by kernel functions

examples

```
compute virial all stress/atom
fix_modify AtC computes add virial volume
fix_modify AtC computes delete virial

compute centrosymmetry all centro/atom
fix_modify AtC computes add centrosymmetry number
```

---

fix_modify on_the_fly

description: Overrides normal mode of pre-calculating and storing bond pair-to-node and kernel atom-to-node matrices. If activated, will calculate elements of these matrices during repeated calls of field computations (i.e. ”on-the-fly”) and not store them for future use. Note: “on” flag is optional - if omitted, on_the_fly will be activated for the specified matrix. Can be deactivated using “off” flag.

syntax: fix_modify [fixID] on_the_fly [bond | kernel] [optional on | off]

- bond | kernel (keyword) = specifies on-the-fly calculation of bond or kernel
- on | off (keyword) = activate or discontinue on-the-fly mode

examples

```
fix_modify AtC on_the_fly bond on
fix_modify AtC on_the_fly kernel
fix_modify AtC on_the_fly kernel off
```

---

fix_modify set

description: Used to set various quantities for the post-processing algorithms. Currently it only sets the zero point for the potential energy density using the value provided for all nodes, or from the current configuration of the lattice if no value is provided. Defaults to lammps zero point i.e. isolated atoms.

syntax: fix_modify [fixID] set reference_potential_energy [value]

- value (double) : optional user specified zero point for PE

examples

```
fix_modify AtC set reference_potential_energy
fix_modify AtC set reference_potential_energy -0.05
```

---

fix_modify read_restart

description: Reads the current state of the fields from a named text-based restart file.

syntax: fix_modify [fixID] read_restart [file_name]

examples

```
fix_modify AtC read_restart ATC_state
```

---

fix_modify write_restart

description: Dumps the current state of the fields to a named text-based restart file. This done when the command is invoked and not repeated, unlike the similar lammps command.

syntax: fix_modify [fixID] write_restart [file_name]

examples

```
fix_modify AtC write_restart restart.mydata
```

---

fix_modify output

description: Creates text and/or binary (Ensight, "gold" format) output of nodal/mesh data which is transfer/physics specific. Output indexed by step or time is possible, by default output indexed by time.

syntax:
fix_modify [fixID] output [filename_prefix] [frequency] [text | full_text | binary | vector_components | tensor_components]
fix_modify [fixID] output index [step | time]

- filename_prefix (string) = prefix for data files
- frequency (integer) = frequency of output in time-steps
- options (keyword/s):

  text = creates text output of index, step and nodal variable values for unique nodes

  full_text = creates text output index, nodal id, step, nodal coordinates and nodal variable values for unique and image nodes

  binary = creates binary Ensight output

  vector_components = outputs vectors as scalar components

  tensor_components = outputs tensor as scalar components (use this for Paraview)

examples

```
fix_modify AtC output heatFE 100
fix_modify AtC output hardyFE 1 text tensor_components
fix_modify AtC output hardyFE 10 text binary tensor_components
fix_modify AtC output index step
```

---

9 Communications

9.1 Publications

J.M.D. Lane and A.P. Thompson, "Molecular Dynamics Simulation of Shock-Induced Phase Transformation in Germanium," *Shock Compression of Condensed Matter, AIP CP1195,* 1157 (2009).

A.P. Thompson, S.J. Plimpton, and W. Mattson, "General Formulation of Pressure and Stress Tensor for Arbitrary Many-body Interaction Potentials under Periodic Boundary Conditions," *J. Chem. Phys.,* **131** 154107 (2009).

A.P. Thompson, J.M.D. Lane, M.P. Desjarlais, and M.I. Baskes, "Molecular Dynamics Simulation of Dynamic Response of Beryllium," *Shock Compression of Condensed Matter, AIP CP1195*, 833 (2009).

T.R. Mattsson, J.M.D. Lane, K.R. Cochrane, M.P. Desjarlais, A.P. Thompson, F. Pierce, and G.S. Grest, "First-Principles and Classical Molecular Dynamics Simulation of Shock Polymers," *Phys. Rev. B*, **81** 054103 (2010).

J.A. Zimmerman, R.E. Jones and J.A. Templeton, "A Material Frame Approach for Evaluating Continuum Variables in Atomistic Simulations", *Journal of Computational Physics*, **229** 2364 (2010).

R.E. Jones, J.A. Zimmerman, J. Oswald, and T. Belytschko, "An atomistic J-integral at finite temperature based on Hardy estimates of continuum fields", *Journal of Physics: Condensed Matter*, **23** 015002 (2011).

J.M.D. Lane, G.S. Grest, A.P. Thompson, K.R. Cochrane, M.P. Desjarlais, and T.R. Mattsson, "Shock compression of dense polymer and foam systems using molecular dynamics and DFT," accepted *Shock Compression of Condensed Matter* (2011).

A.P. Thompson, J.M.D. Lane, and M.P. Desjarlais, "Molecular Dynamics Simulation of Dynamic Response of Beryllium," accepted *Shock Compression of Condensed Matter* (2011)

J.A. Zimmerman, J.M. Winey and Y.M. Gupta, "Elastic anisotropy of shocked aluminum single crystals: use of molecular dynamics simulations", *Physical Review B*, **83** 184113 (2011) .

J.M.D. Lane and A.P. Thompson, "Scaling relation and characteristic curve extraction for ramp-loading simulation," (submitted to *Phys. Rev. E*).

S. Root, T.A. Haill, J.M.D. Lane, A.P. Thompson, G.S. Grest, D.G. Schroen, and T.R. Mattsson, "Shock Compression of Hydrocarbon Foam to 400 Gpa: experiment, mesoscale modeling and atomistic simulation," (submitted to *Phys. Rev. B*).

9.2 Presentations

J.M.D. Lane and A.P. Thompson, "Molecular Dynamics Simulation of Shock-Induced Phase Transformation in Germanium," APS SCCM, Nashville (June, 2009)

A.P. Thompson, J.M.D. Lane, M.P. Desjarlais, and M.I. Baskes, "Molecular dynamics simulation of dynamic response of beryllium," APS SCCM, Nashville (June, 2009).

J.A. Zimmerman, "Extracting Continuum Variables from Atomistic Simulation," Seminar for Department of Mechanical Engineering, University of Houston (October 29, 2009)

J.A. Zimmerman, "Challenges of and Variations on Coupled Atomistic-Continuum Simulation", Joint U.S.-Russia Conference on Advances in Materials Science, Prague, Czech Republic (August 31 September 4, 2009)

J.A. Zimmerman, "Extracting Continuum Variables from Atomistic Simulation," Seminar for Institute for Shock Physics, Washington State University (July 9, 2009)

J.A. Zimmerman, R.E. Jones and J.A. Templeton, "Evaluating Continuum Variables Within Atomistic Simulations: A Material Frame Approach," 2009 MRS Spring Meeting, San Francisco, CA (April 13-17, 2009)

J.A. Zimmerman, R.E. Jones and J.A. Templeton, "A Material Frame Approach for Evaluating Continuum Variables Within Atomistic Simulations," International Symposium on Plasticity, St. Thomas, U.S. Virgin Islands (January 3-8, 2009)

J.A. Zimmerman, "Atoms-to-Continuum (AtC) user package for LAMMPS," LAMMPS Workshop, Albuquerque, NM (February 24-26, 2010)

J.M.D. Lane and A.P. Thompson, "Characteristic curves of shockless compression from atomistic molecular dynamics," APS March Meeting, Portland (March, 2010)

A.P. Thompson, J.M.D. Lane, M.P. Desjarlais, and M.I. Baskes, "Molecular dynamics simulation of dynamic response of beryllium," APS March meeting, Portland (March, 2010).

J.A. Zimmerman, "Extracting Continuum Variables from Atomistic Simulation," Seminar for Department of Mechanical Engineering, University of Colorado at Boulder (April 8, 2010)

J.M.D. Lane and A.P. Thompson, "Scaling relation in MD simulations of ramp-loading," 4th Workshop on Ramp Compression, Albuquerque (January, 2011)

J.M.D. Lane, G.S. Grest, A.P. Thompson, K.R. Cochrane, M.P. Desjarlais and T.R. Mattsson, "Shock Compression of Hydrocarbon Foam to 400 Gpa: experiment, mesoscale modeling and atomistic simulation," SCCM, Chicago (June, 2011).

A.P. Thompson, "Molecular Dynamics Simulation of Dynamic Response of Beryllium," 2011 TMS Annual Meeting and Exposition, San Diego, CA (February 27 - March 3, 2011)

J.A. Zimmerman, R.E Jones, J.A Templeton and G.J. Wagner, "Atoms-to-Continuum (AtC) user package for LAMMPS," 2011 TMS Annual Meeting and Exposition, San Diego, CA (February 27 - March 3, 2011)

A.P. Thompson, J.M.D. Lane, and M.P. Desjarlais, "Molecular dynamics simulation of dynamic response of beryllium," APS SCCM, Chicago (June, 2011).

J.A. Zimmerman, J.M. Winey and Y.M. Gupta, "Elastic response of shocked aluminum single crystals: a continuum analysis of molecular dynamics simulations," APS SCCM, Chicago (June, 2011).

10 Acknowledgements

Funding for this project came from the Laboratory Directed Research and Development program at Sandia National Laboratories.

References

[1] LAMMPS : Large-scale Atom/Molecular Massively Parallel Simulator, Sandia National Laboratories. website is http://lammps.sandia.gov, 2011.

[2] M. D. Knudson, D. L. Hanson, J. E. Bailey, C. A. Hall, J. R. Asay, and W. W. Anderson. Equation of state measurements in liquid deuterium to 70 gpa. *Phys. Rev. Lett.*, 87(22):225501, 2001.

[3] M. P. Desjarlais. Density-functional calculations of the liquid deuterium Hugoniot, reshock, and reverberation timing. *Phys. Rev. B*, 68(6):064204, 2003.

[4] M. D. Knudson, M. P. Desjarlais, and D. H. Dolan. Shock-wave exploration of the high-pressure phases of carbon. *Science*, 322(5909):1822–1825, 2008.

[5] J. D. Kress, S. R. Bickham, L. A. Collins, B. I. Holian, and S. Goedecker. In M. D. Furnish, L. C. Chhabildas, and R. S. Hixson, editors, *Shock Compression of Condensed Matter - 1999*, volume 13 of *AIP Conf. Proc.*, page 381, Melville, New York, 1999. AIP.

[6] P. Hohenberg and W. Kohn, *Phys. Rev.,* **136**, B864 (1964); W. Kohn and L. J. Sham, *Phys. Rev.,* **140**, A1133 (1965).

[7] K. Chenoweth, A. C. T. van Duin, and W. A.Goddard III. ReaxFF reactive force field for molecular dynamics simulation of hydrocarbon oxidation. *J. Phys. Chem. A*, 112:1040, 2008.

[8] Steven J. Stuart, Alan B. Tutein, and Judith A. Harrison. A reactive potential for hydrocarbons with intermolecular interactions. *J. Chem. Phys.*, 112:6472, 2000.

[9] W. L. Jorgensen, D. S. Maxwell, and J. Tirado-Rives. *J. Am. Chem. Soc.*, 118:11225, 1996.

[10] O. Borodin and G. D. Smith, *J. Phys. Chem. B,* **110**, 6279 (2006); O. Borodin, G. D. Smith, and D. Bedrov, *J. Phys. Chem. B,* **106**, 9912 (2002).

[11] J. E. Bailey, G. A. Chandler, S. A. Slutz, G. R. Bennett, G. Cooper, J. S. Lash, S. Lazier, R. Lemke, T. J. Nash, D. S. Nielsen, T. C. Moore, C. L. Ruiz, D. G. Schroen, R. Smelser, J. Torres, and R. A. Vesey. X-ray imaging measurements of capsule implosions driven by a Z-pinch dynamic hohlraum. *Phys. Rev. Lett.*, 89(9), 2002.

[12] G.A. Rochau, J.E. Bailey, G.A. Chandler, G. Cooper, G.S. Dunham, P.W. Lake, R.J. Leeper, R.W. Lemke, T.A. Mehlhorn, A. Nikroo, K.J. Peterson, C.L. Ruiz, D.G. Schroen, S.A. Slutz, D. Steinman, W.A. Stygar, and W. Varnum. High performance capsule implosions driven by the Z-pinch dynamic hohlraum. *Plasma Physics and Controlled Fusion*, pages B591–B600, 2007.

[13] G. A. Rochau, J. E. Bailey, Y. Maron, G. A. Chandler, G. S. Dunham, D. V. Fisher, V. I. Fisher, R. W. Lemke, J. J. MacFarlane, K. J. Peterson, D. G. Schroen, S. A. Slutz, and E. Stambulchik. Radiating shock measurements in the Z-pinch dynamic hohlraum. *Phys. Rev Lett.*, 100(12), 2008.

[14] W. J. Nellis, F. H. Ree, R. J. Trainor, A. C Mitchell, and M. B. Boslough. Equation of state and optical luminosity of benzene, polybutene, and polyethylene shocked to 210 GPa (2.1 Mbar). *J. Chem. Phys.*, 80:2789, 1984.

[15] J. C. F. Millett and N. K. Bourne. The shock induced equation of state of three simple polymers. *J. Phys. D: Appl. Phys.*, 37:2901–2907, 2004.

[16] N. K. Bourne, J. C. F. Millett, and S. G. Goveas. The shock response of polyoxymethylene and polyethylene. *J. Phys. D: Appl. Phys.*, 40:5714–5718, 2007.

[17] N. K. Bourne and J. C. F. Millett. Tacticity in shocked polymer hydrocarbons. *J. Material Science*, 43:185, 2008.

[18] S. P. March, editor. *LASL Shock Hugoniot Handbook*, Berkeley, CA, 1980. University of California Press.

[19] T. A. Haill, T. R. Mattsson, S. Root, D. G. Schroen, and D. G. Flicker. Mesoscale simulation of shocked PMP foams. *Shock Compression in Condensed Matter Proceedings 2011*, to be submitted.

[20] S. Root, T. A. Haill, J. M. D. Lane, A. P. Thompson, G. S. Grest, D. G. Schroen, and T. R. Mattsson. Shock compression of poly(4-methyl-1-pentene) foams to 400 GPa: experiments and multi-scale simulations. *Phys. Rev. B*, to be submitted, September 2011.

[21] M. L. Elert, S. V. Zybin, and C. T. White. Molecular dynamics study of shock-induced chemistry in small condensed-phase hydrocarbons. *J. Chem. Phys.*, 118:9795, 2003.

[22] S. V. Zybin, M. L. Elert, and C. T. White. Molecular dynamics study of non-reacting shock waves in anthracene. In M. D. Furnish, Y. M. Gupta, and J. W. Forbes, editors, *Shock Compression of Condensed Matter - 2003*, volume 706 of *AIP Conf. Proc.*, pages 306–309, Melville, New York, 2004. AIP.

[23] L. Zhang, S. V. Zybin, A. C. T. van Duin, S. Dasgupta, and W. A. Goddard III. Shock induced decomposition and sensitivity of energetic materials by ReaxFF molecular dynamics. In M. D. Furnish, M. Elert, T. Russell, and C. White, editors, *Shock Compression of Condensed Matter - 2005*, volume 845 of *AIP Conf. Proc.*, page 589, Melville, New York, 2006. AIP.

[24] S. Plimpton. Fast parallel algorithms for short-range molecular dynamics. *J. Comp. Phys.*, 117:1, 1995.

[25] P. E. Blöchl, *Phys. Rev. B,* **50**, 17953 (1994); G. Kresse and D. Joubert, *Phys. Rev. B,* **59**, 1758 (1999).

[26] G. Kresse and J. Hafner, *Phys. Rev. B,* **47**, R558 (1993), *Phys. Rev. B,* **49**, 14251 (1994); G. Kresse and J. Furthmüller, *Phys. Rev. B,* **54**, 11169 (1996).

[27] R. Armiento and A. E. Mattsson. Functional designed to include surface effects in self-consistent density functional theory. *Phys. Rev. B*, 72:085108, 2005.

[28] A. E. Mattsson, R. Armiento, J. Paier, G. Kresse, J. M. Wills, and T. R. Mattsson. The AM05 density functional applied to solids. *J. Chem. Phys.*, 128:084714, 2008.

[29] P. Haas, F. Tran, and P. Blaha. *Phys. Rev. B*, 79:085104, 2009.

[30] J. Paier, M. Marsman, K. Hummer, G. Kresse, I. C. Gerber, and J. G. Ángyán. *J. Chem. Phys.*, 124:154709, 2006.

[31] J. Paier, M. Marsman, K. Hummer, G. Kresse, I. C. Gerber, and J. G. Ángyán. *J. Chem. Phys.*, 125:249901, 2006.

[32] A. E. Mattsson and T. R. Mattsson. AM05 density functional applied to the water molecule, dimer, and bulk liquid. *J. Chem. Theory Comput.*, 5:887–894, 2009.

[33] Richard P. Muller, Ann E. Mattsson, and Curtis L. Janssen. Calculation of chemical reaction energies using the AM05 density functional. *J. Comput. Chem.*, 31:1860, 2010.

[34] E. F. C. Byrd and B. M. Rice. *J. Phys. Chem. C*, 111:2787, 2007.

[35] A. E. Mattsson, R. R. Wixom, and T. R. Mattsson, to be published (2010).

[36] M. D. Knudson and M. P. Desjarlais. *Phys. Rev. Lett.*, 103:225501, 2009.

[37] A. E Mattsson, P. A. Schultz, M. P. Desjarlais, T. R. Mattsson, and K. Leung. Designing meaningful density functional theory calculations in materials science - a primer. *Modelling Simul. Mater. Sci. Eng.*, 13:R1, 2005.

[38] T. R. Mattsson and M. P. Desjarlais. Phase diagram and electrical conductivity of high energy-density water from density functional theory. *Phys. Rev. Lett.*, 97:017801, 2006.

[39] EPAPS Document No. E-PRLTAO-97-036628. Supplemental material to T. R. Mattsson and M. P. Desjarlais, *Phys. Rev. Lett.,* **97**, 017801 (2006).

[40] The use of a high cutoff energy (ENMAX*2.0) and volume changes of the order 10% minimize Pulay errors: http://cms.mpi.univie.ac.at/vasp/vasp/node214.html.

[41] S. L. Rempe, T. R. Mattsson, and K. Leung. *Physical Chemistry Chemical Physics*, 10:4685, 2008.

[42] N.D. Mermin. *Phys. Rev.*, 137:A1441, 1965.

[43] A. Strachan, A. C. T. van Duin, D. Chakraborty, S. Dasgupta, and W. A. Goddard III. Shock waves in high-energy materials: The initial chemical events in nitramine RDX. *Phys. Rev. Lett.*, 91(9):098301, Aug 2003.

[44] J. Budzien, A. P. Thompson, and S. V. Zybin. Reactive molecular dynamics simulations of shock through a single crystal of pentaerythritol tetranitrate. *J. Phys. Chem. B*, 113:13142, 2009.

[45] M. L. Elert, S. V. Zybin, and C. T. White. Molecular dynamics study of shock-induced chemistry in small condensed-phase hydrocarbons. *J. Chem. Phys.*, 118:9795, 2003.

[46] W. L. Jorgensen, J. D. Madura, and C. J. Swenson. *J. Am. Chem. Soc.*, 106:6638, 1984.

[47] O. Borodin, G. D. Smith, and D. Bedrov. *J. Phys. Chem. B*, 106:9912, 2002.

[48] O. Borodin and G. D. Smith. *J. Phys. Chem. B*, 110:6279, 2006.

[49] R. W. Hockney and J. W. Eastwood. *Computer simulation using particles*. Adam Hilger-IOP, Bristol, 1988.

[50] F. Pierce, M. Tsige, O. Borodin, D. Perahia, and G. S. Grest. *J. Chem. Phys.*, 128:214903, 2008.

[51] Accelrys Materials Studio http://accelrys.com/.

[52] A. Liu and S. J. Stuart. Empirical bond-order potential for hydrocarbons: Adaptive treatment of van der Waals interactions. *J. Comput. Chem.*, 29(4):601–611, 2008.

[53] T. R. Mattsson, J. M. D. Lane, K. R. Cochrane, M. P. Desjarlais, A. P. Thompson, F. Pierce, and G. S. Grest. First-principles and classical molecular dynamics simulation of shocked polymers. *Phys. Rev. B*, 81:054301, 2010.

[54] M. B. Boslough and J. R. Asay. *Basic principles of shock compression*, page 7. Springer-Verlag, New York, 1993.

[55] R. Ravelo, B. L. Holian, T. C. Germann, and P. S. Lomdahl. Constant-stress Hugoniostat method for following the dynamical evolution of shocked matter. *Phys. Rev. B*, 70:014103, 2004.

[56] M. French, T. R. Mattsson, N. Nettelmann, and R. Redmer. Equation of state and phase diagram of water at ultrahigh pressures as in planetary interiors. *Phys. Rev. B*, 79:054107, 2009.

[57] T. R. Mattsson and R. J. Magyar. In M. Elert and W. Buttler, editors, *Shock Compression of Condensed Matter - 2009*, volume in of *AIP Conf. Proc.*, page print, Melville, New York, 2009. AIP.

[58] A. E. Ismail, M. Tsige, P. J. in't Veld, and G. S. Grest. Surface tension of normal and branched alkanes. *Molecular Physics*, 105:3155–3163, 2007.

[59] A. Warshel and S. Lifson. Consistent force field calculations. ii. crystal structures, sublimation energies, molecular and lattice vibrations, molecular conformations, and enthalpies of alkanes. *J. Chem. Phys.*, 53(2):582–594, 1970.

[60] W. J. Nellis, M. van Thiel, and A. C. Mitchell. Shock compression of liquid xenon to 130 GPa (1.3 Mbar). *Phys. Rev. Lett.*, 48:816, 1982.

[61] F. P. Bundy. Phase diagrams of silicon and germanium to 200 kbar 1000 degrees C. *J. Chem. Phys.*, 41:3809, 1964.

[62] J. Tersoff. New empirical approach for the structure and energy of covalent systems. *Phys. Rev. B*, 37:6991, 1988.

[63] M. I. Baskes. Modified embedded-atom potentials for cubic materials and impurities. *Phys. Rev. B*, 46:2727, 1992.

[64] K. Gaal-Nagy, A. Bauer, P. Pavone, and D. Strauch. Ab initio study of the enthalpy barriers of the high-pressure phase transition from the cubic-diamond to the beta-tin structure of silicon and germanium. *Comp. Mat. Sci.*, 30:1, 2004.

[65] J. M. D. Lane and M. Marder. *APS SCCM 2005 Proc.*, 845:331, 2006.

[66] K Kadau, T. C. Germann, P. S. Lomdahl, and B. L. Holian. Microscopic view of structural phase transitions induced by shock waves. *Science*, 296:1681, 2002.

[67] N. Bloembergen and P.S. Pershan. *Phys Rev.*, 128:606, 1962.

[68] W. K. Burns and N. Bloembergen. *Phys. Rev. B*, 4:3437, 1971.

[69] C.V. Shank, R. Yen, and C. Hirlimann. *Phys. Rev. Lett.*, 51:900, 1983.

[70] V.V. Yakovlev and S.V. Govorkov. *Appl. Phys. Lett.*, 79:4136, 2001.

[71] B.C. Gundrum, R.S. Averback, and D.G. Cagil. *Appl. Phys. Lett.*, 91:011906, 2007.

[72] W. Grigsby and T. Ditmire. *Appl. Phys. B*, 94:389392, 2009.

[73] W. Grigsby. *PhD thesis, University of Texas*, 2007.

[74] R. G. McQueen et al. *Metallurgical Society Conferences*, 22:44 – 132, 1964.

[75] M. Tsujino et al. *Advanced Materials Research*, 26-28:1291–1294, 2007.

[76] A. Ng and T. Ao. *Phys. Rev. Lett.*, 91:035002, 2003.

[77] K.D. Li and P.M. Fauchet. *Appl. Phys. Lett.*, 51:1747–1749, 1987.

[78] J. M. Winey, A. Kubota, and Y. M. Gupta. A thermodynamic approach to determine accurate potentials for molecular dynamics simulations: thermoelastic response of aluminum. *Modelling Simul. Mater. Sci. Eng.*, 17:055004, 2009.

[79] J. M. Winey, A. Kubota, and Y. M. Gupta. Corrigendum to "a thermodynamic approach to determine accurate potentials for molecular dynamics simulations: thermoelastic response of aluminum". *Modelling Simul. Mater. Sci. Eng.*, 18:029801, 2010.

[80] B. L. Holian and P. S. Lomdahl. Plasticity induced by shock waves in nonequilibrium molecular-dynamics simulations. *Science*, 280:2085, 1998.

[81] K. Kadau, T. C. Germann, P. S. Lomdahl, and B. L. Holian. Microscopic view of structural phase transitions induced by shock waves. *Science*, 296(5573):1681, 2002.

[82] E. M. Bringa, K. Rosolankova, R. E. Rudd, B. A. Remington, J. S. Wark, M. Duchaineau, D. H. Kalantar, J. Hawreliak, and J. Belak. Shock deformation of face-centred-cubic metals on subnanosecond timescales. *Nat. Mater.*, 5:805, 2006.

[83] A. Bishop and P. Messina. Scientific grand challenges in national security: The role of computing at the extreme scale. Technical report, U. S. Department of Energy, 2009.

[84] A.F. Voter and S.P. Chen. Accurate interatomic potentials for Ni, Al and Ni_3Al. In *Characterization of Defects in Materials*, volume 82 of *Materials Research Society Symposium Proceedings*, page 175. Materials Research Society, 1987.

[85] A. F. Voter. Embedded atom method potentials for seven FCC metals: Ni, Pd, Pt, Cu, Ag, Au and Al. Technical Report LA-UR 93-3901, Los Alamos National Laboratories, 1993.

[86] F. Ercolessi and J. B. Adams. Interatomic potentials from 1st-principles calculations — the force-matching method. *Europhys. Lett.*, 26:583, 1994.

[87] Y. Mishin, D. Farkas, M. J. Mehl, and D. A. Papaconstantopoulos. Interatomic potentials for monoatomic metals from experimental data and *ab initio* calculations. *Phys. Rev. B*, 59:3393, 1999.

[88] R J Hardy. Formulas for determining local properties in molecular-dynamics simulations: Shock waves. *Journal of Chemical Physics*, 76(1):622–628, 1982.

[89] J A Zimmerman, E B Webb III, J J Hoyt, R E Jones, P A Klein, and D J Bammann. Calculation of stress in atomistic simulation. *Modelling and Simulation in Materials Science and Engineering*, 12:S319–S332, 2004.

[90] Edmund B Webb III, Jonathan A Zimmerman, and Steven C Seel. Reconsideration of continuum thermomechanical quantities in atomic scale simulations. *Mathematics and Mechanics of Solids*, 13:221–266, 2008.

[91] D. C. Wallace. Irreversible thermodynamics of flow in solids. *Phys. Rev. B*, 22(4):1477–1486, 1980.

[92] R. N. Thurston. *Wave propagation in fluids and normal solids*, volume 1A of *Physical Acoustics: Principles and Methods*, pages 1–110. Academic Press, New York, 1964.

[93] D. C. Wallace. *Thermoelastic Theory of Stressed Crystals and Higher-Order Elastic Constants**, volume 25 of *Solid State Physics*, pages 301–404. Academic Press, New York, 1970.

[94] J. F. Thomas Jr. Second- and third-order elastic constants of alkali metals. *Phys. Rev.*, 175:955, 1968.

[95] V. P. N. Sarma and P. J. Reddy. Third-order elastic constants of aluminum. *Phys. Stat. Sol. A*, 10(2):563, 1972.

[96] R. G. McQueen, S. P. Marsh, J. W. Taylor, J. N. Fritz, and W. J. Carter. page 293. High-Velocity Impact Phenomena. Academic Press, New York, 1970.

[97] H. Huang and J. R. Asay. Reshock and release response of aluminum single crystal. *J. Appl. Phys.*, 101:063550, 2007.

[98] D. C. Wallace. *Thermodynamics of Crystals*. Dover, New York, 1998.

[99] J. M. Winey and Y. M. Gupta. Nonlinear anisotropic description for the thermomechanical response of shocked single crystals: Inelastic deformation. *J. Appl. Phys.*, 99:023510, 2006.

[100] A. Kubota, D. B. Reisman, and W. G. Wolfer. Dynamic strength of metals in shock deformation. *Appl. Phys. Lett.*, 88:241924, 2006.

[101] L.X. Benedict, T. Ogitsu, A. Trave, C.J. Wu, P.A. Sterne, and E. Schwegler. Calculations of high-pressure properties of beryllium: Construction of a multiphase equation of state. *Phys. Rev. B*, 79:064106, 2009.

[102] Peter J. Feibelman and R. Stumpf. Physics of the be(0001) surface core-level spectrum. *Phys. Rev. B*, 50(23):17480, Dec 1994.

[103] S.N. Luo, T.J. Ahrens, T. Cagin, A. Strachan, and W.A. Goddard D.C. Swift. *Phys. Rev. B*, 68:134206, 2003.

[104] M. I. Baskes and R. A. Johnson. *Modelling Simul. Mat. Sci. Eng.*, 2:147, 1994.

[105] V. V. Dremov, A. V. Karavaev, A. L. Kutepov, and L. Soulard. *AIP Conf. Proc.*, 955:305, 2008.

[106] V. V. Dremov, A. V. Karavaev, F. A. Sapozhnikov, M. a. Vorobyova, and L. Soulard. *Shock Compression in Condensed Matter, AIP Proc.*, 1195:837, 2009.

[107] S. M. Valone, M. I. Baskes, and R. L. Martin. Atomistic model of helium bubbles in gallium-stabilized plutonium alloys. *Phys. Rev. B*, 73(21):214209, 2006.

[108] A. Migliori, H. Ledbetter, D.J. Thoma, and T.W. Darling. *J. Appl. Phys.*, 95:2436, 2004.

[109] S. Melchionna, G. Ciccotti, and B. L. Holian. *Mol. Phys.*, 78:533, 1993.

[110] W. J. Evans, M.J. Lipp, H. Cynn, C.S. Yoo, M. Somayazulu, D. Hausermann, G. Shen, and V. Prakapenka. *Phys. Rev. B*, 72:094113, 2005.

[111] M. Desjarlais, M. Knudson, and R. Lemke. Personal Communication, 2009.

[112] C. L. Kelchner, S. J. Plimpton, and J. C. Hamilton. Dislocation nucleation and defect structure during surface indentation. *Physical Review B*, 58(17):11085–11088, 1998.

[113] Stanley P. Marsh, editor. *LASL Shock Hugoniot Data*. University of California Press, 1980.

[114] A. A. Selezenev, A. Yu. Aleynikov, N. S. Ganchuk, P.V. Ermakov, S. N. Ganchuk, J. B. Aidun, and A. P. Thompson. *Shock Compression in Condensed Matter, AIP Proc.*, 1195:821, 2009.

[115] R. Ravelo, B. L. Holian, T. C. Germann, and P. S. Lomdahl. Constant-stress hugoniostat method for following the dynamical evolution of shocked matter. *Phys. Rev. B*, 70:014103, 2004.

[116] R. Courant and K. O. Friedrichs. *Supersonic Flow and Shock Waves*. Springer-Verlag, 1976.

[117] D. S. Drumheller. *Introduction to Wave Propagation in Nonlinear Fluids and Solids*. Cambridge University Press, 1998.

[118] A Ian Murdoch. Some primitive concepts in continuum mechanics regarded in terms of objective space-time molecular averaging: The key role played by inertial observers. *Journal of Elasticity*, 84:69–97, 2006.

[119] R J Hardy, S Root, and D R Swanson. Continuum properties from molecular simulations. In *12th International Conference of the American-Physical-Society-Topical-Group on Shock Compression of Condfensed Matter*, volume 620, Pt. 1 of *AIP Conference Proceedings*, pages 363–366. American Institute of Physics, 2002.

[120] S Root, R J Hardy, and D R Swanson. Continuum predictions from molecular dynamics simulations: Shock waves. *Journal of Chemical Physics*, 118(7):3161–3165, 2003.

[121] Jonathan A. Zimmerman, Reese E. Jones, and Jeremy A. Templeton. A material frame approach for evaluating continuum variables in atomistic simulations. *J. Comp. Phys.*, 229(6):2364–2389, 2010.

[122] S. M. Foiles, M. I. Baskes, and M. S. Daw. Embedded-atom-method functions for the fcc metals Cu, Ag, Au, Ni, Pd, Pt, and their alloys. *Phys. Rev. B*, 33:7983–7991, 1986.

[123] ParaDyn, Sandia National Laboratories: http://www.cs.sandia.gov/∼sjplimp/, 2009.

[124] D. A. McQuarrie. *Statistical Mechanics*. Harper and Row, New York, NY, 1976.

[125] C. Kittel and H. Kroemer. *Thermal Physics*. W.H. Freeman and Company, New York, 2nd edition, 1980.

[126] J H Weiner. *Statistical Mechanics of Elasticity*. Dover Publications, Inc., Mineola, New York, 2nd edition, 2002.

[127] M. Born and K. Huang. *Dynamical Theory of Crystal Lattices*. Oxford University Press, Oxford, UK, 1954.

[128] J. M. Rickman, R. Najafabadi, L. Zhao, and D. J. Srolovitz. Finite–temperature properties of perfect crystals and defects from zero–temperature energy minimization. *J. Phys.: Condens. Matter*, 4:4923–4934, 1992.

[129] N. W. Ashcroft and N. D. Mermin. *Solid State Physics*. Holt, Rinehart and Winston, New York, NY, 1976.

[130] C. J. Kimmer and R. E. Jones. Continuum constitutive models from analytical free energies. *J. Phys.-Cond. Mat.*, 19(32), 2007.

[131] P.A. Klein and J.A. Zimmerman. Coupled atomistic-continuum simulations using arbitrary overlapping domains. *Journal of Computational Physics*, 213:86–116, 2006.

[132] F. Armero and J. C. Simo. A new unconditionally stable fractional step method for non-linear coupled thermomechanical problems. *Intl. J. Numer. Meth. Eng.*, 35:737–766, 1992.

[133] H. S. Park and J. A. Zimmerman. Modeling inelasticity and failure in gold namowires. *Phys. Rev. B*, 72:054106, 2005.

[134] J. G. Kirkwood. Statistical mechanics of fluid mixtures. *Journal of Chemical Physics*, 3:300–313, 1935.

[135] E. J. Reed, L. E. Fried, and J. D. Joannopoulos. *Physical Review Letters*, 90:235503, 2003.

Distribution

1	MS	1322	A.P. Thompson, 1425
1		0899	Technical Library, 9536
1		0321	R.W. Leland 1400
1		0889	J.M.D Lane 1814
1		1189	M.P. Desjarlais 1640
1		1189	S.M. Foiles 1814
1		1189	T.R. Mattson 1641
1		1189	D.G. Flicker 1646
1		1189	A.C. Sun 1814
1		1191	J.L. Porter 1670
1		1195	J.R. Asay 1646
1		1195	J.P. Davis 1646
1		1195	M.D. Knudson 1646
1		1303	G.S. Grest 1114
1		1318	B.A. Hendrickson 1440
1		1322	S.J. Plimpton 1426
1		1322	J.H. Carpenter 1443
1		1322	A.E. Mattsson 1443
1		1322	J.B. Aidun 1425
1		1322	O.E. Strack 1443
1		1393	B.W. Atherton 1672
1		9042	J.W. Foulk III 8246
1		9042	C.D. Moen 8246
1		9042	J. Ostien 8246
1		9042	T. Vogler 8246
1		9153	R.G. Miller 8200
1		9154	M.E. Gonzales 8240
1		9403	L.M. Hale 8246

1	9404	R.E. Jones 8246
1	9404	A. Mota 8246
1	9404	X. Zhou 8246
1	9404	J.A. Zimmerman 8246
1	9409	J. Lee 8365
1	9409	K.K. Mandadapu 8365
1	9409	J.A. Templeton 8365
1	9409	G.J. Wagner 8365

Todd Ditmire
Center for High Energy Density Science
The University of Texas at Austin
1 University Station, #C1510
Austin, TX 78712

Hernan Quevedo
Center for High Energy Density Science
The University of Texas at Austin
1 University Station, #C1510
Austin, TX 78712

Michael I. Baskes
410 Whitewood Pl.
Encinitas, CA 92024

Yogendra Gupta
Institute for Shock Physics
PO Box 642816
Washington State University
Pullman, WA 99164-2816

Michael Winey
Institute for Shock Physics
PO Box 642816
Washington State University
Pullman, WA 99164-2816